



MIT
International Center for
Air Transportation

Systems Analysis of Community Noise Impacts of Advanced Flight Procedures for Conventional and Hybrid Electric Aircraft

This report is based on the PhD Thesis of Jacqueline L. Thomas submitted to the Department of Aeronautics and Astronautics in partial fulfillment of the requirements for the degree of Doctor of Philosophy at the Massachusetts Institute of Technology

Jacqueline Thomas
Committee: Dr. R. John Hansman
Dr. Mark Drela
Dr. Robert H. Liebeck

Report No. ICAT-2020-06
June 2020

MIT International Center for Air Transportation (ICAT)
Department of Aeronautics & Astronautics
Massachusetts Institute of Technology
Cambridge, MA 02139 USA

Technical Report Documentation Page

1. Report No.	2. Government Accession No.	3. Recipient's Catalog No.	
4. Title and Subtitle		5. Report Date	
		6. Performing Organization Code	
7. Author(s)		8. Performing Organization Report No.	
9. Performing Organization Name and Address		10. Work Unit No. (TRAIS)	
		11. Contract or Grant No.	
12. Sponsoring Agency Name and Address		13. Type of Report and Period Covered	
		14. Sponsoring Agency Code	
15. Supplementary Notes			
16. Abstract			
17. Key Words		18. Distribution Statement	
19. Security Classif. (of this report) Unclassified	20. Security Classif. (of this page) Unclassified	21. No. of Pages	22. Price

Systems Analysis of Community Noise Impacts of Advanced Flight Procedures for Conventional and Hybrid Electric Aircraft

by

Jacqueline Thomas

Abstract

Recent changes to aircraft approach and departure procedures enabled by more precise navigation technologies have created noise concentration problems for communities beneath flight tracks. There may be opportunities to reduce community noise impacts under these concentrated flight tracks through advanced operational approach and departure procedures and advanced aircraft technologies. A modeling method to assess their impacts must consider the contributions of aircraft engine and airframe noise sources as they vary with the position, thrust, velocity, and configuration of the aircraft during the flight procedure. The objective is to develop an analysis method to design, model, and assess the community noise reduction possibilities of advanced operational flight procedures performed by conventional aircraft and advanced procedures enabled by future aircraft concepts.

An integrated analysis framework is developed that combines flight dynamics and noise source models to determine the community noise impacts of aircraft performing advanced operational approach and departure procedures. Aircraft noise due to the airframe and engine is modeled using an aircraft source noise module as each noise component varies throughout the flight procedure and requires internal engine performance states, the flight profile, and aircraft geometry. An aircraft performance module is used to obtain engine internal performance states and aircraft flight performance given the aircraft technology level. A force-balance-kinematics flight profile generation module converts the flight procedure definition into altitude, position, velocity, configuration, and thrust profiles given flight performance on a segment-by-segment basis. The system generates single-event surface noise grids that are combined with population census data to estimate population noise exposure for a given aircraft technology level and procedure.

The framework was demonstrated for both advanced approach and departure procedures and advanced aircraft technologies. The advanced procedure concepts include modified speed and thrust departures as well as continuous descent, steep, and delayed deceleration approaches for conventional aircraft. The ability to model advanced aircraft technologies was demonstrated in the evaluation of using windmilling drag by hybrid electric aircraft on approach to allow the performance of steep and delayed deceleration approaches for noise reduction beyond the performance capability of standard gas-turbine aircraft.

Acknowledgments

This work is funded by the US Federal Aviation Administration (FAA) Office of Environment and Energy as a part of ASCENT Project 23 and Project 44. Any opinions, findings, and conclusions or recommendations expressed in this material are those of the author and do not necessarily reflect the views of the FAA or other ASCENT Sponsors. The author would like to acknowledge the support of Chris Dorbian, Joseph DiPardo, and Bill He of the FAA Office of Environment and Energy as well as the Massachusetts Port Authority and HMMH. The author would also like to acknowledge the support and flight test collaboration with Boeing, including the help of Gail Barker and Terry Christenson, as well as with the FAA Technical Center, including Ian Levitt and Andrew Cheng. Finally, the author would like to acknowledge the technical support of NASA.

Contents

1	Introduction and Objectives	16
1.1	Problem Introduction	16
1.1.1	The Community Noise Problem Caused by Approaching and Departing Aircraft	16
1.2	Noise Reduction Opportunities of Conventional Aircraft Performing Advanced Operational Approach and Departure Procedures	19
1.3	Reduction Opportunities of Future Aircraft, Including Hybrid Electric Aircraft with Windmilling Drag	20
1.4	Full Flight Procedure Analysis Requires System Approach	21
1.5	Thesis Objective	24
1.6	Thesis Outline	25
2	Literature Review	26
2.1	Primary Aircraft Noise Sources	26
2.2	Aircraft Noise Improvements Since 1969 and Present Considerations	30
2.3	Existing Aircraft Noise Models	34
2.4	Noise Abatement with Advanced Operational Flight Procedures	38
2.4.1	Lateral Profile Adjustments for Noise Abatement	38
2.4.2	Vertical Flight Profile Adjustments for Noise Abatement	40
2.5	Noise Reduction Opportunities of Advanced Configurations	46
2.5.1	Quiet Drag Concepts	46
2.5.2	Background on Hybrid Electric Aircraft	51
3	Framework for Analyzing Performance and Noise of Advanced Operational Flight Procedures of Conventional Aircraft	58
3.1	Aircraft Performance Model	60
3.1.1	Flight Performance from BADA 4	62
3.1.2	Internal Engine Performance Maps and Geometry from TASOPT	62
3.1.3	Geometry Outputs from External Sources	66
3.2	Flight Profile Generation Module	67
3.3	Component-Based Aircraft Noise Module	73
3.3.1	Turbofan Engine Source Noise Modeling	75
3.3.2	Airframe Source Noise Modeling	78
3.3.3	Noise Propagation and Noise Metric Modeling	79
3.4	Noise Impact Metric Module	80

3.5	Validation of Noise Results of Turbofan Aircraft with Existing Certification Data	82
4	Advanced Operational Flight Procedures of Conventional Aircraft—Evaluation of the Impact of Flight Path Angle and Speed on Community Noise	87
4.1	Impact of Aircraft Flight Path Angle and Speed on Aircraft Source Noise	88
4.1.1	Impact of Flight Path Angle and Speed on Engine Noise	88
4.1.2	Impact of Flight Path Angle and Speed on Airframe Noise	89
4.2	Effect of Aircraft Flight Path Angle and Speed on Departure	89
4.2.1	Options to Change Aircraft Flight Path Angle and Speed on Departure	89
4.2.2	Changing Location of the Start of Acceleration and Flap Retraction	90
4.2.3	Reduced Climb Speed	99
4.2.4	Changing the Climb Angle	104
4.2.5	Operational Implications of Altered Climb Angle Departures	106
4.3	Effect of Aircraft Flight Path Angle and Speed on Approach	107
4.3.1	Options to Change Aircraft Flight Path Angle and Speed on Approach	107
4.3.2	Continuous Descent Approaches	110
4.3.3	Delayed Deceleration Approaches	116
4.3.4	Operational Implications of Continuous Descent and Delayed Deceleration Approaches	124
4.4	ecoDemonstrator 2019 Flight Trials of Delayed Deceleration Approaches	126
4.4.1	Proposed Delayed Deceleration Approach Procedure with 3.77° Final Descent	126
4.4.2	ecoDemonstrator Flight Trials and Comparisons to Modeled Noise Results	133
4.5	Chapter 4 Conclusion	143
5	Framework for Analyzing Performance and Noise of Windmilling Drag and Hybrid Electric Aircraft	145
5.1	Aircraft Performance Model to Include Electrified Engines	147
5.1.1	Hybrid-Electric Aircraft Performance Model	147
5.1.2	Windmilling Engine Drag Model	153
5.2	Component-Based Aircraft Noise Module with Windmilling Fan Noise	156
5.2.1	Windmilling Fan Noise Modeling	157
5.3	Validation of Windmilling Engine Drag Coefficients	166
5.4	Validation of Fan Noise Model Adapted for Windmilling	169
5.4.1	Broadband Fan Noise Model Compared to ANOPP Fan Noise Module at Standard Approach Operating Conditions	169
5.4.2	Fan Noise Model Compared to Existing Data at Windmilling Conditions	171
5.4.3	Windmilling Fan Tone Noise	173
6	Case Studies of Advanced Operational Flight Procedures Performed by Hybrid Electric Aircraft with Windmilling Engine Drag	175
6.1	Hybrid Electric Engine Retrofit Sizing Results	176

6.2	Windmilling Engine Noise versus Drag of Retrofit Hybrid Electric Aircraft . . .	178
6.3	Case Study 1: Performance and Noise Analysis of Steeper Approaches with Windmilling Drag	181
6.3.1	Steeper Approach Profile with Windmilling Drag	182
6.3.2	Single Event Flyover Noise Modeling of the Baseline and Steeper Approaches with Windmilling Drag	183
6.4	Case Study 2: Performance and Noise Analysis of Delayed Deceleration Approaches with Windmilling Drag	190
6.4.1	Delayed Deceleration Approach Profile with Windmilling Drag	190
6.4.2	Single Event Flyover Noise Modeling of Baseline and Delayed Deceleration Approaches with Windmilling Drag	192
6.5	Case Study 3: Performance and Noise Analysis of Combined Delayed Deceleration Steeper Approaches with Windmilling Drag	199
6.5.1	Combined Delayed Deceleration Steeper Approach Profile with Windmilling Drag	199
6.5.2	Single Event Flyover Noise Modeling of Baseline and Combined Delayed Deceleration Steeper Approaches with Windmilling Drag . . .	201
6.6	Chapter 6 Conclusion	205
7	Conclusion	207
7.1	Thesis Framework and Analysis Results Summary	207
7.2	Primary Contributions	211
7.3	Discussion and Future Work	211
	References	213

List of Figures

1-1	Comparison of Conventional, RNAV, and RNP Navigation, Figure from FAA	17
1-2	Arrival and Departure Flight Paths and Noise Complaints at BOS in 2010 and 2017, Figures from [3]	18
1-3	Analysis of Community Noise due to Aircraft on Approach and Departure Requires an Integrated system	22
2-1	Primary Conventional Turbofan Aircraft Noise Sources, Engine and Airframe	27
2-2	Sound Exposure Level Calculation Representation, Figure by A. Trani [17]	30
2-3	85 dB Noise Contour of a 1960s Boeing 727 on Departure Compared to a Modern A320-200, Figure from [11]	31
2-4	Turbojet Aircraft Noise Certification Levels by Year Compared to Noise Stage Levels, Figure from FAA [20]	32
2-5	Concentration of Flight Tracks out of Runway 33L at BOS with the Introduction of RNAV (a) and Decrease in DNL 65 dB Noise Contour at BOS by Year (b), Figures from Massport [27]	33
2-6	Complaint Locations Filed at BOS during 2015-2016 Overlaid on 12 days of Departure Tracks (a) and Arrival Tracks (b), Figures from Massport [27]	34
2-7	Sample NPD Curves for an Airbus A300	35
2-8	Lateral Profile Adjustment Example, BOS 22L RNAV Approach with RNP Overlay; Figure from [3]	39
2-9	Profile for a High Thrust Steep Climb Compared to a Standard Departure, Figure from [1] .	41
2-10	Continuous Descent Approach Concept Compared to a Conventional Approach with Level Segments, Figure from [57]	42
2-11	Steep and Two-Segment Approach Concepts Compared to a 3° Continuous Descent Approach, Figure from [1]	43
2-12	Delayed Gear Deployment Concept	44
2-13	Delayed Deceleration Approach Concept, Figure from [56]	45
2-14	Airbus A320 Fuel Burn and Performance Profiles, Figure from [56]	45
2-15	Resultant Blade Section Forces for Two RPM Operations, V_∞ = free stream velocity, Ωr = rotational velocity at radius r , U = total velocity, α = angle of attack	48
2-16	Using Windmilling Engines as Drag Generators on Descent Concept	49
2-17	Example “Electrified” Aircraft Concepts	52
2-18	Electrified Propulsion Systems	55
3-1	Framework to Analyze Aircraft Community Noise Impacts of Advanced Operational Procedures Composed of Flight Profile Generation and Component-Based Aircraft Noise Models Integrated via Performance Models	60
3-2	Aircraft Performance Module Detailed Inputs and Outputs	61
3-3	Turbofan Engine Layout used in TASOPT’s Engine Sizing [4]	64
3-4	Turbofan Specific Fuel Consumption Variation with Bypass Ratio (μ), Turbine Entry Temperature (TET), and Overall Pressure Ratio, Figure from [100]	65
3-5	Commercial and Military Landing Gear Tire Ratings, from Airplane Design, R. H. Liebeck [103]	67

3-6	Flight Profile Generation Module Detailed Inputs and Outputs	68
3-7	Force-balance Approach to Calculate Each Profile Segment from Procedure Definitions	69
3-8	Force-balance Approach for Takeoff-Roll (a) and Landing Roll (b) to Calculate Each Profile Segment for Profile Definitions	70
3-9	Example Segment Structure for a Departure Procedure	70
3-10	ASDEX Boeing 737-800 Radar Altitude Departure Data Over 20 Days in 2017 from all Runways at BOS	71
3-11	Example Segment Structure for an Approach Procedure	72
3-12	ASDEX Boeing 737-800 Radar Altitude Approach Data into Runway 4R at BOS in 2017	72
3-13	ASDEX Boeing 737-800 Radar Velocity Approach Data into Runway 4R at BOS in 2017	73
3-14	Component-Based Aircraft Noise Module Inputs and Outputs	74
3-15	Required Inputs for the ANOPP Engine Noise Models	76
3-16	(a) Turbofan Engine Layout Used in TASOPT’s Engine Model, (b) Example Outputted Engine Performance Map at Each Engine Component Station for a Boeing 737-800 at a Climb Mach number of 0.4713, Thrust of 62.051 kN/engine, and Altitude of 8,375 ft	77
3-17	Noise Impact Metric Module Framework, population Figure from [47]	81
3-18	Noise Certification Procedures and Microphone Locations	83
3-19	EPNL (dB) for Several Aircraft Types Modeled in ANOPP and AEDT 2b and Compared to Noise certification Data	86
4-1	Typical Departure Procedure Divided into Segments, Consistent with NADP 2	90
4-2	Difference in Acceleration Height on Departure Represented by NADP 1 (3,000 ft acceleration height) and NADP 2 (1,500 ft Acceleration Height) Comparison	91
4-3	ASDEX Radar Altitude and Velocity Data of Boeing 737-800s on Departure at BOS in 2017	92
4-4	Comparison of Altitude, Velocity, and Thrust Profiles for a Narrow Body Aircraft Performing NADP 1 (magenta) and NADP 2 (black)	93
4-5	Undertrack $L_{A,MAX}$ (dB), NADP 2 and NADP 1 Noise for a Representative Narrow Body Aircraft	94
4-6	Reduction in Undertrack $L_{A,MAX}$ (dB), NADP 1 compared to NADP 2 for a Representative Narrow Body Aircraft	94
4-7	NADP 1 and 2 $L_{A,MAX}$ (dB) contours for a Representative Narrow Body Aircraft	95
4-8	ASDEX Radar Altitude and Velocity Data of Boeing 777-300s on Departure at BOS in 2017	96
4-9	Comparison of Altitude, Velocity, and Thrust Profiles for a Wide Body Aircraft Performing NADP 1 (magenta) and NADP 2 (black)	97
4-10	Undertrack $L_{A,MAX}$ (dB), NADP 2 and NADP 1 Noise for a Representative Narrow Body Aircraft	98
4-11	Reduction in Undertrack $L_{A,MAX}$ (dB), NADP 1 compared to NADP 2 for a Representative Narrow Body Aircraft	98
4-12	NADP 1 and 2 $L_{A,MAX}$ (dB) contours for a Representative Narrow Body Aircraft	99
4-13	Reduced Climb Speed Departure Definitions	100
4-14	$L_{A,MAX}$ (dB) Under the Flight Track for 250 knot Climb Speed Departures and 220 knot Climb Speed Departures for a Representative Narrow-Body Aircraft	101
4-15	Reduction in $L_{A,MAX}$ (dB) for 220 knot Compared to 250 knot Climb Speed Departure for a Representative Narrow-Body Aircraft	101
4-16	$L_{A,MAX}$ (dB) Noise Contours 220 and 250 knot Climb Speed Departures for a Representative Narrow-Body Aircraft	102
4-17	$L_{A,MAX}$ (dB) Under the Flight Track for 250 knot Climb Speed Departures and 240 knot Climb Speed Departures for a Representative Wide-Body Aircraft	103
4-18	Reduction in $L_{A,MAX}$ (dB) for 220 knot Compared to 250 knot Climb Speed Departure for a Representative Wide-Body Aircraft	103
4-19	$L_{A,MAX}$ (dB) Noise Contours 240 and 250 knot Climb Speed Departures for a Representative Wide-Body Aircraft	104
4-20	Increased Thrust Departure Definitions	105

4-21	BOS BLZZR4 RNAV Standard and Increased Thrust Departure Noise Contours for the Representative Narrowbody Aircraft	105
4-22	Typical Approach Procedure Divided into Segments	108
4-23	ASDEX Radar Altitude and Velocity Data of Boeing 737-800s Performing ILS Approaches with a 4,000 ft level segment into Runway 4R at BOS in 2017	109
4-24	Comparison of Altitude, Velocity, and Thrust Profiles for a Narrow Body Aircraft Performing Baseline Approaches with Level Segments (black) and Continuous Descent Approaches (magenta)	112
4-25	Reduction in $L_{A,MAX}$ (dB) Under the Flight Track for a Representative Narrow Body Aircraft, Baseline Approaches with Level Segments minus Continuous Descent Approach Noise Impact	113
4-26	Arrival Tracks into BOS Runways in 2017 from ASDEX	114
4-27	Reduction in $L_{A,MAX}$ 60 (dB) Contour for the Representative Narrowbody Aircraft Performing CDAs into Runways at BOS, Baselines with Level Segments minus CDAs	115
4-28	Comparison of Altitude, Velocity, and Thrust Profiles for a Narrow Body Aircraft Performing Standard Deceleration (black) and Delayed Deceleration (magenta) Approaches with 4,000 ft Level Segment	117
4-29	Reduction in $L_{A,MAX}$ (dB) Under the Flight Track for a Representative Narrow Body Aircraft, Standard Deceleration minus Delayed Deceleration Approach Noise Impact	118
4-30	Noise Levels Under the Flight Track for Different Noise Components, Representative Narrow Body Aircraft Approaches with 4,000 ft Level Segment	119
4-31	Comparison of Altitude, Velocity, and Thrust Profiles for a Wide Body Aircraft Performing Standard Deceleration (black) and Delayed Deceleration (magenta) Approaches with a 4,000 ft Level Segment	121
4-32	Reduction in $L_{A,MAX}$ (dB) Under the Flight Track for a Representative Wide Body Aircraft, Standard Deceleration minus Delayed Deceleration Approach Noise Impact	122
4-33	Noise Levels Under the Flight Track for Different Noise Components, Representative Wide Body Aircraft Approaches with a 4,000 ft Level segment	122
4-34	Reduction in $L_{A,MAX}$ 60 (dB) Contour for the Representative Narrow and Wide Body Aircraft Performing Delayed Deceleration Approaches Compared to Standard Deceleration Approaches into Runway 4R at BOS, Standard minus Delayed Deceleration	123
4-35	2019 ecoDemonstrator Boeing 777-200 Test Aircraft, Figure from Boeing	126
4-36	Delayed Deceleration Approach Procedure with 3.77° Final Descent into Runway 31 at Atlantic City International Airport, RNAV procedure diagram from [119]	127
4-37	Comparison of Altitude, Velocity, and Thrust Profiles for the Standard (black) and Proposed (magenta) Approaches	129
4-38	Noise Levels Under the Flight Track for Different Noise Components, Standard and Proposed Procedures	130
4-39	Reduction in $L_{A,MAX}$ (dB) Under the Flight Track for the Boeing 777-200 Performing the Proposed Delayed Deceleration and 3.77° Final Descent Compared to the Standard Deceleration and 3° Final Descent	131
4-40	$L_{A,MAX}$ (dB) Contours for the Boeing 777-200 Performing the Standard and Proposed Approaches into Runway 31 at ACY, Standard minus Proposed Procedure	132
4-41	Reduction in $L_{A,MAX}$ 60 (dB) Contour for the Boeing 777-200 Performing the Approaches into Runway 31 at ACY, Standard minus Proposed Procedure	132
4-42	Flight Profile Data and Modeled $L_{A,MAX}$ (dB) Contours for the Boeing 777-200 ecoDemonstrator Procedure into Atlantic City International Airport	134
4-43	Comparison of Altitude, Velocity, and Thrust Profiles for the Proposed Delayed Deceleration Approach with 3.77° Final Descent (black) and Flown ecoDemonstrator Procedure (magenta)	135
4-44	Flight Profile Data and Modeled $L_{A,MAX}$ (dB) Contours for Baseline 1	136
4-45	Flight Profile Data and modeled $L_{A,MAX}$ (dB) Contours for Baseline 2	137
4-46	Comparison of Altitude, Velocity, and Thrust Profiles for Baseline 1 (black) and ecoDemonstrator Flight (magenta)	138
4-47	Noise Levels Under the Flight Track for Baseline 1 and the ecoDemonstrator Procedure	139

4-48	Comparison of Altitude, Velocity, and Thrust Profiles for Baseline 2 (black) and the ecoDemonstrator Procedure (magenta)	140
4-49	Noise Levels Under the Flight Track for Baseline 2 and the ecoDemonstrator Procedure	141
5-1	Framework to Analyze Aircraft Community Noise Impact of Hybrid Electric Aircraft Utilizing Windmilling Drag on Approach	146
5-2	Aircraft Retrofitting for (a) Standard Turbofan and (b) Turboelectric Fan	147
5-3	Power in and out definitions for a (a) standard turbofan and (b) turboelectric fan	148
5-4	Retrofit Hybrid Electric Aircraft Sizing Loop given Input $Power_{core,conventional}$, $Drag_{conventional}$, $Area_{conventional}$ from TASOPT, Values Labeled with $^{\natural}$ from Hall et al [87] and † from Technology Level Assumptions [95][73]	153
5-5	Actuator Disk Theory Diagram for a Simplified Ducted Fan	154
5-6	Blade Element Theory Diagram (a) and Force Vectors in a Blade Section Diagram (b), Figures from [122]	155
5-7	Component-Based Aircraft Noise Module, Including Windmilling Fan Noise	157
5-8	Representation of Noise Generation by Rotor Wake Turbulence Interacting with Stator, Figure from [124]	158
5-9	Blade Self Noise Representation, Figure from [126]	158
5-10	Representation of Duct Boundary Layer Interaction with Turbulence at Blade Tip, Figure from [125]	159
5-11	Representation of Stalling Blade Noise Mechanism, Figure from [126]	159
5-12	Broadband Fan Noise Components from BFANS used for Modeling Windmilling Fan Noise in Framework	160
5-13	Effect of Rotor Flow on Stator, Figure adapted from [135]	163
5-14	Flow Chart for Modeling Windmilling Fan Noise	164
5-15	Ducted Fan Design Code method, Figure from [136]	165
5-16	CFM56-3 Engine	166
5-17	XROTOR Outputs for Modeled CFM56-7B-Size Engine at the Maximum Windmilling Drag Operating Condition	168
5-18	Turbojet and Turbofan Windmilling: Internal Drag Coefficient versus Specific Thrust and Mach Number; Figures from <i>Gas Turbine Performance, 2nd Ed</i> [137]	169
5-19	Assumed Duct and Hub Geometry used in DFDC to Obtain CFM56-7B Flow Velocities at the Rotor/Stator Leading and Trailing Edges	170
5-20	Fan Noise Component Breakdown Comparison between Boeing 18 in Fan Noise Data and Modeled CFM56-7B Engine; Figure (a) from [71]	172
5-21	Comparison of Fan Noise During an Approach Condition versus Windmilling for Boeing 18 in Fan Noise Data and Modeled CFM56-7B engine; Figure (a) from [71]	173
6-1	Maximum Windmilling Drag versus Velocity of Retrofit Distributed Engine and Supercooled Motors Compared to Conventional Aircraft Gear Drag and Idle Thrust	179
6-2	Broadband Overflight Noise Outputs for Fans of Retrofit Hybrid Electric Aircraft at Altitude 120m	180
6-3	Baseline Profile with 3° Continuous Descent Compared to Steeper Descent Procedure with Windmilling Drag	182
6-4	Modeled Altitude, Velocity, Configuration, and Thrust of the Baseline and Steeper Descent Profile with windmilling drag	183
6-5	$L_{A,MAX}$ Component Breakdown for (a) Baseline Approach and (b) Steeper Descent Windmilling Approach	184
6-6	Reduction in $L_{A,MAX}$ (dB) Under the Flight Track for a Retrofit Hybrid Electric Aircraft Performing a 4.6° Descent with Windmilling Drag Compared to a Conventional Boeing 737-800 Performing a Baseline 3° Descent	185
6-7	$L_{A,MAX}$ (dB) Contours for the Retrofit Hybrid Electric Aircraft Performing a 4.6° Descent with Windmilling Drag Compared to a Conventional Boeing 737-800 Performing a Baseline 3° Descent	186

6-8	Reduction in $L_{A,MAX}$ 60 (dB) Contour for the Retrofit Hybrid Electric Aircraft Performing a 4.6° Descent with Windmilling Drag Compared to a Conventional Boeing 737-800 Performing a Baseline 3° Descent	186
6-9	Modeled Altitude, Velocity, Configuration, and Thrust Baseline, Steeper Descent Profile without Windmilling Drag, and Steeper Descent Profile with Windmilling Drag	188
6-10	$L_{A,MAX}$ (dB) Under the Flight Track for a Retrofit Hybrid Electric Aircraft Performing a 4.6° Descent with Windmilling Drag and 3.4° Descent without Windmilling Drag, and a Conventional Boeing 737-800 Performing a Baseline 3° Descent	189
6-11	Baseline Profile with Standard Deceleration Compared to Delayed Deceleration Procedure with Windmilling Drag	191
6-12	Modeled Altitude, Velocity, Configuration, and Thrust Baseline and Delayed Deceleration Profile with Windmilling Drag	191
6-13	$L_{A,MAX}$ Component Breakdown for (a) Baseline, Standard Deceleration Approach and (b) Delayed Deceleration Windmilling Approach	193
6-14	Reduction in $L_{A,MAX}$ (dB) Under the Flight Track for a Retrofit Hybrid Electric Aircraft Performing a delayed deceleration approach with Windmilling Drag Compared to a Conventional Boeing 737-800 Performing a Baseline Standard Deceleration Approach	194
6-15	$L_{A,MAX}$ (dB) Contours for the Retrofit Hybrid Electric Aircraft Performing a Delayed Deceleration Approach with Windmilling Drag Compared to a Conventional Boeing 737-800 Performing a Baseline Standard Deceleration Approach	195
6-16	Reduction in $L_{A,MAX}$ 60 (dB) Contour for the Retrofit Hybrid Electric Aircraft Performing a Delayed Deceleration Approach with Windmilling Drag Compared to a Conventional Boeing 737-800 Performing a Baseline Standard Deceleration Approach	195
6-17	Modeled Altitude, Velocity, Configuration, and Thrust Baseline Standard Deceleration Profile, Delayed Deceleration Approach Profile without Windmilling Drag, and Delayed Deceleration Approach Profile with Windmilling Drag	197
6-18	$L_{A,MAX}$ (dB) Under the Flight Track for a Retrofit Hybrid Electric Aircraft Performing a Delayed Deceleration Approach with Windmilling Drag and Delayed Deceleration Approach without Windmilling Drag, and a Conventional Boeing 737-800 Performing a Baseline Standard Deceleration Approach	198
6-19	Baseline Profile with Standard Deceleration Compared to Combined Delayed Deceleration Steeper Procedure with Windmilling Drag	200
6-20	Modeled Altitude, Velocity, Configuration, and Thrust Baseline and Combined Delayed Deceleration, Steeper Profile with Windmilling Drag	201
6-21	$L_{A,MAX}$ Component Breakdown for (a) Baseline, Standard Deceleration Approach and (b) Combined Delayed Deceleration and Steeper Windmilling Approach	202
6-22	Reduction in $L_{A,MAX}$ (dB) Under the Flight Track for a Retrofit Hybrid Electric Aircraft Performing a Combined Delayed deceleration Steeper approach with Windmilling Drag Compared to a Conventional Boeing 737-800 Performing a Baseline Standard Deceleration Approach	203
6-23	$L_{A,MAX}$ (dB) Contours for the Retrofit Hybrid Electric Aircraft Performing a Delayed Deceleration Approach with Windmilling Drag Compared to a Conventional Boeing 737-800 Performing a Baseline Standard Deceleration Approach	204
6-24	Reduction in $L_{A,MAX}$ 60 (dB) Contour for the Retrofit Hybrid Electric Aircraft Performing a Combined Delayed Deceleration Steeper Approach with Windmilling Drag Compared to a Conventional Boeing 737-800 Performing a Baseline Standard Deceleration Approach	204

List of Tables

3.1	Summary of Inputs and Solved-for Unknowns to Generate Thrust, Velocity, Configuration, and Flightpath Angle Profiles for each Certification Procedure	84
4.1	Population Exposure Comparison in $L_{A,MAX}$ of the Standard and Increased Thrust BLZZR4 RNAV Departures for the Representative Narrowbody Aircraft	106
4.2	Increase in Total Fuel Burn and Time when Flying an Increased Thrust Departure Compared to a Standard Departure for the Representative Narrowbody Aircraft	107
4.3	Mean Level Segment Altitude and Percentage of Arrivals that were Continuous Descent Approaches by Runway in BOS in 2017	114
4.4	Population Exposure Comparison in $L_{A,MAX}$ of the Continuous Descent Approach Compared to a Baseline Approaches with Level Segments for the Representative Narrowbody Aircraft	116
4.5	Population Exposure Comparison in $L_{A,MAX}$ of the Delayed Deceleration Approaches Compared to Standard Deceleration Approaches into BOS Runway 4R for the Representative Narrow body and Wide body Aircraft	124
5.1	CFM56 Blade Geometry used in Blade Element Theory Model	167
5.2	Overflight Noise Outputs of ANOPP and BFANS for a Representative CFM56-7B Engine at Altitude 120m	170
5.3	Broadband versus Tone Overflight Noise Outputs of ANOPP for a Representative CFM56-7B Engine at Altitude 120m	174
6.1	Hybrid Retrofit Technology Level Assumptions	177
6.2	Boeing 737-800 Retrofit Results Assuming Maintained Mission Range and Velocity, Airframe Geometry, at Different Technology Levels	178
6.3	RPM at Maximum Windmilling Drag (Assumed to Occur at Minimum RPM before Blade Tip Stall) versus Aircraft Velocity	179
6.4	Population Exposure of Baseline Approach Procedure versus Windmilling Steeper Descent Approach	187
6.5	Contour Area of Baseline Approach Procedure versus Windmilling Delayed Deceleration Approach	196
6.6	Population Exposure of Baseline Approach Procedure versus Combined Delayed Deceleration Steeper Approach with Windmilling Drag	205
7.1	Summary of Advanced Procedure Noise Impact for Conventional Aircraft	209
7.2	Summary of Advanced Procedure Noise Impact for Hybrid Electric Aircraft Using Windmilling Drag	210

List of Acronyms

AEDT	FAA Aviation Environmental Design Tool
A	Area
AC	Alternating Current
ANOPP	NASA Aircraft NOise Prediction Program
AR	Aspect Ratio
ASDEX	Airport Surface Detection Equipment, Model X
ATC	Air Traffic Control
ATL	Atlanta Hartsfield-Jackson International Airport
BADA 4	Base of Aircraft Data Family 4
BFANS	Broadband Fan Noise Prediction System
BOS	Boston Logan Airport
BPR	Bypass Ratio
CDA	Continuous Descent Approach
CAEP	Committee on Aviation Environmental Protection
C_D	Drag Coefficient
C_L	Lift Coefficient
CLT	Charlotte Douglas Airport
d	Fan Diameter
dB	Decibel
DC	Direct Current
DDA	Delayed Deceleration Approach
DFDC	Ducted Fan Design Code
DNL	Day-Night Annual Average Sound Level
EPNL	Effective Perceived Noise Level
FAA	Federal Aviation Administration
FAR-36	Federal Aviation Rule Part 36
ICAO	International Civil Aviation Organization
ILS	Instrument Landing System
$L_{A,MAX}$	Maximum A-Weighted Sound Pressure Level
LNAS	Low Noise Augmentation System
loc	Engine Station Location
M	Mach Number
MLW	Max Landing Weight
MTOW	Max Takeoff Weight
NAVAIDS	Radio Navigation Aids
NADP	Noise Abatement Departure Procedure
NPD	Noise-Power-Distance
P	Power
Pa	Pascals
PBN	Precision-Based-Navigation
pt	Total Pressure
r	radial location
Re	Reynolds Number

RNAV	Area Navigation
RNP	Required Navigation Performance
SEA	Seattle-Tacoma
SEL	Sound Exposure Level
SNA	John Wayne Airport
S_{Ref}	Reference Area
SPL	Sound Pressure Level
TASOPT	Transport Aircraft System OPTimization
Tt	Total Temperature
u	Flow Velocity (used in TASOPT)
V	Velocity
V_2	Aircraft Takeoff Safety Speed
V_{REF}	Aircraft Landing Reference Speed
V_{stall}	Aircraft Stall Speed
α	Angle of Attack
ρ	density
η	efficiency
Ω	Rotation Rate

Chapter 1

Introduction and Objectives

1.1 Problem Introduction

This thesis presents an analysis framework to model community noise impacts of advanced operational approach and departure procedures for conventional and hybrid electric aircraft. The goal of the framework is to combine the aircraft, flight procedure, and component-based noise analysis to design, model and assess community noise reduction possibilities of advanced operational flight procedures flown by conventional aircraft and aircraft with advanced technologies. The utility of this framework is demonstrated with the design and the performance and noise analysis of advanced flight procedures for conventional aircraft and hybrid electric aircraft utilizing windmilling drag.

1.1.1 The Community Noise Problem Caused by Approaching and Departing Aircraft

Community noise near airports produced by aircraft on approach and departure is an important factor in aircraft environmental impact assessments and many methods have been formulated to assess aircraft noise impacts. Historically, regulations for community noise surrounding airports due to approaching and departing aircraft have been focused on regions near final approach or initial takeoff. This can be seen in regulatory noise limitations

for civil turbojet aircraft which are defined for conditions close to the airport, such as the Federal Aviation Rule Part 36 (FAR-36) standards [1] which regulate the maximum allowed total effective perceived noise due to aircraft within 3.5 nmi from the airport. In addition, the U.S. Federal Aviation Administration legal definition of the region of significant noise exposure around airports is the 65 dB Day-Night Annual Average Sound level (DNL) contour [2], which also concentrates close to the airport runway ends. In these regions, aircraft are typically at steady state climb or descent rate, velocity, thrust level, and configuration.

Recent changes to approach and departure procedures for aircraft enabled by more precise navigation technologies have resulted in noise concentration further from the airport. As shown in Figure 1-1, navigation was historically accomplished via routes defined by radio navigation aids (NAVAIDS) located on the ground or by heading vectors. Approach and departure procedures would vary as a result of navigational precision and the timing of air traffic controller instruction given during a route. Aircraft on approach and departure have since adopted higher precision Performance-Based-Navigation (PBN) approach and departure procedures, such as Area Navigation Procedures (RNAV) and Required Navigation Performance (RNP) procedures, also illustrated in Figure 1-1. PBN procedures, due to increased precision, result in flight track concentration as opposed to the natural variation in flight tracks that existed when less precise navigation technology was still used.

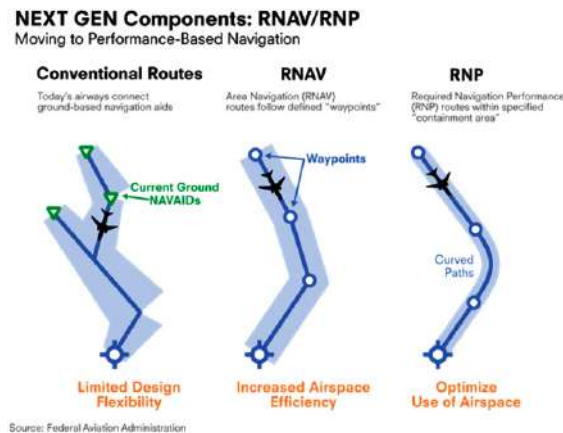


Figure 1-1: Comparison of Conventional, RNAV, and RNP Navigation, Figure from FAA

An example of this concentration of flight tracks can be seen in Figure 1-2, which

compares flight tracks out of Boston Logan Airport in 2010 (a) before these procedures were implemented, and in 2017 (b) after they were implemented. Locations where complaints were filed by the surrounding communities due to the noise of approaching and departing aircraft are shown in the red dots.

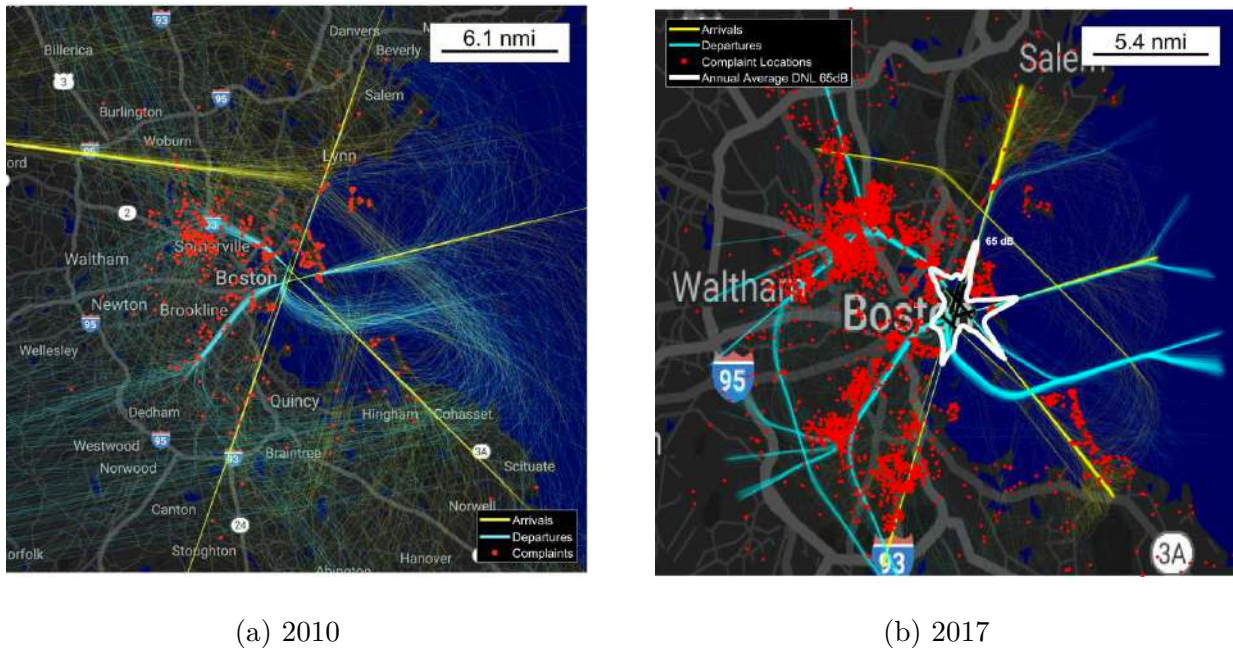


Figure 1-2: Arrival and Departure Flight Paths and Noise Complaints at BOS in 2010 and 2017, Figures from [3]

As Figure 1-2 also indicates, there is a correlation between the locations of concentrated flight tracks and the increase in the number of complaint locations. The complaint locations also concentrate further from the airport and at lower noise levels than than the 65 DNL contour, represented in white in Figure 1-2 (b).

There is a desire to mitigate the noise under these concentrated flight tracks further from the airport. In the regions close to the airport, aircraft are typically at steady-state climb or descent rate, velocity, thrust level, and configuration. However, in the regions after initial takeoff and before final approach, there is more flexibility in aircraft lateral and vertical trajectories, and aircraft are not in steady state flight or operating conditions. Advanced operational approach and departure procedures, where aircraft are maneuvered or operating at velocity, thrust, or configuration states that are different from standard procedures, may

result in noise reductions further from the airport. Future aircraft may also be capable of performing certain advanced operational flight procedures beyond the capabilities of current aircraft and that may yield additional noise benefits.

1.2 Noise Reduction Opportunities of Conventional Aircraft Performing Advanced Operational Approach and Departure Procedures

Advanced operational flight procedures are one method to reduce aircraft noise in regions further from the airport. Flight procedures are the operational description of how the aircraft will fly. Modifications to standard approach and departure procedures in the vicinity of the airport typically consist of one of two types. The first type is modification to the lateral track. Lateral flight tracks can be designed to reduce noise impact by being positioned to avoid over-flight of sensitive communities.

The second type is the modification to the vertical procedure, which includes altering the thrust, altitude, velocity, and configuration profiles in order to reduce community noise compared to standard flight procedures. Aircraft noise is attributed engine noise components, airframe noise components, and the distance between the aircraft and the observers. Engine noise is impacted primarily by the thrust and velocity in the flight procedure, while airframe noise is impacted primarily with velocity and configuration setting. Noise reduction with this method involves maneuvering or trading thrust, altitude, and speed of the aircraft such that the cumulative noise produced by the aircraft, due to both its engine and airframe source components as well as its altitude per distance from the runway, is reduced compared to standard procedures. This is particularly effective in regions outside the traditional 65 dB DNL contour where aircraft are typically at higher altitudes and have flexibility in how they are maneuvered. These regions are also outside the locations traditionally monitored for Federal Aviation Rule Part 36 (FAR-36) noise standard [1].

1.3 Reduction Opportunities of Future Aircraft, Including Hybrid Electric Aircraft with Windmilling Drag

Additional methods for reducing community noise exposure beneath flight tracks may be possible with advanced concepts enabled by future aircraft. Aircraft source noise may be improved with future aircraft configurations or technologies. For example, these may include improved engine technologies that are quieter than current gas-turbine engines commonly used in civil aviation, by advanced configurations that enable engine noise shielding by the airframe, through overall cleaner airframes, or through quieter drag and configuration techniques that either reduce the noise of or replace standard high noise speed brakes, high lift devices, and landing gear that are deployed in approach procedures.

Additionally, advanced aircraft configurations or technologies may offer improvements to the performance of certain advanced operational flight procedures. For example, in order to reduce community noise exposure to aircraft on approach, aircraft should maintain a high altitude for as long as possible in the form of continuous descent or steep approaches to take advantage of additional noise attenuation through the atmosphere [1]. Performing such procedures requires aircraft to have enough drag on approach for controllability. However, as demonstrated in the Breguet range equation, fuel expended in flight is directly proportional to the aircraft drag, thus designs for more energy efficient transport aircraft require aircraft with increasingly less drag [4]. To remove energy on approach, aircraft must fly level segments or deploy high noise, high drag devices such as high lift devices, speedbrakes, or landing gear [5], thus resulting in noisier approaches.

An alternative high drag mechanism that has potential to produce less noise for the same drag as high lift devices, landing gear, or speedbrakes on approach is windmilling engines. Windmilling, where engines are driven by the external flow or operated at low rotation rates, is an alternative mechanism to create drag during descent that is potentially quieter than bluff body drag such as landing gear. While typically associated with engine failure for traditional gas-turbine engines, windmilling is possible in architectures where the

fan is powered by an electric motor, such as in certain hybrid electric or full electric aircraft configurations.

Many studies have shown that noise reduction potential can be greatest through an examination of not only reducing noise at the aircraft source but also by reducing noise via operational adjustments [6][7][8][9] [10] [5]. When noise is considered in the development of future aircraft, it can become an additional value attribute for these concepts.

1.4 Full Flight Procedure Analysis Requires System Approach

The previous sections described methods for reducing the noise impacts to communities further from the airport via advanced operational approach and departure procedures both for current aircraft and future aircraft; however such procedures have to modeled in order for their potential noise impacts to be assessed. Analysis of community noise due to aircraft in full approach and departure procedures, including regions before final approach or after initial takeoff where aircraft fly in non-steady state conditions, requires modeling the aircraft, flight procedure, and noise sources. These components are all interconnected, and thus must be examined as an integrated system, as diagrammed in Figure 1-3.

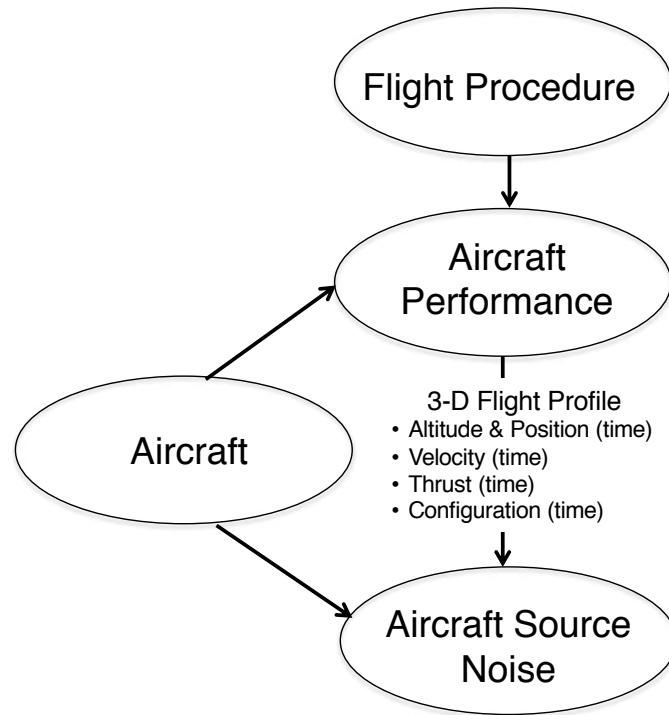


Figure 1-3: Analysis of Community Noise due to Aircraft on Approach and Departure Requires an Integrated system

This system is summarized as follows:

- Flight procedures are the operational description of how the aircraft will fly and the full procedure includes regions where the aircraft state varies
- The aircraft flies that procedure, its performance will determine the non-steady state conditions to yield the 3-D flight profile and will influence aircraft noise sources
- Aircraft source noise is dependent on the aircraft and the flight profile.

More specifically, noise in advanced operational flight procedures must be modeled with enough detail such that the varying contributions of each noise component are reflected. Flight procedures define the three dimensional aircraft position, thrust, velocity, and configuration profiles as a function of time. These profiles are dependent on one another by the aircraft drag performance and weight as well as wind conditions. Aircraft noise is attributed to both engine and airframe sources [11] and the contribution of each component varies differently with the position, thrust, velocity, and configuration of the aircraft during the flight procedure. While in the past it was reasonable to approximate noise impact by

examining the aircraft in the steady state conditions on final approach or initial takeoff close to the airport, aircraft can be operated with more flexibility in its procedure further from the airport and thus the component noise impacts due to operational variability must be considered.

Given an aircraft design, various flight procedure modifications within its performance capabilities can be implemented strategically to alter the position, altitude, velocity, configuration, and thrust and yield a resulting community noise reduction on approach or departure. Additionally, the magnitude of generated noise sources will also depend on aircraft aircraft specific geometry and internal engine states.

In order to be able to model the full range of options for different advanced operational flight procedures for both current and future aircraft, a modeling method must be developed that goes beyond existing capabilities.

Existing methods for analyzing aircraft flight procedure noise can be summarized in two primary categories: noise-power-distance (NPD) based models and noise source component models. NPD models are interpolations of noise from data tables of existing aircraft and engines. Examples models that utilize NPD methods include the Aviation Environmental Design Tool, which is the standard tool in the US to provide FAA stakeholders with environmental impact information [12]. Such data tables consist of noise measured during flight tests of existing aircraft and engine combinations. These methods are useful for quickly simulating many approach and departure events. However, these methods are limited to the aircraft and engine combinations as well as aircraft states available in their databases, and thus model resolution is not good enough to assess complex flight procedures or future technologies.

Alternatively, noise source component models contain functional relationships between the various aircraft noise sources and the aircraft operation state. Example methods include the NASA Aircraft NOise Prediction Program (ANOPP), which contains a series of modules for analyzing aircraft component level noise based on a combination of semi-empirical and physics based methods. The functional relationships depend on geometry or state information about the aircraft, such as wing or turbine entry temperature, rather than a named aircraft or engine. Such methods enable assessment of noise due to detailed aircraft

components, but require extensive set of inputs and are not well set up on their own to consider the entire flight procedure because these inputs will vary in the non-steady state regions of the flight procedure. Component level source noise modeling requires an extensive set of information about the aircraft attributes including the aircraft geometry, internal engine states including performance at design and off-design conditions, and high lift device and landing gear configuration, throughout the flight procedure. The details of the flight procedures assessed must also be modeled with accurate aircraft performance estimations.

1.5 Thesis Objective

Advanced operational approach and departure procedures performed by conventional and future aircraft have the potential to reduce community noise. To model the noise impacts of these procedures, there is a need for modeling techniques that can evaluate advanced operational flight procedures away from the airport that include noise impacts due to the aircraft position, thrust, velocity, and configuration setting as well as considerations for future aircraft concepts.

Thus the thesis objective is to:

- Develop systems analysis method that combines the aircraft, flight procedure, and component-based noise analysis to design, model, and assess community noise reduction possibilities of advanced operational flight procedures flown by conventional aircraft and aircraft with advanced technologies
- To exercise the analysis method through the examination of several noise abatement approach and departure procedure concepts performed by conventional aircraft and assessing the community noise impacts compared to standard procedures
- To exercise the analysis method through the examination of several advanced noise abatement approach procedure concepts enabled by advanced concepts. The particular example is the examination of hybrid electric aircraft implementing windmilling drag on approach and comparing the noise impacts of conventional gas-turbine engine aircraft to showcase the additional noise reduction potential

1.6 Thesis Outline

Given the research goals above, the thesis is structured as follows.

Chapter 2 gives background of historical and current trends in community noise surrounding airports. Followed is a summary of the literature of existing noise analysis methods and advanced operational flight procedures that have potential for noise reduction.

Chapter 3 describes the framework developed to model advanced operational approach and departure procedures for conventional aircraft. This chapter details the flight profile generation method, the aircraft performance model for turbofan aircraft, the component-based aircraft noise model, and the community noise impact assessment module. It concludes with validation of the noise of several aircraft types against existing certification data.

Chapter 4 details case studies of performance and noise of some of the advanced operational flight procedures that were first introduced in chapter 2 as performed by conventional aircraft. Results are compared against aircraft performing standard flight procedures to quantify the noise benefit potential of the concepts.

Chapter 5 is an extension of the framework described in Chapter 3 to include the aircraft performance model for hybrid electric aircraft, the drag model for windmilling engines, and the component-based aircraft noise model including windmilling engine noise. It concludes with validation of the windmilling drag model and an assessment of the modeled windmilling fan noise.

Chapter 6 is an examination of several case studies involving the use of the windmilling drag concept with hybrid electric aircraft. Performance and noise for each procedure due to both standard turbofan aircraft and hybrid electric aircraft are compared to quantify the noise benefit potential of these concepts.

Chapter 7 draws conclusions of the thesis, including the potential noise benefits of the procedures assessed with the framework, the identification of the need for validation of the noise impacts of the modeled flight procedures, and the potential for using the windmilling drag concept in advanced operational approach procedures as a noise benefit mechanism for hybrid electric aircraft.

Chapter 2

Literature Review

2.1 Primary Aircraft Noise Sources

Community noise from aircraft on approach or departure is the unwanted sound heard by observers on the ground that is produced by the aircraft source components. Modeling aircraft noise requires identification of the primary noise sources. Aircraft noise can be divided into two main components: engine noise and airframe noise. The sub-components of engine noise depend on the type of engine. Common aircraft engine types, including those of hybrid electric aircraft, are propeller, turboprop/turboshaft, or turbofan engines. A brief summary of engine noise components are listed below:

The primary categories of turbofan engine noise are as follows [11]:

- Fan noise, or noise produced by turbulent air passing over fan blades, noise due to the interactions between fan rotor wakes and stator vanes, and shocks forming at blade tips moving at supersonic speeds;
- Core noise, or noise produced due to mechanical interactions and vibrations in the compressor, combustor, and turbine, as well as from the combustion of hot gasses in the engine core and subsequent propagation through the turbine;
- Jet noise, or noise produced from the shear layer between the fast airflow from the jet of the engine mixing with slower ambient air or the bypass stream

Propeller engine noise is composed primarily of noise due to or noise produced both by turbulent air passing over the propeller blades and rotational noise due to oscillating pressure as blades through the air [11]. Turboprop/turboshaft engines typically consist of propeller, core, and jet noise. This thesis focuses primarily on aircraft with turbofan engine noise components.

Airframe noise comes from turbulence generated by the aircraft airframe, usually around geometry changes. This includes noise from the basic wing and tails, known as trailing edge noise, as well as additional noise from the devices that extend into the airflow such as flaps, slats, and landing gear [11].

Figure 2-1 highlights the primary source noise components for a conventional aircraft with turbofan engines. Detailed descriptions of the aircraft noise sources are presented in section 3.3.

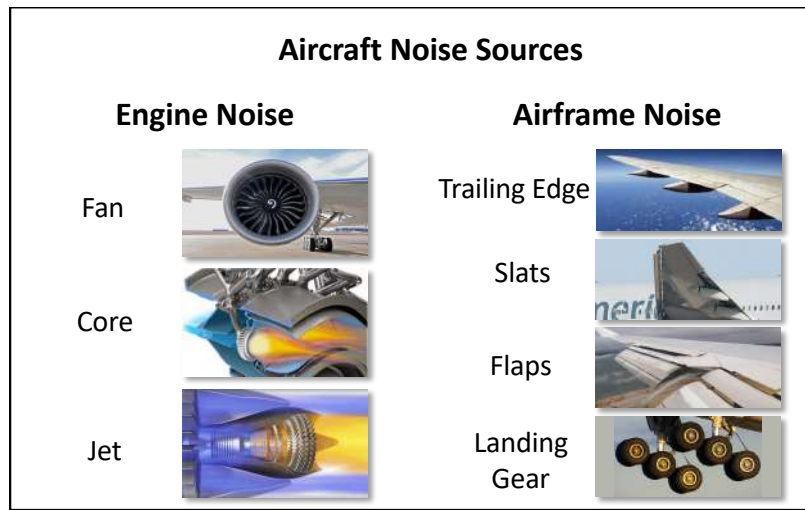


Figure 2-1: Primary Conventional Turbofan Aircraft Noise Sources, Engine and Airframe

The distribution of engine and airframe noise dominance depends on the aircraft's flight procedure. An aircraft in the early stages of departure is often in a state of high thrust, low speed, and relatively clean (flaps and slats retracted, landing gear retracted) configuration. This leads to the engine being the dominant noise source compared to the airframe. Thus, on departure, thrust and climb rate management have a significant impact on total noise. On approach, the engines of an aircraft on approach are often in a relatively low thrust state

while the aircraft is configured with high lift devices and landing gear extended in preparation for landing. Thus, on approach, airframe noise tends to be as loud as or dominate to engine noise, making reduction in or removal of airframe noise sources significant for overall noise reduction on approach.

Noise consists of pressure waves over a wide range of amplitudes and frequencies. Noise intensity is measured in units of decibel (dB), which is a logarithmic ratio of the actual sound pressure level (SPL) to the threshold of hearing of $20 \mu Pa$. While the audible frequency range for humans is 20 Hz to 20,000 Hz, humans are particularly responsive to and annoyed by frequencies in the 2 kHz to 4 kHz range. Thus, different noise metrics are weighted to reflect the significance of certain frequencies.

Many factors influence the noise perceived by observers. Noise sources are typically either broadband or tonal in nature. Broadband components are typically associated with random turbulence or mixing that occur over a wide range of frequencies (such as turbulence generated by the airframe components extending into the airflow) while tonal components are associated with periodic steady state movements that excite certain frequencies (such as rotating engine components).

Noise emitted from a source decays with the distance between the source and observer due to spherical spreading. Additional factors that will change the magnitude of noise received include atmospheric attenuation and ground reflection. Atmospheric absorption refers to the decrease in noise intensity due to the dissipation of acoustic energy to viscous effects and molecular interactions and is a function of meteorological factors such as temperature, pressure and humidity. Generally higher frequency noise sources dissipate energy and thus are more attenuated in the atmosphere than lower frequencies [13]. Noise attenuation through the atmosphere at a given frequency increases with decreased humidity [13] as dry air is more dense and absorbs more acoustical energy than moist air. Temperature impact on attenuation depends on frequency and humidity [13]. Ground effects, terrain, and any additional sound insulation at the observers are also factors. Whether the surface at the observers is acoustically "hard" or "soft" will impact the noise signature at the ground. Acoustically hard surfaces will generally result in stronger reflection of sound waves and depending on the geometry of the sound wave source and observer location can result in

constructive or destructive interference of sound waves [14]. Acoustically soft surfaces such as grassy terrain will result in a stronger absorption of sound wave energy.

In addition, noise sources add logarithmically. Therefore, if a component is already producing a given amount of noise, every addition of an additional equal noise source results a +3.01 dB increase in total noise, regardless of the magnitude of the noise components. Adding an additional noise source to a system that is below the original system noise will result in little change to the logarithmic sum of all noise components.

Some common metrics for representing noise that are used in this thesis are as follows [15]:

- **$L_{A,MAX}$** : The maximum A-weighted sound pressure level ($L_{A,MAX}$) heard by an observer during an aircraft's entire flight. The A-weighting applied to this metric reduces the decibel values of sounds at low frequencies, as the human ear is less sensitive at low frequencies [15].
- **EPNL**: The Effective Perceived Noise Level (EPNL) is built from perceived noise levels, or measures of the human response to sound of constant intensity across the range of frequencies in the audible range. The perceived noise levels are further corrected at specific tones depending on their level above the local ambient sound level and their frequency. For a given observer, the tone-corrected perceived noise levels received during an entire flight event that are within 10 dB from the maximum level received are integrated in time for a representation of annoyance due to the duration of the noise event. This final integrated value is the EPNL [28]. EPNL is the noise metric used for Part 36 noise certification levels [16].
- **SEL**: The Sound Exposure Level (SEL) at a particular observer, similar to EPNL, is an integration in time of noise levels heard from a flight event that are within 10 dB from the maximum sound level, as shown in Figure 2-2. SEL is also a measure of sound intensity and its duration. Rather than being an integration of perceived noise levels however, this metric is an integration of A-weighted sound pressure levels [15].

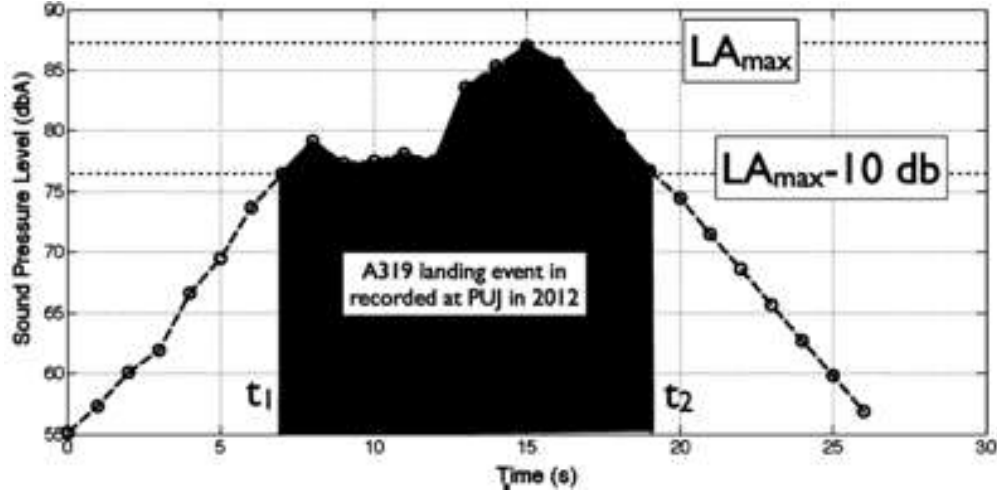


Figure 2-2: Sound Exposure Level Calculation Representation, Figure by A. Trani [17]

- **DNL:** The Day Night Average Sound Level (DNL) is the average noise level over a 24-hour period and is computed as shown in equation 2.1 [18]. Ten to the power of the SEL contours of all flights occurring during the day and ten to the power of the SEL contours occurring at night between 10pm and 7am summed with an additional 10 dB are added together and normalized by the 86,400 seconds in a day. DNL is then equal to 10 times the logarithm of this value.

$$DNL = 10 \log_{10} \left[\frac{1}{86,400} \left(\sum_{day\ flights} 10^{\frac{SEL}{10}} + \sum_{night\ flights} 10^{\frac{SEL+10}{10}} \right) \right] \quad (2.1)$$

The 65 dB DNL contour is used by the FAA as the noise threshold below which residential land use is compatible according to 14 CFR Part 150 and below which noise impacts in residential areas are no longer considered "significant" under The National Environmental Policy Act of 1969 (NEPA) [2].

2.2 Aircraft Noise Improvements Since 1969 and Present Considerations

Increasing traffic of aircraft equipped with engines that were not originally designed for noise suppression in the late 1960's resulted in great pressure for noise control around airports.

This resulted in the creation of Federal Aviation Rule Part 36 (FAR-36) in 1969, which set a limit on the maximum noise levels for certification of new aircraft [19]. With this standard in place, aircraft noise became a significant consideration in engine and aircraft design. One of the major design changes was transitioning from equipping aircraft with turbojets originally designed for military aircraft to equipping them with high-bypass ratio turbofans. This change, which has the benefit of improving propulsive efficiency on cruise [19], also leads to a reduction of jet noise by reducing the jet exit velocity (further discussed in section 3.3.1). Figure 2-3 shows a sample comparison of the 85 dB noise contour on departure of a 1960s Boeing 727 with a modern A320-200 equipped with modern high-bypass ratio CFM56 engines [11]. The contour for the A320-200 is nearly 9 times smaller than the area of the Boeing 727, showing the significant noise reduction due to engine improvements.

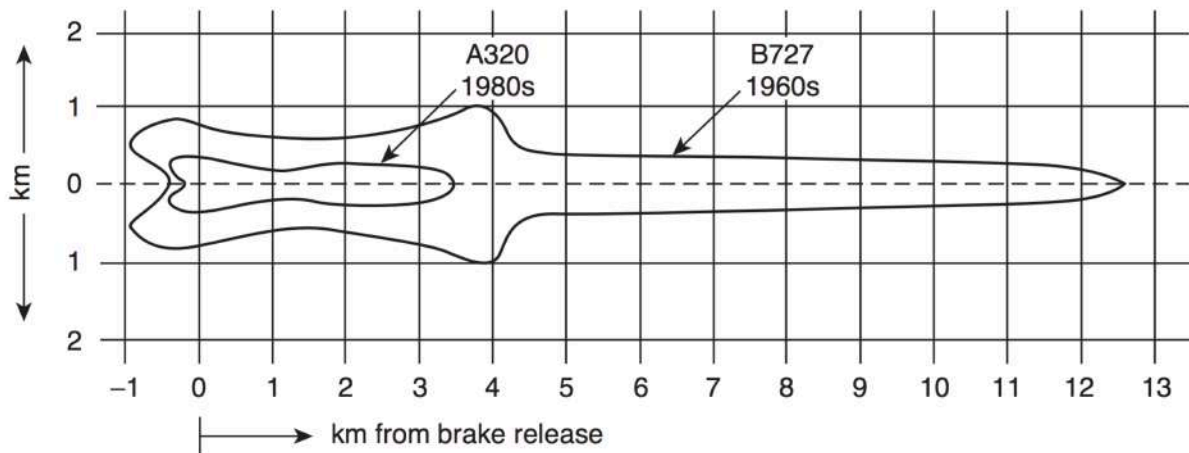


Figure 2-3: 85 dB Noise Contour of a 1960s Boeing 727 on Departure Compared to a Modern A320-200, Figure from [11]

Aircraft noise has continued to decrease as stricter noise standards have been introduced. The cumulative effective perceived noise levels from the three certification locations defined in the Part 36 regulations of new aircraft must fall below thresholds referred to as "stages". These stages which have become stricter over time. Certification noise levels of various aircraft types compared to stage regulations by year are shown in Figure 2-4.

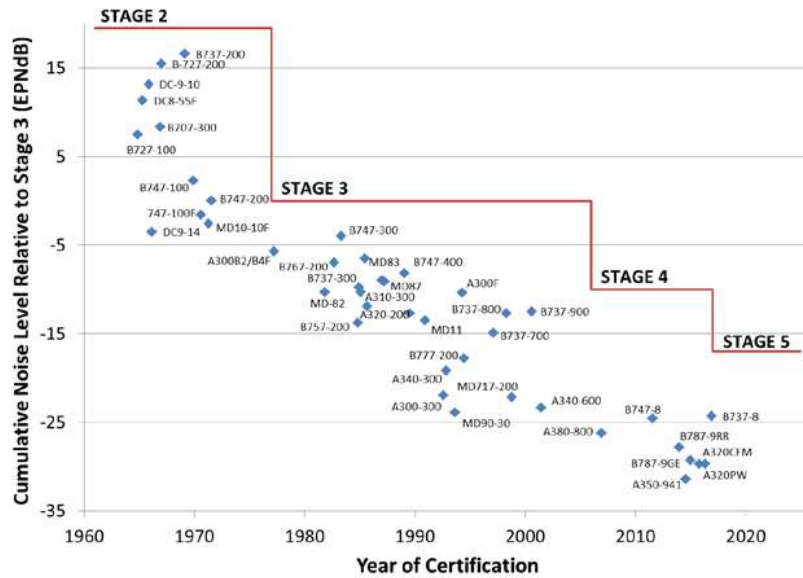


Figure 2-4: Turbojet Aircraft Noise Certification Levels by Year Compared to Noise Stage Levels, Figure from FAA [20]

Since 2003 the Federal Aviation Administration has published over 9000 performance-based-navigation (PBN) procedures through NextGen [21], including area navigation (RNAV) and more precise required navigation performance (RNP) procedures. PBN procedures are precise 3D flight paths utilizing GPS. Aircraft flying PBN procedures save time and fuel compared to traditional ground-based radar navigation and air traffic control can have greater confidence in routing aircraft and placing routes closer together given that the aircraft position and performance is more predictable [22].

PBN procedures have been implemented at airports such as Seattle-Tacoma (SEA) [23], Charlotte Douglas (CLT) [24], and Boston Logan (BOS) [25] through the implementation of NextGen. While they have yielded benefits in efficiency and throughput at these airports, an unexpected noise challenge has arisen due to the concentration of once well spread flights into concentrated tracks. It has become evident that some PBN procedures have potential unintended consequences for community noise impact [26].

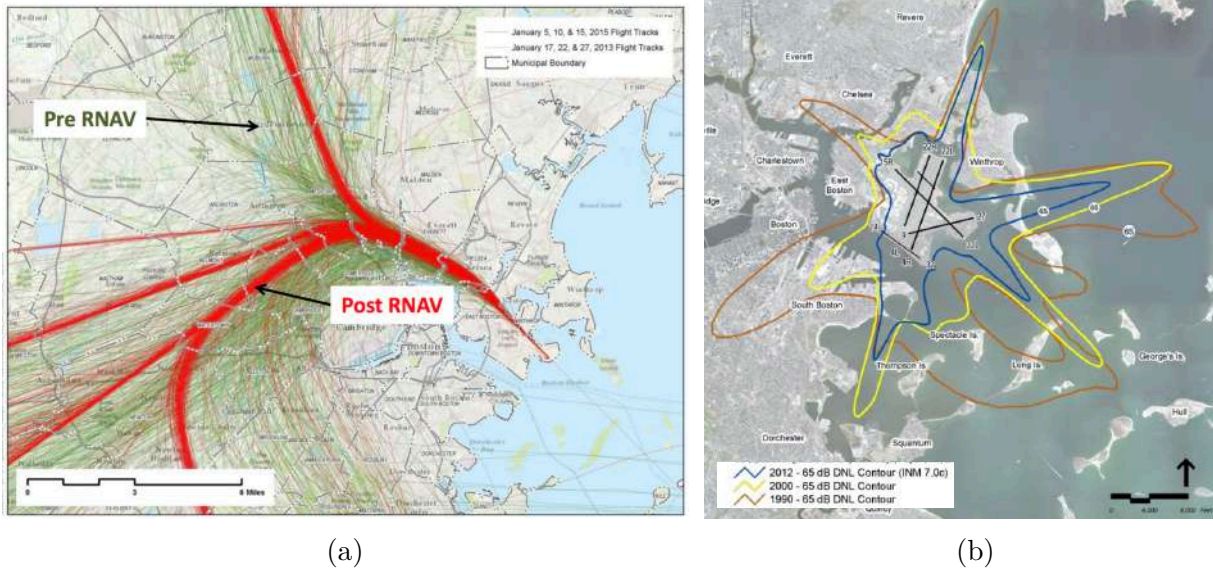


Figure 2-5: Concentration of Flight Tracks out of Runway 33L at BOS with the Introduction of RNAV (a) and Decrease in DNL 65 dB Noise Contour at BOS by Year (b), Figures from Massport [27]

Figure 2-5 (a) above shows the concentration of flight tracks out of RWY 33L at BOS with the introduction of RNAV procedures. As shown in Figure 2-5 (b), the population exposed to BOS's 65 dB DNL noise contour has actually decreased significantly since 1990 [27]. However, as shown by the map of complaints around BOS in 2015-2016 in Figure 2-6 below, in the regions extending far from the BOS 65 dB DNL contours, beneath both the concentrated departure and arrival tracks, there are a large number of locations where aircraft noise complaints were filed.

Increased precision of aircraft navigation technologies has allowed several operational benefits such as improved safety, reduced ATC workload, higher runway throughput, reduced fuel burn, better terrain avoidance, and lower approach minimums [28]. However, the noise concentration has led to community opposition and frustration around the U.S. [29].

the Noise-Power-Distance (NPD) based approach. In the NPD approach, aircraft noise is empirically determined via an interpolation of noise data tables. An example are the curves represented in Figure 2-7, where noise is interpolated as a function of thrust and distance between the observer and aircraft. An NPD method is implemented in the Aviation Environmental Design Tool (AEDT), which is the standard tool in the US to provide FAA stakeholders with environmental impact information [12]. The Civil Aviation Authority Aircraft Noise Contour Model (ANCON) is utilized in the UK with a similar NPD approach [30]. This approach is beneficial for rapidly simulating a large number approach and departure events to model metrics such as the 65 DNL level. However, it is limited by the variety of operating conditions available in the databases from which noise is being interpolating from.

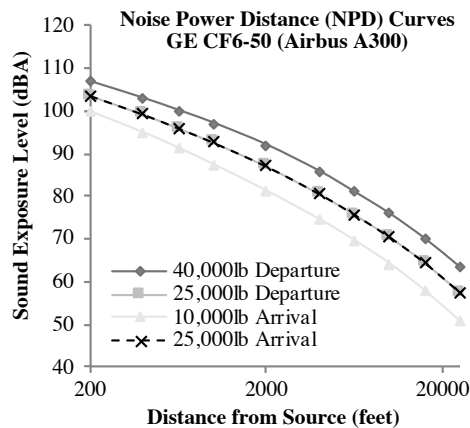


Figure 2-7: Sample NPD Curves for an Airbus A300

The empirical data used in NPD methods is collected from approach and departure procedure measurements in different performance states for a given aircraft and engine combination. In AEDT, the NPD curves are specified for aircraft at various power settings in both approach and departure, with approach curves provided in an approach condition with flaps and landing gear extended. Changes in airspeed are reflected in the calculation of duration based metrics such as SEL, however noise source magnitude as a function of airspeed is not reflected. In addition, this tool is not sufficient for modeling noise impacts due to changes in configuration settings because of the limited set of curves for different configurations.

Noise modeling methods that model source noise impacts of various components as a function of more detailed aspects of a flight procedure (such as speed or configuration changes) address these limitations. One method to do this is with higher-fidelity NPD data sets that reflect changes in speed or configuration as desired for modeling. Georgia Tech is developing methods to incorporate variables such as speed and configuration into existing NPD sets [31]. Models with more extensive databases that represent more aircraft states have also been developed. For example, the German Aerospace Center (DLR) has developed SIMUL, which is a database of source noise from wind tunnel and flyover testing that separates noise into engine and airframe components [32]. The noise prediction tool FLULA by the Swiss Federal Laboratories for Materials Testing and Research [33] is another method developed from dedicated noise measurements for several aircraft types.

In general, methods relying on noise databases are limited to the flight procedure conditions corresponding to when the noise levels were measured as well as the aircraft and engines available within their databases. Alternative methods include noise component based modeling provide functions representing relationships between noise and physical characteristics of the aircraft state rather than databases corresponding to specific aircraft or engines.

An example component based model that uses a combination of semi-empirical and physics based methods for assessing noise is the NASA Aircraft Noise Prediction Program (ANOPP) [34]. Modules within ANOPP include methods to model standard engine sources, such as fan, core, jet, propeller sources, as well as trailing edge, landing gear, flap, and slat airframe sources at a user-defined observer grid for a single event flight procedure. Prediction methods are based on noise data measurements combined with physics based models and continue to be improved over time. Models within ANOPP are not linked to specific aircraft and engines. Instead, they require details about the aircraft geometry, such as wing area and landing gear geometry, and performance state of the aircraft, such as mass flow through the fan or jet velocity, rather than, for example, a named engine and throttle setting. The model can thus be used for predictions of new aircraft types or engines, although noise modeling of specific components with this method is limited by the modules available within the program. External noise sources that cannot be modeled using the modules available within ANOPP,

such as a windmilling engine, can be incorporated as inputs to the program.

Another example component noise model developed by DLR is the Parametric Aircraft Noise Analysis Module (PANAM) [32]. PANAM predicts noise for aircraft on arbitrary approach and departures and is composed of semi-empirical engine and airframe source noise methods. These include the jet noise method by Stone [35] and the fan noise method by Heidmann [36], which are also implemented in ANOPP. Methods for the airframe components were developed at DLR via wind tunnel of Airbus A320/A340 family aircraft geometries and flyover measurements of Airbus A320 family aircraft [37][38][39]. The airframe modeling methods in ANOPP include both the Fink methods [40] for wing and tail trailing edge noise and Guo methods for slats, flaps, and landing gear noise [41][42][43][44].

These methods are useful as a stand alone for analyzing component-level aircraft noise. However an extensive set of inputs are required for modeling of different aircraft configurations or advanced flight procedures. Modeling component level noise from such functions requires detailed information about the aircraft geometry, engine performance states, and flight profiles. These parameters must be obtained from external data or modeling sources that also accurately represent how they are related to each other (such as how aircraft velocity or thrust impacts the engine internal performance state or how flight speed relates to the aircraft configuration and deployed geometry). Flight profiles for the desired procedure must also be supplied externally.

Example systems and frameworks have been formulated that incorporate aircraft performance information with the component based noise methods. The conceptual level aircraft design environment SUAVE from Stanford has incorporated ANOPP into an aircraft conceptual design process with acoustic constraints based on certification points [45]. A framework was created for the Silent Aircraft Initiative—the goal of which was to design an aircraft that has an imperceptible noise footprint outside of the airport perimeter—consisting of aircraft design and noise analysis using industry standard methods such as Fink methods for trailing edge noise and Stone and Heidmann methods for jet and fan noise with modifications to account for flight corrections, fan liner attenuation, and shielding applicable to the silent aircraft design [7][6]. PANAM [32] has been incorporated into a framework consisting of an aircraft preliminary, multidisciplinary design model [46], capable

analyzing unconventional aircraft configurations with numerical methods for aerodynamic and structural analysis, and flight simulation tools to model aircraft noise at the conceptual design phase as well as to be able to examine noise abatement flight procedures.

2.4 Noise Abatement with Advanced Operational Flight Procedures

Several noise abatement flight procedure concepts have been proposed and assessed in the literature. These include both lateral profile adjustments and vertical profile adjustments.

2.4.1 Lateral Profile Adjustments for Noise Abatement

Lateral profile adjustments, or change in the aircraft horizontal flight track, can be used for noise abatement if designed to avoid overflying noise sensitive communities. Several examples of lateral track adjustments so that the number of people impacted by fly over events is minimized have been examined for various airports [47][3][1][48].

The design of procedure tracks is limited by the design criteria for different navigation technologies. The criteria for procedure design are given in the US Standard for Terminal Information Procedures (TERPS) [49]. Relevant aspects of approach criteria design include fix-to-fix leg length, required obstacle clearance, final approach segment length, and glidepath angle [47]. RNP Authorization Required (RNP-AR) technology allows for horizontal flight path designs that are less restrictive than RNAV flight path designs. RNAV technology allows for navigation between waypoints, while the less restrictive RNP AR technology also allows for definition of the flight track between waypoints. For example, some of the procedure design criteria that must be considered for RNAV and RNP procedures is that the RNAV final approach intercept angle must be 15° or less for procedures with vertical guidance, while RNP final approach angles may be as great as 90° .

The total equipage levels are also an important consideration for procedure design and air traffic considerations. Although RNP-AR procedures have advantages in flexibility of design, in the United States National Air Space, only about 50% of the aircraft fleet are

equipped with RNP-AR technology; while greater than 95% of the aircraft fleet are RNAV equipped [50].

An example procedure consisting of a lateral track adjustment for noise abatement is presented for the arrival into Runway 22L at BOS. Because BOS is near water, one method of providing noise abatement is over-water RNAV and RNP procedures. Figure 2-8 the standard ILS approach path into BOS Runway 22L. Beyond 5 nmi from the runway threshold, the flight track is concentrated over land during the standard 22L ILS final approach.

An alternative RNAV approach concept with an RNP overlay to Runway 22L at BOS is also shown in Figure 2-8. Figure 2-8 also shows the population density per square mile taken from 2010 census data plotted on land. Aircraft on the standard ILS approach procedure into Runway 22L overfly a region of 50,000+ population/square mile near the VOCUS waypoint. The proposed procedure instead incorporates a turn over the Nahant Causeway and a 15° intercept with the final approach segment. Compared to the standard ILS approach procedure, the modified lateral procedure concept approach remains over-water and thus overflies much less people.

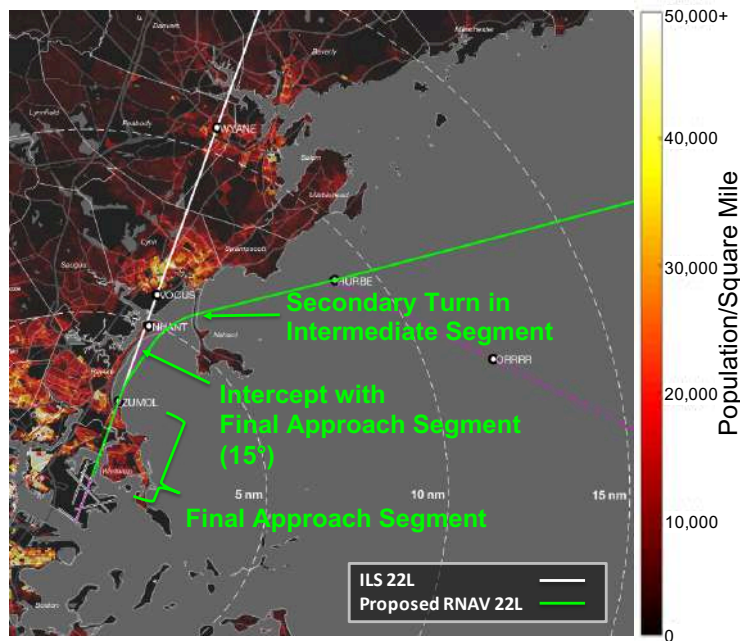


Figure 2-8: Lateral Profile Adjustment Example, BOS 22L RNAV Approach with RNP Overlay; Figure from [3]

Another example of lateral profile adjustments includes returning to the dispersed flight

tracks similar to the pre-RNAV conditions as seen in Figure 2-5 (a). Doing so redistributes noise for communities, potentially benefiting some while potentially dis-benefiting others. BOS is one airport where such dispersion concepts have been examined [51] [3].

While lateral profile adjustments for particular airports and runways may provide opportunity for noise abatement, airspace constraints and aircraft separation criteria limit the extent to which tracks that can be moved for noise abatement. Additionally, redistributing noise has the potential to dis-benefit some communities.

2.4.2 Vertical Flight Profile Adjustments for Noise Abatement

Vertical profile adjustments, or adjustments to the aircraft's altitude, velocity, thrust, or configuration profile, are also methods for noise abatement. Vertical profile adjustments can be carried out both on departure and approach.

Thrust Management Departures

Vertical profile adjustments for departure often focus on thrust, climb rate, and altitude adjustments given that the cleaner configuration and higher engine power in these procedures results in the noise being dominated by the engine.

While procedures vary by airline, a typical departure profile in the US consists of an initial high thrust climb segment to a transition altitude, usually between 1,000 and 2,000 feet above ground level, followed by a thrust reduction and acceleration segment to a target climb speed, typically 250 kts below 10,000 feet. This thrust reduction is recommended for noise reduction in ICAO document 8168 [52]. After the thrust reduction and as the aircraft accelerates, the flaps are incrementally retracted until the wing is in its flap and slats retracted configuration. This is consistent with what the International Civil Aviation Organization (ICAO) describes as Noise Abatement Departure Procedure 2 (NADP 2) in document 8168. An example variation of this standard procedure is the FAA Noise Abatement Departure Procedure 1 (NADP 1), during which the aircraft holds its initial climb speed to 3,000 ft before accelerating to the target climb speed for altitude gain.

An additional departure procedure that results in a steep initial climb profile is

performed by maintaining high thrust and the initial takeoff speed during the procedure [1], as shown in Figure 2-9. Such a procedure may have less noise benefit close to the airport, but potential benefit further from the airport due to the higher altitude of the departing aircraft.

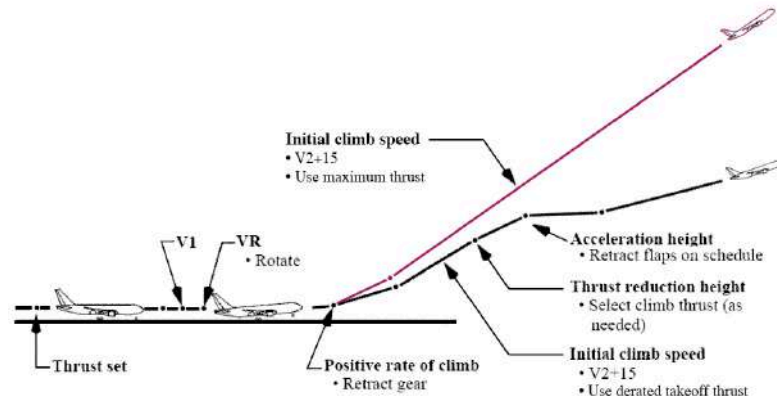


Figure 2-9: Profile for a High Thrust Steep Climb Compared to a Standard Departure, Figure from [1]

Additional variations of departure climb profiles for noise mitigation have been assessed. One example is of a high thrust initial climb followed by a cutback compared to standard departures at Boston Logan International Airport [5]. John-Wayne Airport in Santa Ana, California utilizes a similar high thrust initial departure followed by a cutback after 800 ft in order to meet the noise regulations at the airport [53]. Behere et al. assessed various vertical departure procedure modifications for specific aircraft for takeoff noise mitigation at Atlanta Hartsfield-Jackson International Airport (ATL) [54]. Helby et al. has also developed method for examining optimal departure climb profiles to minimize population noise exposure utilizing an NPD method for noise modeling [55].

Continuous Descent and Steeper Approaches

In conventional approach procedures, aircraft descend and decelerate relatively early in the approach and fly level segments until interception with the ILS glide slope and finally touching down. As a result, aircraft may fly in dirty, high thrust configurations at low altitudes for longer in the approach profile than necessary, creating noise for the communities below [56]. Alternatives to the standard approach procedure keep aircraft high, cleanly

configured, and at low thrust for as long as possible to reduce both engine and airframe noise.

Continuous Descent Approaches (CDAs) are an example of an altitude management procedure for noise abatement. During CDAs, aircraft maintain a continuous glide path from initial descent before intercepting the ILS glide slope. Figure 2-10 shows a comparison of a CDA versus a standard approach with level segments.

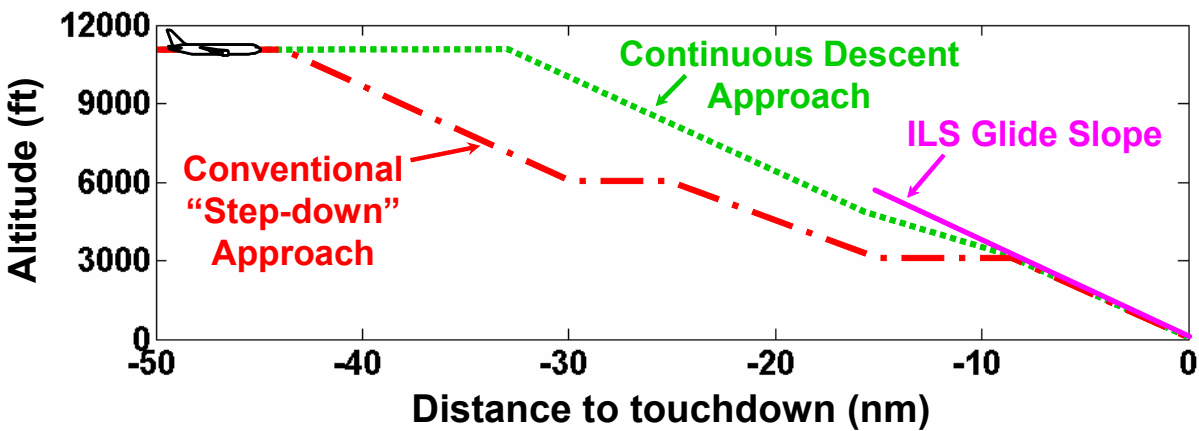


Figure 2-10: Continuous Descent Approach Concept Compared to a Conventional Approach with Level Segments, Figure from [57]

CDA procedures have been assessed in the literature. This includes the work of Clarke et al. [58], who assessed CDA procedures for noise reduction at Louisville International Airport. A helical noise abatement procedure where the aircraft approaches the airport at a high altitude and performs a spiralling descent to the runway has also been examined at DLR [59]. CDA procedures have also been implemented at various airports; for example, they account for the majority of arrivals at London Heathrow Airport [60].

Additional variations of CDAs, such as steeper approaches where aircraft descend at higher than the standard 3° descent angle, and two-segment approaches, where aircraft are flown at steeper descent angles enabled by their performance capabilities before intersecting with the ILS glide slope, increase the altitude between the aircraft and population even greater extents, depending on the achievable descent angle. These concepts are diagrammed in Figure 2-11.

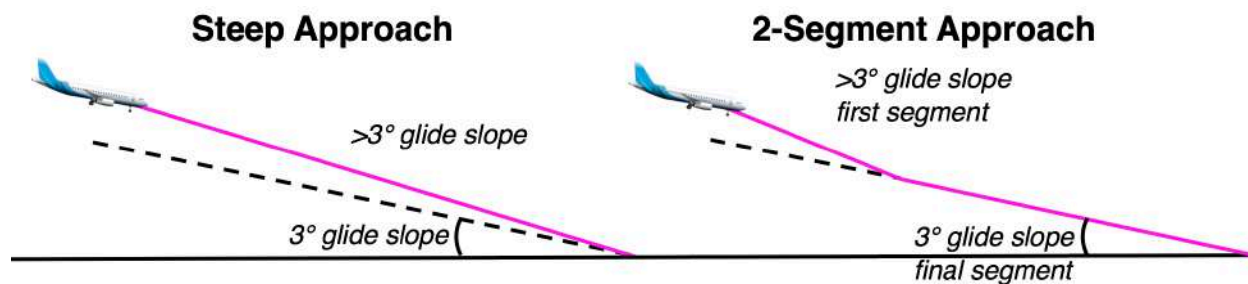


Figure 2-11: Steep and Two-Segment Approach Concepts Compared to a 3° Continuous Descent Approach, Figure from [1]

Steeper descent approaches have also been examined in the literature, including the noise impacts of an aircraft performing a 3.77° descent compared to a 3° descent [1]. The noise benefits of steeper descents have also been examined experimentally during a steep approach demonstration study at London Heathrow Airport [61], where aircraft following a 3.2° glide slope were shown to have a reduced noise signature of about 1 dB compared to aircraft flying 3° glide slopes. Visser et al. also examined optimal descent profiles for minimal noise exposure using an NPD noise analysis method [62].

Delayed Gear Approaches

Another example of vertical profile adjustment is profile management to delay the onset of configuration noise. As indicated in section 4.3.2, delaying gear deployment can have a significant impact reducing approach noise. An example delayed gear approach is shown in Figure 2-12. In this example, rather than deploying gear at 1,700 ft, landing gear deployment is conceptually delayed until 1,000 ft where aircraft are required to be fully configured and at the final approach velocity.

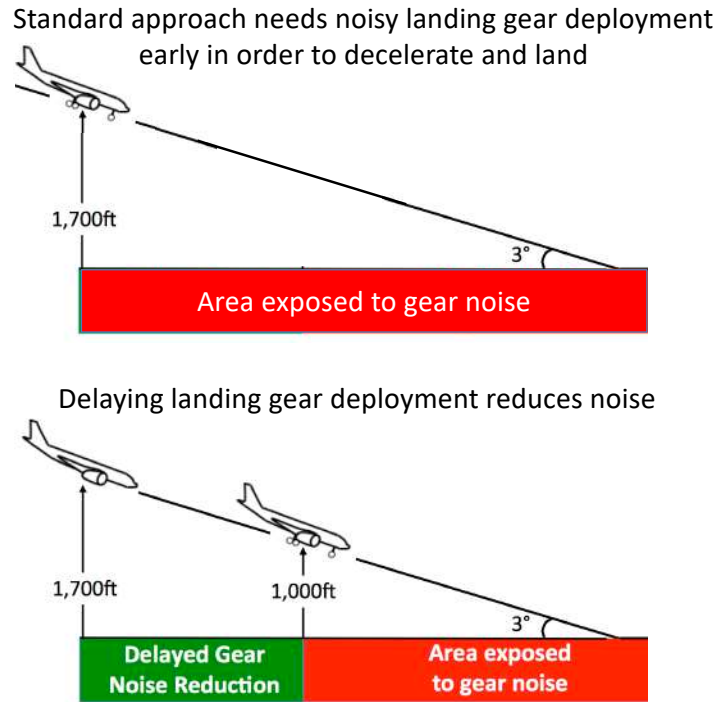


Figure 2-12: Delayed Gear Deployment Concept

Delayed gear deployment has the potential for noise reduction due to both the delay of gear noise as well as noise due to any associated reduced thrust. DLR has examined a continuous descent approach procedure concept with delayed landing gear extension [32] studied with PANAM.

Delayed Deceleration Approaches

An additional alteration of the vertical profile that may have a noise benefit is velocity and high lift device deployment management. This is done in Delayed Deceleration Approach procedures (DDAs), diagrammed in Figure 2-13. Compared to a standard approach, where aircraft decelerate and deploy flaps and slats early and maintain required higher than idle thrust through these segments, in delayed deceleration approaches the aircraft maintains the initial approach speed until a closer distance to touchdown, thus delaying when high lift devices must be deployed.

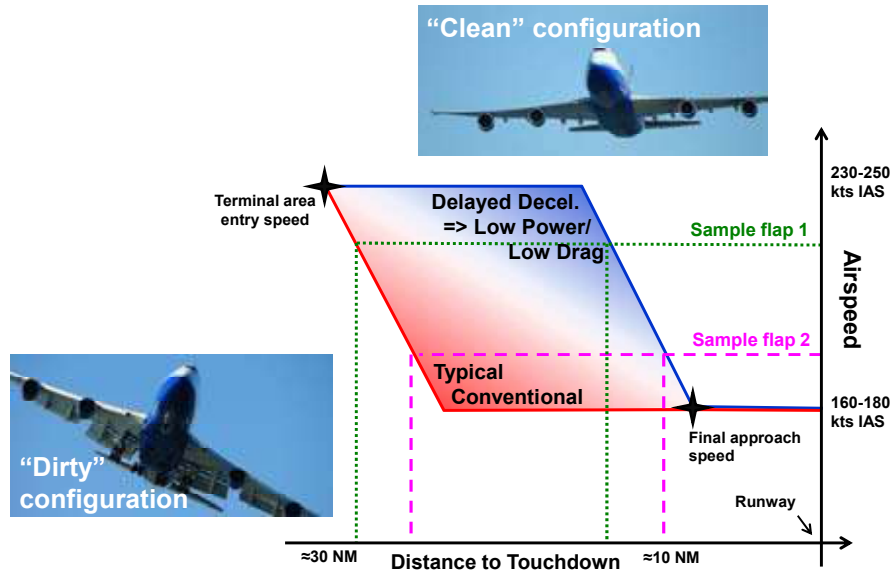


Figure 2-13: Delayed Deceleration Approach Concept, Figure from [56]

Prior analyses have shown that the reduced flight time and thrust during this procedure yields significant reductions in fuel burn [56]. An example of this is shown in Figure 2-14. As can be seen in Figure 2-14, flight recorder data for Airbus A320 flights associated with lower airspeeds versus distance to touchdown were also associated earlier flap deployment, higher thrust settings, and higher fuel burn.

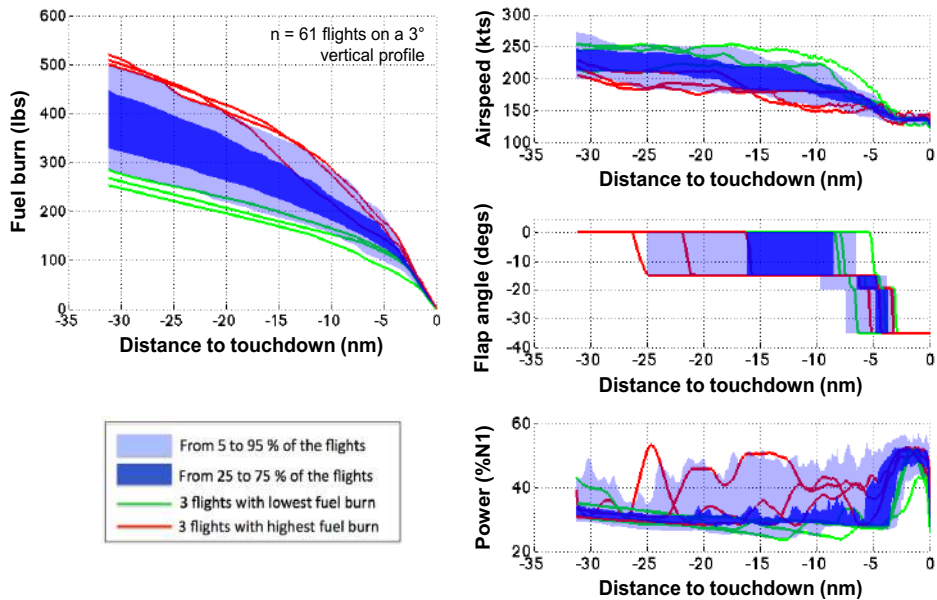


Figure 2-14: Airbus A320 Fuel Burn and Performance Profiles, Figure from [56]

In addition to fuel burn reduction, the reduced thrust and delay of deployment of required high lift devices also has the potential for noise reduction. These benefits have lead to the development of pilot assistance systems such as the Low Noise Augmentation System (LNAS) at DLR [63]. This system was designed to show the pilots the optimal moments to retract flaps with minimum thrust in the approach so that the lowest noise and fuel burn can be achieved.

2.5 Noise Reduction Opportunities of Advanced Configurations

Various advanced configuration concepts can be implemented to reduce aircraft noise at the vehicle level. These include both direct modifications to reduce noise for various sources as well as hybrid or electrified aircraft configurations that may not be specifically designed for noise reduction but have noise reduction potential.

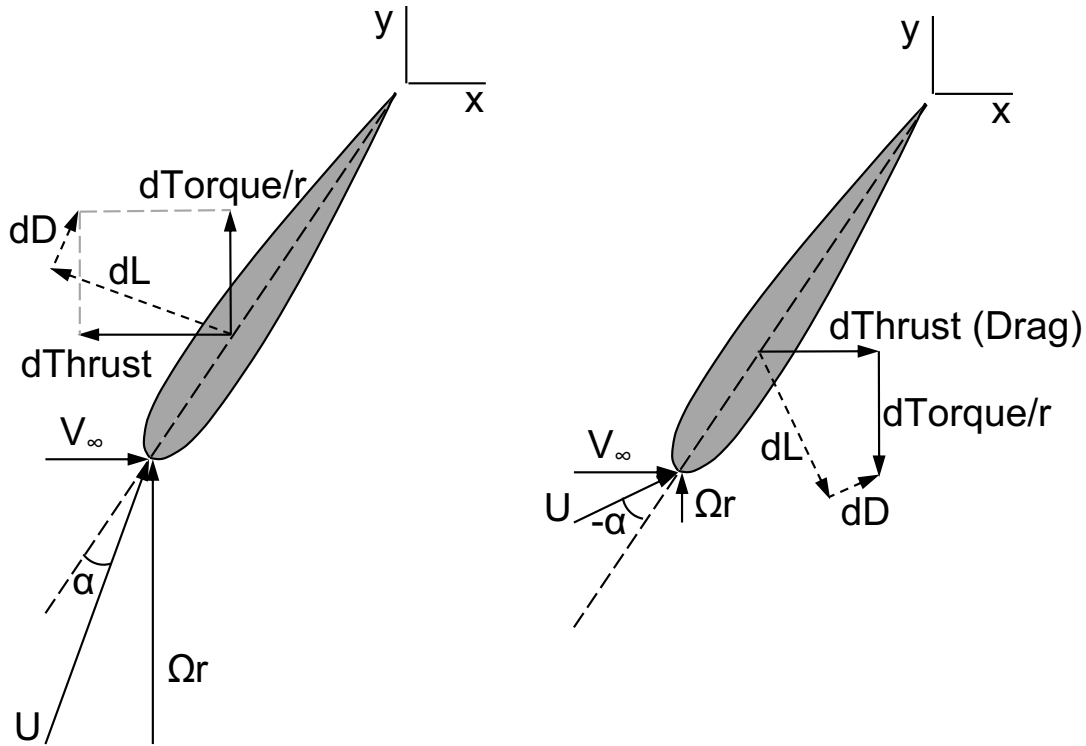
2.5.1 Quiet Drag Concepts

Performing advanced operational noise abatement approaches often requires considering whether or not the aircraft will have adequate drag to control its deceleration profile. Traditionally, this drag is provided by spoilers, high lift devices, or landing gear. However, the trailing edge flap noise, as well as noise due to blunt bodies such as landing gear interacting with the airflow can add significant airframe noise [5] [64]. Releasing gear is a common method by pilots to dissipate aircraft energy on approach, especially for aircraft with high lift to drag ratios. Thus, there is also a safety concern with these vertical management approaches because they increase approach energy and thus may increase the risk of runway excursion. Runway excursions were the third leading cause of fatal commercial jet aircraft accidents between 2008 and 2017 [65]. If gear or speed brakes are released upon glideslope intercept in order to aid in deceleration, or if air traffic requires a quicker deceleration for sequencing aircraft, additional noise due to these high drag devices could offset the benefits of a higher altitude in a continuous descent approach.

One method for which the noise benefits of continuous descent, steeper, and delayed configuration approaches could be realized is by equipping aircraft with alternative sources of drag that are quieter than traditional drag-generating aircraft components. Several concepts that reduce the crevices of high-lift devices and landing gear and thereby reducing noise sources attributed to flow disruption have been studied. One example is the use of continuous mould-line technology that provides noise reduction by removing the gaps between flaps [66]. Another example are fairings used to bend the wheels and axles of landing gear to create a smoother surface than with traditional landing gear that can reduce gear noise [67]. While these technologies have been shown to reduce the noise of their components by several decibels, they may alter the performance characteristics of various components. Landing gear fairings, for example, were shown to result in up to a 1/3 gear drag reduction [67], which is contrary to the desired performance necessary to perform a steeper, slow descent.

Another quiet drag concept separate from alterations from high lift devices and landing gear is the “engine air brake” concept proposed by Shah [68]. This concept creates drag in a traditional turbofan engine through the use of deployable non-rotating vanes behind a fan pumping stage that swirl the exit flow and create a momentum deficit. Such devices were shown conceptually to produce enough drag to enable an increase in glideslope from 3° to 6° for several aircraft.

A third potentially quiet alternative drag concept is to reduce the rotation rate of the engine fan or propeller to that of windmilling conditions. This condition also creates a momentum deficit behind the engine. The physical mechanism of drag production by a windmilling or low RPM fan is shown conceptually in Figure 2-15, which shows diagrams of the resultant forces on fan blades in different RPM operations. As Figure 2-15 shows, in a windmilling condition, the rotational velocity Ωr at a blade section is reduced to below the freestream velocity V_∞ . The high advance ratios ($V_\infty/\Omega r$) result in the blade airfoils operating at angles of attack (α) that are negative. The resulting lift (dL) and drag (dD) forces on a blade section yield net resolved thrust (dThrust) and torque/r (dTorque/r) forces in the x and y axes. This produces overall net thrust in the direction of flight for normal operations and potentially net thrust opposite of the direction of flight, or drag, for windmilling or low RPM operations, depending on the blade performance characteristics.



(a) High RPM, Thrust Producing (b) Windmilling Low RPM, Drag Producing

Figure 2-15: Resultant Blade Section Forces for Two RPM Operations, V_∞ = free stream velocity, Ωr = rotational velocity at radius r , U = total velocity, α = angle of attack

The drag that this condition produces is great enough that pilots often must mitigate it by stopping rotation or feathering the blades. A 1973 NTIS report cites that windmilling engines were demonstrated to enable high rates of descent under full control of a Douglas DC-4 [69]. However such a procedure was never deemed operational due to safety considerations such as the uncertainty in being able to ensure that the engines could return to normal operation right before landing.

The windmilling operating condition of a standard gas-turbine engine is typically only encountered in the event of an engine failure. For aircraft with standard gas-turbine engines, a gas-turbine mechanically drives a compressor, and thus the fan rotation rate must be high enough to prevent compressor stall, resulting in thrust being produced when the engine is at idle. Windmilling however is possible in architectures where the fan is powered by an electric motor and thus can be operated at low rotation rates, such as in certain hybrid electric or

full electric aircraft configurations.

If the noise of windmilling engines is low enough such that they have little impact the logarithmic sum of the noise of the remaining components of the aircraft, then they can be considered valuable for implementing steep approaches or for increasing deceleration rate and thus replacing the need to use noisier drag devices during descent, as diagrammed in Figure 2-16.

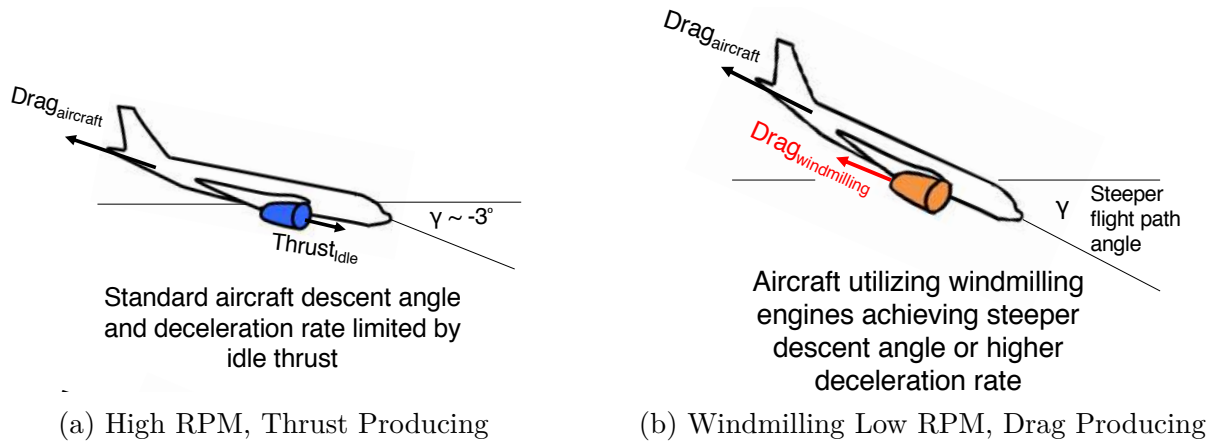


Figure 2-16: Using Windmilling Engines as Drag Generators on Descent Concept

Operating at in windmilling conditions also removes the residual idle thrust that limits the maximum rate of descent for aircraft with standard gas-turbine engines. Another advantage to obtaining drag via windmilling is that it requires no installation of additional blades to the baseline engine, and thus would not impact the normal operation of the engine. Varying the engine friction torque and thus the windmilling rotation rate can also control the amount of windmilling drag obtained.

Noise of Windmilling Engines

The literature provides some insight on the potential noise of using engines as drag devices. For example, with the “engine-air brake” the noise produced by flow entering a wind tunnel model engine nacelle with installed vanes that swirled the exit flow was found to produce less than 48 dB when extrapolated to a full-scale engine at an observer location of 120 meters from the source, depending on the vane blade angle [68]. Further extrapolation for this “engine air brake” concept, assuming noise would scale with the exit flow velocity of the

engine, showed that the addition of a fan pumping the vanes to increase drag would increase the noise to about 80 dB at the same location depending on the engine assumed. Such noise was reported to be about 6 to 9 dB below the total source noise for various aircraft on approach, and thus was assumed to have minimal impact to the total aircraft noise [68].

Few studies have reported the noise of windmilling engines. However, one study from NASA wind tunnel experiments carried out to determine the acoustics characteristics of a 2-foot diameter propeller showed that the noise generated when the propeller was in a windmilling condition was not detectable compared to the tunnel background noise [70]. Noise data was also obtained from a series of tests to examine broadband fan noise of a Boeing 18 in fan rig, conducted in the Boeing Low-Speed Aeroacoustics Facility (LSAF) [71]. Windmilling fan broadband noise was shown to be approximately 20 dB below fan noise across the spectra at standard approach conditions.

These few studies suggest that the noise of drag generating engines is variable depending on the specific configuration and operating condition. As the engine air brake study showed, operating engines in off-design conditions could cause flow instability and subsequent increase in noise [68]. However, these noise sources are also potentially below typical commercial aircraft noise levels and thus may be viable concepts for enabling noise abatement steep approaches and delayed deceleration or configuration procedures.

2.5.2 Background on Hybrid Electric Aircraft

Windmilling or low-RPM engines are potential methods for obtaining drag that doesn't contribute significantly to the total aircraft noise signature while enabling aircraft to perform advanced approach procedures with noise abatement capabilities beyond those of standard aircraft. However, because combustion must be maintained a standard gas-turbine engine, fans of standard engines cannot be operated at rotation rates low enough to produce drag with their engines. Instead, idle thrust is produced at the lowest engine RPM setting. A potential technology to enable the performance of windmilling on approach is to use aircraft with hybrid electric engines. In many hybrid electric engine configurations, a gas generator and/or battery supplies power to an electric motor and propulsor rather than there being a mechanical connection between the gas generator and propulsor. Not only can the electric motor be operated at low enough RPMs to result in windmilling drag, but there is no longer residual idle thrust being produced by the engine at idle. Hybrid electric aircraft thus may present possibilities for advanced operational noise reduction strategies that aircraft with conventional gas-turbine propulsion architectures are limited in performing.

Overview of Hybrid Electric Aircraft—Current Advantages and Challenges

Hybrid electric aircraft are those that have traditional gas turbine engines replaced with some amount of electric propulsion. The amount of electric propulsion may vary. For example, the Boeing SUGAR (Subsonic Ultra Green Aircraft Research) Volt aircraft concept contains turboelectric fans that are supplemented or entirely powered by electricity after initial climb [8]. Airbus, Rolls-Royce, and Siemens have proposed a demonstrator with one turbofan replaced by an electric fan to test E-Fan X hybrid electric technology [72]. Boeing has proposed several hybrid wing body concepts with turboelectric, distributed propulsion [73]. NASA has proposed a single aisle turboelectric aircraft with fuselage boundary layer ingestion, known as the STARC-ABL (Single-aisle Turbo-electric Aircraft with an Aft Boundary Layer propulsor) [74]. NASA has also proposed full electric aircraft such as the blown wing concept [75]. Example renderings of a few of these concepts are shown in Figure 2-17. Brelje and Martins provide a summary of various proposed electrified

aircraft concepts being proposed in industry and academia [76]¹.



(a) SUGAR Volt Concept, Figure from NASA/ The Boeing Company [80]

(b) NASA STARC-ABL Turboelectric Concept, Figure from NASA [80]

(c) E-Fan X Hybrid Electric Demonstrator Concept, Figure from Airbus [81]

Figure 2-17: Example “Electrified” Aircraft Concepts

Despite being a relatively new concept, the potential benefits of hybrid electric aircraft have been detailed in literature. Besides the benefits of less hydrocarbon fuel burned [82] [83], hybrid electric aircraft also provide some avenues for improvements in aircraft performance. For example, electric motors can be used to supplement power for combustion engine aircraft during high thrust portions of flight such as takeoff and climb, thus enabling the engine design to be optimized for the cruise portions of flight that are more fuel efficient [84]. Hybrid electric systems for turboprop aircraft could improve efficiency during low efficiency portions of the flight mission such as taxi [84]. Use of electric motors to drive engines may reduce thrust response time [85] and thus vertical tail size may possibly be reduced if differential thrust is instead used for lateral control. The low weight of and ability to scale electric motors without significant efficiency losses creates the potential for various distributed propulsion concepts that offer improved aerodynamic performance of the wing [86] and facilitate boundary layer ingestion [87].

Hybrid electric aircraft present source noise reduction opportunities compared to aircraft powered by traditional gas turbine engines. For example, blade tip speed and jet exit velocity can be reduced when utilizing several smaller propulsors in a distributed propulsion concept

¹Various entities have published goals to make aircraft less environmentally polluting. These include the European Commission’s Flightpath 2050 Vision for Aviation towards sustainable transports, which includes a reduction of CO₂ by 75%, NO_x by 90% and noise by 65% [77]. NASA has published similar N+3 goals with the intent to foster research into more environmentally friendly technologies such as those that result in a reduction in fuel burn of 70% relative to the state of the art 2006 era reference aircraft, a reduction in NO_x or 75% below the standards developed during the sixth Committee on Aviation Environmental Protection (CAEP 6), and a reduction in cumulative noise of 71 dB below the Federal Aviation Administration’s stage 4 noise standards [78]. In response for growing demand for aircraft that are less environmentally polluting, aircraft that are powered via electric propulsion have been studied as one avenue to reduce emissions [79].

[86] [73] instead of a few larger engines, as well as can be strategically placed on the airframe for noise shielding [88]. Distributed propulsion concepts that improve airframe performance may also enable an airframe size reduction [75] and a subsequent reduction in airframe noise. These factors have more impact with increasing degree of hybridization, which also has an overall impact on aircraft performance.

Various studies have examined noise reduction via combined conceptual design and noise abatement operational procedure adjustments that take advantage of electric and hybrid aircraft technologies. For example, a low noise departure mode where blade pitch angle is increased, thereby enabling propeller tip speed and subsequent noise to be reduced, has been suggested that can be accomplished with electric or hybrid electric general aviation aircraft [89]. Certain electric motors deliver maximum shaft power over wide ranges of shaft speed and thereby permit a reduced propeller tip speed without reducing the needed power and thrust for takeoff. Distributed propulsion made possible by electric aircraft has also been shown to be a potential noise reduction mechanism on departure, as the concept enables the same thrust to be achieved as in a traditional gas-turbine two engine aircraft but with increased mass flow and reduced jet velocity, the later of which reduces the departure jet noise [90]. Such hybrid electric engine operating modes are not as valuable in reducing noise on approach, where engine noise is not the major contributor. In fact, due to increases in weight expected to accompany aircraft with distributed propulsion, noise on approach may be expected to increase if operated similarly to a traditional gas turbine aircraft because of the increased lift, and thus flap deflection, requirements [90].

While having many benefits, hybrid electric aircraft are faced with challenges. The primary inhibitor is that the specific energy available in current battery technology is a limiter in the size and range of electric aircraft [91]. Batteries currently have on the order of 50 times lower specific energy than liquid fuels. For comparison, Jet-A fuel has a specific energy of approximately 11,900 Whr/kg while lithium-ion batteries have approximately 200 Whr/kg [92] with various studies for novel lithium ion batteries in the 2035 timeframe predicted to be in the 700 to 2,000 Wh/kg range [87]. The Breguet range equation shows that aircraft range is directly proportional to fuel energy density, and thus for the same range, a fully battery powered aircraft would be significantly heavier than a liquid fuel powered aircraft for the same

range. Additionally, there are weight penalties due to the addition of electrical components and electrical storage devices in hybrids [84], which may further limit range compared to similarly sized aircraft powered by traditional gas turbine engines. These drawbacks limit the possible missions that hybrid electric aircraft can perform.

Use of windmilling engines on hybrid electric aircraft have been considered potential methods for energy regeneration to recharge a battery on approach. A study reported by Barnes also studied the regenerative flight concept for electric aircraft [93]. The study showed that while regenerative electric flight was possible for an electric self-launching sailplane configuration, 3 minutes of regeneration on descent was needed to recover the energy expended for every 1 minute of cruise [93]. A second conceptual energy study reported by the University of Toulouse for a regional aircraft showed that the additional drag incurred by enabling windmilling engines on approach resulted in needing to descend more steeply. However, the aircraft was required to fly a longer cruise segment due to the steeper descent profile in order to maintain the same total range. Occurring to this analysis, despite the regeneration of energy on the descent segment, the resulting energy expended for the necessary longer cruise segment resulted in the total energy expenditure being higher than a normal descent profile without windmilling regeneration [84]. Noise however, was not considered in these analyses.

Despite the challenges facing hybrid and full electric aircraft in their competitiveness in the civil aviation industry that strives for long endurance vehicles, the opportunity these aircraft provide to reduce emissions is worth considering.

“Electrified” Propulsion Systems for Hybrid Electric Aircraft

Several forms of electrified propulsion systems have been proposed, with some examples highlighted in Figure 2-17, each with various propulsion system configurations. Diagram representing various forms of an electrified propulsion systems for aircraft is shown in Figure 2-18.

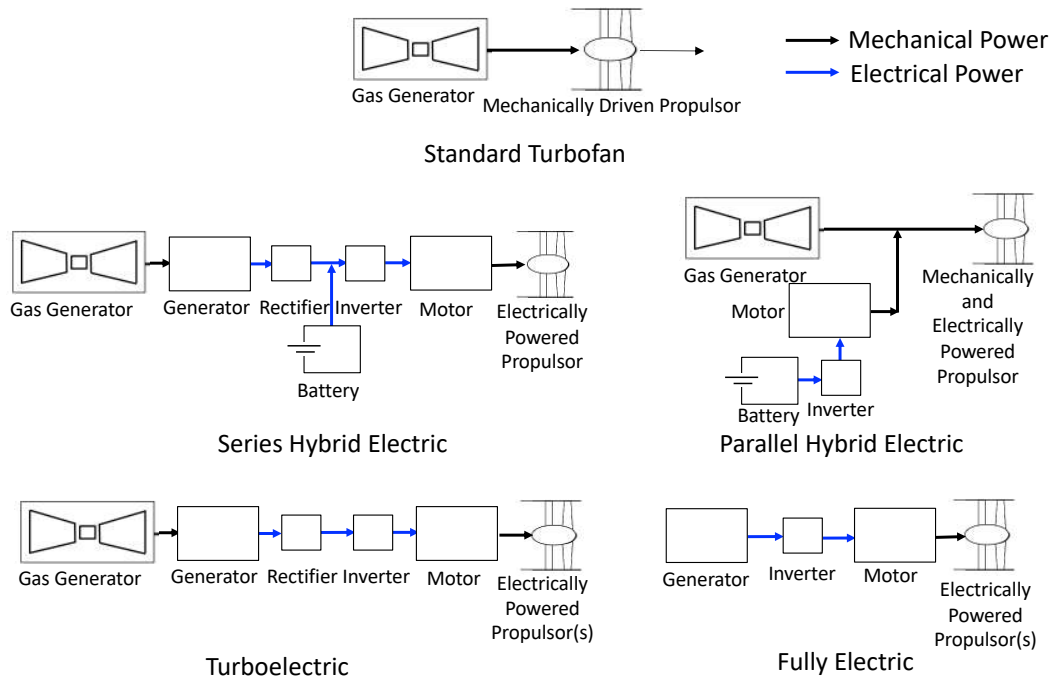


Figure 2-18: Electrified Propulsion Systems

A standard turbofan engine, as shown in Figure 2-18 (a), receives mechanical energy from a turboshaft that is mechanically connected to a propulsor. Electrified engines may have a series of electrical components supplying energy to the propulsor, with or without a turboshaft. The primary components represented in Figure 2-18 include: a generator which converts mechanical shaft power to alternating current (AC) electrical power, a rectifier which converts AC power to direct current (DC) electrical power, an inverter which converts DC electrical power to AC power, a motor which converts AC current to mechanical shaft power, and a battery [87].

In hybrid electric engines, propulsors obtain power from both a turboshaft and battery source. In a series hybrid electric engine (Figure 2-18 (b)), motors supply electrical energy from the turboshaft and battery to the propulsors. In a parallel hybrid electric engine (Figure 2-18 (c)), mechanical power is supplied to a propulsor when a motor and turbo-generator operate on the same shaft.

For a partial or fully turbo-electric architecture as diagrammed in Figure 2-18 (c), a turboshaft is the sole energy source that supplies energy to a generator. Electrical energy

from the generator is distributed to one or more propulsors.

Finally, in a fully electric architecture, one or more propulsors receive all power from a battery. In this thesis, a hybrid electric or “electrified” aircraft will refer to aircraft equipped with a form of the propulsion architecture shown in Figure 2-18 that includes electrically-powered propulsors.

When sizing electrified engines, the technology level assumptions of the electric components must be considered. Future self-cooled motors and generators for flight applications have been estimated to have a max continuous power in the 1-2.5 MW class [94][95]. Power densities of motors have been predicted with Conservative estimates by the NSF at 9 kW/kg and 98 percent efficiency [94] and more optimistic estimates by NASA of 13-16 kW/kg and up to 99 percent efficiency in the 2035 time frame [95]. Power converters in this time frame have also been conservatively predicted to be able to achieve between 9 kW/kg power density for 0.5 MW of maximum power [94] and optimistically predicted to be able to achieve between 19 kW/kg power density for 1 MW of maximum power [95].

Superconducting motors and generators, which lose electrical resistance below a critical temperature and thus can carry high currents and thus have maximum shaft powers up to 35 MW and approximately 30 kW/kg power density, have also been predicted for applications in the 2050 time frame, such as the NASA N3-X turboelectric hybrid-wing-body aircraft [73]. Superconducting power converters have also been predicted to have similar power densities [73]. Cryocoolers are needed for such machines in order to achieve the low critical superconducting temperatures [73], which adds system complexity and poses uncertainty for such components.

Compared to a traditional gas-turbine powered aircraft propulsors, electrically-powered propulsors offer more flexibility in propulsion architecture. While rotation speed of a propulsor is coupled to the rotation speed of the turbine in a standard turbofan, DC architectures such as those shown in Figure 2-18 have electrically powered propulsors that are disconnected from the turbine speed [76]. Additionally, because electrically powered propulsors are not mechanically connected to a turboshaft, a single turboshaft can supply power to a series of distributed propulsors. Distributed propulsion offers several advantages. One is in facilitating boundary layer ingestion (BLI) to increase overall efficiency. BLI

is most beneficial when the entire boundary layer is ingested, which is more effectively accomplished with a series of propulsors distributed along the wing than one large propulsor [87]. Additionally, propulsor weight has been shown to scale approximately with volume (length cubed) while mass flow rate scales with area (length squared) [87]. The result is that a single large propulsor will weigh more than a series of small propulsors with the same total frontal area and thus the same thrust.

Configurations with electrically-powered propulsors can also offer advantages in scenarios requiring quick power demand compared to gas-turbine engines, as there is a decrease in the lag in spool-up time [96]. This precision is ideal for a windmilling engine concept for descent controllability on approach. Additionally, the hybrid electric architecture would enable windmilling electrically-powered propulsors to act as generators that can recharge the battery during descent.

Chapter 3

Framework for Analyzing Performance and Noise of Advanced Operational Flight Procedures of Conventional Aircraft

To analyze performance and community noise of advanced operational approach and departure procedures for conventional aircraft, the framework shown in Figure 3-1 is implemented. The core of this framework is the Aircraft Noise Module, where noise due to both airframe and engine components is modeled using a source noise prediction method. The method used in this framework is NASA's Aircraft NOise Prediction Program (ANOPP) [34]. ANOPP was selected due to its modularity, described in section 3.3, enabling the source noise and propagation prediction of each component of a standard turbofan aircraft. Given aircraft geometry and internal engine performance states as they vary with each segment of a flight profile for a specific procedure provided by the Flight Profile Generation Module and Aircraft Performance Module shown in Figure 3-1, component noise and its propagation to specified ground observers due to aircraft performing advanced flight procedures is modeled in ANOPP.

The Flight Profile Generation Module converts a flight procedure definition into the

details of the flight profile needed for source noise modeling, given flight performance. Flight procedures are defined by the aircraft's lateral track combined with a vertical profile defined by the segment-by-segment constraints to the altitude, configuration, velocity, or thrust as a function of lateral track position. Secondary vertical profile parameters, which are implied from the specified constraints (e.g. thrust level to achieve a required climb constraint), are determined by the Flight Profile Generation Module, given the aircraft flight performance from the Aircraft Performance Module. The flight performance characteristics include: drag versus velocity and configuration, weight, and allowable operating velocities for each configuration. For this thesis, the Eurocontrol Base of Aircraft Data Family 4 (BADA 4) [97], a database of aircraft performance parameters obtained from aircraft manufacturers, was used for this performance information. The resulting flight profile is used to determine the internal engine performance states throughout the procedure, the aircraft configuration, and the aircraft altitude for noise propagation.

Engine noise is modeled via correlations that account for changes in internal engine performance states (e.g. fan rotational speed, internal engine temperatures, and jet exit velocity). These engine states, which vary with the thrust and flight velocity throughout the flight profile, are obtained from the Transport Aircraft System OPTimization (TASOPT) program 2.16 [98] within the Aircraft Performance Module. TASOPT is a physics-based model that jointly optimizes the airframe, engine, and flight trajectory of a "tube and wing" transport aircraft. Engine sizing within TASOPT is a work-balance-based, engine component-matching formulation [19] that sizes an engine for design conditions and then provides a mapping of the internal engine performance states as a function of off-design thrusts and velocities. Design conditions for a given aircraft and engine, or the design turbine inlet temperature, Mach number, bypass ratio, and the pressure ratios and efficiencies of the various engine stages, are obtained from publicly available aircraft performance data [99] [100]. The internal engine performance states used to model engine noise are determined from the thrust and velocity states of the flight profile via this engine mapping.

Airframe noise is modeled via correlations that account for airframe geometry, obtained from publicly available geometry data [99], and changes in configuration and velocity throughout the flight profile.

Given the geometry of the aircraft position with respect to a surface grid, propagation of engine and airframe source noise to the ground is modeled in the Aircraft Noise Module, creating single event flyover noise grids for that flight procedure. The single event over-flight noise is coupled in the Noise Impact Metric module with demographic variables such as the population distribution, airport geometry, and the aircraft fleet schedule to model integrated noise impact metrics such as DNL or population exposure to a specified noise level. More details on each module are provided below.

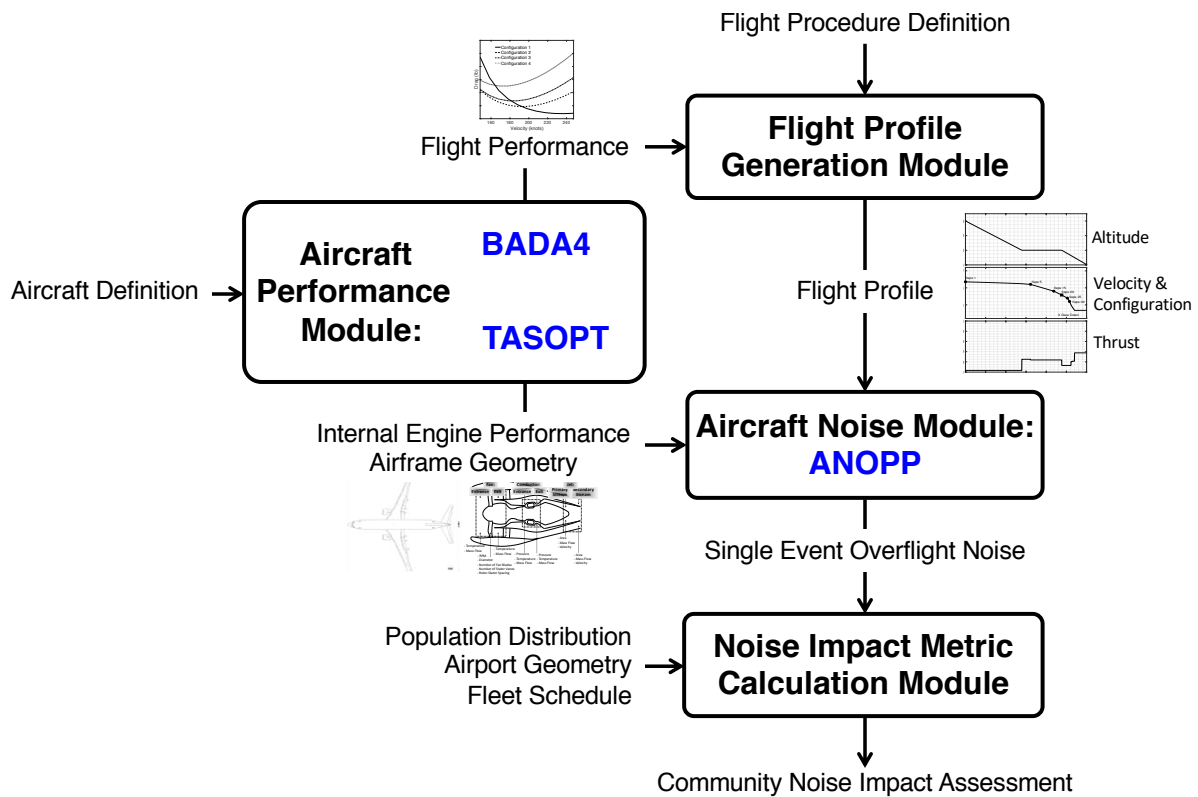


Figure 3-1: Framework to Analyze Aircraft Community Noise Impacts of Advanced Operational Procedures Composed of Flight Profile Generation and Component-Based Aircraft Noise Models Integrated via Performance Models

3.1 Aircraft Performance Model

The Aircraft Performance Model takes an aircraft definition and determines the aircraft flight performance, internal engine performance maps, and geometry. The Aircraft Performance Model consists of the Base of Aircraft Data Family 4 (BADA 4), which outputs flight

performance needed for the Flight Profile Generation Module, and the Transport Aircraft System OPTimization (TASOPT), which outputs internal engine performance maps and airframe geometry needed for the Aircraft Noise Module. Additional geometry required for the Aircraft Noise Module that are not outputted by TASOPT are obtained from external sources such as airport planning guides and *Jane's All the World's Aircraft* [99]. This is detailed in Figure 3-2.

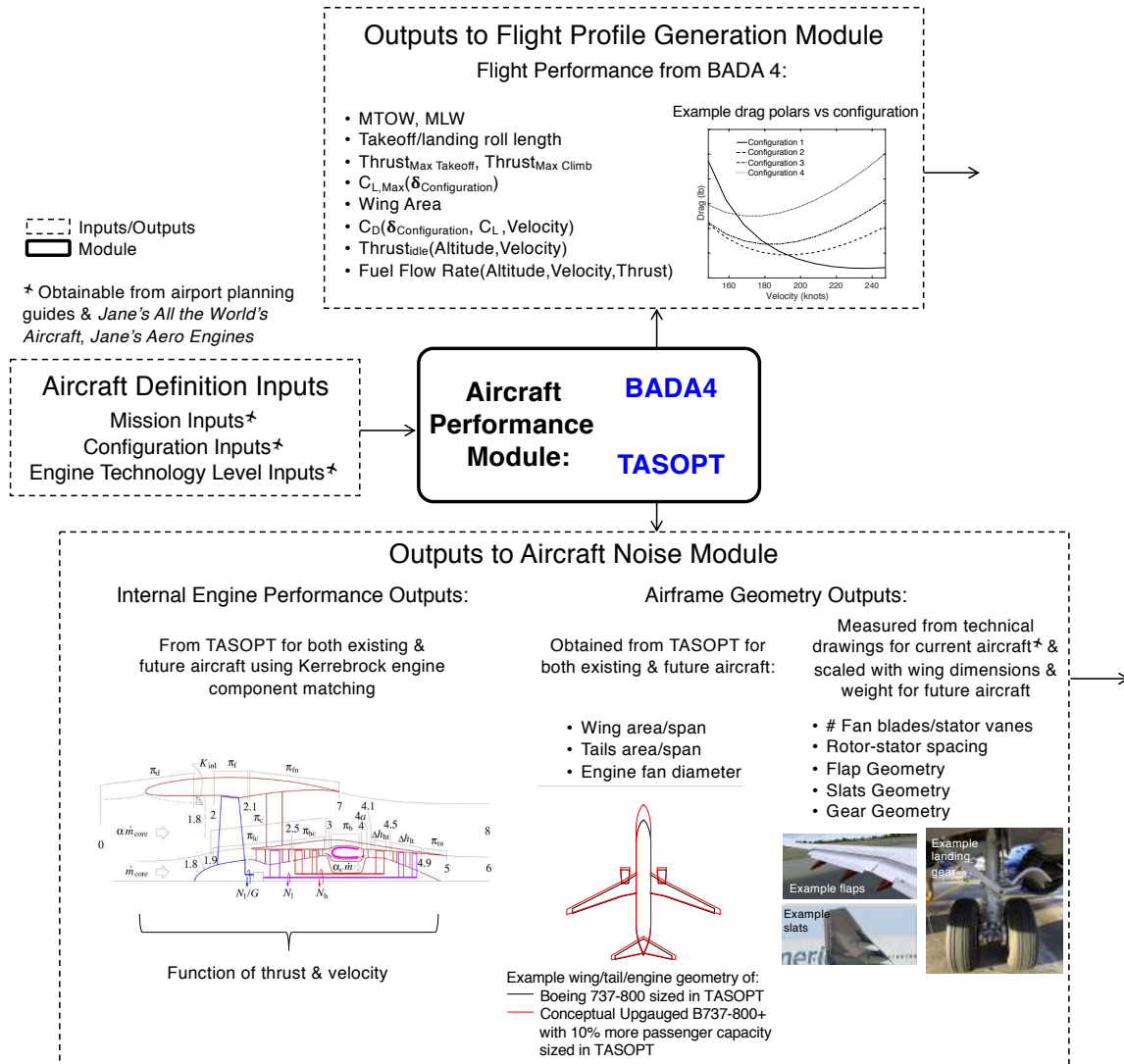


Figure 3-2: Aircraft Performance Module Detailed Inputs and Outputs

3.1.1 Flight Performance from BADA 4

Flight performance characteristics from the Aircraft Performance Module are obtained from the Eurocontrol Base of Aircraft Data Family 4 (BADA 4) [97], a database of aircraft performance parameters obtained from aircraft manufacturers. The flight performance parameters for each aircraft available in the database include the maximum takeoff and landing weight (MTOW and MLW), the maximum takeoff and landing roll length, idle and max climb thrust verses velocity and altitude, the maximum takeoff thrust, the fuel flow rate versus altitude, velocity, and thrust, and finally the aircraft aerodynamic performance at each configuration (flap, slat, and landing gear deployment) setting. The aerodynamic performance at each configuration setting includes the maximum structural operation velocity, the maximum lift coefficient ($C_{L,Max}$), and the drag coefficients as a function of C_L and velocity. These flight performance characteristics are used to model the flight profile in the Flight Profile Generation Module.

3.1.2 Internal Engine Performance Maps and Geometry from TASOPT

The internal engine performance maps needed for the Aircraft Noise Module are obtained from the Transport Aircraft System OPTimization (TASOPT) program [4]. Geometry outputs such as wing area and span, tail area and span, and engine fan diameter needed for the Aircraft Noise Module are also obtained from TASOPT. TASOPT is an aircraft design tool that jointly optimizes the airframe, engine, and flight trajectory of a "tube and wing" transport aircraft using first-principles physics based methods, rather than relying on traditional empirical drag and weight prediction methods. Thus, the internal engine performance maps and geometry outputs that are obtained from TASOPT can be obtained for both current aircraft and future aircraft concepts as specified by the aircraft definition.

TASOPT requires aircraft mission inputs, configuration inputs, and engine technology level inputs to size an aircraft. These can be matched to an existing aircraft type's specifications from external data when modeling an existing aircraft or be modified to desired requirements for a future aircraft concept. The required inputs, and how they are used for

sizing an aircraft in TASOPT, are as follows:

1. The aircraft's mission inputs include the aircraft's number of passengers and weights per passenger, maximum range, start of cruise altitude, cruise Mach number, and load limits. The weight per passenger is assumed to follow standard average passenger weights listed in Advisory Circular 120-27E [101] while the aircraft load limits follow the minimum required structural load limits described in 14 CFR 25.333 and 25.337 [102]. The remaining parameters are readily available for existing aircraft types in external data [99]. This information becomes the basis for subsequent calculations.
2. The aircraft configuration inputs define the tube-and-wing aircraft configuration.

The configuration inputs include the shape definition of the wings and tails, such as the sweep, aspect ratio, taper ratio, thickness-to-chord ratio, and tail volumes, as well as historical weight fractions for secondary wing components such as the slats, flaps, etc. These parameters are assigned to the wings and tails, which are then sized to survive critical bending loads at the maximum allowable load limit cases. The internal size of the wing also gives the maximum fuel volume.

The configuration inputs also include the geometry of the fuselage such as the fuselage diameter, fuselage length, height of the fuselage floorboard, and location of aircraft sub-components along the length of the fuselage such as the auxiliary power unit location and the landing gear location. The fuselage skin, stringers, and floor are then sized assuming the aircraft is a pressure vessel to meet various loading scenarios, while the weights of secondary components such as windows, seats, etc. are estimated using historical weight fractions which are proportional to the number of passengers.

Aerodynamic performance is also modeled assuming that lifting forces balance weight while drag balances thrust, with thrust computed as a power balance [4]. A parameterized transonic airfoil family spanning a range of thicknesses is used to obtain airfoil lift and drag performance that is applied to the 3-dimensional wing. The fuselage drag is obtained from viscous/inviscid CFD based on the user-supplied fuselage geometry. Nacelle drag is obtained assuming it is a power dissipation based

on the nacelle’s exterior velocity distribution. Finally, overall drag is predicted using a Trefftz-Plane analysis.

The configuration parameters needed for the fuselage, wing, and tail sizing are obtained from detailed aircraft technical drawings found within airport planning guides for existing aircraft, while the weight fractions are typically held constant at historical values.

3. The engine technology level inputs are used to determine the engine performance. These inputs include the engine’s maximum turbine inlet temperature T_{t4} , the design point bypass ratio, and the design point pressure ratios and efficiencies of the various engine components. TASOPT uses a work balance-based component matching formulation [19] based on the layout shown in Figure 3-3 to size the engine. The method is used to obtain the engine areas, temperatures, pressures, and mass flow rates at the various stations within a turbofan. The engines are sized for start of cruise. After the engine is sized, performance state maps in off-design conditions are generated for specified array of thrust, velocity, and altitude settings.

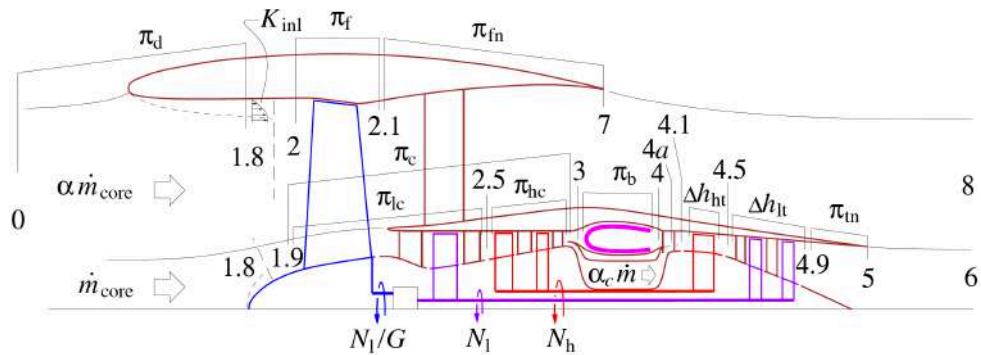


Figure 3-3: Turbofan Engine Layout used in TASOPT’s Engine Sizing [4]

Many of the engine technology level inputs, such as overall pressure ratio and fan pressure ratio, can be obtained from publicly available engine data [100] for a specific engine. Some properties such as maximum turbine inlet temperature can be approximated based on historical engine charts of turbine inlet temperature versus overall pressure ratio, bypass ratio, and specific fuel consumption such as that in

Figure 3-4. Remaining engine technology level inputs that aren't directly obtainable from publicly available resources, primarily engine component efficiencies, are held at constant values across various aircraft types.

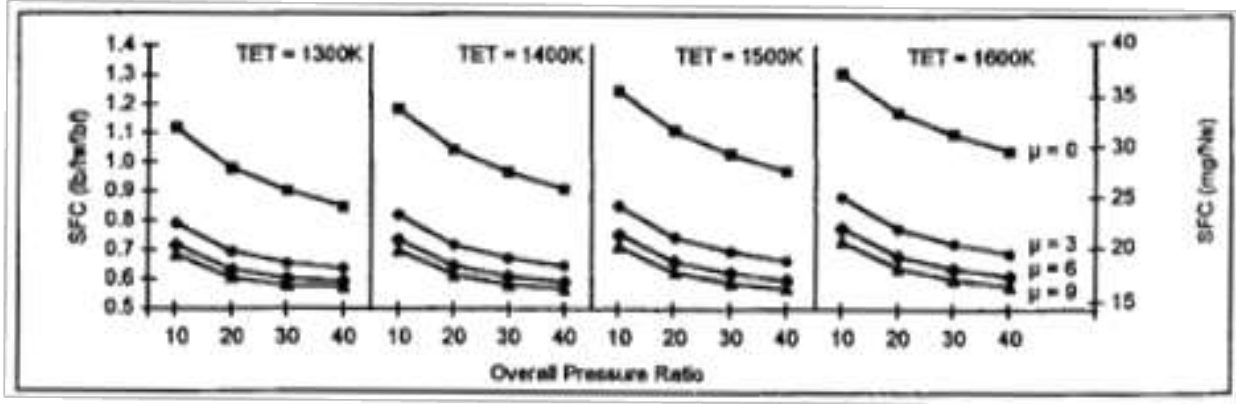


Figure 3-4: Turbofan Specific Fuel Consumption Variation with Bypass Ratio (μ), Turbine Entry Temperature (TET), and Overall Pressure Ratio, Figure from [100]

Given all of the inputs described above, TASOPT carries out the remainder of the aircraft sizing as follows:

5. The various weights and locations of the aircraft and the overall aircraft pitching moment from the aerodynamic analysis are used to enforce pitch stability, which then sets the locations of the aircraft tails.
6. The aircraft mission trajectory including takeoff, climb, cruise, and descent is computed on a segment-by-segment basis assuming a cruise-climb at a fixed cruise Mach number, cruise lift coefficient, and cruise turbine inlet temperature. Takeoff turbine inlet temperature inputs are used to set the climb profile while a descent angle constraint results in the turbine inlet temperature on descent becoming an output. Balance field length requirements are also checked in a takeoff performance model.
7. In a sizing loop, a guess in the initial fuel weight varied until the resulting range from the trajectory generation equals the initial inputted design range. An aircraft that meets the mission requirements given the aircraft configuration inputs and the engine technology level inputs is thus sized.

3.1.3 Geometry Outputs from External Sources

There are additional geometry details required for the aircraft noise model that aren't sized in TASOPT and thus are obtained from external data for existing aircraft. The method for how these are used for aircraft source noise modeling is explained in section 3.3. These geometry details include:

- The flap system spans, chords, side edge thicknesses, and deflection angles (defined in [43])
- The slat system spans, chords, gap width of the slat cove, and deflection angles (defined in [41])
- The main and nose landing gear geometry, including the number of wheels and struts, the tire diameter and width, and the lengths and diameters of the struts and any exposed linkages (defined in [44])
- The fan internal geometry, including the number of fan blades and stator vanes, and the rotor-stator spacing.

Flap and slat plan-form geometry can be measured from aircraft technical drawings, whereas deflection angles for each configuration setting are obtained from pilot forums. Landing gear geometry can be extensive and is therefore obtained from photographs of the gear. Example measured landing gear geometry for a Boeing 737-800 and 777-200 can be found in NASA CR 2005-213780 [44]. Internal fan geometry can be obtained from Jane's All the Worlds Engines [100].

For estimates of noise of future aircraft, flap and slat span, chord, and edge thickness of a similarly sized existing aircraft are scaled proportionally by the wing geometry of the future aircraft. Landing gear geometry is sized based on commercial off the shelf tire and wheel ratings, such as those shown in Figure 3-5, that can support the future aircraft weight. Landing gear strut lengths for future aircraft are adjusted as necessary to ensure ground clearance for wing mounted engines and to prevent a tail strike on takeoff.

Tire Size	Ply Rating	Max Width inches	Max Diam. inches	Loaded Radius inches	Tire and tube wt. lbs.	Commercial		Military	
						Press lbs/sq.in.	Rated Load lbs	Press lbs/sq.in.	Rated Load lbs.
24 x 7.25	10	7.3	24.0	10.3	29.7	120	6,600		
29 x 7.7	12-16	7.6	28.0	12.2	36-44	160	9,800	220	13,800
34 x 11	18	11.0	33.0	13.9	84.1	125	15,500		
36 x 11	24	11.1	35.0	15.0	86.2			220	25,600
40 x 14	22	13.5	39.2	11.8	112	145	25,000		
44 x 13	26	13.4	43.2	18.4	141.5			200	35,000
44 x 16	26	15.6	43.1	18.0	151.6	165	35,500		
56 x 16	24	16.0	55.8	24.1	258.7			178	45,000
56 x 16	32	16.1	55.8	24.1	296.3			240	60,000
56 x 16	36	16.1	55.8	24.1	297.0			280	71,000

AERODYNAMIC DESIGN

Figure 3-5: Commercial and Military Landing Gear Tire Ratings, from Airplane Design, R. H. Liebeck [103]

3.2 Flight Profile Generation Module

Given the flight procedure definition and the aircraft flight performance, the Flight Profile Generation Module models the flight profile. The flight procedure definition specifies the desired aircraft takeoff or approach operation. The flight procedure definition is inputted as the ground track plus a series of constraints for each segment of the procedure. The outputted flight profile is the altitude, thrust, velocity, configuration, and lateral position per time and is inputted to the Aircraft Noise Module.

Though not the focus of this thesis, fuel burn per time is also outputted from the flight profile generation and can be used to examine additional benefits or potential trade-offs in fuel burn to consider with the design of a modified procedure for noise abatement. It can also be used to model secondary emission effects such as carbon dioxide produced.

These inputs and outputs are detailed in Figure 3-6.

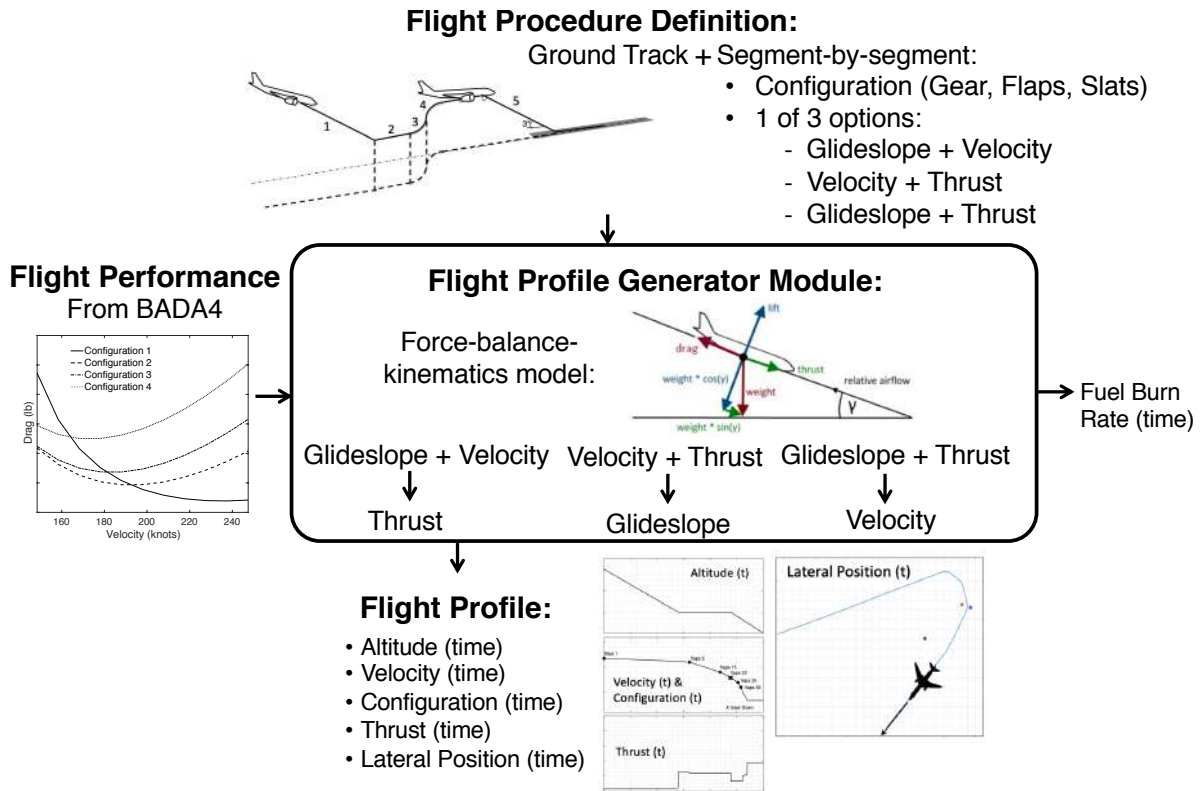


Figure 3-6: Flight Profile Generation Module Detailed Inputs and Outputs

Modeling within the Flight Profile Generator is as follows: on a segment-by-segment basis, with the weight and configuration of the aircraft also specified for each segment, and the flight performance given from BADA 4, force-balance and kinematics are used to determine either: the required thrust from a flight path angle (or glideslope) and velocity change constraint; the resulting flight path angle (or glideslope) from a thrust and velocity change constraint; or the resulting velocity change from a flight path angle (or glideslope) and thrust constraint. The ending conditions of one segment become the starting conditions of the next segment. The Flight Profile Generation Module fits the two-dimensional altitude versus distance profile to the desired ground lateral track to create the entire three-dimensional flight profile.

This segment-by-segment approach is based on a force-balance kinematics point-mass model shown in Figure 3-7.

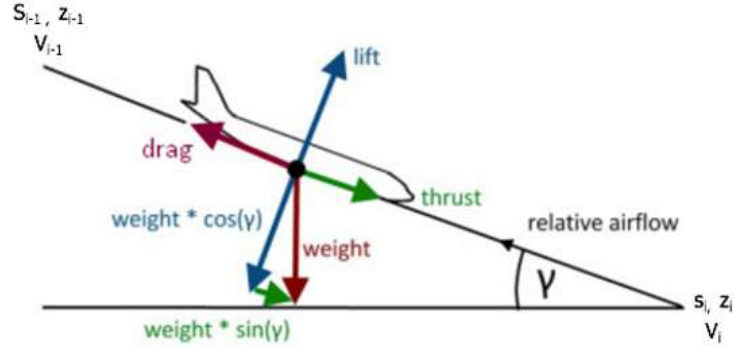


Figure 3-7: Force-balance Approach to Calculate Each Profile Segment from Procedure Definitions

Based on the model shown in Figure 3-7, the acceleration of the aircraft along the direction of flight is given by the sum of the forces in the direction of flight divided by the mass of the aircraft shown in Equation 3.1.

$$a = \left(\frac{\sum Forces}{m} \right) = \left(\frac{Thrust + Weight * \sin(\gamma) - Drag}{Weight/g} \right) \quad (3.1)$$

With the acceleration of the aircraft known, the distance traveled along the aircraft's flight path, $s_i - s_{i-1}$, or the change in altitude, $z_i - z_{i-1}$, given a change in velocity $V_i - V_{i-1}$ can be determined from kinematics, shown in Equation 3.2.

$$\left(\frac{V_{i-1}^2 - V_i^2}{2a} \right) = s_{i-1} - s_i = \left(\frac{z_{i-1}^2 - z_i^2}{\sin(\gamma)} \right) \quad (3.2)$$

In addition, a takeoff or landing roll includes the friction from the runway. A landing roll may also include reverse thrust. The diagrams for these cases are shown in Figure 3-8.

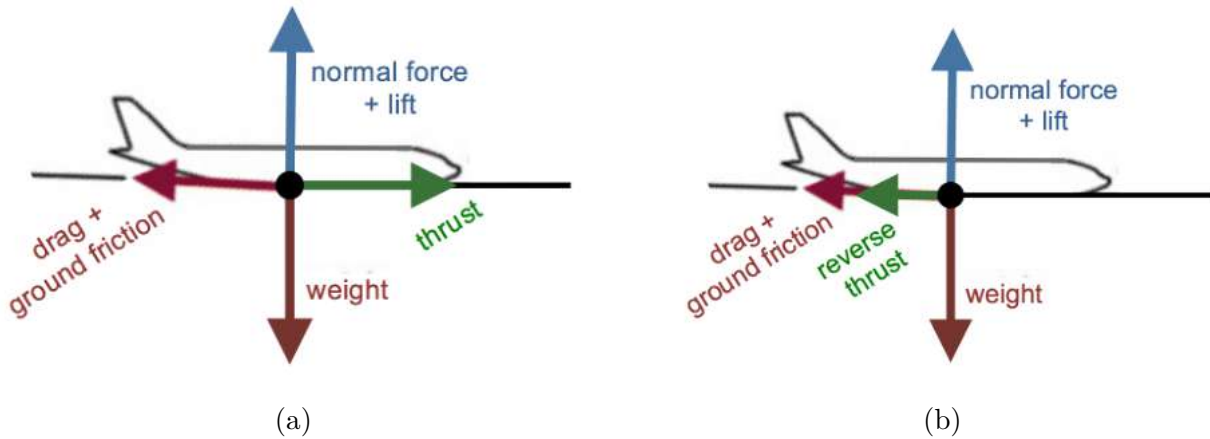


Figure 3-8: Force-balance Approach for Takeoff-Roll (a) and Landing Roll (b) to Calculate Each Profile Segment for Profile Definitions

A typical segment structure used for departure procedures is shown in Figure 3-9. There is an initial high thrust takeoff roll to takeoff safety speed V_2 , a high thrust initial climb segment with retracted gear and acceleration to V_2+15 knots, acceleration segments where the aircraft has cutback to climb thrust and flaps are incrementally retracted, and a climb segment at or below the maximum allowable speed below 10,000 ft of 250 knots.

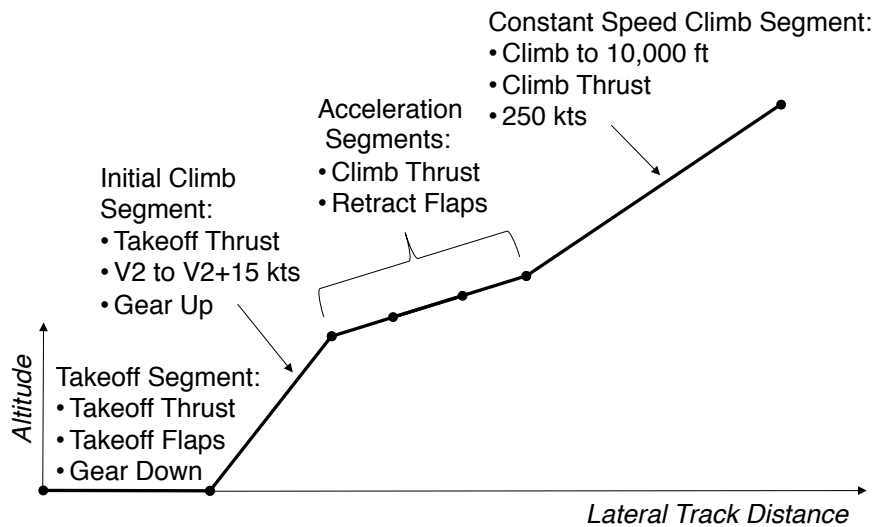


Figure 3-9: Example Segment Structure for a Departure Procedure

This structure for a departure procedure can then be defined such that the altitude versus position profile matches the mean altitude profile from a set of radar data such as Airport Surface Detection Equipment, Model X (ASDEX) data, an example of which is shown in

Figure 3-10. The required thrust that satisfies this altitude profile, as constrained by the aircraft weight, drag, and assumed velocity and configuration changes, can be modeled during each segment.

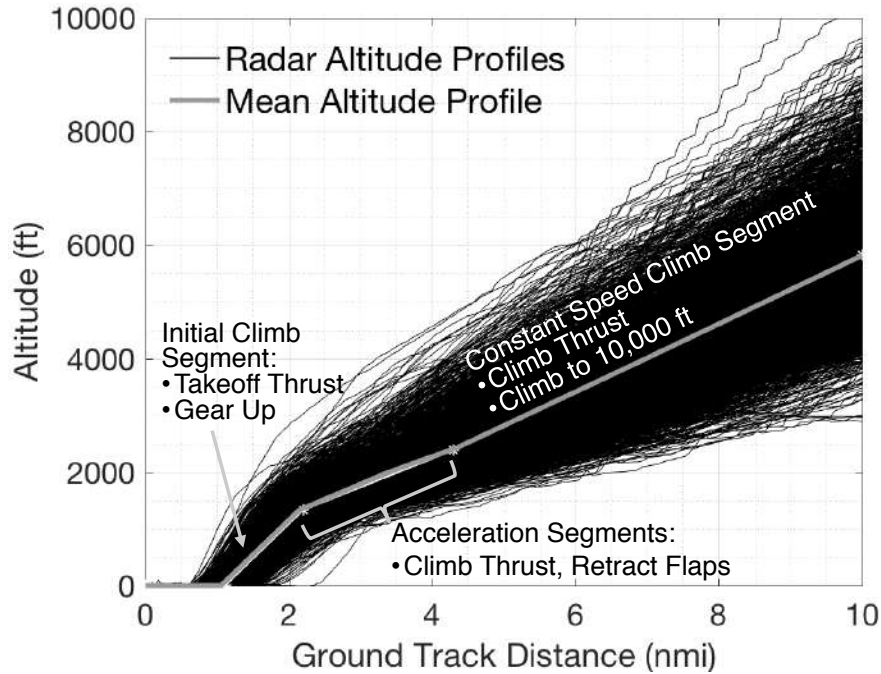


Figure 3-10: ASDEX Boeing 737-800 Radar Altitude Departure Data Over 20 Days in 2017 from all Runways at BOS

A typical segment structure for approach procedures is shown in Figure 3-11. There is an initial descent segment from a starting altitude and velocity, a series of deceleration segments where flaps are deployed, a series of final approach segments consisting of an intercept with the Instrument Landing System (ILS) glideslope followed by segments where the aircraft deploys gear, deploys landing flaps, and then maintains a constant configuration and landing reference speed V_{REF} to the ground, and a landing roll segment with reverse thrust. The deceleration segments may consist of one or more level offs or may be a continuous descent all the way to the ILS intercept or to the ground.

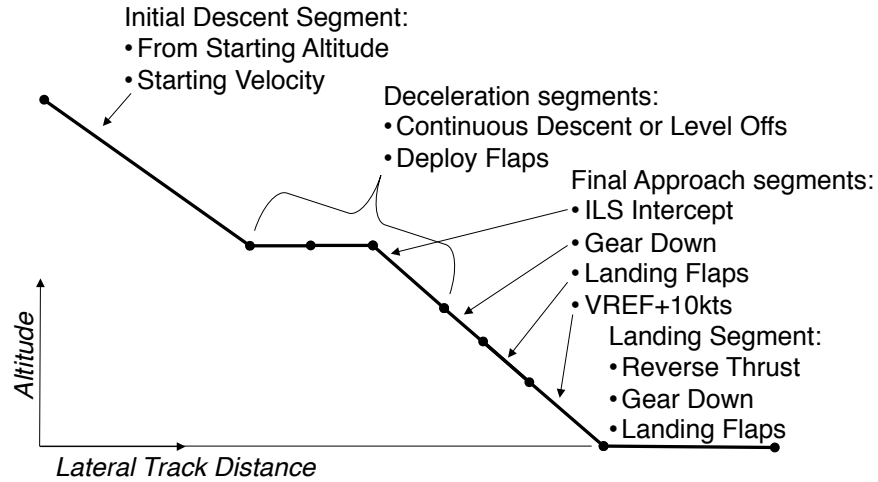


Figure 3-11: Example Segment Structure for an Approach Procedure

This structure for an approach procedure can then be defined such that the altitude versus position profile matches the mean altitude profile and the velocity profile from ASDEX radar data, such as that shown in Figure 3-12 and Figure 3-13.

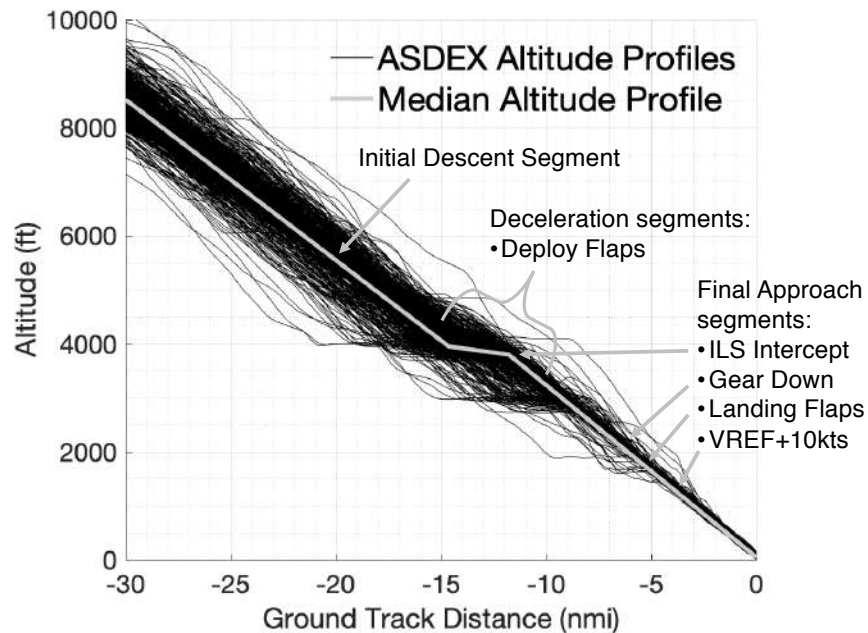


Figure 3-12: ASDEX Boeing 737-800 Radar Altitude Approach Data into Runway 4R at BOS in 2017

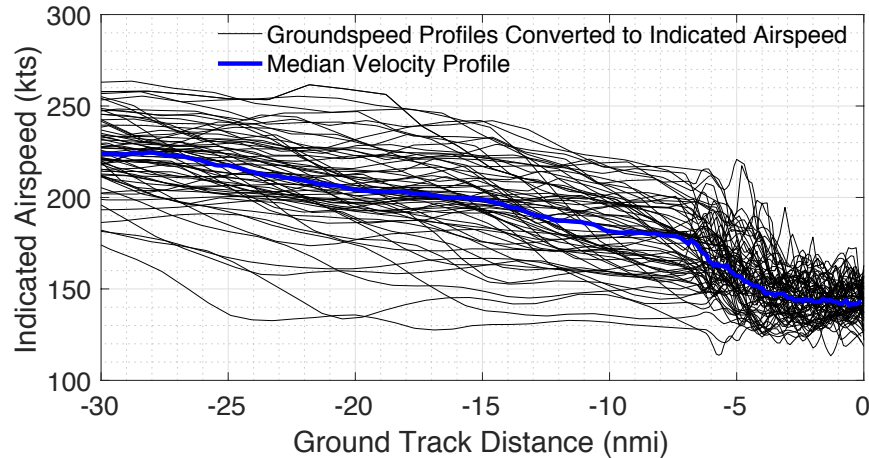


Figure 3-13: ASDEX Boeing 737-800 Radar Velocity Approach Data into Runway 4R at BOS in 2017

Because the configuration changes the aircraft drag model, it is necessary to estimate where the flap, slat, and gear changes that occur in these procedures. For departure procedures an aircraft is assumed to have retracted flaps when it has accelerated above the minimum safe airspeed for each configuration at the modeled departure weight. The minimum safe airspeeds of each were assumed to be 1.3 times V_{stall} , where V_{stall} corresponds to the $C_{L,max}$ speed in each configuration from BADA 4. For approach procedures, an aircraft is assumed to have deployed flaps where it has decelerated to 10 knots below the maximum flap speed for each configuration. The maximum flap speed for each configuration is also obtained from BADA 4. V_2 is assumed to be 1.2 times V_{stall} , while V_{REF} is modeled as 1.3 times V_{stall} . Gear deployment or retraction is typically defined by set altitudes depending on the procedure.

For fuel burn assessments, the Flight Profile Generation method also provides the total fuel burn during the duration of the flight profile based on fuel flow rate from BADA 4, which is a function of thrust, velocity, and altitude.

3.3 Component-Based Aircraft Noise Module

The Component-Based Aircraft Noise Module for conventional aircraft, shown in Figure 5-7, determines the engine and airframe source noise and propagation using models from ANOPP.

The internal engine performance states are inputted to the engine source noise models and are interpolated from the internal engine performance maps from TASOPT at each thrust, velocity, and altitude state of the flight profile. The velocity and configuration profiles and the airframe geometry from TASOPT and external sources are inputted to the airframe noise model.

Source noise in ANOPP is modeled as mean square acoustic pressure over the 1/3 octave band noise spectrum from 50 Hz to 10 kHz. The mean square acoustic pressure is also modeled for the range directivity angles representing the lower hemisphere of the aircraft. Modeled engine and airframe source noise is summed together at all frequencies and directivity angles at each segment in the flight profile. Propagation of this total source noise to the surface is modeled given the altitude and position profile, creating single event flyover noise grids. The inputs and outputs are detailed in Figure 5-7.

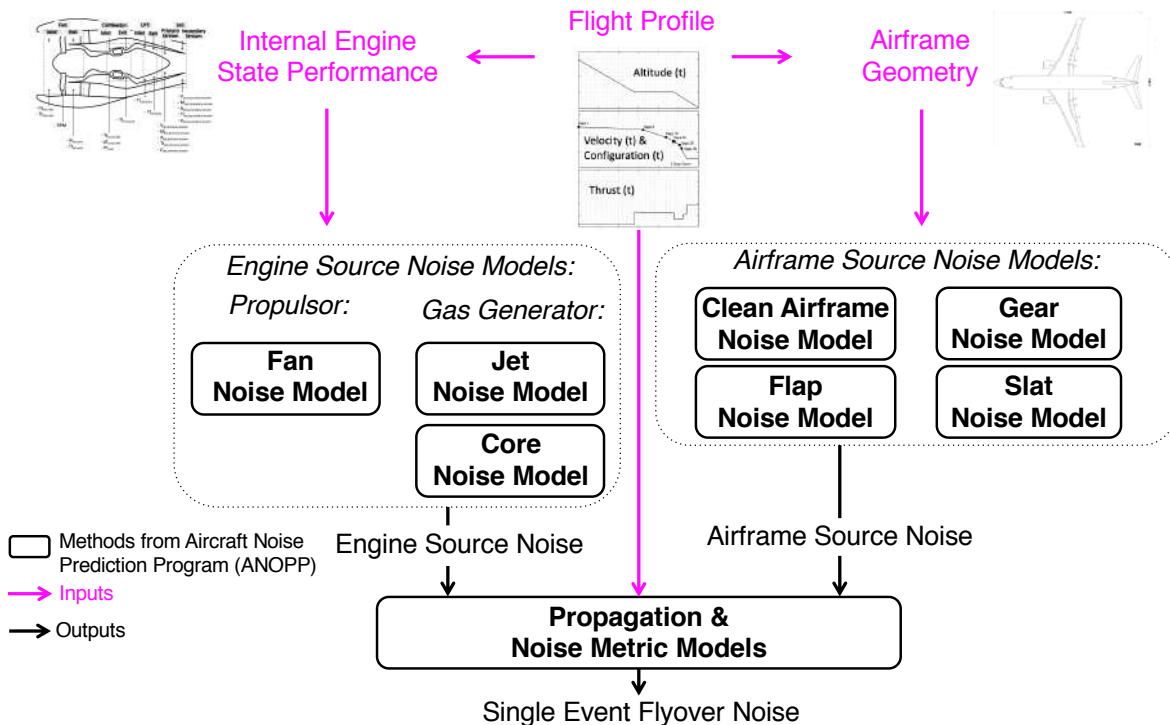


Figure 3-14: Component-Based Aircraft Noise Module Inputs and Outputs

Each of the source noise and propagation models and inputs are described below.

3.3.1 Turbofan Engine Source Noise Modeling

Turbofan engine source noise is modeled using the ANOPP engine source noise models given the internal engine performance characteristics of the aircraft as a result of the thrust, velocity, and altitude state at each segment of the flight profile. The specific internal engine noise parameters required for this framework are determined from the following models:

- Fan noise (for existing turbofan aircraft) within this framework is modeled by ANOPP’s Heidmann Fan Noise model [36], which is applicable to high bypass ratio turbofan engines. This method assumes fan noise is produced by turbulent air passing over fan blades and is related to the specific work across the fan, which is proportional to the temperature rise across the fan, and mechanical power, which is proportional to the mass flow rate through the fan. The temperature rise ($Tt_{fan,exit} - Tt_{fan,inlet}$) and mass flow rate through the fan ($\dot{m}_{fan,exit}$, $\dot{m}_{fan,inlet}$) is obtained from the internal engine performance maps from TASOPT. This method assumes fan noise is also produced by the interactions between fan rotor and stator vanes and airflow passing over fan blade tips moving at supersonic speeds and is dependent on the number of rotor blades and stator vanes and the rotor-stator spacing, which in this framework obtained from publicly available engine geometry data [100], and the fan’s rotational speed (RPM), which in this framework is obtained from TASOPT internal engine performance maps.
- Core noise within this framework is modeled by ANOPP’s Combustion Noise model [34], which is based on the original method by Emmerling [104] and detailed with modifications in the SAE ARP876 method [105] for predicting combustion noise from turboshaft, turbojet, and turbofan engines and subsequent propagation through the turbine. This method assumes combustion noise results from the mass density and momentum fluctuation in the combustor due to unsteady burning [104]. It is proportional to the pressure ($pt_{core,inlet}$), temperature rise ($Tt_{core,exit} - Tt_{core,inlet}$), and mass flow rate through the combustor (\dot{m}_{core}). Attenuation through the turbine is based on the SAE method and is a function of the design-point temperature drop across the low pressure turbine ($Tt_{LPT,inlet} - Tt_{LPT,exit}$). In this framework, these inputs are obtained from TASOPT internal engine performance maps.

- Jet noise within this framework is modeled by ANOPP’s Stone Jet Noise model [106], which is applicable to single stream and coaxial circular jets. This method assumes jet noise is produced from the fast airflow from the jet mixing with slower ambient air and scales with the difference of the velocities of the primary and secondary streams ($V_{jet,primarystream}, V_{jet,secondarystream}$) and the mass flow, inputted as area ($A_{jet,primarystream}, A_{jet,secondarystream}$) times velocity times density ($\rho_{jet,primarystream}, \rho_{jet,secondarystream}$) in ANOPP, and temperature of the streams ($Tt_{jet,primarystream}, Tt_{jet,secondarystream}$), all of which are obtained from TASOPT internal engine performance maps.

A summary of the required inputs described above for the ANOPP engine noise models is shown in Figure 3-15.

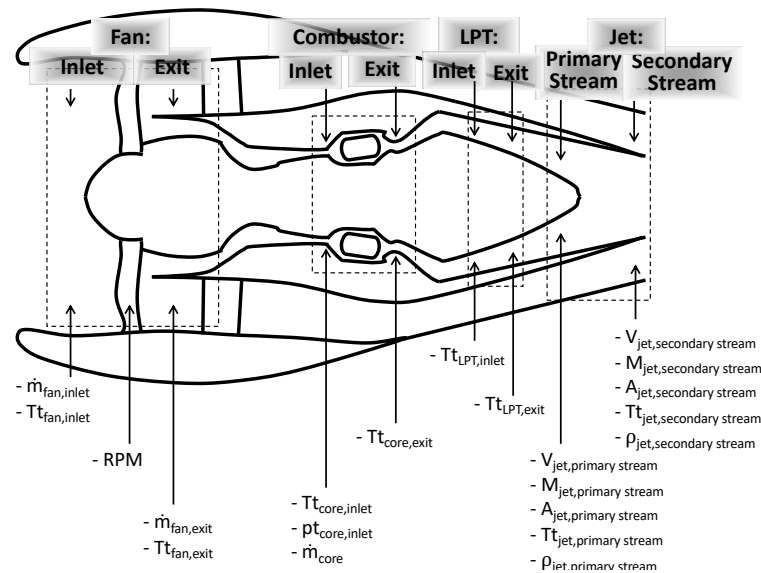
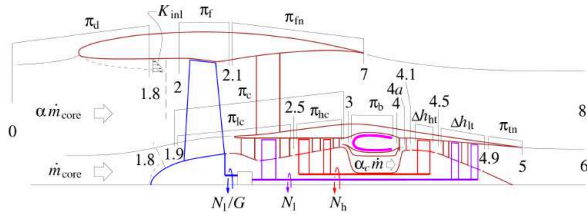


Figure 3-15: Required Inputs for the ANOPP Engine Noise Models

These inputs are interpolated from the TASOPT internal engine performance maps such depending on the thrust, velocity, and altitude at each flight profile operating point. Figure 3-16 shows an example engine internal performance state table from TASOPT based on the turbofan engine layout used in TASOPT’s engine model. These state tables can be obtained for any thrust, velocity, and altitude condition after sizing the engine for design conditions.



(a)

B2: alt. = 8375. ft		B2: Mach = 0.4713		B2: BPR = 5.0970		B2: N1 = 1.0635		B2: Feng = 62.051 kN		B2: mcore = 50.867 kg/s	
B2: loc	Tt	pt	cpt	R	cpt/(cpt-R)						
	K	kPa	J/kg K	J/kg K							
0	283.6	86.24	1008.7	288.3	1.4002						
2	283.6	85.81	1008.7	288.3	1.4002						
21	331.8	141.46	1011.1	288.7	1.3989						
7	331.8	138.63	1011.1	288.3	1.3989						
0	283.6	86.24	1008.7	288.3	1.4002						
18	283.6	85.81	1008.7	288.7	1.4002						
19	283.6	85.81	1008.7	288.7	1.4002						
25	378.9	214.14	1014.9	288.7	1.3968						
3	815.1	2565.67	1105.6	288.3	1.3527						
4	1509.0	2411.73	1265.7	288.8	1.2956						
41	1423.0	2256.59	1248.5	288.7	1.3008						
45	1052.3	547.08	1189.6	288.7	1.3205						
49	759.9	128.63	1122.2	288.7	1.3464						
5	759.9	127.99	1122.2	288.7	1.3464						
B2: loc	T	p	M	u	A	Fsp	eta_p				
	K	kPa		m/s	m ²						
0	271.6	74.12	0.4713	155.66	2.0943	0.6058					
2	264.6	67.31	0.5993	195.87	1.7944						
25	353.5	167.76	0.6013	226.98	0.1361						
5	659.2	74.12	0.9300	472.74	0.2810						
6	659.2	74.12	0.9300	472.74	0.2810	0.1615	0.4954				
7	277.5	74.12	0.9896	331.18	0.8448						
8	277.5	74.12	0.9896	331.18	0.8448	0.4443	0.6395				

(b)

Figure 3-16: (a) Turbofan Engine Layout Used in TASOPT's Engine Model, (b) Example Outputted Engine Performance Map at Each Engine Component Station for a Boeing 737-800 at a Climb Mach number of 0.4713, Thrust of 62.051 kN/engine, and Altitude of 8,375 ft

The engine performance inputs to ANOPP are determined from the internal engine performance maps from TASOPT as follows:

$$\begin{aligned}
 \dot{m}_{fan,inlet} &= m_{core} * (BPR + 1) & V_{jet,primarystream} &= u_{loc6} \\
 Tt_{fan,inlet} &= Tt_{loc2} & M_{jet,primarystream} &= M_{loc6} \\
 RPM &= N1 * (RPM_{Fan,Max}) & A_{jet,primarystream} &= A_{loc6} \\
 \dot{m}_{fan,exit} &= m_{core} * (BPR) & Tt_{jet,primarystream} &= T_{loc6} * (1 + 0.5(\gamma - 1)M_{loc6}^2) \\
 Tt_{fan,exit} &= Tt_{loc7} & \rho_{jet,primarystream} &= \frac{m_{core}}{A_{loc6} * u_{loc6}} \\
 Tt_{core,inlet} &= Tt_{loc3} & V_{jet,secondarystream} &= u_{loc8} \\
 pt_{core,inlet} &= pt_{loc3} & M_{jet,secondarystream} &= M_{loc8} \\
 \dot{m}_{core} &= m_{core} - m_{cool} & A_{jet,secondarystream} &= A_{loc8} \\
 Tt_{core,exit} &= Tt_{loc4} & Tt_{jet,secondarystream} &= T_{loc8} * (1 + 0.5(\gamma - 1)M_{loc8}^2) \\
 Tt_{LPT,inlet} &= Tt_{loc4.5} & \rho_{jet,secondarystream} &= \frac{m_{core}}{A_{loc8} * u_{loc8}} \\
 Tt_{LPT,exit} &= Tt_{loc4.9} & &
 \end{aligned}$$

3.3.2 Airframe Source Noise Modeling

Airframe source noise is modeled given flight velocity and configuration maintained in the flight profile and airframe geometry that is obtained from publicly available aircraft geometry data [99]. Trailing edge noise of the clean wing and tail is modeled in ANOPP using the Fink Airframe noise model [40]. Configuration noise from the leading edge slats, trailing edge flaps, and landing gear is modeled with the Boeing Airframe noise model [107]. The theory and required airframe geometry parameters for these methods are described below:

- Wing and tail trailing edge noise is assumed due to convection of the turbulent boundary layer past the trailing edges and is modeled based on the Fink method [40] that was derived from airframe noise measurements from the 1970s [108] [109] of multiple aircraft in flaps up, gear up, idle thrust configurations, at flight speeds up to 350 knots. The clean wing overall sound pressure level (OASPL) according to Fink’s method is represented by equation 3.3.

$$OASPL = 50\log\left(\frac{V}{100kt}\right) + 10\log\left(\frac{\delta_w b_w}{h^2}\right) + 10\log\left(\frac{\cos\phi \sin\theta \cos\theta}{2}\right)^2 + C + K \quad (3.3)$$

OASPL is a function of the 5th power of the flight velocity V , a geometry term consisting of the wing boundary layer thickness δ_w , the wing span b_w , and the over flight height h , and a directivity factor where θ and ϕ are directivity angles. The flight test data also showed a residual variability for different aircraft types which was suggested to be due to variability in wing surface aerodynamic smoothness between high performance sailplanes and conventional aircraft. To represent the residual variability, suggested to be due to variability in wing surface smoothness, Fink used a wing smoothness correction factor K [40]. A correction factor of $K = 8$ dB, termed here as the “conventional” wing surface assumption, was consistent with the noise of conventional low speed aircraft, for example retractable landing gear, propeller driven aircraft such as the Douglas DC-3, and some jets, such as the Boeing 747. A correction factor of $K = 0$ dB, termed here as the “aerodynamically smooth” wing surface assumption, was consistent with noise of aerodynamically smooth wings such as high performance

sailplanes. The term C in equation 3.3 represents an additional offset that corrects for units. Clean tail noise is modeled similarly with variation in the geometry, directivity, and C terms.

Recent data and expert recommendations indicates the aerodynamically smooth wing surface assumption is likely more appropriate for modern jet aircraft [110] that may have smoother airframes than the aircraft used in the 1970s flight tests.

- Leading edge slat noise in the Boeing Airframe noise model [107] is attributed to unsteady flow and pressure fluctuations in the slat cove [41]. It scales with the slat span, slat chord, slat sweep, slat gap from the wing, and approximately the 5th to 6th power of velocity.
- Flap side-edge noise in the Boeing Airframe noise model [107] is assumed due to interactions between vortices and the flap side edges and is based on the method by Guo [43]. It scales with the 5th power of velocity for low frequencies and the 6th power of velocity for high frequencies and depends on the flap span, chord, sweep, thickness, deflection angle, and whether the edge is isolated or abutted.
- Landing gear noise in the Boeing Airframe noise model [107] is assumed due to the wake shedding of the deployed gear, the exposed components of which act as bluff bodies. It is based on the method by Guo [44] [42]. This method enables a detailed examination of noise due to not only the stock strut of the gear, but also the additional structural members of the gear assembly and wheels given their dimensions. Noise in this method scales with the 6th power of velocity.

3.3.3 Noise Propagation and Noise Metric Modeling

ANOPP's noise propagation and noise metric modules are used to model the propagation of the source noise to user-specified sample grid points on the ground, given the engine and airframe source noise throughout the flight profile. After the source noise components are summed for each flight segment, the source noise is broken into emission time elements in the flight profile. The distance and directivity angles between the aircraft and each sample grid point are modeled for each emission time, along with the noise reception time at the grid points. The mean square acoustic pressures received at each grid point are then modeled by

applying a spherical spreading and an acoustic impedance in air corrections to the source mean square acoustic pressures produced during the emission time and at the directivity angles associated with each grid point and reception time. Sound intensity loss due to atmospheric attenuation is also computed assuming losses due to thermal and viscous effects that are a function of temperature, pressure, and humidity as well as distance between the emitted noise at the source and the observer on the ground [111]. The method also applies a sound intensity loss correction due to destructive interference of reflecting sound waves when the aircraft is near the ground [14]. This results in mean square acoustic pressure in frequency and time at the observing grid locations.

The availability of mean square acoustic pressure in frequency and time at the observers enables the integration of these pressures over the frequency spectra at each sample grid point to obtain A-weighted sound pressure levels and perceived noise levels for each time segment received at the grid points. The maximum A-weighted sound pressure levels ($L_{A,MAX}$) at each sample grid point is determined to assess the flight procedure in terms of $L_{A,MAX}$. The A-weighted sound pressure levels and perceived noise levels can also be integrated in time to produce Sound Exposure Level (SEL) and Effective Perceived Noise Level (EPNL) metrics.

3.4 Noise Impact Metric Module

In order to model community noise impacts, single event flyover noise grids are coupled with airport geometry, the surrounding population distribution, and the schedule of departures and arrivals for each type of aircraft in the aircraft fleet, as diagrammed in Figure 3-17. The single event flyover noise grids can be rotated such that the lateral tracks of their associated flight profiles are aligned with the runways according to the airport geometry.

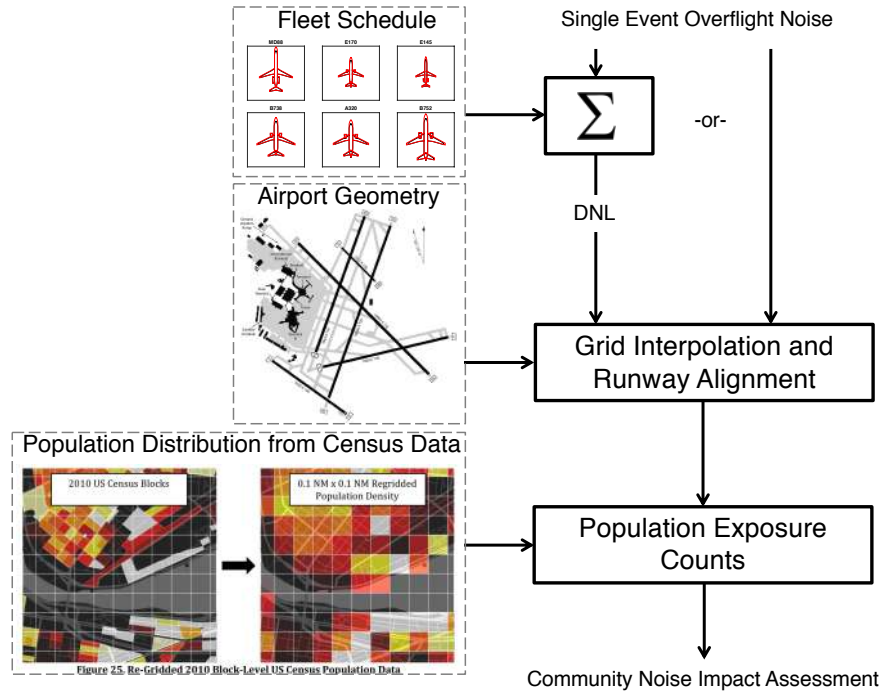


Figure 3-17: Noise Impact Metric Module Framework, population Figure from [47]

The single event flyover noise grids and population distribution obtained from Census data are indexed and overlaid on a consistent grid in the Noise Impact Module. Population exposure, or the number of people exposed to certain noise levels, can then be modeled given a flight schedule that includes aircraft type and procedure schedule. This analysis enables examination of procedure changes on specific runways around a given airport, as well as optimization of advanced procedures to minimize location-specific population impact. If an integrated noise impact metric such as DNL is examined, the SEL single event noise grids for each aircraft in the associated aircraft fleet are summed over an average annual day of operations with a 10 dB penalty factor for night-time operations. The resulting DNL grid is also indexed and overlaid on grid that is consistent with the population distribution to model population exposure to certain noise levels in terms of DNL.

The modeling framework presented provides the ability to assess a wide variety of flight procedures through the flexibility in building the flight profile in the flight profile generation method, provides a noise assessment of both airframe noise and engine noise on a component basis through the component-based modular noise analysis framework at a

variety of thrust, velocity, and configuration settings, and provides the ability for procedure design for minimization of noise impact to specific communities given the geometry of the airport and population of interest.

3.5 Validation of Noise Results of Turbofan Aircraft with Existing Certification Data

The framework was used to model noise and performance of existing turbofan aircraft and results were compared to publicly available noise certification data of existing aircraft types. FAR Part 36 [16] certification data at three specific observer locations with aircraft flying three specific flight procedures is publicly available from the Federal Aviation Administration (FAA) [112] and the European Aviation Safety Agency (EASA) [113]. Each aircraft flies the procedures and at the weights shown in Figure 3-18. The effective perceived noise levels (EPNL) were recorded at the observer locations also summarized in Figure 3-18.

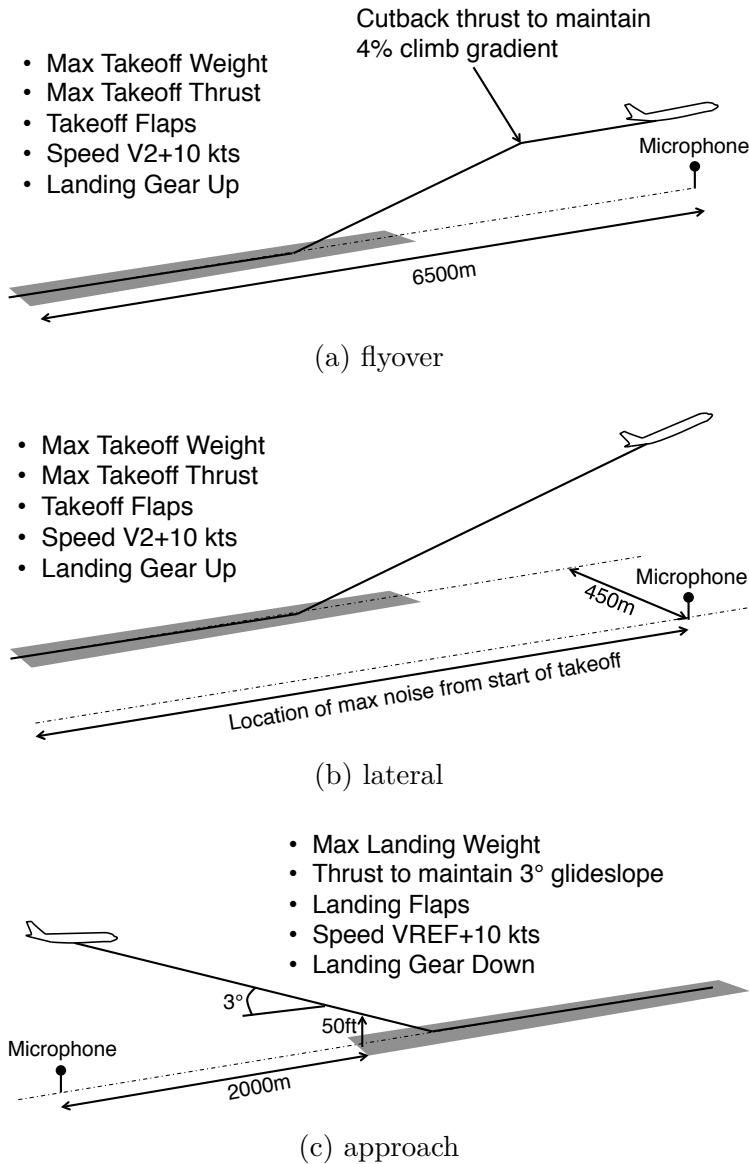


Figure 3-18: Noise Certification Procedures and Microphone Locations

Noise at each of the certification microphone (observer) locations for six aircraft was modeled with the Component-Based Aircraft Noise Module. The flight profiles for each aircraft were modeled in the Flight Profile Generation Module according to the noise certification flight procedures described in Figure 3-18. A summary of how the thrust, velocity, configuration, and flightpath angle profiles were obtained for each certification procedure is shown in Table 3.1. The defined inputs and the unknowns that are solved in the Flight Profile Generation Module depend on the procedure.

Table 3.1: Summary of Inputs and Solved-for Unknowns to Generate Thrust, Velocity, Configuration, and Flightpath Angle Profiles for each Certification Procedure

Procedure	Certification Procedure Definition from FAA Part 36 [16]	Inputs Based on Procedure Definitions		Unknowns Solved in Flight Profile Generation Module
		Provided with Certification Noise Levels [112]	Obtained from BADA 4	
Flyover	<ul style="list-style-type: none"> • Max Takeoff Weight • Configuration: Takeoff Flaps, Gear Up • Speed: V_2+10 • Before 300 m altitude: Max Takeoff Thrust • After 300 m altitude: 4% climb gradient 	<ul style="list-style-type: none"> • Max Takeoff Weight • Takeoff Flaps Setting • Max Takeoff Thrust Rating 	<ul style="list-style-type: none"> • Drag for Gear Up, Takeoff Flaps Configuration • V_2 	<ul style="list-style-type: none"> • Before 300 m altitude: Climb Angle • After 300 m altitude: Required Thrust
Lateral	<ul style="list-style-type: none"> • Max Takeoff Weight • Configuration: Takeoff Flaps, Gear Up • Speed: V_2+10 • Thrust: Max Takeoff 	<ul style="list-style-type: none"> • Max Takeoff Weight • Takeoff Flaps Setting • Max Takeoff Thrust Rating 	<ul style="list-style-type: none"> • Drag for Gear Up, Takeoff Flaps Configuration • V_2 	<ul style="list-style-type: none"> • Climb Angle
Approach	<ul style="list-style-type: none"> • Max Landing Weight • Configuration: Landing Flaps, Gear Down • Speed: $V_{REF}+10$ • GlideSlope: 3° 	<ul style="list-style-type: none"> • Max Landing Weight • Landing Flaps Setting 	<ul style="list-style-type: none"> • Drag for Gear Up, Landing Flaps Configuration • V_{REF} 	<ul style="list-style-type: none"> • Required Thrust

Max landing and takeoff weights, takeoff and landing flap settings, and max takeoff

thrust ratings for each aircraft were obtained from the aircraft performance provided with the certification noise levels [112]. V_2 and V_{REF} , shown in Figure 3-18, were defined from stall speeds which were derived from $C_{L,max}$ data from BADA 4. V_2 was assumed equal to 1.2 times V_{Stall} in takeoff configuration and V_{REF} equal to 1.3 times V_{Stall} in landing configuration. These stall speeds were assumed to correspond to when the aircraft is operating at $C_{L,max}$ for each configuration. Additionally, drag polars for each configuration and aircraft were obtained in BADA 4.

Results are presented in Figure 3-19. An agreement within -2.2 to 3.7 dB between the noise results obtained from ANOPP and the certification data was found for each of these six aircraft and the three observer locations, with many of the measurements agreeing within 1 dB of the recorded value. The flyover and approach results on average match the recorded values more closely than the high thrust lateral cases. It should be noted that the certification data is taken at slow airspeeds corresponding to final approach or initial departure and it is therefore difficult to validate the dependence of the ANOPP results on high airspeed and configuration.

To provide a comparison of these results obtained with this framework with another noise tool used for airport community noise assessments, the Aviation Environmental Design Tool (AEDT), the same flight procedures were modeled in AEDT and results are shown in Figure 3-19. An agreement within -3.7 to 7.5 dB was found between the AEDT results and certification data across all aircraft and observer locations, indicating overall the results modeled in ANOPP have less variability from the certification data than the AEDT results. The differences between ANOPP results and certification data and are also in better agreement for most aircraft than AEDT with exceptions of the A320 where ANOPP under-predicted the overflight noise levels and the MD-88 over-predicted the approach and lateral noise levels.

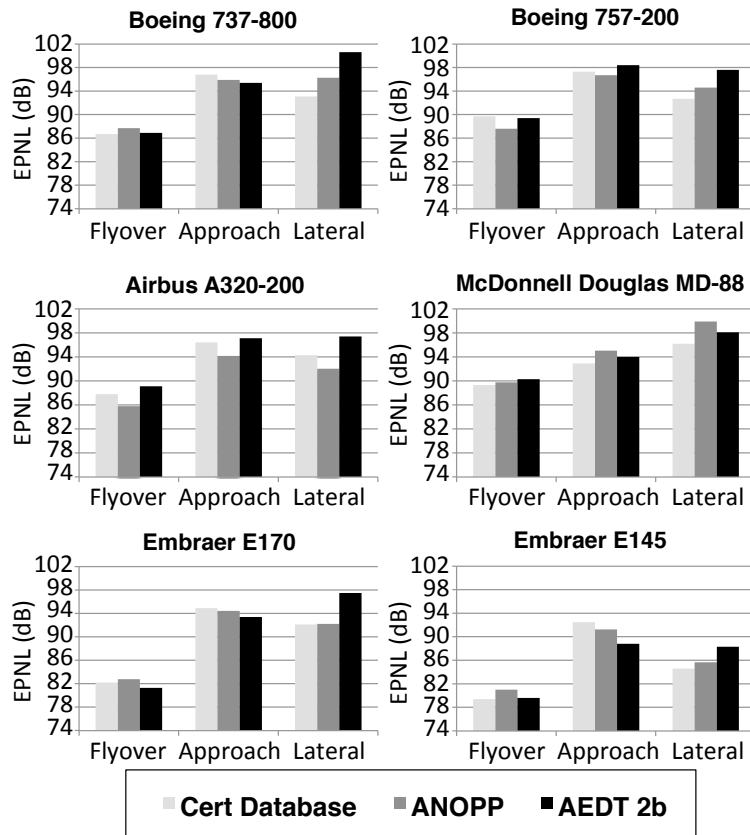


Figure 3-19: EPNL (dB) for Several Aircraft Types Modeled in ANOPP and AEDT 2b and Compared to Noise certification Data

Chapter 4

Advanced Operational Flight Procedures of Conventional Aircraft—Evaluation of the Impact of Flight Path Angle and Speed on Community Noise

In this chapter, the framework presented in chapter 3 is used to evaluate the noise impacts of several advanced operational flight procedures flown by conventional aircraft. Specifically, the procedure modifications examined show the impacts of changing aircraft flight path angle and speed during approach and departure on community noise for transport category jet aircraft.

Example opportunities to modify aircraft altitude and speed on both typical departure procedures and typical approach procedures are identified. Example flight procedures with altitude and/or speed modifications for each case and resulting community noise impacts are also presented. Flight trials of approach procedures with altitude and flight speed modifications conducted during the Boeing ecoDemonstrator program in November 2019 are also shown. Finally, for procedures where significant noise reductions were obtained by

changing aircraft altitude or speed, the operational implications and limitations of those procedures are also discussed.

For each arrival and departure procedure evaluated, the community noise impact was modeled for a representative narrow body jet transport aircraft (a Boeing 737-800 with CFM56-7B engines) and a representative wide body jet transport aircraft (a Boeing 777-300 with Trent 892 engines for departure examples and a Boeing 777-200 with PW4077 engines was used for approach examples).

4.1 Impact of Aircraft Flight Path Angle and Speed on Aircraft Source Noise

As mentioned in chapter 3, the primary sources of noise from aircraft are engine and airframe noise. Historically jet engine noise has been the dominant noise source particularly during high power settings on takeoff. Modern engines have become significantly quieter and airframe noise has become increasingly important during landing and for some reduced power settings. Aircraft speed impacts engine and airframe noise differently, as discussed briefly below.

4.1.1 Impact of Flight Path Angle and Speed on Engine Noise

Engine noise arises primarily due fan, core, and jet noise. Fan noise arises due to turbulent air passing rotating fan blades and stator vanes [36], core noise arises due to the combustion of hot gasses in the engine core and subsequent propagation through the turbine [105], and jet noise arises primarily due to the turbulent mixing of fast jet exhaust airflow with slower ambient air [106]. In general, the engine noise will increase with increased power setting. On departure, an increase in climb angle to obtain more altitude is typically associated with an increase in power setting and therefore an increase in engine noise. On approach, a greater descent angle typically results in a decrease in engine noise. Engine noise also increases with increasing difference between the speed of the high velocity jet airflow and the speed of the aircraft, which impacts the turbulent mixing of the shear layers in the engine exhaust.

4.1.2 Impact of Flight Path Angle and Speed on Airframe Noise

Airframe noise arises from turbulence generated by the aircraft airframe, usually around geometry changes. This includes noise from the basic wing and tails, known as trailing edge noise, as well as additional noise from the devices that extend into the airflow such as flaps, slats, and landing gear. All of these airframe noise sources are highly sensitive to aircraft speed. Clean trailing edge and slat noise scales with velocity to the 5th power [40][41]. Flap noise scales with the 5th power of velocity for low frequencies and the 6th power of velocity for high frequencies [43]. Landing gear noise scales with the 6th power of velocity [44][42].

In addition to the source noise effect described above, speed is also tightly coupled to aircraft flight aerodynamics and thus impacts the configuration of the aircraft (i.e. flaps, slats, and landing gear settings). At slower speeds, the flaps and slats are extended to reduce the stall speed which will also cause an increase in airframe noise. In addition, increasing flight path angle on descent tends to require more drag and thus requires extending drag generating devices such as flaps, slats, and gear which will also cause an increase in airframe noise.

4.2 Effect of Aircraft Flight Path Angle and Speed on Departure

4.2.1 Options to Change Aircraft Flight Path Angle and Speed on Departure

A typical departure procedure is shown in Figure 4-1 to provide a basis of comparison to consider how varying flight path angle and speed on departure would impact community noise. In a typical departure, the aircraft accelerates on the runway and performs its initial climb segment at a predetermined takeoff thrust and at an initial takeoff speed. The initial takeoff speed is set by safety and performance considerations and is dependent on aircraft weight to provide stall margin. Because of the criticality of stall margin and climb gradient at low altitude, the initial takeoff speed is not considered a candidate to be modified.

After reaching a transition altitude, usually between 1,000 ft and 2,000 ft, the thrust is reduced to a climb setting and the aircraft accelerates to a target climb speed. The thrust reduction is recommended for noise reduction in ICAO document 8168 [52]. The target climb speed is typically 250 knots, which is the maximum speed permitted below 10,000 ft in the United States. After the thrust reduction and as the aircraft accelerates, the flaps are incrementally retracted until the wing is in its flaps and slats retracted configuration. This is consistent to what ICAO describes as Noise Abatement Departure Procedure 2 (NADP 2) in document 8168 [52].

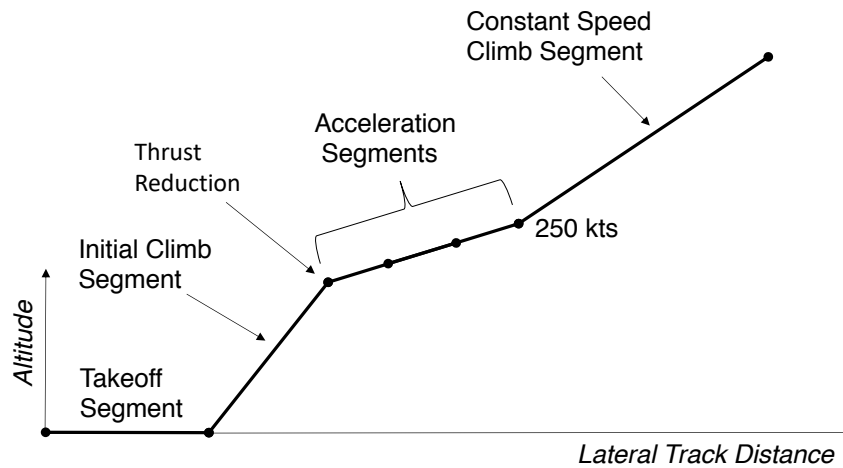


Figure 4-1: Typical Departure Procedure Divided into Segments, Consistent with NADP 2

There are two primary options to consider for varying flight path angle and speed in the departure phase after the takeoff and initial climb segment:

- Changing location of the start of acceleration and flap retraction
- Reducing the climb speed
- Changing the climb angle

4.2.2 Changing Location of the Start of Acceleration and Flap Retraction

Modifying the acceleration and flap retraction location has been considered previously. ICAO has recommended two procedures that consider where the location of the start acceleration

and flap retraction occurs in ICAO document 8168 published in 2006 [52]. They are Noise Abatement Departure Procedures (NADP) 1 and 2, shown in Figure 4-2. These procedures are used as examples to show how modifying the location of the start acceleration and flap retraction impacts community noise.

In the NADP 1, after the initial thrust reduction at a cutback altitude, typically between 800 ft and 1,500 ft, the aircraft holds its initial climb speed of up to $V_2 + 20$ knots to an altitude of 3,000 ft. At 3,000 ft, the aircraft accelerates to its final climb speed of 250 knots. In the NADP 2, after the transition altitude, the aircraft accelerates to either its flaps up speed + 20 knots or its final climb speed. The NADP 2 is the standard procedure in the United States and NADP 1 is the standard procedure internationally.

The altitude gain of the NADP 1 between the thrust cutback altitude and 3,000 ft due to holding $V_2 + 20$ knots is meant to benefit close in communities, while the altitude gain in the NADP 2 after the aircraft has accelerated to its final climb speed is meant to benefit far out communities.

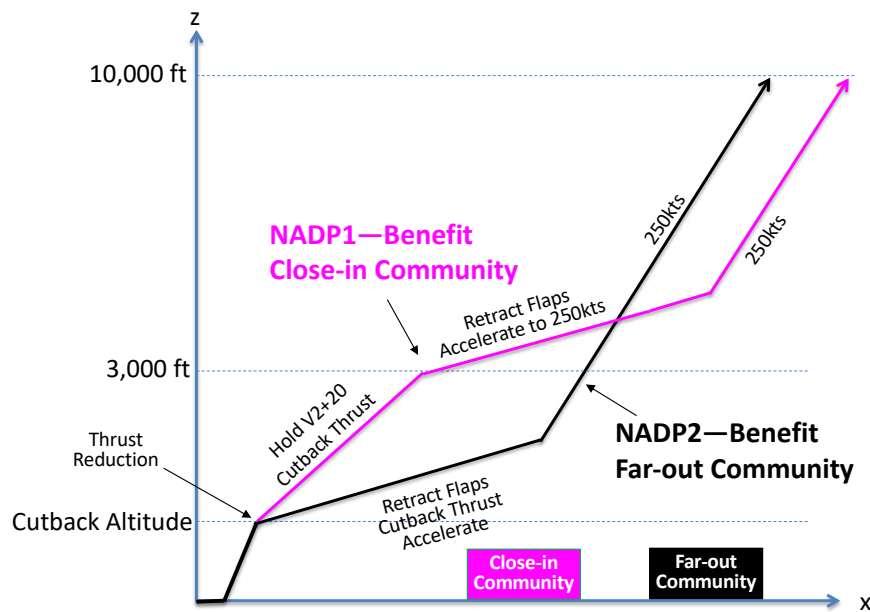


Figure 4-2: Difference in Acceleration Height on Departure Represented by NADP 1 (3,000 ft acceleration height) and NADP 2 (1,500 ft Acceleration Height) Comparison

The noise impact of a representative narrow body jet aircraft (Boeing 737-800) performing an NADP 2 procedure compared to an NADP 1 procedure was investigated.

The NADP 1 and 2 definitions are ambiguous in terms of the climb angle specified during the acceleration segments. Thus, the climb angles in this example were determined to be the mean climb angles of Boeing 737-800 departures at Boston Logan Airport (BOS) from Airport Surface Detection Equipment, Model X (ASDEX) radar data in 2017. The altitude and velocity profiles from this data are shown in Figure 4-3 along with the mean profiles of this data. The velocity data shows that for Boeing 737-800 departures at BOS, the start of acceleration occurs beginning after the initial cutback at about 1,500 ft, which is consistent with the NADP 2 procedure definition.

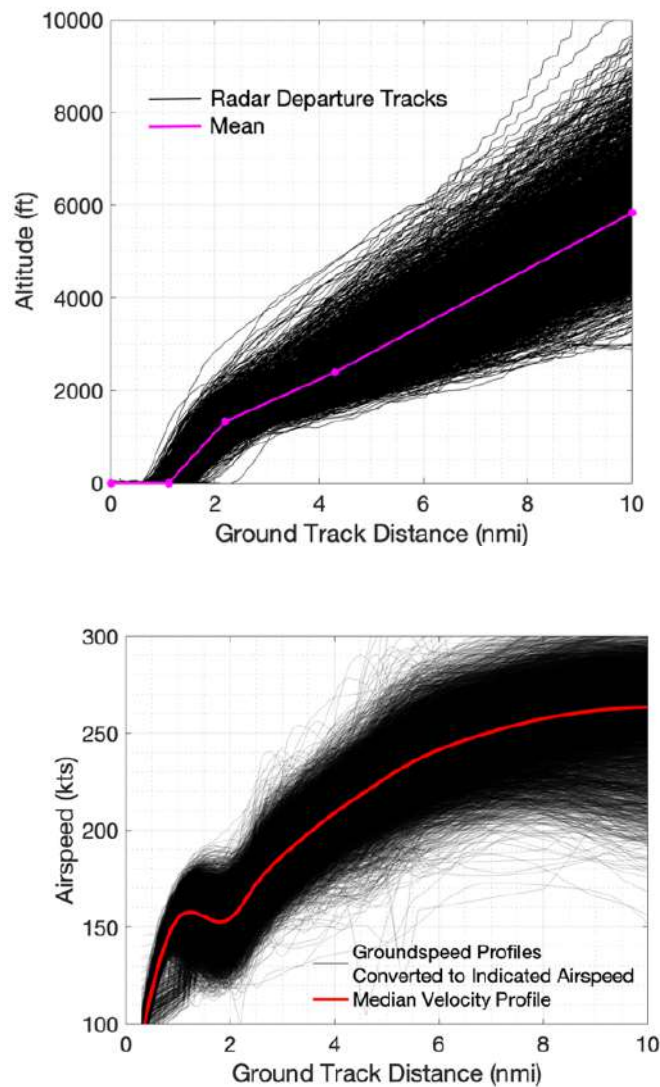


Figure 4-3: ASDEX Radar Altitude and Velocity Data of Boeing 737-800s on Departure at BOS in 2017

Modeled flight profiles of the representative narrow body aircraft for both the NADP 1 and NADP 2 are depicted in Figure 4-4, which shows the comparison of altitude, velocity, and thrust profiles. The weight was assumed to be 90 percent of the maximum takeoff weight for this aircraft¹. The thrust was assumed to be the same between the two procedures to provide a comparison of impacts due only to the change in acceleration height. Between the thrust cutback altitude and 3,000 ft, the aircraft performing the NADP 1 had a steeper climb angle than in the NADP 2 due to maintaining $V_2 + 20$ knots in this region rather than accelerating.

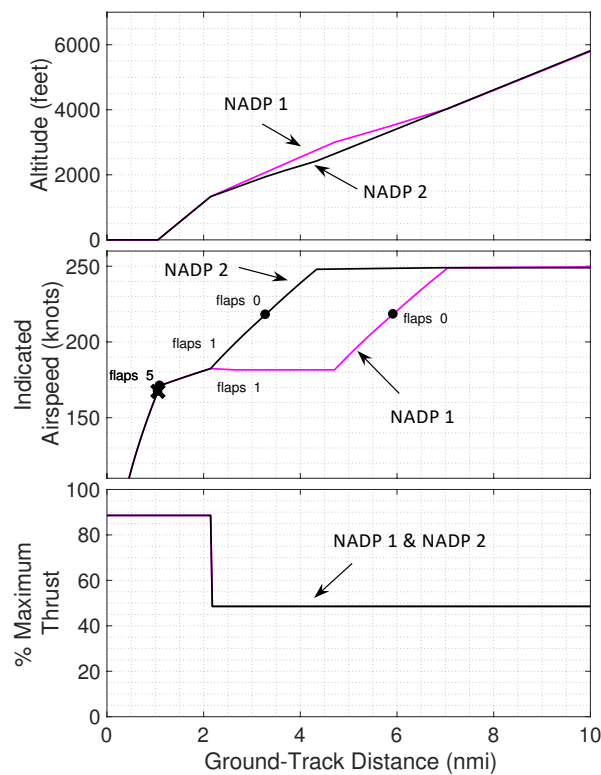


Figure 4-4: Comparison of Altitude, Velocity, and Thrust Profiles for a Narrow Body Aircraft Performing NADP 1 (magenta) and NADP 2 (black)

Noise impacts for the representative narrow body aircraft performing the NADP 1 and NADP 2 are shown in Figure 4-5 as the total $L_{A,MAX}$ under the flight track during a straight out departure. The difference in $L_{A,MAX}$ noise under the flight track of the representative narrow body aircraft performing the NADP 2 and NADP 1 is shown Figure 4-6. Figure 4-7 shows the corresponding $L_{A,MAX}$ contours.

¹Maximum Takeoff Weight assumed to be 174,000 lbs for the Boeing 737-800.

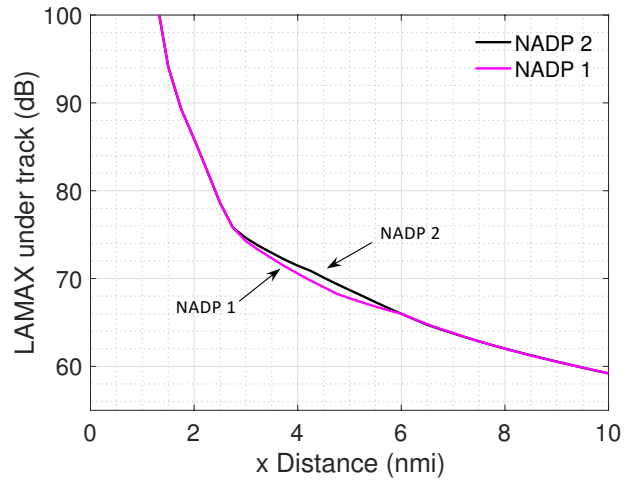


Figure 4-5: Undertrack $L_{A,MAX}$ (dB), NADP 2 and NADP 1 Noise for a Representative Narrow Body Aircraft

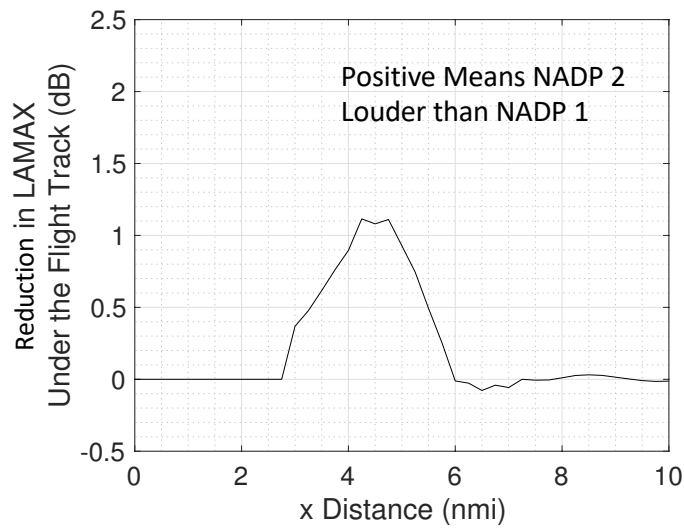


Figure 4-6: Reduction in Undertrack $L_{A,MAX}$ (dB), NADP 1 compared to NADP 2 for a Representative Narrow Body Aircraft

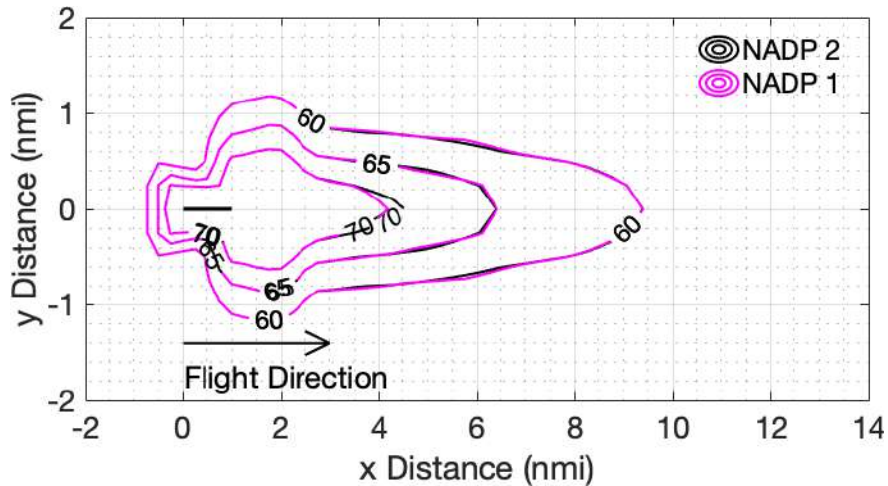


Figure 4-7: NADP 1 and 2 $L_{A,MAX}$ (dB) contours for a Representative Narrow Body Aircraft

Figure 4-6 shows that with the assumed procedures from Figure 4-4 the NADP 1 results in a small noise reduction where the NADP 1 holds $V_2 + 20$ knots due to the extra altitude gained during the climb in this segment. This results in a small reduction of the extent of the 70 dB contour when flying the NADP 1 compared to the NADP 2, as can be seen in Figure 4-7. After about 6 nmi where the two procedures converge, there is insignificant difference between NADP 1 and NADP 2 for this aircraft. The small, 1.2 dB, maximum noise reduction is over a limited spatial area and is therefore not considered a significant noise reduction.

The noise impacts were also investigated for a representative wide body aircraft (Boeing 777-300) performing an NADP 2 procedure compared to an NADP 1 procedure. The climb angles in this example were set at the mean climb angles of Boeing 777-300 departures at Boston Logan Airport (BOS) from ASDEX radar data in 2017. The altitude and velocity profiles from this data are shown in Figure 4-8 along with the mean profiles of this data. The velocity data shows that for Boeing 777-300 departures at BOS, the start of acceleration occurs beginning after the initial cutback at about 1,900 ft, which is consistent with the NADP 2 procedure.

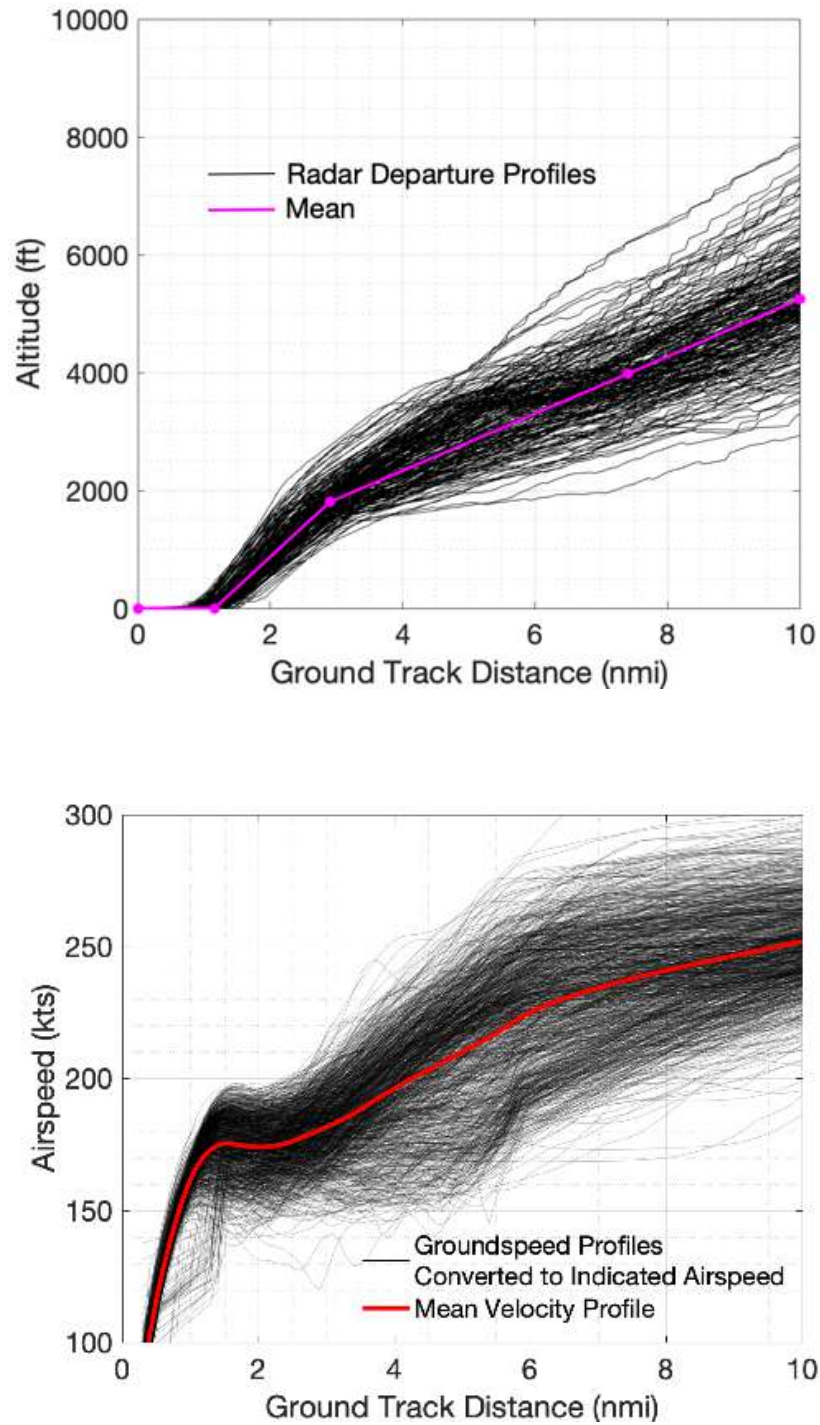


Figure 4-8: ASDEX Radar Altitude and Velocity Data of Boeing 777-300s on Departure at BOS in 2017

Modeled flight profiles of the representative wide body aircraft for both the NADP 1 and NADP 2 are depicted in Figure 4-9, which shows the comparison of altitude, velocity,

and thrust profiles. The weight was assumed to be 90 percent of the maximum takeoff weight for this aircraft².

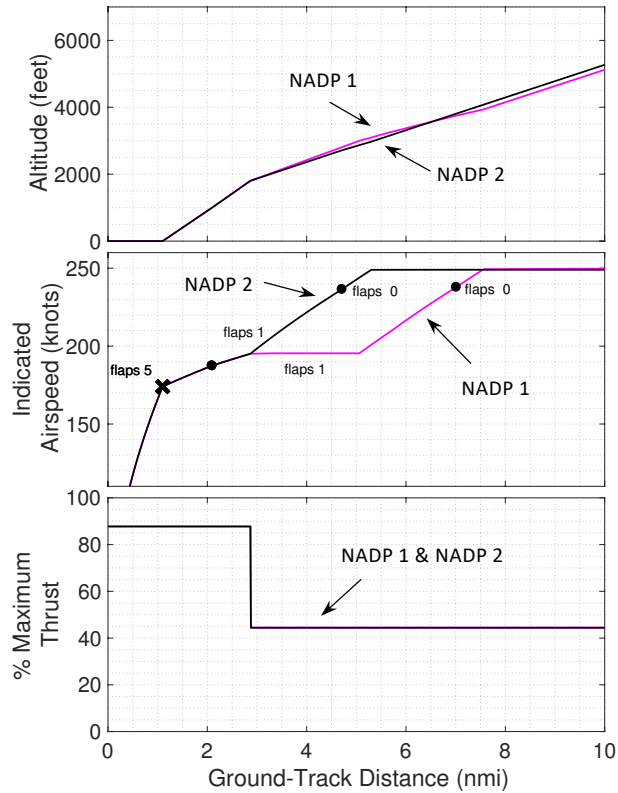


Figure 4-9: Comparison of Altitude, Velocity, and Thrust Profiles for a Wide Body Aircraft Performing NADP 1 (magenta) and NADP 2 (black)

Noise impacts for the representative wide body aircraft performing the NADP 1 and NADP 2 are shown in Figure 4-10 as the total $L_{A,MAX}$ under the flight track during a straight out departure. The difference in $L_{A,MAX}$ noise under the flight track of the representative wide body aircraft performing the NADP 2 and NADP 1 is shown Figure 4-11. Figure 4-12 shows the corresponding $L_{A,MAX}$ noise contours.

²Maximum Takeoff Weight assumed to be 659,550 lbs for the Boeing 777-300.

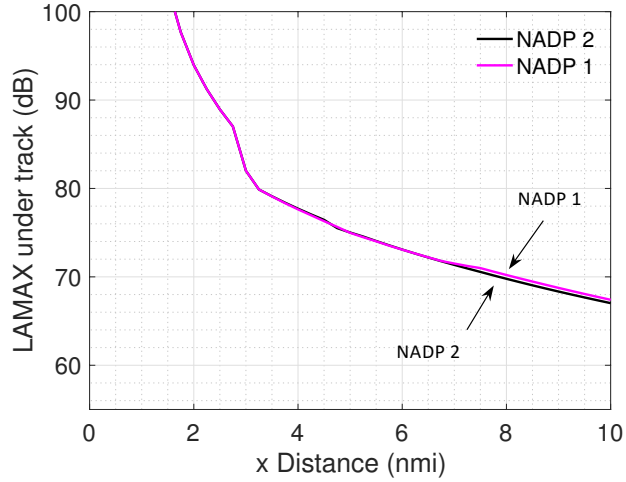


Figure 4-10: Undertrack $L_{A,MAX}$ (dB), NADP 2 and NADP 1 Noise for a Representative Narrow Body Aircraft

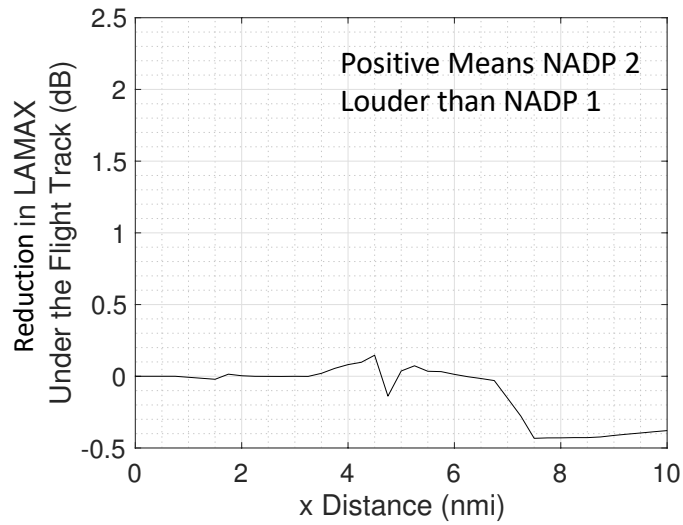


Figure 4-11: Reduction in Undertrack $L_{A,MAX}$ (dB), NADP 1 compared to NADP 2 for a Representative Narrow Body Aircraft

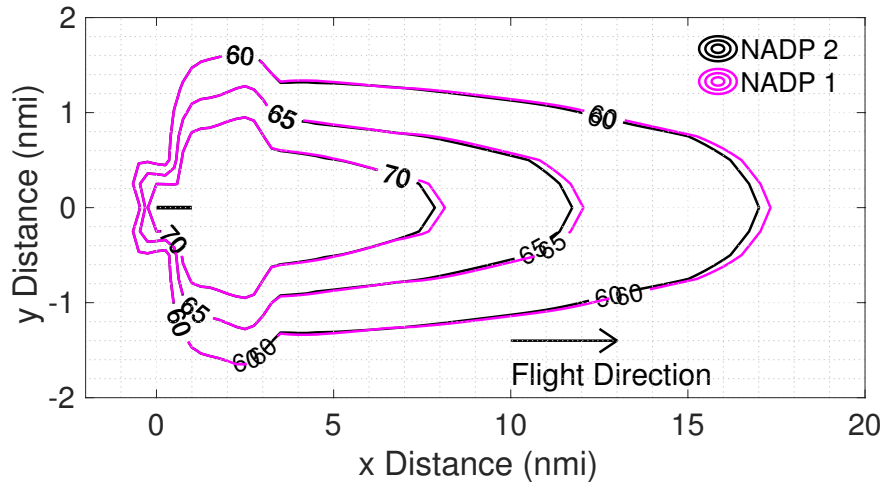


Figure 4-12: NADP 1 and 2 $L_{A,MAX}$ (dB) contours for a Representative Narrow Body Aircraft

Results in Figure 4-11 show that the undertrack noise levels are quite similar up until 7 miles after which the NADP 2 has a slightly lower (0.4 dB) noise level due to the slightly higher altitude of the NADP 2 procedure in this region. This can also be seen in a small reduction of the 60, 65, and 70 dB contours shown in Figure 4-12.

The results show that changes in the acceleration location on departure results in small differences in community noise impacts compared to current departure procedures. Currently observed procedures in the U.S. are consistent with NADP 2 and it does not appear that changing the acceleration location would result in significant reduction in community noise impacts.

4.2.3 Reduced Climb Speed

Another option for varying the speed on departure is to reduce the climb speed, which will reduce the highly speed dependent airframe noise during the climb segment after initial thrust reduction. The typical departure from Figure 4-1 is used to provide a basis of comparison to consider where varying the speed on departure would impact community noise.

In the reduced speed departures, aircraft were assumed to maintain the same weight, altitude profile, and velocity profile as the typical departure through the initial climb segment until the aircraft accelerated to the minimum safe airspeed with flaps up, which was maintained to 10,000 ft as shown in Figure 4-13. The minimum safe airspeed in the flaps

up configuration, assumed $1.3 \times V_{stall}$, was assumed to be the minimum reasonable climb speed to 10,000 ft because of concerns about icing with flaps deployed at high altitudes. Aircraft were assumed to have maintained the same thrust profile as the typical departure resulting in higher climb profiles for the reduced speed departures. 220 knots was assumed to be the minimum safe airspeed in the flaps up configuration for the representative narrow body aircraft, while 240 knots was assumed for the representative wide body aircraft. The weight was assumed to be 90 percent of the maximum takeoff weight for both aircraft as referenced in the previous section.

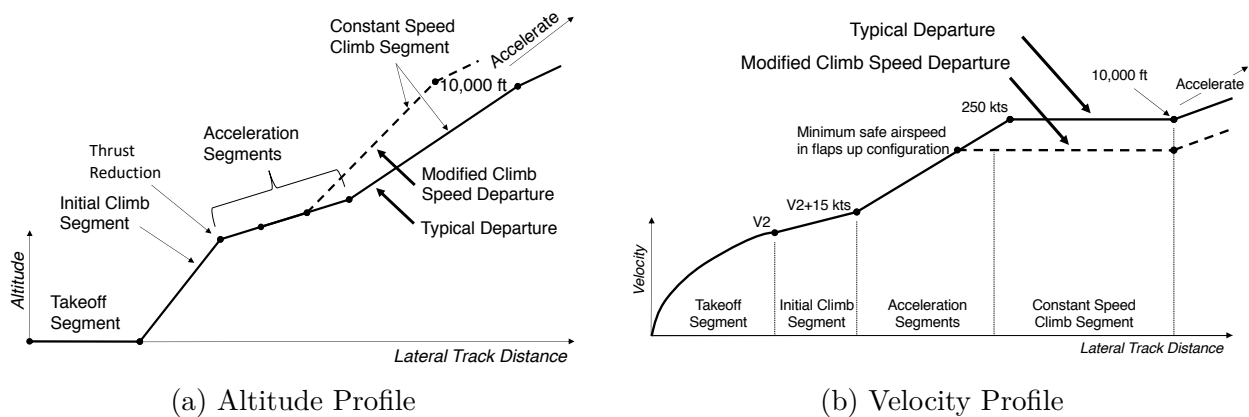


Figure 4-13: Reduced Climb Speed Departure Definitions

Because the flaps, slats, and gear are retracted during reduced speed climb, the airframe noise is from only the trailing edge noise and improvement from a reduced climb speed would only occur only if the trailing edge noise is greater than the engine noise during climb. The trailing edge noise is normally not an important factor during initial takeoff when the noise is dominated by engine or during landing when the noise is dominated by engine or flap, slat, and landing gear noise. As a consequence there is very little public data for trailing edge noise for modern aircraft in the clean (flaps, slats and gear retracted) configuration.

As mentioned in section 3.3, the ANOPP noise model for trailing edge noise has the option to use the “aerodynamically smooth” or “conventional” wing surface assumption. Based on the public 1970s data, most transport aircraft would have the louder “conventional” wing surface. However, recent data provided by NASA [110] indicates that modern aircraft wing surfaces are closer to the “aerodynamically smooth” aircraft assumption. As a consequence, the quieter “aerodynamically smooth” trailing edge noise levels were used in

this analysis.

The noise impacts of each aircraft performing reduced speed departures compared to typical departures was investigated. The $L_{A,MAX}$ noise under the flight track of the representative narrow body aircraft for the 220 and 250 knots climb speeds Figure 4-14. The corresponding difference in $L_{A,MAX}$ noise under the flight track between the 250 knots climb speed departure and 220 knots climb speed departure is shown in Figure 4-15. The reduction in noise from reducing the climb speed from 250 to 220 knots occurs between 3.5 and 8 miles and is less than 0.5 dBA.

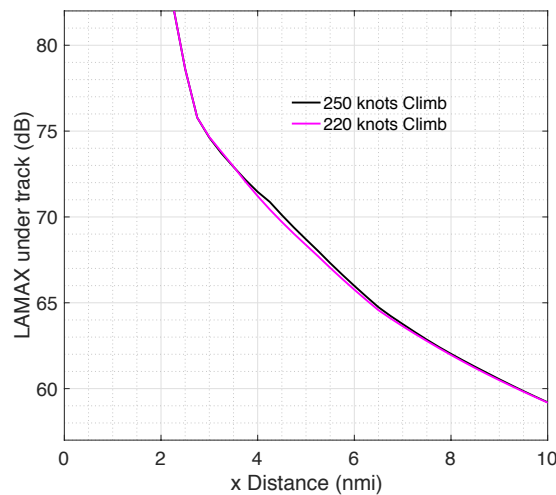


Figure 4-14: $L_{A,MAX}$ (dB) Under the Flight Track for 250 knot Climb Speed Departures and 220 knot Climb Speed Departures for a Representative Narrow-Body Aircraft

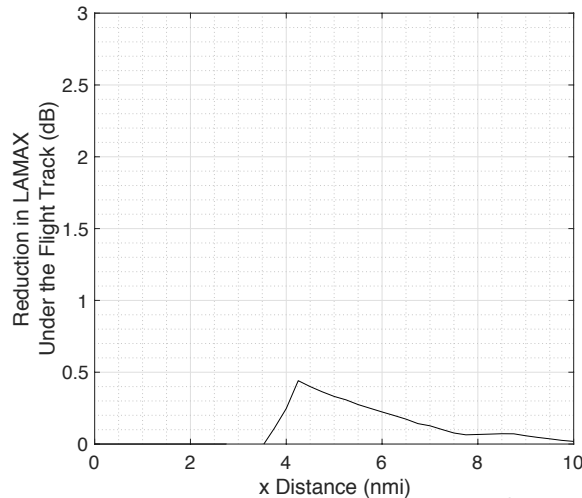


Figure 4-15: Reduction in $L_{A,MAX}$ (dB) for 220 knot Compared to 250 knot Climb Speed Departure for a Representative Narrow-Body Aircraft

Engine, airframe, and total $L_{A,MAX}$ noise contours of a takeoff from for the representative narrow body aircraft are shown in Figure 4-16 for typical and reduced climb speeds of 250 knots and 220 knots with the aerodynamically smooth wing surface assumption.

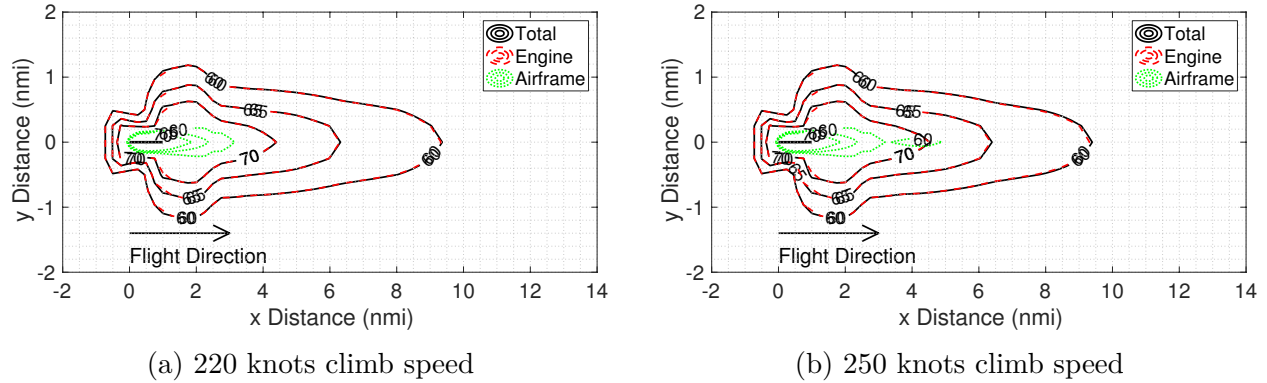


Figure 4-16: $L_{A,MAX}$ (dB) Noise Contours 220 and 250 knot Climb Speed Departures for a Representative Narrow-Body Aircraft

The reason for there being only a small noise difference from varying the climb speed can be seen in the noise contours in 4-16, which break out the airframe and engine noise. Because the noise is dominated by engine noise during the climb the climb speed does not have a significant effect on the noise contour

Similar trends in noise impact were seen in with the representative wide body aircraft. The $L_{A,MAX}$ noise under the flight track for the 240 and 250 knots climb speeds with the “aerodynamically smooth” wing surface assumption are shown in Figure 4-17. The difference in the resulting $L_{A,MAX}$ noise under the flight track is insignificant as shown in Figure 4-18. Again this is due to the dominance of engine noise during climb, which can be seen in the noise contours in Figure 4-19.

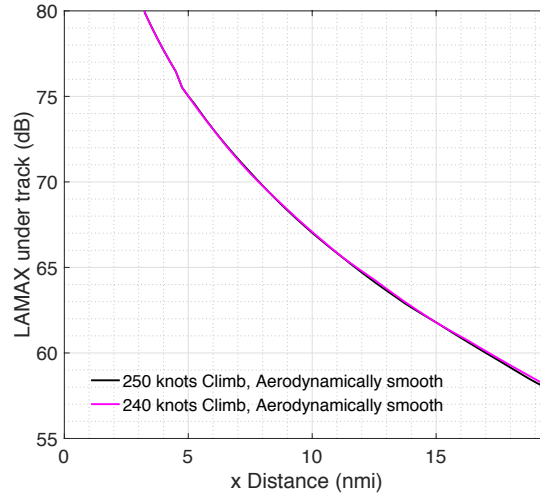


Figure 4-17: $L_{A,MAX}$ (dB) Under the Flight Track for 250 knot Climb Speed Departures and 240 knot Climb Speed Departures for a Representative Wide-Body Aircraft

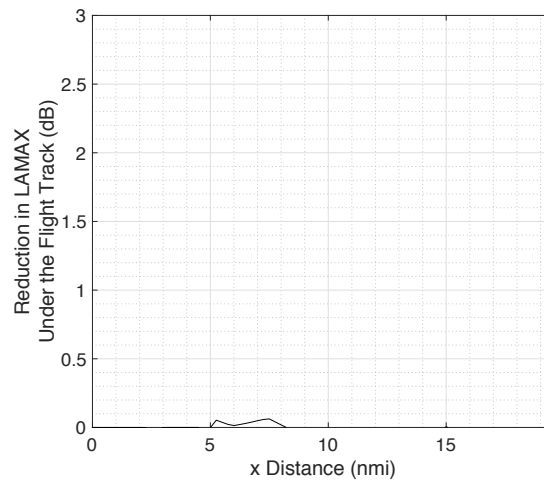


Figure 4-18: Reduction in $L_{A,MAX}$ (dB) for 220 knot Compared to 250 knot Climb Speed Departure for a Representative Wide-Body Aircraft

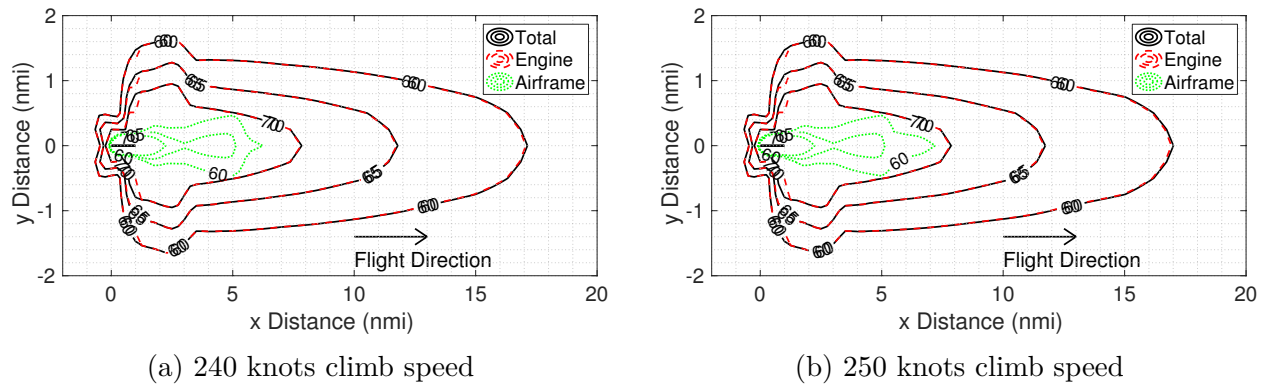


Figure 4-19: $L_{A,MAX}$ (dB) Noise Contours 240 and 250 knot Climb Speed Departures for a Representative Wide-Body Aircraft

The results for both the representative narrow body and wide body aircraft that for aircraft with aerodynamically smooth wing surfaces, the reduced climb speed does not show noise benefits.

4.2.4 Changing the Climb Angle

Another modification to departures is changing the climb angle, which requires both a change in thrust, and thus engine noise, as well as a change in altitude. The typical departure from Figure 4-1 is used to provide a basis of comparison to consider where varying the climb angle on departure would impact community noise.

The example departure with a modification in the climb profile, represented in Figure 4-20 (a) was obtained by modeling the representative narrowbody aircraft at the same weight as the standard departure case from Figure 4-1 but with thrust increased throughout the procedure. The increased thrust departure was assumed to perform the takeoff and initial climb segments at a thrust level 10% higher than the standard departure until the aircraft accelerated to V_2+15 knots, as shown in Figure 4-20 (b). The acceleration and constant speed climb segments were then performed at a thrust level 5% higher than the standard departure. These thrust levels enabled the aircraft at 90% MTOW to follow an altitude profile similar to that of the highest 15% of altitude profiles derived from the ASDEX radar data of Figure 4-3.

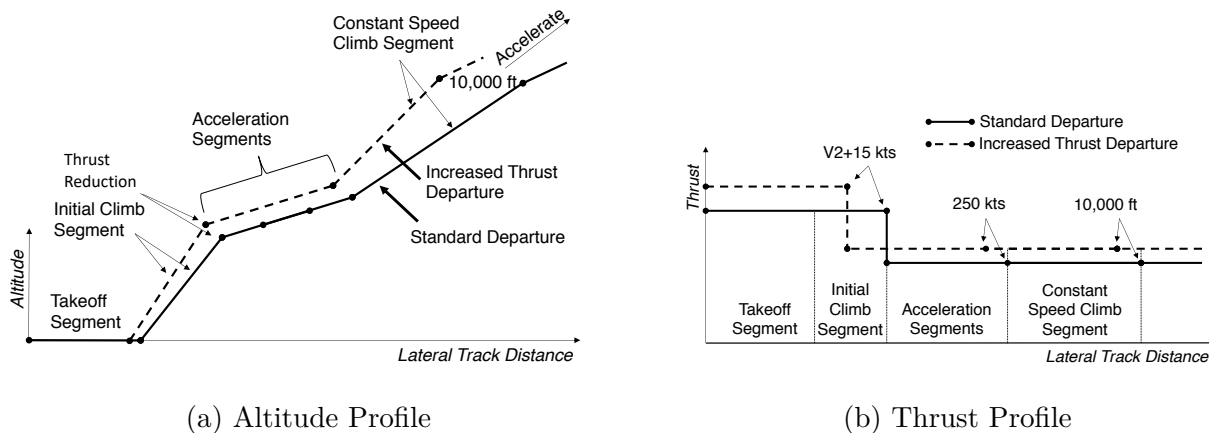


Figure 4-20: Increased Thrust Departure Definitions

Single event flyover noise of the standard and increased thrust departure procedures was modeled using the framework to demonstrate the noise impacts on a representative population. $L_{A,MAX}$ results were obtained for the representative narrowbody aircraft on a flight track representing the BLZZR4 RNAV departure for Runway 33L at BOS in this example. Results are shown in Figure 4-21.

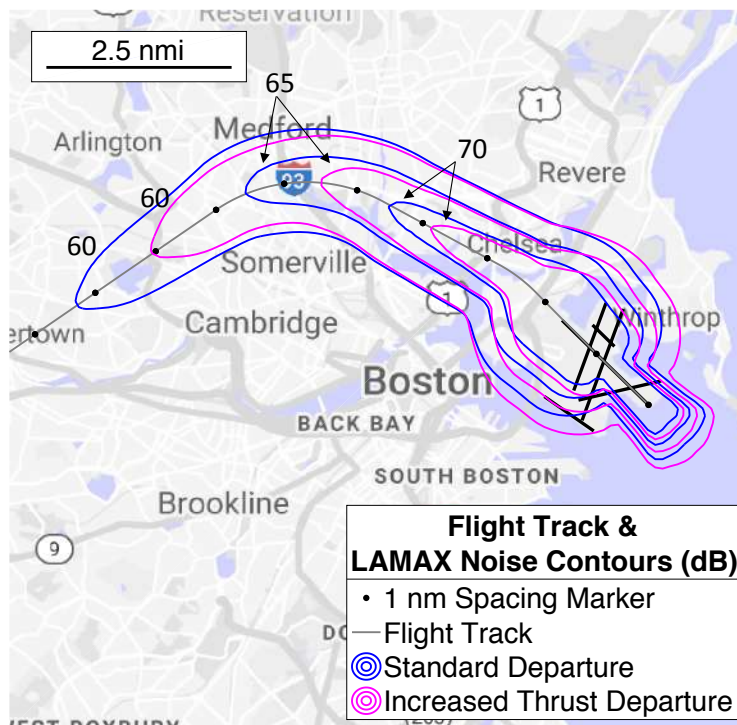


Figure 4-21: BOS BLZZR4 RNAV Standard and Increased Thrust Departure Noise Contours for the Representative Narrowbody Aircraft

As seen in Figure 4-21, noise contour shape and area differed with thrust and altitude. Compared to the standard departure, the contours of the increased thrust departure shown in Figure 4-21 are wider near the airport due to the initial high thrust level. However, the altitude gain during the initial climb segment results in an overall shrinking of the contour extent beneath the flight track for the remainder of the procedure.

To quantify the noise reduction, modeled population exposure at each of the 60 dB, 65 dB, and 70 dB $L_{A,MAX}$ noise levels for each case are shown in Table 4.1.

Table 4.1: Population Exposure Comparison in $L_{A,MAX}$ of the Standard and Increased Thrust BLZZR4 RNAV Departures for the Representative Narrowbody Aircraft

$L_{A,MAX}$ Level (dB)		60	65	70
	Standard	159,624	61,375	28,140
Population Exposed	Increased Thrust	138,063	57,245	21,853
	Decrease	21,561	4,130	6,287

Table 4.1 shows that by reducing the extent of the departure contour for the increased thrust departure over the densely populated area beneath the BOS BLZZR4 RNAV departure track, there are overall reductions in population exposure due to the higher altitudes attained in the climb. However there is an increase in the width of the contour near the airport due to the initial high power, which would negatively impact communities in this region.

4.2.5 Operational Implications of Altered Climb Angle

Departures

Of the departure procedure modifications shown, only changing the departure climb angle via thrust increase had a significant impact on noise. The operational implications of this procedure are thus discussed.

Altering thrust and climb angle during departure yields differences in departure fuel burn and flight time compared to the standard. To assess this impact, the differences were calculated between the standard and increased thrust departure using the framework. Fuel burn and time was evaluated by recording the difference between the fuel burn, time, and

length of the ground track travelled for the standard and altered thrust profiles to reach the same flight state at 15,000 ft. Since the increased thrust profiles had different ground track lengths to 15,000 ft than the standard, the difference in ground track lengths was made up in cruise. Fuel burn and time in that segment was added assuming it was compensated for at the cruise speed provided from each aircraft’s performance data from BADA 4. Results for these comparisons are shown in Table 4.2. Compared to the standard departure, the increased thrust departure resulted in a decrease in overall flight time due to the increased acceleration rates at the beginning of this procedure. This procedure however resulted in a fuel consumption increase of 59 lbs due to the higher thrust levels throughout the procedure.

Table 4.2: Increase in Total Fuel Burn and Time when Flying an Increased Thrust Departure Compared to a Standard Departure for the Representative Narrowbody Aircraft

Fuel Consumption Increase (lbs)	59
Total Flight Time Decrease (s)	24

The noise contours from Figure 4-21 show that altered thrust procedures also result in a redistribution of noise beneath the flight track rather than a reduction in noise everywhere. Thus, alternative thrust departures that yield the most noise reductions will be dependent on the specific airport layout and population distribution. In this example, while the increased thrust departure resulted in an overall reduction in population exposure at BOS, this may not be the case for an airport with more concentrated populations near the airport.

4.3 Effect of Aircraft Flight Path Angle and Speed on Approach

4.3.1 Options to Change Aircraft Flight Path Angle and Speed on Approach

A typical approach procedure is shown in Figure 4-22 to provide a basis of comparison to consider where varying the speed on approach would impact community noise. Typical approach procedures consist of an initial descent segment from a starting altitude,

deceleration segments where flaps and slats are released, a level segment and an interception with the Instrument Landing System (ILS) glide slope (in some cases approach procedure may also be a continuous descent to the ground), and a final descent to touchdown, as depicted in Figure 4-22. Some options for modifying aircraft flight path angle and speed are discussed below.

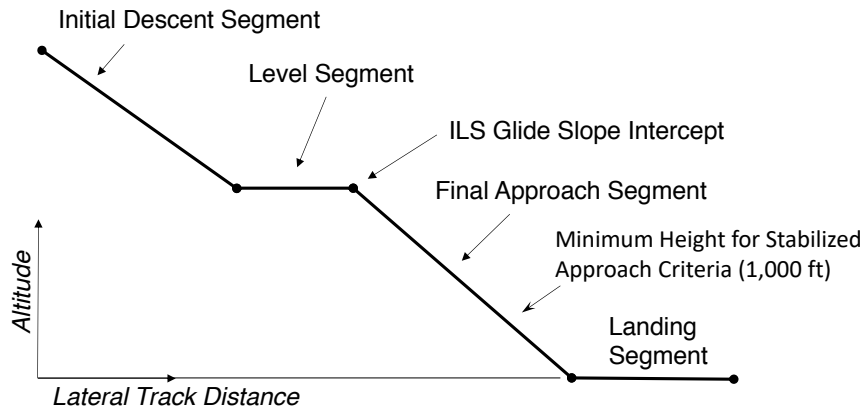


Figure 4-22: Typical Approach Procedure Divided into Segments

Flight Path Angle

Instead of flying an approach with a level segment, the aircraft can maintain a continuous descent all the way to touchdown. In addition, the aircraft could fly certain portions of a flight procedure with a steeper than the standard glide slope of 3° . Compared to the typical approach procedure continuous descent profiles result in increased altitude for every distance outside the glide slope intercept point.

Speed

Speed in the approach can be modified in regions outside of the stabilization point. The Flight Safety Foundation Approach-and-Landing Accident Reduction Briefing Note 7-1 suggests that all aircraft must meet stabilized approach criteria at a minimum of 1,000 feet above the airport surface in instrument meteorological conditions [114], meaning the aircraft is fully configured for landing and at a constant final approach speed between V_{REF} and $V_{REF} + 20$ knots. This point is highlighted on Figure 4-22. The stabilization point may occur further from touchdown than 1,000 ft.

Example approach procedures from Airport Surface Detection Equipment, Model X (ASDEX) radar data are depicted in Figure 4-23, which shows Boeing 737-800s approaches into Runway 4R at Boston Logan International Airport (BOS). The data shown in Figure 4-23 were aircraft leveling off at 4,000 ft before intercepting the ILS glide slope. Figure 4-23 also shows the corresponding velocity profiles. As is observed in the velocity data in Figure 4-23, most of the flights are stabilized at 1,700 ft, which corresponds to the outer marker location at BOS runway 4R [115]. Before the stabilization point, deceleration rates may vary, as is seen in the velocity data in Figure 4-23. The mean velocity profile of this data, along with an example profile where the aircraft decelerated early and with an example profile where the aircraft delayed its deceleration, are highlighted.

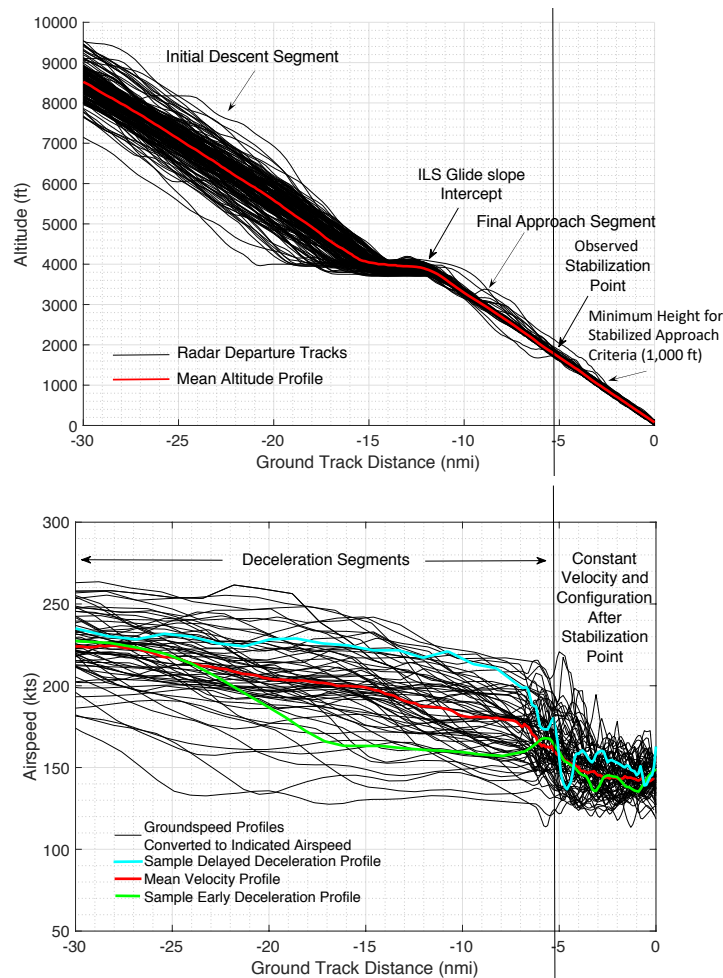


Figure 4-23: ASDEX Radar Altitude and Velocity Data of Boeing 737-800s Performing ILS Approaches with a 4,000 ft level segment into Runway 4R at BOS in 2017

Flaps and slats are required to be deployed on approach to allow the wing to maintain lift at the lower speeds required for landing and to provide drag to slow the aircraft. Aircraft typically deploy flaps and slats when they have decelerated to 10 knots below the maximum allowable speed for each configuration. Aircraft typically have between four and seven flap and slat settings, with higher settings corresponding to higher degrees of flap and slat extension. Aircraft that decelerate relatively early in the approach require flaps and slats to be deployed early and to set engines at above idle thrust for much of the approach profile [56]. This results in an early onset of configuration noise from flaps and slats and additional engine noise.

An alternative is a delayed deceleration approach. In a delayed deceleration approach, the deceleration is delayed such that the aircraft can have flaps and slats up and operate at low thrust for as long as possible to reduce both configuration and engine noise. The aircraft deceleration is delayed to a location such that it is still able to slow to the final approach speed at the stabilization point. Prior analyses have shown that the reduced flight time and thrust during this type of procedure yields significant reductions in fuel burn [56]. The reduced thrust and delaying of flap and slat deployment are also beneficial for noise.

4.3.2 Continuous Descent Approaches

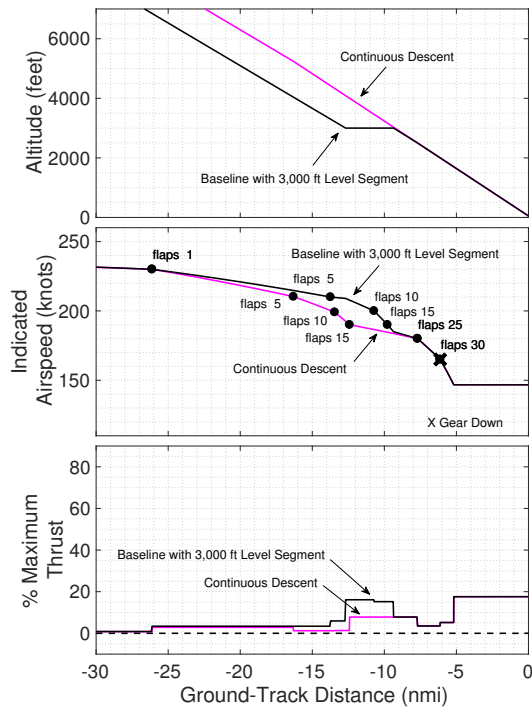
Varying flight path angle on approach involves descending at a higher glideslope than standard or maintaining a constant descent until touchdown without level segments, known as a continuous descent approach. Continuous descent approaches have been studied previously [58][59][60] and pose unique challenges for different airports and runways. Speed, altitude, configuration, and thrust are highly coupled on approach and various modifications to the approach can be carried out. In this section, example noise impacts of a representative narrow body aircraft performing continuous descent approach procedures are compared to standard approaches with a level segment.

Flight profiles of the representative narrow body aircraft (Boeing 737-800) for both baseline and continuous descent approach procedures were generated and are shown in Figure 4-24. The weight was assumed to be maximum landing weight³. The baseline cases are

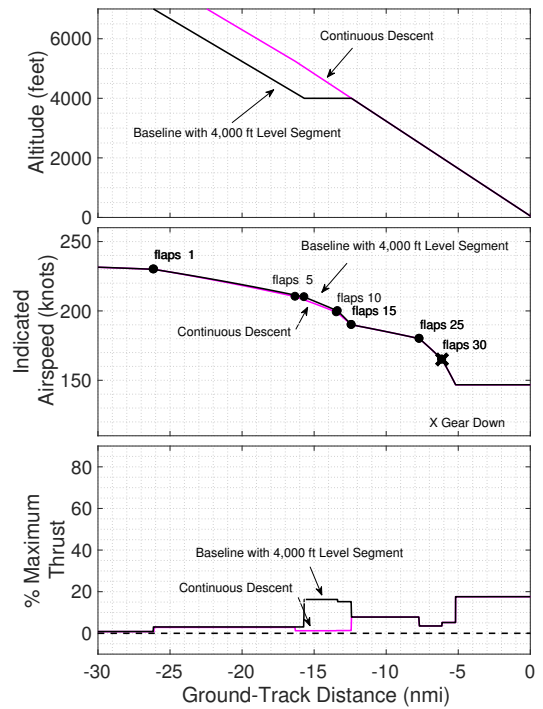
³The maximum landing weight of the Boeing 737-800 assumed to be 146,000

performing a 3 degree ILS approach with a level segment and a standard deceleration profile. There are two baseline cases, one with a level segment at 4,000 ft and one with a level segment at 3,000 ft. The standard deceleration profile was assumed to be the mean deceleration profile seen in the ASDEX velocity data in Figure 4-23. Flap and slat deployment were assumed to occur once the aircraft decelerated to 10 knots below the maximum slat and flap speeds for each configuration. The 1,700 ft location, which corresponds to the outer marker location at BOS runway 4R [115], was assumed to be the stabilization point where the aircraft was at the final approach speed—assumed to be $V_{REF} + 10$ knots—and fully configured for landing. This was consistent with observations and is a 700 ft buffer from the stabilized approach criteria minimum height of 1,000 ft.

The baseline cases with a level segment at 4,000 ft and 3,000 ft are compared to a continuous descent approach. For the continuous descent approach, the velocity profile was assumed to be the same as in the baselines but with thrust reduced in order for the aircraft to fly the continuous descent in the region prior to the glideslope intercept. The resulting flight profiles are shown in Figure 4-24. The distance to touchdown where the flaps 1 through flaps 30 configuration settings were deployed are marked on the indicated airspeed profiles.



(a) Baseline with 3,000 ft Level Segment

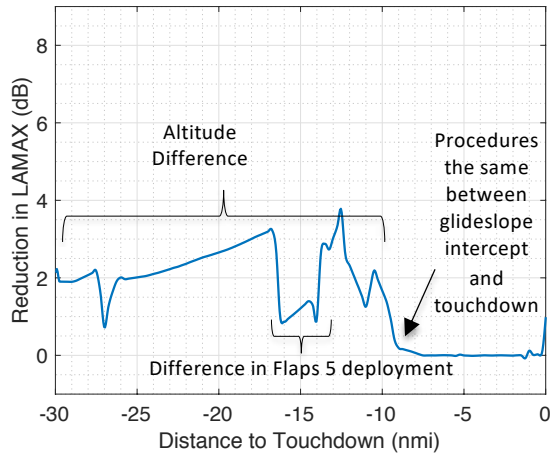


(b) Baseline with 4,000 ft Level Segment

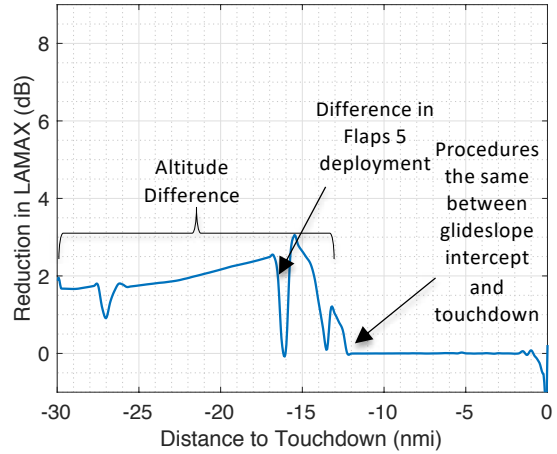
Figure 4-24: Comparison of Altitude, Velocity, and Thrust Profiles for a Narrow Body Aircraft Performing Baseline Approaches with Level Segments (black) and Continuous Descent Approaches (magenta)

The black lines in Figure 4-24 represent the altitude, velocity, and thrust profiles of the baseline approaches with level segments. A thrust increase occurs during the level segments for both cases and the deceleration from flaps 5 to flaps 15 occurs closer to touchdown for the baseline with the 3,000 ft level segment than the 4,000 ft level segment. The magenta lines in Figure 4-24 represent the continuous descent approach procedure altitude, velocity, and thrust profiles. The thrust is reduced compared to the baselines at the locations where level segments were flown in the baselines.

Figure 4-25 shows the reduction in the total $L_{A,MAX}$ noise under the flight track due to the continuous descent approach compared to the baseline cases.



(a) Baseline with 3,000 ft Level Segment

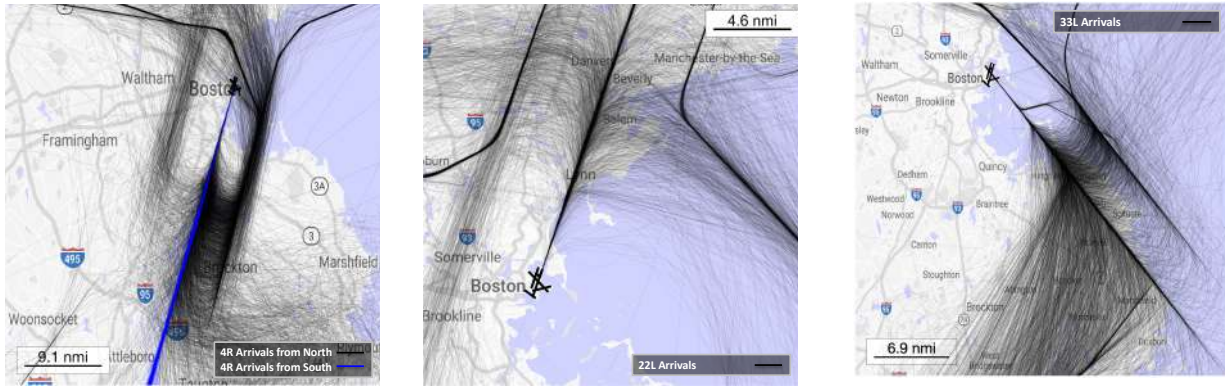


(b) Baseline with 4,000 ft Level Segment

Figure 4-25: Reduction in $L_{A,MAX}$ (dB) Under the Flight Track for a Representative Narrow Body Aircraft, Baseline Approaches with Level Segments minus Continuous Descent Approach Noise Impact

Figure 4-25 shows that before the location of the final glideslope intercept in the baseline cases, the altitude gain in the continuous descent approach results in an approximately 2 dB decrease in noise compared to the baseline cases, with some regions of smaller decrease due to the difference in locations where flaps are released and thrust reductions occur. After the location of glideslope intercept of the baseline cases, the procedures have equal noise impact. The decrease in noise thus occurs until about 10 nmi to touchdown when comparing to the 3,000 ft level segment baseline and occurs until about 12 nmi to touchdown when comparing to the 4,000 ft level segment baseline.

The impacts to population exposure of continuous descent approaches compared to the baseline approaches with level segments can be shown for different runways and airports. To illustrate the impacts at Boston Logan Airport (BOS), the impacts of the approaches are shown into Runways 4R, 22L and 33L. The arrival tracks into these runways at BOS in 2017 were obtained from ASDEX data and are plotted in Figure 4-26. The arrivals into runway 4R from the south and from the north were separated into two categories, with the arrivals from the south into Runway 4R are highlighted in blue in Figure 4-26.



(a) RWY 4R

(b) RWY 22L

(c) RWY 33L

Figure 4-26: Arrival Tracks into BOS Runways in 2017 from ASDEX

The percentage of arrivals that were continuous descents as well as the average altitude for which level segments were performed by aircraft not flying CDAs is shown in Table 4.3 for each runway. It is notable that about 51% of the arrivals into Runway 4R on a peak day of operations in 2017 were coming from the south. Arrivals performing level segments coming from the south into 4R on average performed 4,000 ft level segments. All other arrivals performing level segments into the other runways on average performed 3,000 ft level segments. Other than the aircraft arriving from the south into Runway 4R, about 6% or less of all arrivals into the runways at this airport contained level segments, likely for sequencing of traffic with different base leg lengths in the arrival.

Table 4.3: Mean Level Segment Altitude and Percentage of Arrivals that were Continuous Descent Approaches by Runway in BOS in 2017

Runway	Percent CDAs	Mean Level Segment Altitude
4R (Arrivals from the South)	38%	4,000 ft
4R (Arrivals from the North)	6%	3,000 ft
22L	4.6%	3,000 ft
33L	3.3%	3,000 ft

The noise impacts for the narrowbody aircraft performing the arrivals into each of the runways from Figure 4-26 was modeled assuming the aircraft flew straight-ins except for

arrivals from the north into Runway 4R. For arrivals from the north into Runway 4R, the aircraft was assumed to follow an RNP-like turn to final. The difference in the $L_{A,MAX}$ noise contours of the representative narrowbody aircraft for both the baselines with level segments and continuous descent approaches on approaches into Runway 4R (arrivals from the south and north), Runway 22L, and Runway 33L at BOS are shown in 4-27. The baseline for each case was based on the mean level segment altitude for each of the runways from Table 4.3. The reductions in noise at each runway impact different communities.

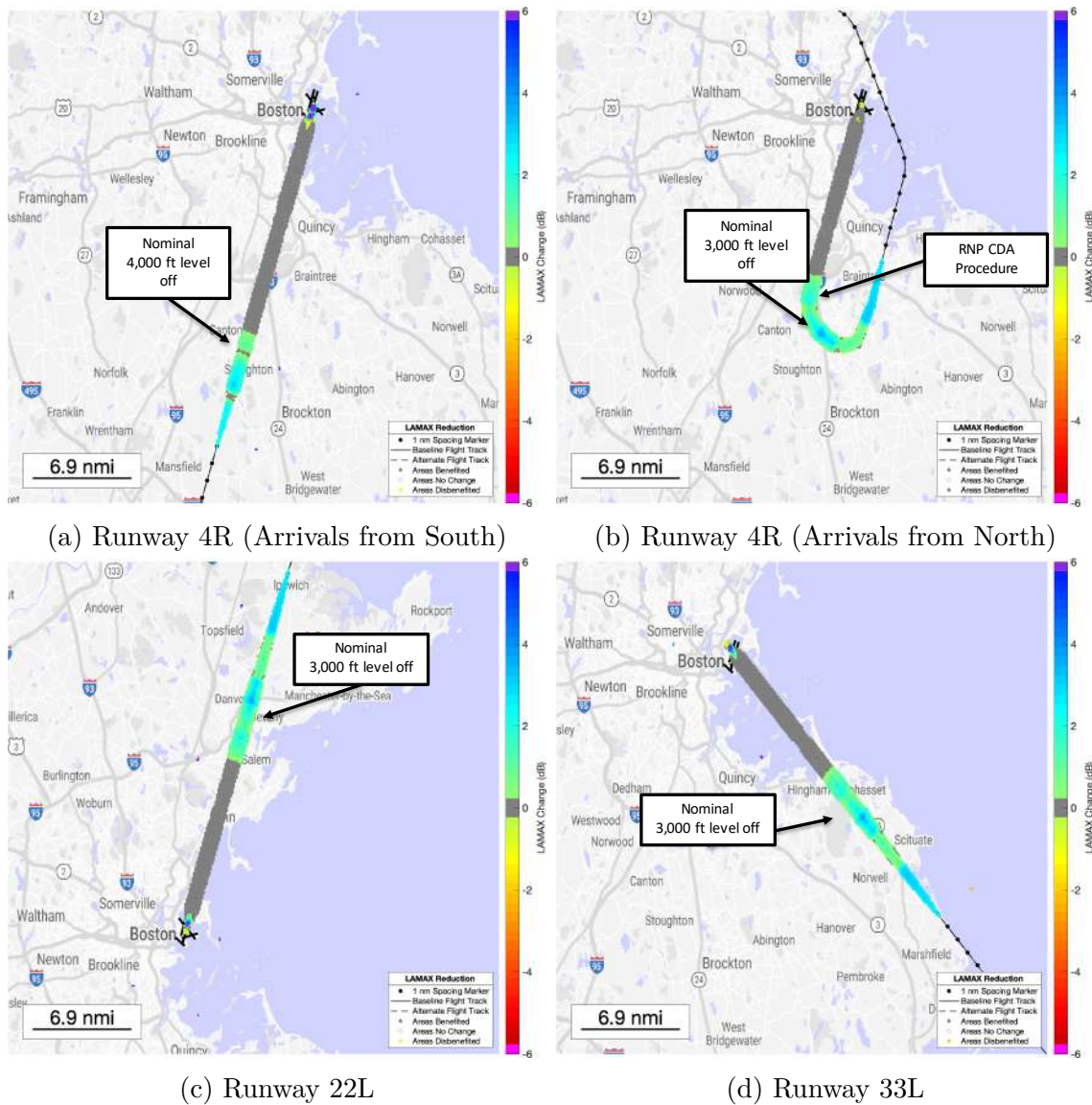


Figure 4-27: Reduction in $L_{A,MAX}$ 60 (dB) Contour for the Representative Narrowbody Aircraft Performing CDAs into Runways at BOS, Baselines with Level Segments minus CDAs

To quantify the noise reduction, modeled population exposure at each of the 60 dB, 65 dB, and 70 dB $L_{A,MAX}$ noise levels for each case are shown in Table 4.4. Reductions in noise primarily occur at the 65 and 60 dB noise contours. There are larger reductions in population exposure when comparing the continuous descent approach to the baseline approaches with 3,000 ft level segments compared to the baseline approach with a 4,000 ft level segment.

Table 4.4: Population Exposure Comparison in $L_{A,MAX}$ of the Continuous Descent Approach Compared to a Baseline Approaches with Level Segments for the Representative Narrowbody Aircraft

$L_{A,MAX}$ Level (dB)		60	65	70
Runway 4R (Arrivals from South)	Baseline (4,000 ft Level Segment)	37,690	12,305	3,074
	Continuous Descent	35,749	12,284	3,040
	Population Exposed	Decrease	1,941	21
$L_{A,MAX}$ Level (dB)		60	65	70
Runway 4R (Arrivals from North)	Baseline (3,000 ft Level Segment)	43,331	14,052	3,143
	Continuous Descent	36,937	12,647	3,143
	Population Exposed	Decrease	6,394	1,405
$L_{A,MAX}$ Level (dB)		60	65	70
Runway 22L	Baseline (3,000 ft Level Segment)	104,416	60,772	17,573
	Continuous Descent	100,508	54,038	17,027
	Population Exposed	Decrease	3,908	6,734
$L_{A,MAX}$ Level (dB)		60	65	70
Runway 33L	Baseline (3,000 ft Level Segment)	10,828	2,386	11
	Continuous Descent	8,481	1,432	11
	Population Exposed	Decrease	2,347	954

4.3.3 Delayed Deceleration Approaches

Varying speed on approach involves delaying the start of the deceleration segments, known as a delayed deceleration approach, while maintaining the safety requirement that the aircraft

must be fully configured and at the final approach speed at the stabilization point. Example noise impacts of a representative narrow body and wide body aircraft performing a delayed deceleration approach procedure are compared to a standard deceleration approach.

The baseline 3 degree ILS approach with a 4,000 ft level segment from section 4.3.2 is compared to a delayed deceleration approach. For the delayed deceleration approach, the location of the start of the deceleration from 250 knots was assumed to be the point at which at idle thrust, the aircraft would be able to meet the final flaps 30 configuration speed at 2,000 ft. The resulting flight profiles are shown in Figure 4-28. The distance to touchdown where the flaps 1 through flaps 30 configuration settings were deployed are marked on the indicated airspeed profiles.

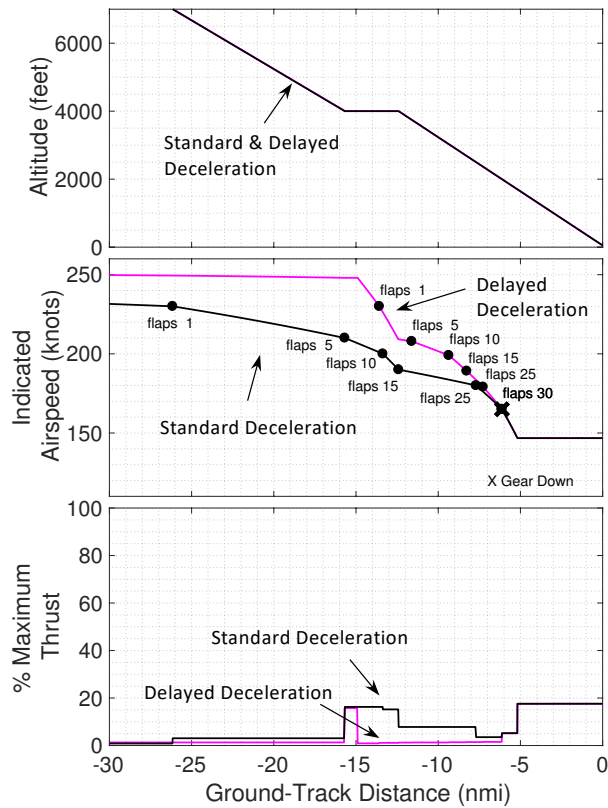


Figure 4-28: Comparison of Altitude, Velocity, and Thrust Profiles for a Narrow Body Aircraft Performing Standard Deceleration (black) and Delayed Deceleration (magenta) Approaches with 4,000 ft Level Segment

The black lines in Figure 4-28 represent the velocity and thrust profiles of the baseline, standard deceleration approach. Because the aircraft decelerates early in these procedures,

the thrust must increase to maintain velocity in order to meet the stabilized final approach velocity at 1,700 ft. The magenta lines in Figure 4-28 represent the delayed deceleration approach procedure velocity and thrust profiles. The locations of flap deployment are closer to touchdown than in the baseline case, and the thrust is at idle for most of the procedure.

Figure 4-29 shows the reduction in the total $L_{A,MAX}$ noise under the flight track due to the delayed deceleration approach compared to the standard deceleration. Modeled $L_{A,MAX}$ under the flight track of the various noise components for the ILS procedure with a 4,000 ft level segment is shown in Figure 4-30 for reference.

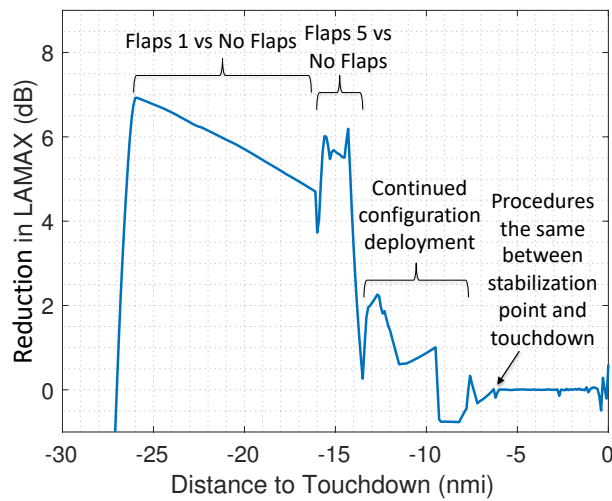
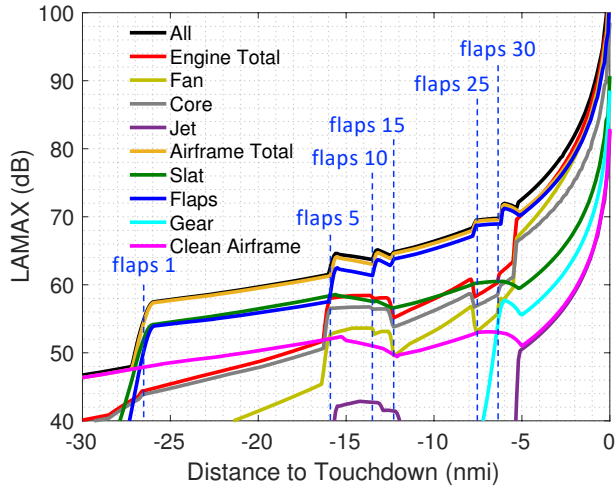
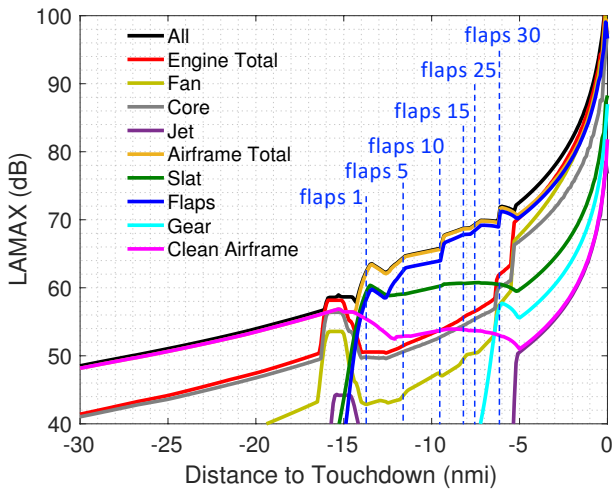


Figure 4-29: Reduction in $L_{A,MAX}$ (dB) Under the Flight Track for a Representative Narrow Body Aircraft, Standard Deceleration minus Delayed Deceleration Approach Noise Impact



(a) Standard Deceleration



(b) Delayed Deceleration

Figure 4-30: Noise Levels Under the Flight Track for Different Noise Components, Representative Narrow Body Aircraft Approaches with 4,000 ft Level Segment

As Figure 4-29 indicates, between 26 and 16 nmi from touchdown, flaps 1 were deployed in the standard deceleration case but not in the delayed deceleration case. Noise is reduced by approximately 6 dB by delaying the flaps 1 deployment in this region. Between 16 and 14 nmi from touchdown, flaps 5 were deployed in the standard deceleration case but no flaps were deployed in the delayed deceleration case, resulting in an additional 6 dB reduction in this region. The most significant reductions are beyond 14 nmi from touchdown. The two procedures have the same noise impact between the stabilization point and touchdown. Figure 4-30 shows that the flap and slats dominate the overall noise levels before the

stabilization point. The delay in the flap and slat deployment, as well as the decrease in thrust, resulted in a delay in the flap and slat noise onset and decrease in engine noise for the delayed deceleration approach compared to the standard deceleration approach. Thus, delaying the deceleration such that the aircraft can maintain the flaps and slats up configuration and idle thrust levels for as long as possible in the approach in this example would have a significant impact on reducing community noise.

Similar results were observed for a representative wide body aircraft (Boeing 777-200). Noise impacts of the representative wide body aircraft performing a delayed deceleration approach procedure are compared to a standard deceleration procedure. The mean velocity versus ground track distance from Airport Surface Detection Equipment, Model X (ASDEX) velocity radar data of Boeing 777s at Boston Logan International Airport (BOS) was determined to be the standard deceleration rate for this aircraft. The aircraft in this data were also performing 4,000 ft level segments before intercepting the ILS.

Flight profiles for both baseline and delayed deceleration approach procedures were generated and are shown in Figure 4-31. The weight was assumed to be 65 percent of the maximum landing weight⁴. The baseline case was performing a 3 degree ILS approach with a 4,000 ft level segment with a standard deceleration profile. The standard deceleration profile was assumed to be the mean deceleration profile seen in the ASDEX data for Boeing 777s at Boston Logan Airport. Flap and slat deployment were assumed to occur once the aircraft decelerated to 10 knots below the maximum slat and flap speeds for each configuration. At the 1,700 ft location, which corresponded to the outer marker location at BOS runway 4R [115], was assumed to be the stabilization point where the aircraft were at $V_{REF} + 10$ knots and fully configured.

⁴The maximum landing weight of the Boeing 777-200 assumed to be 455,000

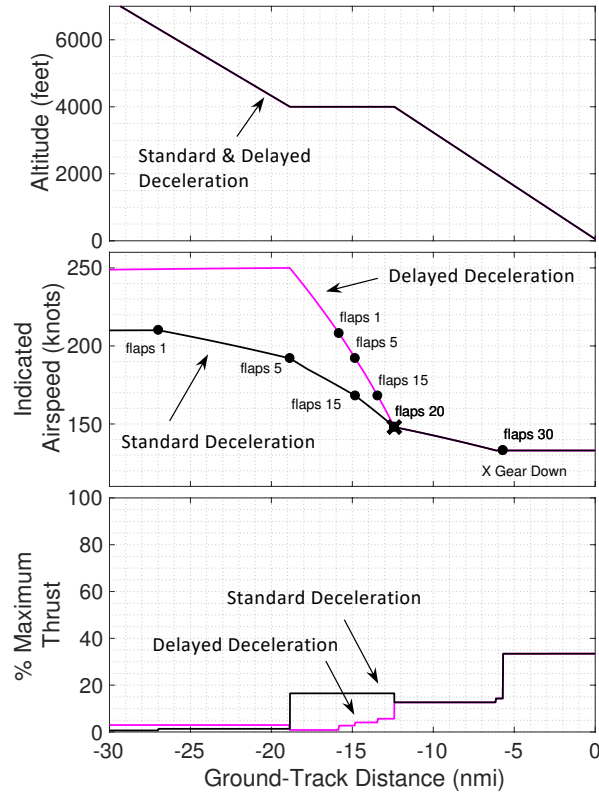


Figure 4-31: Comparison of Altitude, Velocity, and Thrust Profiles for a Wide Body Aircraft Performing Standard Deceleration (black) and Delayed Deceleration (magenta) Approaches with a 4,000 ft Level Segment

The black lines in Figure 4-31 represent the velocity and thrust profiles of the baseline standard deceleration approach. Because the aircraft decelerates early in these procedures, the thrust must increase to maintain velocity in order to meet the stabilization velocity at 1,700 ft. The magenta lines in Figure 4-31 represent the delayed deceleration approach procedure velocity and thrust profiles. The locations of flap deployment are closer to touchdown than in the baseline case, and the thrust is at idle for the entire 4,000 ft level segment. Flaps 20 and gear down are required for this aircraft to have enough drag to perform the 3 degree final descent after the ILS intercept. Thus, the two procedures are the same after the ILS intercept.

Figure 4-32 shows the reduction in the total $L_{A,MAX}$ noise under the flight track due to the delayed deceleration approach compared to the standard deceleration. Modeled $L_{A,MAX}$ under the flight track of the various noise components for the ILS procedure with a 4,000 ft level segment is shown in Figure 4-33 for reference.

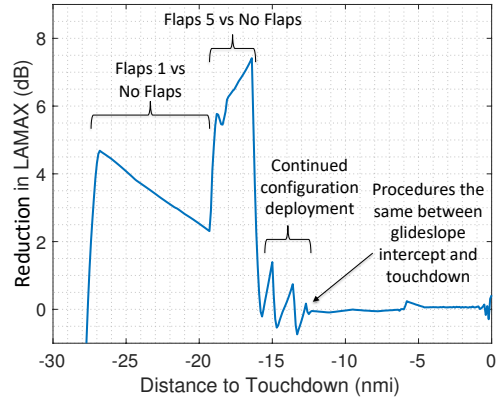
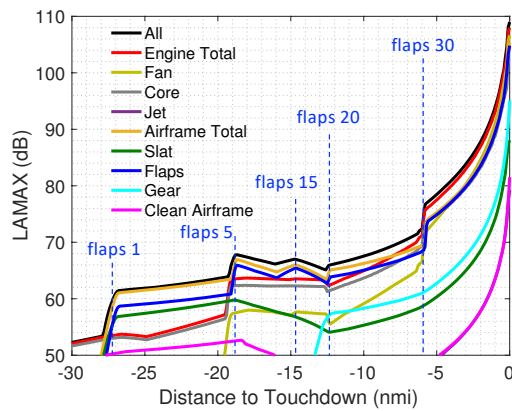
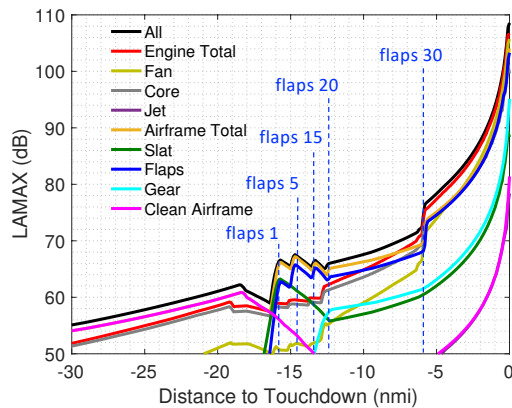


Figure 4-32: Reduction in $L_{A,MAX}$ (dB) Under the Flight Track for a Representative Wide Body Aircraft, Standard Deceleration minus Delayed Deceleration Approach Noise Impact



(a) Standard Deceleration



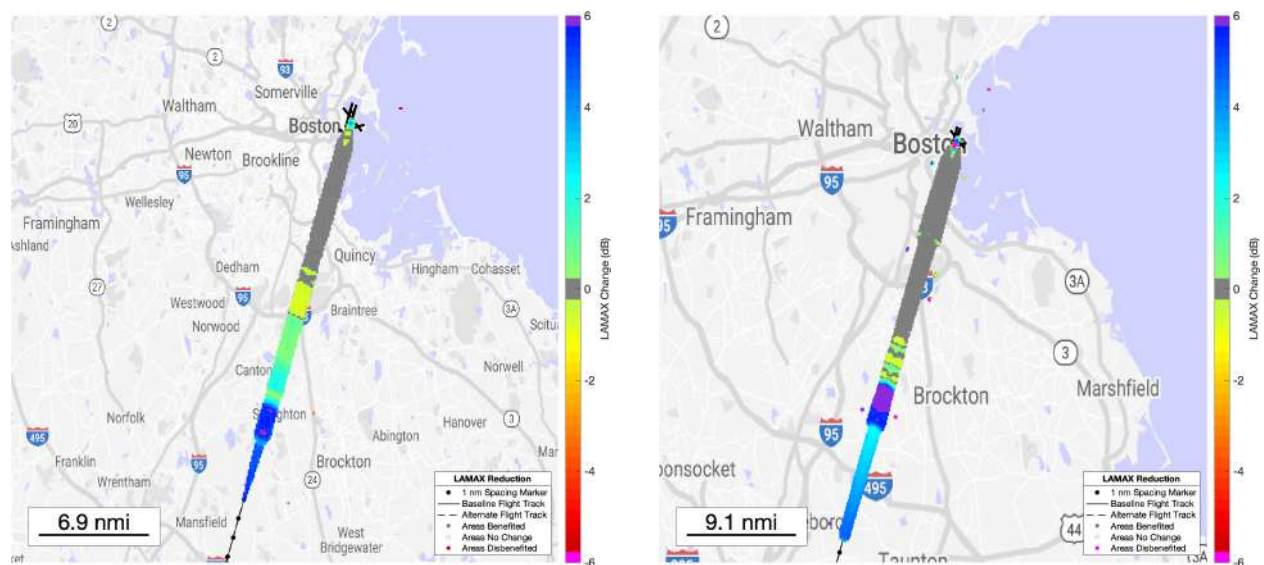
(b) Delayed Deceleration

Figure 4-33: Noise Levels Under the Flight Track for Different Noise Components, Representative Wide Body Aircraft Approaches with a 4,000 ft Level segment

As shown in Figure 4-32, noise is reduced by about 4 to 6 dB by delaying the deceleration

and subsequent flaps 1 and flaps 5 deployment. The most significant reductions are beyond 15 nmi from touchdown. The delay in the flap and slat deployment, as well as the decrease in thrust during the level segment between 19 and 13 nmi to touchdown, results in a decrease in the configuration noise and engine noise for the delayed deceleration approach compared to the standard deceleration approach. After the intercept with the ILS at 13 nmi, the two procedures have the same noise impact. In this example, beyond the ILS intercept at 13 nmi from touchdown, delaying the deceleration such that the aircraft can maintain a clean configuration and idle thrust levels for as long as possible is shown to have a significant impact on reducing community noise.

To illustrate the population exposure impacts of these procedures, population exposure is model at Boston Logan Airport (BOS). The noise contours of the narrow body and wide body aircraft are shown for straight-in arrivals into Runways 4R. The difference in the $L_{A,MAX}$ noise contours for each aircraft flying the delayed deceleration approach compared to the standard deceleration approach are shown in Figure 4-34.



(a) Representative Narrow Body

(b) Representative Wide Body

Figure 4-34: Reduction in $L_{A,MAX}$ 60 (dB) Contour for the Representative Narrow and Wide Body Aircraft Performing Delayed Deceleration Approaches Compared to Standard Deceleration Approaches into Runway 4R at BOS, Standard minus Delayed Deceleration

To quantify the noise reduction, modeled population exposure at each of the 60 dB, 65 dB, and 70 dB $L_{A,MAX}$ noise levels for each aircraft are shown in Table 4.5. Reductions

in noise primarily occur at the 65 and 60 dB noise contours. As a comparison to the continuous descent case, population exposure reduction due to the narrow body aircraft flying the delayed deceleration approach is greater at the 60 dB level than the narrow body aircraft flying the continuous descent into Runway 4R from Table 4.4. This is despite the aircraft having less altitude gain in this region.

Table 4.5: Population Exposure Comparison in $L_{A,MAX}$ of the Delayed Deceleration Approaches Compared to Standard Deceleration Approaches into BOS Runway 4R for the Representative Narrow body and Wide body Aircraft

$L_{A,MAX}$ Level (dB)		60	65	70
Narrow Body	Standard Deceleration	37,690	12,305	3,074
Population Exposed	Delayed Deceleration	32,389	11,944	3,074
	Decrease	5,301	361	0
$L_{A,MAX}$ Level (dB)		60	65	70
Wide Body	Standard Deceleration	99,708	45,486	17,714
Population Exposed	Delayed Deceleration	88,968	44,657	17,653
	Decrease	10,740	829	61

Significant noise benefits were observed when delaying accelerating and subsequent flap and slat deployment for both aircraft assessed. Thus there does appear to be a significant noise benefit from delayed deceleration approaches.

4.3.4 Operational Implications of Continuous Descent and Delayed Deceleration Approaches

Continuous descent approaches are shown to offer noise benefits, but there are operational challenges associated with the procedure. Continuous descents could be implemented by establishing intercept with the ILS at a higher altitude. However, approaches that incorporate level segments are easier to manage from an air traffic control perspective. Level flight segments and earlier deceleration give ATC more time to sequence traffic flows.

In addition, while there does appear to be a significant noise benefit from delayed deceleration approaches, there are operational challenges associated with this procedure

from both a cockpit and air traffic control perspective that also require further study.

From the cockpit perspective, pilots will need procedures or guidance to manage aircraft deceleration on approach considering aircraft weight, winds, and air density to assure that the aircraft reaches the stable approach criteria prior to the stabilization point. The guidance or procedures could include speed, thrust and configuration targets. Some initial work has been done on cockpit displays or planning optimal flap, slat, and landing gear release locations based on operating conditions. A few example systems include the Low Noise Augmentation System (LNAS) by DLR Flight Systems [63], which is an electronic flight bag function that shows the closest or latest location from the runway where flaps, slats, and gear can be deployed and still meet the stable approach at a target location. Another similar system is an Airbus Flight Management System mode on the A350 that gives deceleration and flap deployment guidance [116]. Such tools would also be useful in implementing continuous descent approaches.

From an air traffic control perspective, different deceleration rates for different aircraft will also create challenges in sequencing aircraft. Airborne aircraft are subject to minimum separation requirements. In general, aircraft must be separated by 3 nautical miles horizontally and/or 1,000 feet vertically. Detailed separation requirements are specified in FAA Joint Order 7110.65Y [117]. Air traffic controllers must provide a sufficient time interval between approaching aircraft to ensure 3 nautical mile separation between leading and trailing aircraft. However, the delayed deceleration schedules that yield the greatest noise reduction will vary by aircraft, as seen in the narrow body and wide body examples. As a result, a trailing aircraft may be unable to perform the delayed deceleration approach that yields the greatest noise reduction for that aircraft if the leading aircraft must slow down earlier based on its drag performance in order to meet stabilization criteria.

An additional air traffic consideration is that procedure design criteria may need to be adjusted to allow larger turn radii which would be required for higher speed turns.

Thus, full implementation of delayed deceleration approach procedures for noise abatement would require careful assessments about the proper deceleration rates for different aircraft to get the maximum benefit for the entire fleet.

4.4 ecoDemonstrator 2019 Flight Trials of Delayed Deceleration Approaches

Given the simulated noise benefits of notional delayed deceleration flight procedures, the procedure was tested for flyability in a joint effort between the Boeing Company, the Massachusetts Institute of Technology, and the Federal Aviation Administration, as a part of the 2019 Boeing ecoDemonstrator program. Boeing's ecoDemonstrator program is a part of the company's efforts to evaluate and develop technologies and features that improve operational efficiency and long-term sustainability. The 2019 Boeing ecoDemonstrator Program test bed was a Boeing 777-200 shown in Figure 4-35.



Figure 4-35: 2019 ecoDemonstrator Boeing 777-200 Test Aircraft, Figure from Boeing

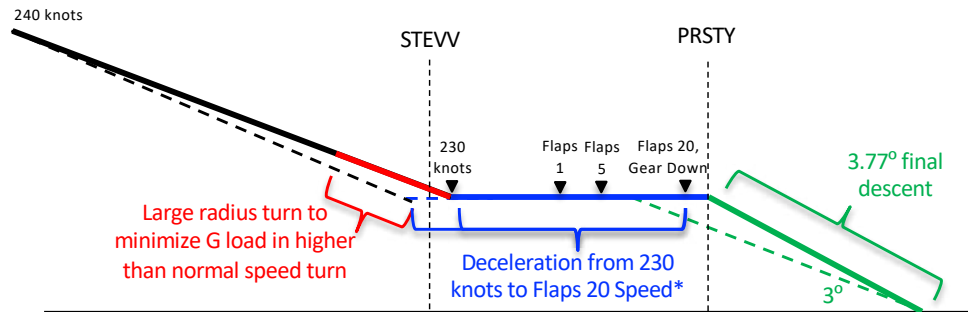
A delayed deceleration approach procedure with a 3.77° steeper final descent was demonstrated on the 2019 ecoDemonstrator during an arrival into Runway 31 at Atlantic City International Airport (ACY) from Frankfurt Airport in Germany⁵.

4.4.1 Proposed Delayed Deceleration Approach Procedure with 3.77° Final Descent

The proposed flight procedure for the ecoDemonstrator was a delayed deceleration approach with a 3.77° steeper final descent. The delayed deceleration approach was added onto a 3.77°

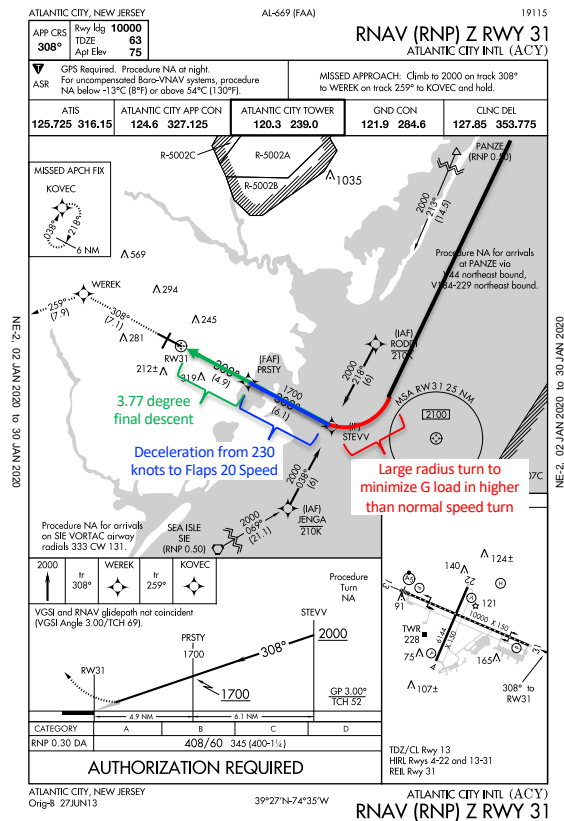
⁵The 2019 ecoDemonstrator also featured advanced technology demonstrations that included aerodynamic improvements such as shape memory alloy vortex generators, recyclable cabin materials, and operational efficiency improving technologies such as head-worn displays and advanced air traffic management and airline operational control (AOC) technologies [118]

steeper final descent planned for the 2019 ecoDemonstrator. A representation of the vertical procedure, and the lateral track of the procedure overlaid on the Runway 31 RNAV (RNP) approach procedure at ACY, is shown in Figure 4-36.



*Length of deceleration segment dependent on aircraft weight, wind, and weather conditions

(a) Vertical Approach Procedure



(b) Lateral Approach Procedure

Figure 4-36: Delayed Deceleration Approach Procedure with 3.77° Final Descent into Runway 31 at Atlantic City International Airport, RNAV procedure diagram from [119]

The procedure consisted of the following two primary phases:

- **Delayed Deceleration Approach phase:** The aircraft would maintain 240 knots on an initial descent and on a lateral track parallel to the RNAV (RNP) Z procedure. The aircraft would then perform a 90°, descending turn to a 2,000 ft level segment, including a deceleration to 230 knots. Because the aircraft would maintain the 240 knots initial descent speed for longer than standard in this procedure, the approach track into Runway 31 needed to be modified with a larger radius during the final 90° turn (highlighted in red in Figure 4-36 (b)). This would minimize the G loads in the higher than normal speed turn at that location. The level segment was determined to occur at 2,000 ft due to an altitude constraint at ACY at the STEVV waypoint, as seen in Figure 4-36 (b). The level segment, diagrammed in blue in Figure 4-36, was determined to be the length at which the aircraft could decelerate at idle thrust from 230 knots to the Flaps 20 speed. The deceleration rate was also determined by the drag performance when releasing Flaps 1, Flaps 5, Flaps 20, and landing gear on this segment. The length of the deceleration segment is dependent on the aircraft weight and wind conditions during the day of the flight.
- **Steeper 3.77° Final Descent phase:** The aircraft would intercept the 3.77° near the PRSTY waypoint and perform a 3.77° final descent.

This procedure was modeled and compared to a notional standard approach procedure to demonstrate the expected noise impacts. In the standard procedure, the aircraft was assumed to perform a standard deceleration that was observed in ASDEX data at BOS and the final glideslope was assumed to be 3°.

The modeled altitude, velocity, and thrust profiles for both the standard and proposed procedure are shown in Figure 4-37. The aircraft performing the proposed flight procedure, shown in magenta, was at lower thrust levels for most of the procedure. Flap release occurred closer to touchdown in the proposed procedure compared to the standard procedure.

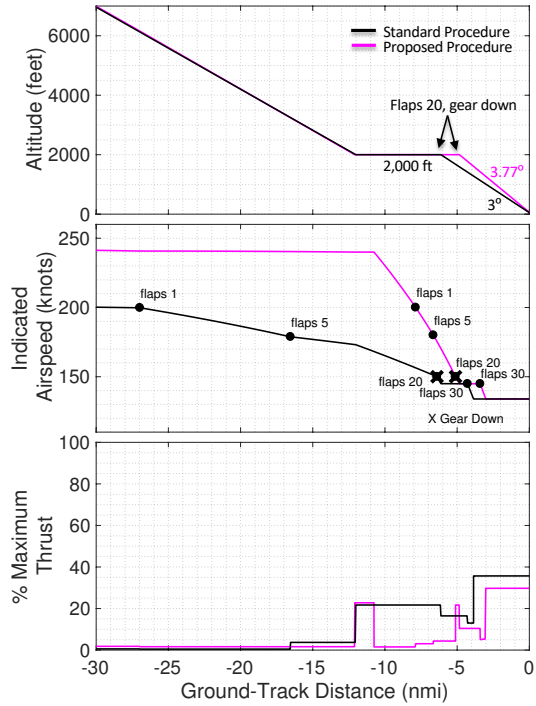
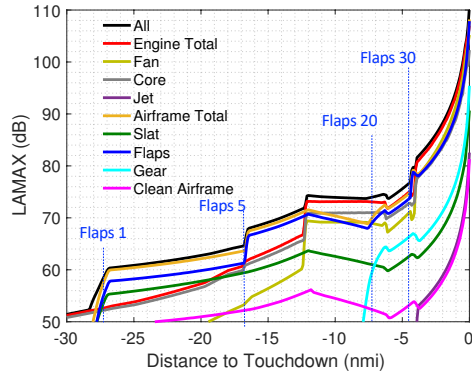
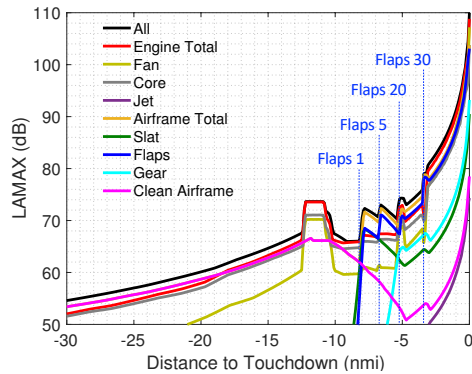


Figure 4-37: Comparison of Altitude, Velocity, and Thrust Profiles for the Standard (black) and Proposed (magenta) Approaches

Modeled $L_{A,MAX}$ noise under the flight track at the component level for both procedures is shown in Figure 4-38.



(a) Standard Deceleration and 3° Final Descent



(b) Proposed Delayed Deceleration and 3.77° Final Descent

Figure 4-38: Noise Levels Under the Flight Track for Different Noise Components, Standard and Proposed Procedures

The delay in the flap and slat deployment, as well as the decrease in thrust, results in a decrease in the configuration noise and engine noise for the delayed deceleration approach compared to the standard deceleration approach. The 3.77° final descent yields additional noise reductions closer to touchdown.

To illustrate the contribution to noise reduction under the flight track for the delayed deceleration and the steeper final descent, the reduction in total $L_{A,MAX}$ under the flight track for the standard procedure compared to the modified procedure is shown in Figure 4-39.

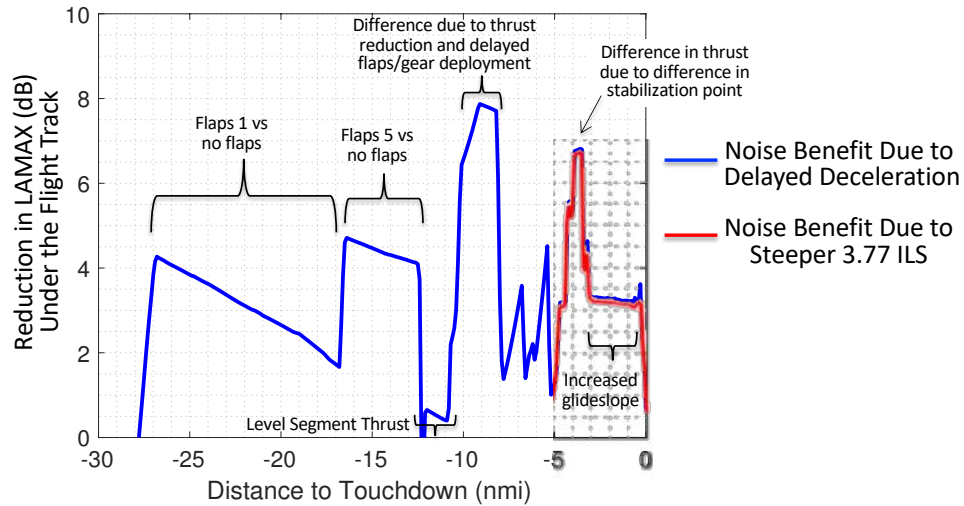
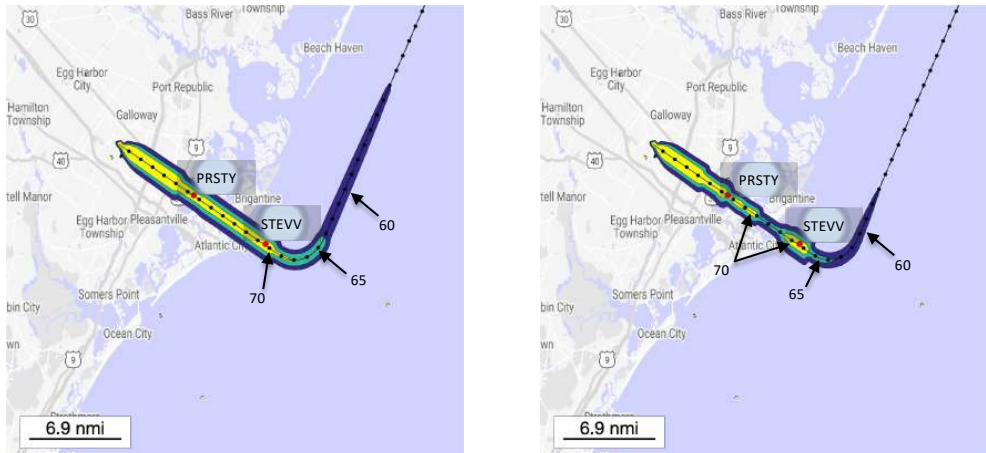


Figure 4-39: Reduction in $L_{A,MAX}$ (dB) Under the Flight Track for the Boeing 777-200 Performing the Proposed Delayed Deceleration and 3.77° Final Descent Compared to the Standard Deceleration and 3° Final Descent

The portion of the procedure shown in blue is the noise benefit primarily due to the delay in deceleration, while the portion of the procedure in red is the noise benefit primarily due to the steeper, 3.77° final descent. Significant noise reductions are apparent from 27 to 12 nmi to touchdown, where the flaps 1 and flaps 5 configuration is deployed during the standard procedure, while the aircraft is still clean during the alternate procedure. When both procedures have a thrust increase during the level segment from about 12 to 10.5 nmi, the engine noise dominates and the difference in noise between the two procedures is minimal. A significant noise reduction between 10.5 and 5 nmi is apparent due to the thrust reduction and delayed flaps and slats deployment for the delayed deceleration procedure. The benefit for the 3.77° descent is present from 5 nmi to touchdown.

Finally, the $L_{A,MAX}$ noise contours of both the standard approach and proposed delayed deceleration approach with the 3.77° final descent is shown in Figure 4-40. The difference in the $L_{A,MAX}$ noise contours for both the standard and proposed approaches are shown for this procedure on approach into Runway 31 at Atlantic City Airport (ACY) is shown in Figure 4-41. Significant reductions in the noise along the entire approach procedure are apparent. The exposure to the 60, 65, and 70 dB noise contours is also shown, also indicating significant noise reductions for the delayed deceleration approach with a 3.77° final descent

compared to the standard approach with a 3° final descent.



(a) Standard Deceleration and 3° Final Descent (b) Proposed Delayed Deceleration and 3.77° Final Descent

Figure 4-40: $L_{A,MAX}$ (dB) Contours for the Boeing 777-200 Performing the Standard and Proposed Approaches into Runway 31 at ACY, Standard minus Proposed Procedure

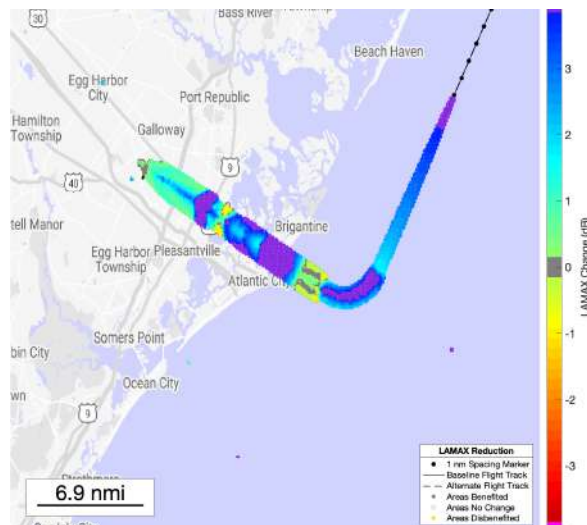


Figure 4-41: Reduction in $L_{A,MAX}$ 60 (dB) Contour for the Boeing 777-200 Performing the Approaches into Runway 31 at ACY, Standard minus Proposed Procedure

Significant noise reductions from the proposed delayed deceleration approach procedure with a 3.77° final descent compared to the notional standard deceleration procedure with a 3° final descent were observed.

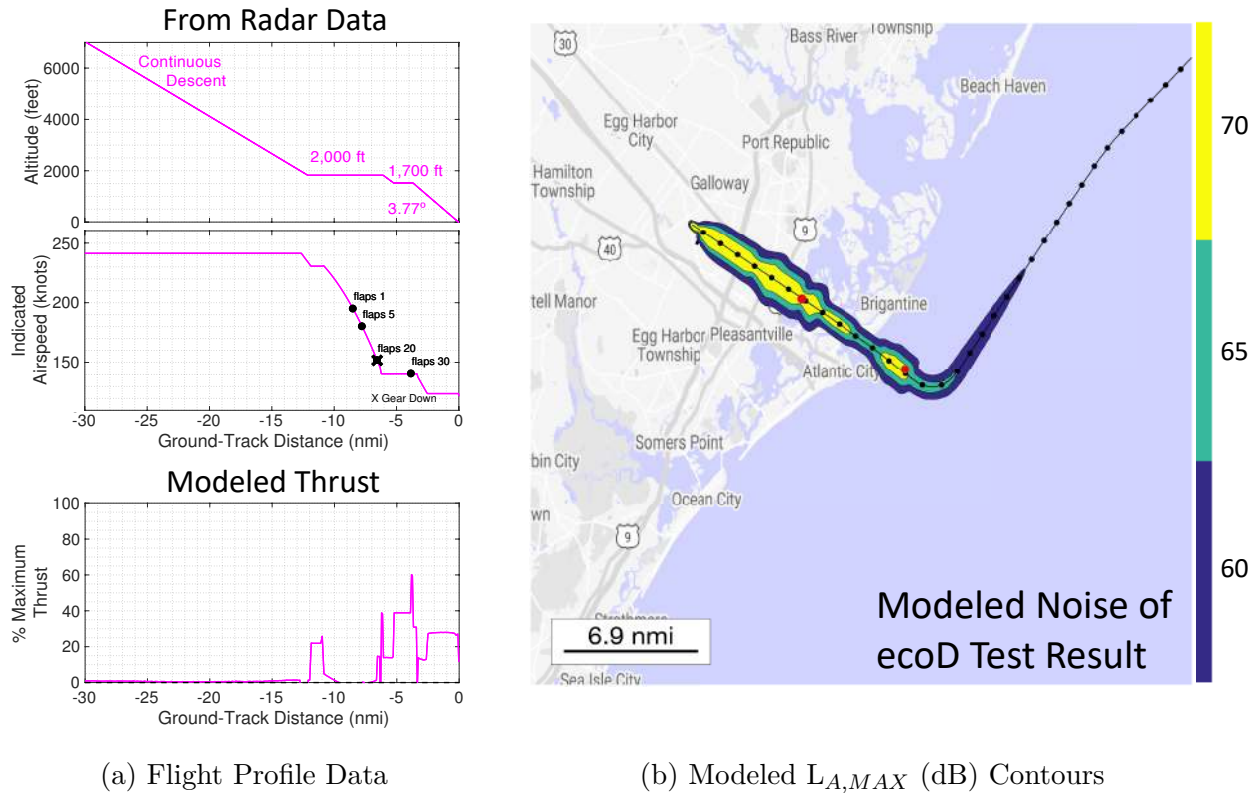
4.4.2 ecoDemonstrator Flight Trials and Comparisons to Modeled Noise Results

The delayed deceleration approach procedure with a 3.77 degree final descent was flown into Runway 31 at ACY on November 21, 2019 by the Boeing ecoDemonstrator 777-200. To demonstrate impacts of the ecoDemonstrator Procedure, the noise was modeled and results were compared with modeled noise results of two baseline flight procedures also flown by the aircraft during the program. The baselines consisted of the following two approach procedures:

- Baseline 1: A standard deceleration and flap deflection, standard 3° glideslope
- Baseline 2: An early deceleration and flap deflection, standard 3° glideslope

ecoDemonstrator Flight

The flight profiles of the ecoDemonstrator procedure, the delayed deceleration approach with a 3.77° final descent into ACY, is shown in Figure 4-42 (a). The altitude and groundspeed of this flight was obtained from radar data and the groundspeed profiles were converted into indicated airspeed by correcting for density altitude and available winds aloft data. The thrust profile was modeled in the Profile Generator. The pilots reported no flyability issues. The flown procedure was consistent with the proposed procedure and contained a level segment at 2,000 ft between 12 and 6 nmi to touchdown and an additional level segment at 1,700 ft between 5 and 4 nmi to touchdown to intercept the 3.77° ILS. The aircraft decelerated from 240 knots to 230 knots before the 2,000 ft level segment and held 230 knots for about 1 nmi, requiring a thrust increase between about 12 and 11 nmi. The aircraft reduced thrust and decelerated from 230 knots to about 140 knots during the 2,000 ft level segment. Flaps 1 and 5 were deployed starting at about 9 nmi from touchdown. Flaps 20 and gear were deployed about 1 nmi before the end of the 2,000 ft level segment. Thrust was increased and 140 knots held between 6 and 3 nmi until the aircraft intercepted with the 3.77° ILS. The resulting $L_{A,MAX}$ contours at the 60, 65, and 70 dB levels are shown in Figure 4-42 (b).



(a) Flight Profile Data

(b) Modeled $L_{A,MAX}$ (dB) Contours

Figure 4-42: Flight Profile Data and Modeled $L_{A,MAX}$ (dB) Contours for the Boeing 777-200 ecoDemonstrator Procedure into Atlantic City International Airport

Delayed deceleration approaches are also expected to result in fuel burn reductions compared to standard procedures. To assess this, fuel burn during this procedure was also modeled using BADA 4. From 30 nmi to touchdown, the modeled total fuel burn was 810 lbs. This value is compared to the fuel burn of the baseline flights to also demonstrate the potential for fuel burn reduction of this procedure.

The profile data of the proposed delayed deceleration approach with a 3.77° final descent from section 4.4.1 is shown in Figure 4-43 overlaid on the ecoDemonstrator procedure flight data from Figure 4-42 (a) for comparison. Thrust for both procedures was modeled using the Flight Profile Generator.

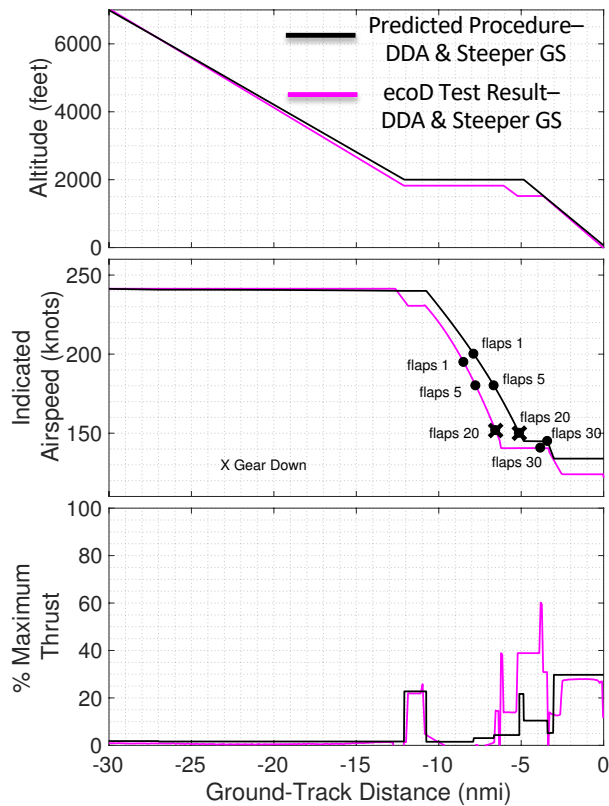


Figure 4-43: Comparison of Altitude, Velocity, and Thrust Profiles for the Proposed Delayed Deceleration Approach with 3.77° Final Descent (black) and Flown ecoDemonstrator Procedure (magenta)

As seen in Figure 4-42 (a), the deceleration profile during the 2,000 ft level segment of the ecoDemonstrator procedure is shifted back about 1 nmi compared to the proposed procedure. This is because in the ecoDemonstrator flight, the deceleration from 240 to 230 knots was performed earlier and a buffer between the Flaps 20, gear down stabilization point and the glideslope intercept was included. The deceleration from 230 knots to 140 knots in the ecoDemonstrator flight profile has similar rates to those calculated in the proposed profile. There is additional thrust in the ecoDemonstrator profile between 6 and 5 nmi to touch down and 5 to 3 nmi to touchdown compared to the proposed procedure due to the aircraft being on condition (Flaps 20, gear down) earlier in the procedure and due to the presence of the additional 1,700 ft level segment.

Baseline 1 Flight

The flight profiles of Baseline 1, a standard deceleration approach with a 3° final descent into Boeing Field Airport, is shown in Figure 4-44 (a). The altitude and groundspeed of this flight was obtained from radar data and the groundspeed profiles were converted into indicated airspeed by correcting for density altitude and available winds aloft data. The thrust profile was modeled in the Profile Generator. The approach consisted of a level segment at 4,000 ft between 35 and 20 nmi to touchdown and a level segment at 2,000 ft between 12 and 5.5 nmi to touchdown. The aircraft decelerated from its initial approach speed of 240 knots to about 200 knots during the 4,000 ft level segment and then held 200 knots until 12 nmi, requiring additional thrust during the 4,000 ft level segment. Flaps were deployed starting at about 11.5 nmi from touchdown. The resulting $L_{A,MAX}$ contours at the 60, 65, and 70 dB levels are shown in Figure 4-44 (b).

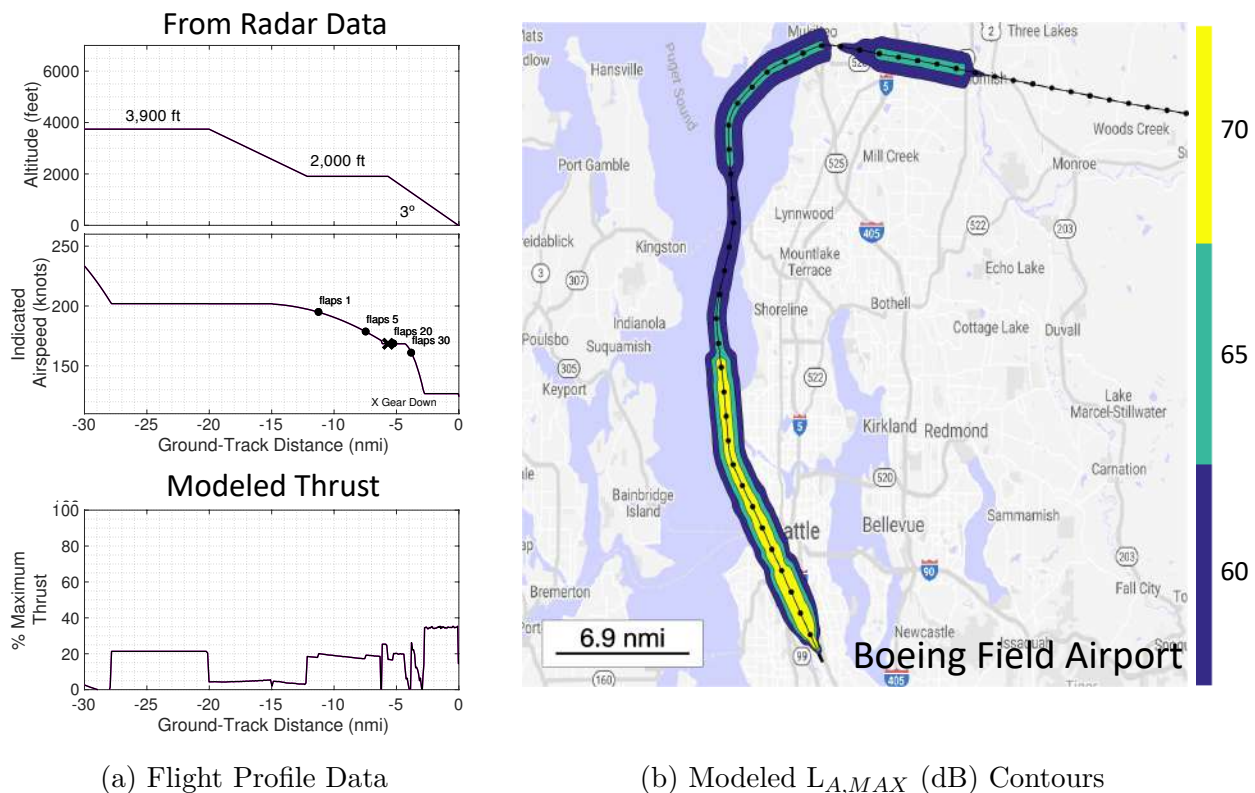


Figure 4-44: Flight Profile Data and Modeled $L_{A,MAX}$ (dB) Contours for Baseline 1

Finally, the fuel burn during this procedure, modeled using BADA4 from 30 nmi to

touchdown, was 1,230 lbs.

Baseline 2 Flight

The flight profiles of Baseline 2, an early deceleration approach with a 3° final descent into Paine Field Airport, is shown in Figure 4-45 (a). The altitude and groundspeed of this flight was obtained from radar data and the groundspeed profiles were converted into indicated airspeed by correcting for density altitude and available winds aloft data. The thrust profile was modeled in the Profile Generator. The approach consisted of a level segment at 3,800 ft between 29 and 17 nmi to touchdown and a level segment at 3,000 ft between 14 and 8 nmi to touchdown. The aircraft decelerated from about 200 knots to about 170 knots during the 4,000 ft level segment and then held 170 knots until 8 nmi, requiring additional thrust during the 4,000 ft level segment. Flaps 1 and 5 were deployed starting at about 24 nmi from touchdown. The resulting $L_{A,MAX}$ contours at the 60, 65, and 70 dB levels are shown in Figure 4-45 (b).

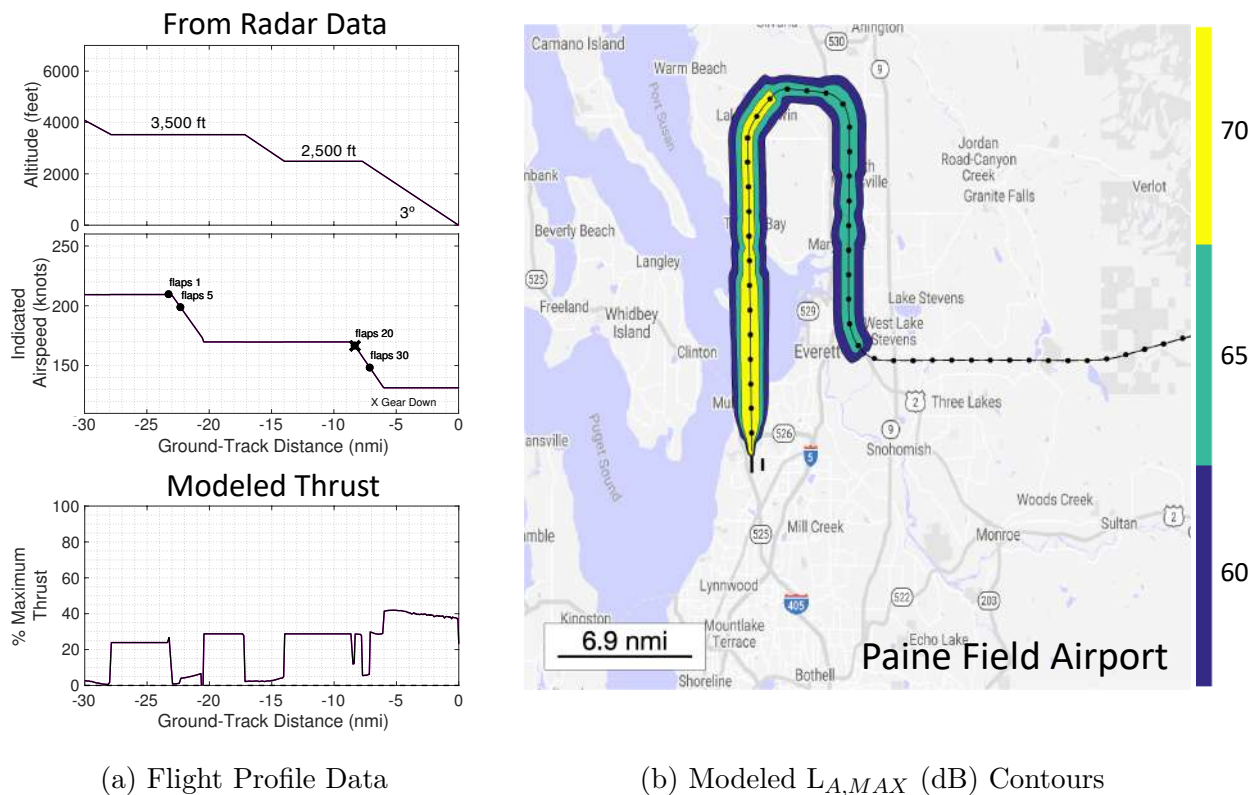


Figure 4-45: Flight Profile Data and modeled $L_{A,MAX}$ (dB) Contours for Baseline 2

Finally, the fuel burn during this procedure, modeled using BADA4 from 30 nmi to touchdown, was 1,780 lbs.

Comparison of ecoDemonstrator Flight Modeled Noise Impacts with Baselines

The profile data of Baseline 1 (black) is shown in Figure 4-46 overlaid on the ecoDemonstrator Flight (magenta) for comparison. Thrust for both procedures was modeled using the Flight Profile Generator.

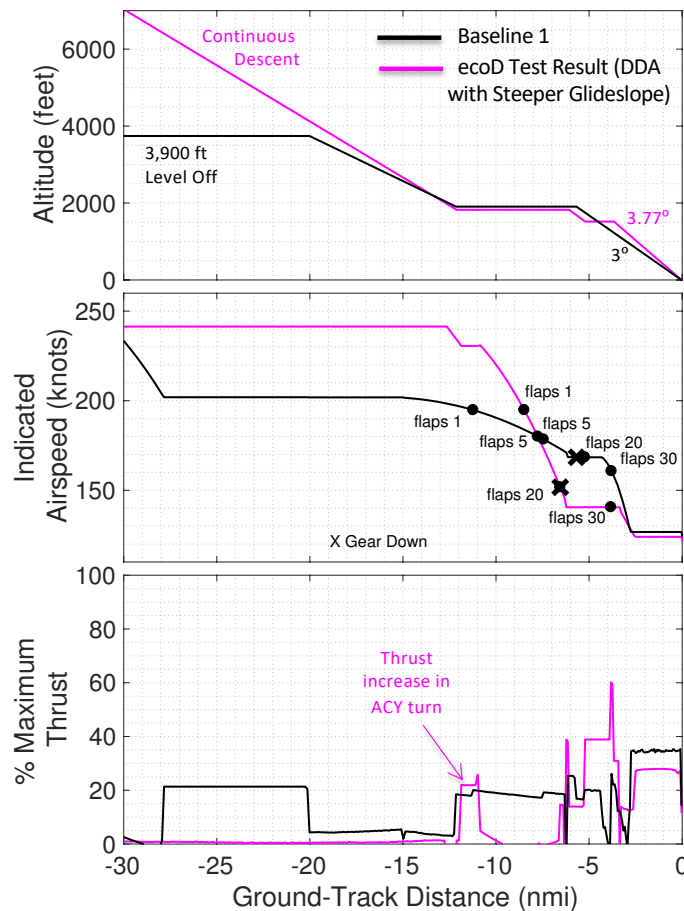
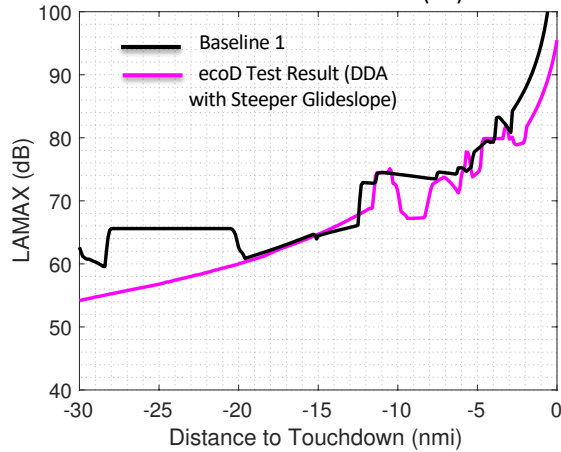
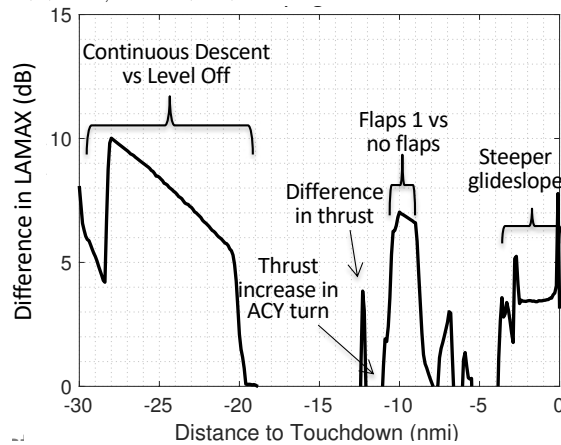


Figure 4-46: Comparison of Altitude, Velocity, and Thrust Profiles for Baseline 1 (black) and ecoDemonstrator Flight (magenta)

Noise under the flight track for both procedures is shown in Figure 4-47 (a). The reduction in noise under the flight track when flying the ecoDemonstrator procedure compared to Baseline 1 is shown in Figure 4-47 (b).



(a) $L_{A,MAX}$ (dB) Noise Under the Flight Track



(b) Reduction in $L_{A,MAX}$ (dB) Noise Under the Flight Track when Flying the ecoDemonstrator Procedure compared to Baseline 1

Figure 4-47: Noise Levels Under the Flight Track for Baseline 1 and the ecoDemonstrator Procedure

As shown in Figure 4-47, an approximately 6-10 dB reduction in $L_{A,MAX}$ is observed between 27 and 20 nmi to touchdown when flying the continuous descent in the ecoDemonstrator procedure compared to the 4,000 ft level segment and subsequent thrust increase in Baseline 1. The two procedures have similar noise profiles between about 20 and 12 nmi to touchdown. Differences in the thrust onset at the start of the 2,000 ft level segment between the two procedures result in spikes in the noise reduction between 12 and 10 nmi shown in Figure 4-47 (b). An approximately 6 dB noise reduction when flying the ecoDemonstrator procedure is observed between about 10 nmi and 7 nmi due to the delay in the deployment of Flaps 1. Finally, the steeper, 3.77° final descent glideslope of the

ecoDemonstrator procedure results in an over 5 dB noise reduction compared to the 3° final descent glideslope of Baseline 1 between 3 nmi to touchdown.

Finally, the profile data of Baseline 2 (black) is shown in Figure 4-49 overlaid on the ecoDemonstrator Procedure (magenta) for comparison. Thrust for both procedures was modeled using the Flight Profile Generator.

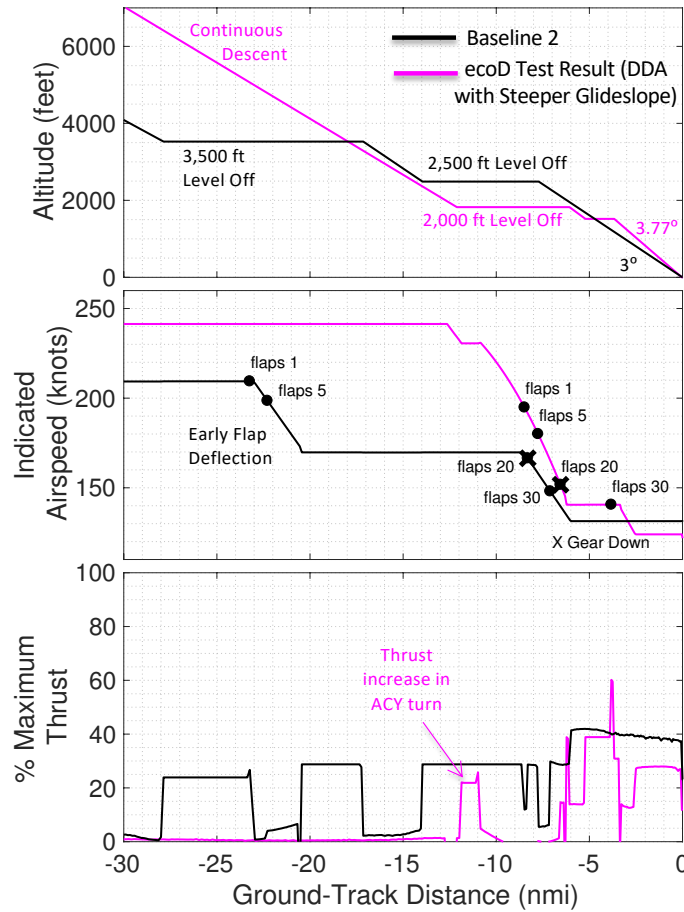
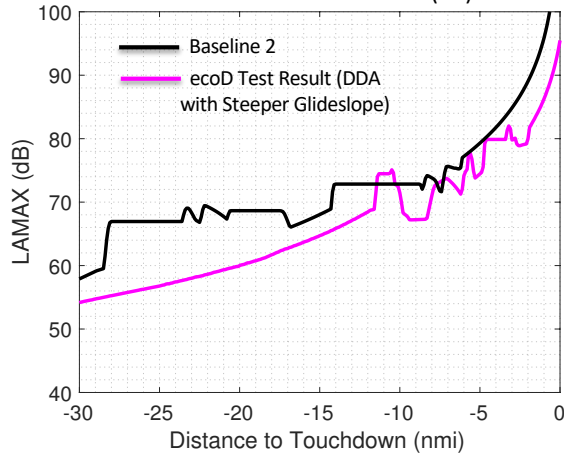
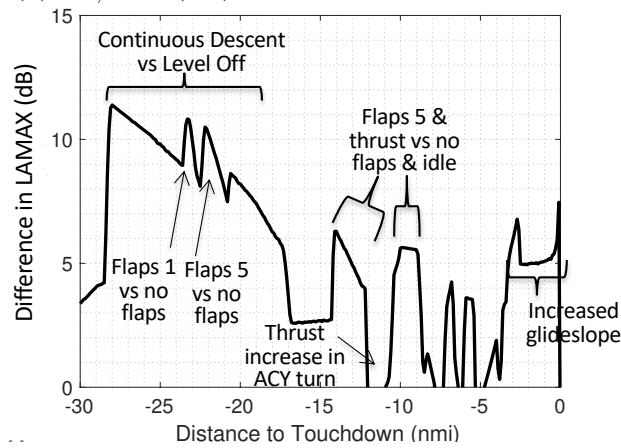


Figure 4-48: Comparison of Altitude, Velocity, and Thrust Profiles for Baseline 2 (black) and the ecoDemonstrator Procedure (magenta)

Noise under the flight track for both procedures is shown in Figure 4-49 (a). The reduction in noise under the flight track when flying the ecoDemonstrator procedure compared to Baseline 2 is shown in Figure 4-49 (b).



(a) $L_{A,MAX}$ (dB) Noise Under the Flight Track



(b) Reduction in $L_{A,MAX}$ (dB) Noise Under the Flight Track when Flying the ecoDemonstrator Procedure compared to Baseline 2

Figure 4-49: Noise Levels Under the Flight Track for Baseline 2 and the ecoDemonstrator Procedure

As shown in Figure 4-49, an approximately 6-10 dB reduction in $L_{A,MAX}$ is observed between 27 and 17 nmi to touchdown when flying the continuous descent in the ecoDemonstrator procedure compared to the 3,800 ft level segment and subsequent thrust increase in Baseline 2. Additional reductions in noise are observed in this region due to the Flaps 1 and Flaps 5 release in Baseline 2. Between 15 and 7 nmi, an approximately 6 dB noise reduction is observed due to the delayed flap deployment and idle thrust of the ecoDemonstrator procedure. This reduction occurs despite the fact that the aircraft levels off at a higher altitude in this region than in the ecoDemonstrator procedure. Finally, the steeper, 3.77° final descent glideslope of the ecoDemonstrator procedure results in an over 5

dB noise reduction compared to the 3° final descent glideslope of Baseline 2 between 3 nmi to touchdown.

ecoDemonstrator Flights Summary

The ecoDemonstrator flight of the delayed deceleration approach with a steeper 3.77° final descent was reported by the pilots to have no significant flyability issues.

Subsequent noise modeling of the flight also showed there are noise benefits of various components of this procedure. Those noise benefits included the 6-10 dB noise noise reduction observed when flying a continuous descent versus level segments as seen when comparing both Baseline 1 and 2 to the ecoDemonstrator flight. The noise benefits included approximately 6 dB noise reductions due to delaying the deceleration and subsequent Flaps 1 and 5 deployment. Additional noise reductions of approximately 5 dB were also observed due to the steeper, 3.77° final descent glideslope compared to the standard 3° final descent glideslope.

The ecoDemonstrator flight also showed significant fuel burn reduction compared to the baselines. The total fuel burn as modeled in BADA 4 from 30 nmi to touchdown for each flight was:

- ecoDemonstrator Flight: 810 lbs
- Baseline 1: 1230 lbs
- Baseline 2: 1780 lbs

The results indicate that the ecoDemonstrator flight resulted in a fuel burn reduction of 420 lbs compared to Baseline 1 and 970 lbs compared to Baseline 2.

These comparisons highlight the potential for significant community noise and fuel burn reductions through the implementation of continuous descents, delayed deceleration and configuration deployment, and steeper descents in approach procedure design.

4.5 Chapter 4 Conclusion

The case studies of this chapter show that for modern aircraft on departure, changes in aircraft speed have minimal impact on the overall aircraft departure noise. Varying flap retraction and acceleration location was shown to result in minimal differences in the departure profile and thus insignificant differences in noise. Furthermore, aircraft on departure operate at moderate to high thrust levels, and aircraft are cleanly configured relatively early in departure procedure. Thus changing departure climb speed does not significantly impact overall departure noise. While changes in aircraft speed significantly impact the noise of the clean airframe, airframes have gotten cleaner and quieter over time and thus the engine noise still dominates. Modifications to departure climb angle via changes in thrust have a significant impact on departure noise. For example, gaining altitude by performing a high thrust climb in the beginning of the departure before performing a thrust cutback was shown to yield higher noise close to the airport due to the higher initial thrust, followed by a reduction in the extent of the noise contour underneath the flight track for the later part of the procedure. The balance between climb gradient and thrust level means that one procedure may be more beneficial for some communities surrounding an airport than others. Because this procedure results in a redistribution of noise rather than a reduction in noise at all locations, the impacts on population exposure are dependent on location. However this example demonstrates the potential use of the framework to design an optimal departure procedure for minimum population exposure for a given airport and population distribution.

The case studies of this chapter also show that for modern aircraft on arrival, changes in both descent angle and approach airspeed can have a significant impact on the overall aircraft noise. Maintaining a higher glidepath angle such as in continuous descent approaches or steeper approaches compared to approaches with level segments benefits noise with additional altitude gain but requires the presence of enough drag to perform the approach. Also, engine thrust on approach is often low and thus airframe noise components, such as flap and slat noise, have a more significant impact on approach than on departure. If aircraft decelerate early in an approach procedure, then flaps and slats must be released. These devices are

shown to have a significant impact on approach noise. Thus, a delayed deceleration approach where the aircraft can maintain a flaps and slats retracted configuration for as long as possible and also delay the need to increase thrust on approach is beneficial for noise. This procedure has the potential to reduce community noise but has implementation challenges, including the ability of pilots to know where to begin the deceleration for different aircraft weights and wind conditions and how air traffic controllers will sequence aircraft with different deceleration rates. These challenges require further study.

Chapter 5

Framework for Analyzing Performance and Noise of Windmilling Drag and Hybrid Electric Aircraft

In addition to conventional aircraft, certain advanced aircraft configurations have community noise reduction potential. This is due to both potential to reduce the noise source levels of certain components and reduction of noise through performance of certain flight procedures made possible with advanced configurations. In Chapter 2 the use of windmilling drag on approach by hybrid electric aircraft for community noise reduction was identified as one such concept with the potential for noise reduction. Thus, hybrid electric aircraft concepts using windmilling engines on approach are shown as case studies of using the developed analysis framework to analyze noise of combined flight procedure and aircraft design level concepts.

To analyze performance and community noise of advanced operational approach procedures for hybrid electric aircraft including windmilling drag, the framework introduced in Chapter 3 is modified to include the necessary performance and noise analysis components, as shown in Figure 5-1.

Because assessing noise reduction potential is the primary focus of this thesis, hybrid

electric aircraft performance within the Aircraft Performance Module is modeled using a retrofit approach. Given a conventional aircraft with turbofan engines modeled in TASOPT, the aircraft is modeled with "retrofitted" hybrid electric engines while maintaining the same airframe geometry and mission performance. The TASOPT engine core and propulsor area is resized to obtain the performance parameters for hybrid electric aircraft. More detail of this retrofit process is described in section 5.1.1.

Drag data for windmilling engines is obtained from blade element theory as described in section 5.1.2 and is coupled with BADA 4 drag polars to obtain the aircraft flight performance.

In the Aircraft Noise Module, ANOPP's normal turbofan source noise models are used given the performance of the retrofit hybrid electric engines. For windmilling procedures, ANOPP's gas generator source noise modules are combined with windmilling engine noise from external sources for the total aircraft noise prediction. Methods for the prediction of windmilling noise are discussed in section 5.2.1.

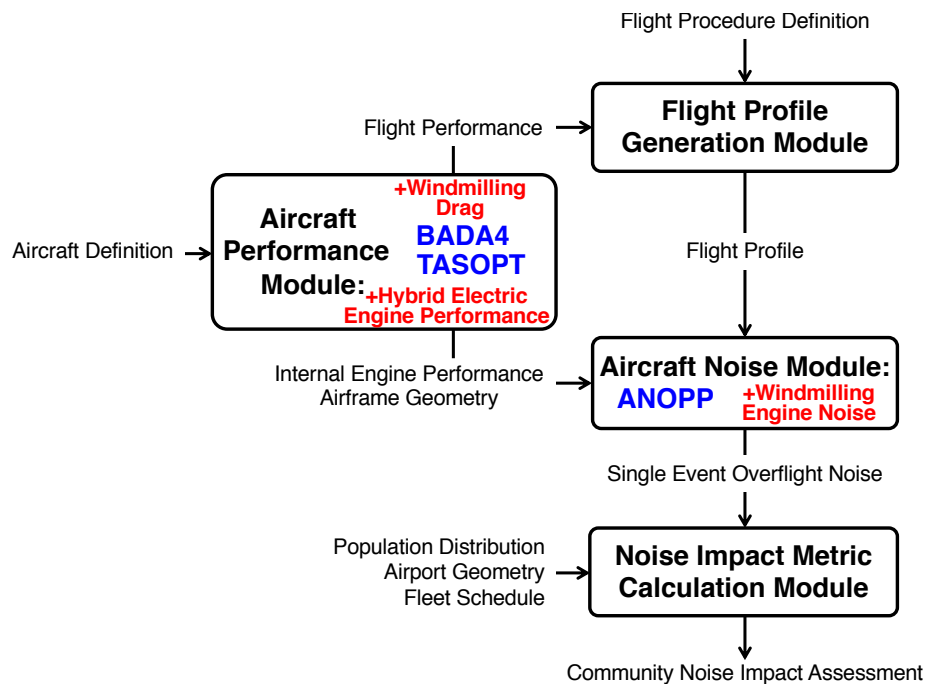


Figure 5-1: Framework to Analyze Aircraft Community Noise Impact of Hybrid Electric Aircraft Utilizing Windmilling Drag on Approach

5.1 Aircraft Performance Model to Include Electrified Engines

5.1.1 Hybrid-Electric Aircraft Performance Model

For turbofan engine performance modeling (including internal engine performance states, aircraft weight, engine diameter, and nacelle drag), the framework uses TASOPT and BADA 4 respectively, which provide modeling capabilities for the engine states of turbofan-equipped aircraft. Alternative sources of engine state and drag information are required for modeling the geometry and performance of hybrid electric engines.

Hybrid electric engines can be sized by either:

1. Retrofitting a turbofan aircraft with hybrid electric engines, maintaining the same airframe
2. Sizing a new aircraft with hybrid electric engines from scratch given mission requirements

Because assessing noise reduction potential is the primary focus of this thesis, hybrid electric aircraft performance is modeled using the retrofit method. In the **retrofit method**, aircraft sized in TASOPT has its engines modified to be turboelectric, such as is shown in Figure 5-2, with the engines for both aircraft shown schematically in Figure 5-3. It should be noted that one approach to the **new sizing method** is to modify the aircraft and engine sizing routines in TASOPT to include the weight and performance expected with hybrid electric engines.



Figure 5-2: Aircraft Retrofitting for (a) Standard Turbofan and (b) Turboelectric Fan

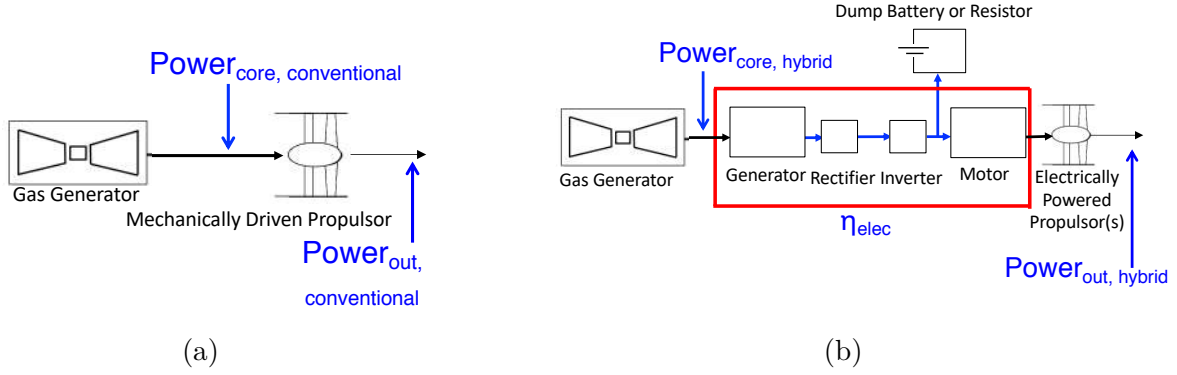


Figure 5-3: Power in and out definitions for a (a) standard turbofan and (b) turboelectric fan

In the retrofit method implemented, the airframe of the aircraft sized in TASOPT is fixed and the engines are conceptually retrofitted to be turboelectric in order to obtain a representative new aircraft total weight, drag, and engine area. It is assumed that for the conventional turbofan sized in TASOPT (Figure 5-3 (a)), the gas generator produces a core power $Power_{core,conventional}$ which mechanically drives a propulsor. This propulsor then converts the $Power_{core,conventional}$ into $Power_{out,conventional}$, based on the fan efficiency, which then propels the aircraft in flight. Similarly, the power produced by the gas generator of a hybrid electric engine produces $Power_{core,hybrid}$ which is then converted into $Power_{out,hybrid}$ by the propulsor(s). Unlike the conventional engine, the conversion from the core to output power is additionally reduced by the efficiency of the electrical system η_{elec} that is highlighted in Figure 5-3 (b), requiring a higher core power than in the conventional case. These electrical components and change in engine size also contribute to changes in weight of the aircraft, and thus changes in drag due to the additional induced drag from higher lift requirements and profile drag from changes in engine and nacelle size.

Thus if the retrofitted aircraft is sized to maintain the same mission velocity V_∞ , then $Power_{out,hybrid} = Drag_{hybrid}V_\infty$ (assuming steady level flight) must increase relative to $Power_{out,conventional}$. The required $Power_{core,hybrid}$ needed is thus increased by the relation given by equation 5.1.

$$Power_{core,hybrid} = Power_{core,conventional} \left(\frac{1}{\eta_{elec}} \right) \left(\frac{Drag_{hybrid}}{Drag_{conventional}} \right) \quad (5.1)$$

Equation 5.1 is the primary retrofit equation and is implemented in a sizing loop described below to obtain the final sized components of the retrofit aircraft. Knowing the required core power of the hybrid retrofit aircraft enables the sizing of the electrical components and aircraft weight as well as the sizing of the retrofit fan area. This sizing loop is a post-processing step applied to TASOPT outputs in order to obtain the retrofit aircraft.

Retrofit Sizing Loop

To perform a hybrid electric aircraft retrofit given a conventional aircraft from TASOPT, the turboelectric engine from Figure 5-3 is assumed. A dump battery/resistor that would collect the residual power when windmilling was included in sizing.

The overall efficiency of the electrical system η_{elec} is obtained considering the efficiencies of the electrical system. For a gas generator supplying power to a generator which is then used to power N motors that power N fans, the power conversion from the core to the fan output can be obtained as:

$$P_{out,hybrid} = \eta_{elec} P_{core,hybrid} = \eta_{motor} \eta_{inverter} \eta_{rectifier} \eta_{generator} P_{core,hybrid} \quad (5.2)$$

Engine thrust scales with the fan face area. Assuming drag equals thrust for steady level flight, the ratio of the required hybrid engine fan area and the conventional engine area is obtained as:

$$\frac{Area_{hybridengine}}{Area_{conventionalengine}} = \frac{Drag_{hybrid}(\Delta Weight_{hybridengine})}{Drag_{conventional}} \quad (5.3)$$

where $\Delta Weight_{hybridengine}$ represents the difference in weight between the hybrid engine and the conventional engine, given by:

$$\begin{aligned}
\Delta Weight_{hybridengine} \sim & \Delta Weight_{core}(Power_{core,hybrid}) \\
& + \Delta Weight_{fan}(Area_{hybridengine}) \\
& + \Delta Weight_{nacelle}(Area_{hybridengine}) \\
& + Weight_{electricalsystem}(Power_{core,hybrid}) \quad (5.4)
\end{aligned}$$

The weight and performance of the electrical components of electrified engines, such as cables, generators, inverters, etc., denoted with † in Figure 5-4 are sized based on power density and efficiency predictions depending on the assumed technology level. The technology level assumptions given by NASA as stated in Chapter 2 were used in this retrofit analysis. Future self-cooled motors and generators for flight applications have been estimated by NASA to have a max continuous power in the 1-2.5 MW class and a power density of 13-16 kW/kg and up to 99% efficiency in the 2035 time frame [95]. Power converters in this time frame have also been predicted by NASA to be able to achieve 19 kW/kg power density for 1 MW of maximum power. Future Superconducting motors and generators have also been predicted to have maximum shaft powers up to 35 MW and approximately 30 kW/kg power density for applications in the 2050 time frame, along with similar power densities for converters [73], although with less certainty. The assumed technology level for each case study shown in Chapter 6 will be stated.

The weight of the core, fan, and nacelles and nacelle drag are assumed to scale with updated mass flow rate requirements and fan diameter derived by Hall et al [87].

An initial guess for the mass flow rate difference between the conventional and retrofitted aircraft ($\Delta\dot{m}$) provides an initial guess for the hybrid electric aircraft mass flow rates:

$$\dot{m}_{core,hybrid} = \Delta\dot{m} + \dot{m}_{core,conventional} \quad (5.5)$$

$$\dot{m}_{core,hybrid} = \Delta\dot{m} + \dot{m}_{fan,conventional} \quad (5.6)$$

These mass flow rates and the power in the electrical system components provides the guessed increase in weight of the hybrid electric aircraft. The core, fan, and nacelle masses

as a function of core and fan mass flow rates are as follows, as implemented by Hall et al [87]:

$$m_{core,hybrid} = N_{cores}K_{core}(\dot{m}_{core,hybrid}^{1.2}), K_{core} = 45.6 \frac{kg}{(kg/s)^{1.2}} \quad (5.7)$$

$$m_{fan,hybrid} = N_{fans}K_{fan}(\dot{m}_{fan,hybrid}^{1.2}), K_{fan} = 1.3 \frac{kg}{(kg/s)^{1.2}} \quad (5.8)$$

$$m_{nacelle,hybrid} = N_{fans}K_{nacelle}(\dot{m}_{fan,hybrid}), K_{nacelle} = 4.56 \frac{kg}{(kg/s)} \quad (5.9)$$

The electrical system mass is obtained from the power to mass ratios of the electrical components for whichever technology level is assumed:

$$\begin{aligned} m_{electricalsystem,hybrid} = & m_{battery} + P_{generator}/\left(\frac{P}{mass}\eta_{generator}\right) \\ & + P_{inverter}/\left(\frac{P}{mass}\eta_{inverter}\right) + P_{rectifier}/\left(\frac{P}{mass}\eta_{rectifier}\right) \\ & + P_{motor}/\left(\frac{P}{mass}\eta_{motor}\right) \end{aligned} \quad (5.10)$$

It was assumed that the excess power generated during windmilling could be extracted into a resistor or dump battery (The excess power generated during windmilling was outputted from blade element theory described in section 5.1.2). For sizing the retrofit hybrid electric aircraft, the maximum power generated during windmilling was used to size a dump battery. The dump battery was assumed to have a battery specific power (BSP), or maximum power available per unit mass, of 2,700 W/kg, as was implemented by Hall et al [87]. Thus the weight of the dump battery was determined by equation 5.11, assuming there is an additional rectifier to convert the AC power of the electric motor (now acting as a generator) into DC power for the battery:

$$m_{battery} = P_{windmilling}/BSP + P_{windmilling}/\left(\frac{P}{mass}\eta_{rectifier}\right) \quad (5.11)$$

Thus the hybrid electric aircraft weight is obtained, enabling fan area to be obtained from equation 5.3 given the conventional aircraft weight and fan area.

Induced drag of the hybrid electric aircraft is also obtained from the expected lift

coefficient assuming the lift is equal to weight:

$$C_L = \frac{Weight_{hybrid}}{\frac{1}{2}\rho V_\infty^2 S_{ref}} \quad (5.12)$$

$$C_{D,i} = \frac{C_L^2}{\pi A Re} \quad (5.13)$$

The change in profile drag due to the change in nacelle size is obtained from the TASOPT nacelle sizing model [98]:

$$length_{nacelle,hybrid} = 0.15 r_{S_{nace}} d_{fan,hybrid} \quad (5.14)$$

$$Re_{nacelle,hybrid} = \frac{V_\infty length_{nacelle,hybrid}}{\nu} \quad (5.15)$$

$$C_{f,nacelle,hybrid} = \frac{0.074}{Re_{nacelle,hybrid}^{0.2}}; \quad (5.16)$$

$$C_{D,profile,nacelle,hybrid} = r_{V_{surf}^3} \frac{r_{S_{nace}} Area_{fan,hybrid}}{S_{wing}} C_{f,nacelle,hybrid}; \quad (5.17)$$

$r_{S_{nace}}$ is the nacelle wetted-to-flow area ratio assumption and $r_{V_{surf}^3}$ is the ratio of the nacelle local velocity to the freestream velocity.

The change in drag due to the hybrid electric system is used to obtain the ratio of drag between the hybrid electric aircraft and the conventional. This drag ratio, the electrical system power core to power out efficiency from equation 5.2, and the conventional aircraft core power gives the core power for the hybrid electric aircraft. The updated fan and core mass flow rates, which scale with the fan area and core power respectively, are then obtained. These are then used to update the weights using equations 5.7, 5.8, 5.9, and 5.10. If the updated weights equal the initial guess weights, the hybrid aircraft is sized. If they are not equal, the process is repeated with updated $\Delta(\dot{m})$ guesses for the fan and core, as shown in Figure 5-4.

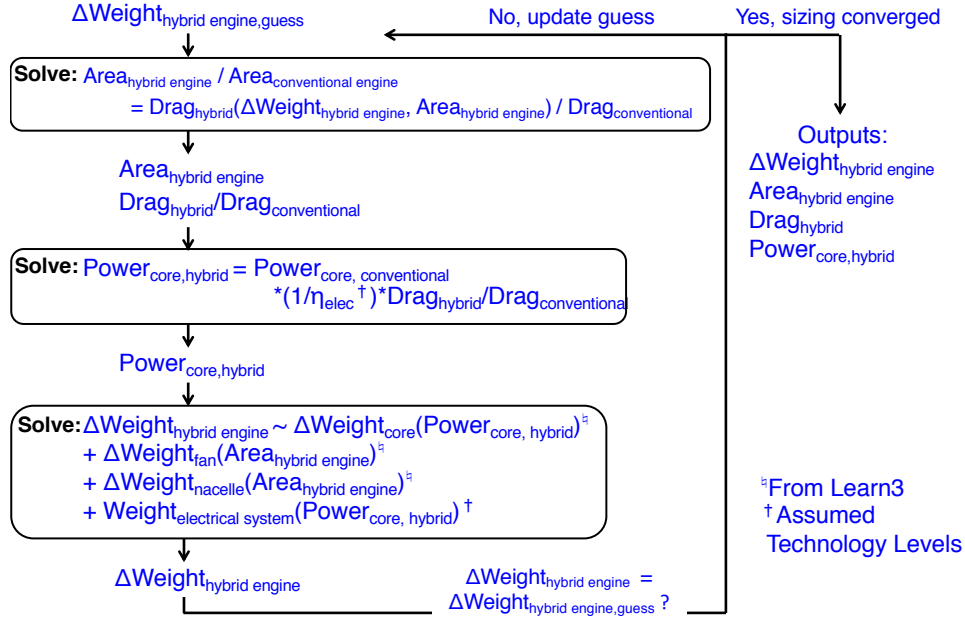


Figure 5-4: Retrofit Hybrid Electric Aircraft Sizing Loop given Input $Power_{core,conventional}$, $Drag_{conventional}$, $Area_{conventional}$ from TASOPT, Values Labeled with \ddagger from Hall et al [87] and \dagger from Technology Level Assumptions [95][73]

Given $Power_{core,hybrid}$, the internal operating states of the retrofitted aircraft required to obtain the noise of the turbo-generator components of the engine (jet and combustion) discussed in section 3.3.1 are obtained from the TASOPT-generated internal engine performance maps at the $Power_{core,hybrid}$ operating conditions.

5.1.2 Windmilling Engine Drag Model

As discussed in section 3.2, because TASOPT does not incorporate configuration drag (flaps, slats, and landing gear drag) modeling, BADA 4 is used to obtain configuration drag for existing aircraft.

For flight profile modeling of hybrid electric aircraft, sources of weight and drag that are not included within the BADA 4 database are modeled separately. These include drag increase estimates of windmilling engines and potential weight difference estimates of hybrid electric engine components compared to traditional gas-turbine engines. For an initial estimate, BADA 4 drag polars are used to model the drag of hybrid electric aircraft that have little changes in the external airframe compared to an existing aircraft to provide

a drag estimate when the aircraft is not windmilling. An estimate of windmilling drag is then added for instances of windmilling during a flight procedure.

One method for estimating the drag of windmilling ducted fans is by employing actuator disk theory. Actuator disk theory, also known as momentum theory, is a formulation for modeling the thrust and power of airflow impinging on an ideal rotor, ducted or open, by assuming the rotor face is an actuator disk that creates a discontinuity in the flow pressure field [120]. The conservation of linear momentum relates the thrust (or drag) of an engine as equal to the change in momentum of the airflow plus the change in exit pressure from the free stream within the control volume. This is diagrammed in Figure 5-5 for a duct of constant cross sectional area equal to the rotor disk area A_{disk} .

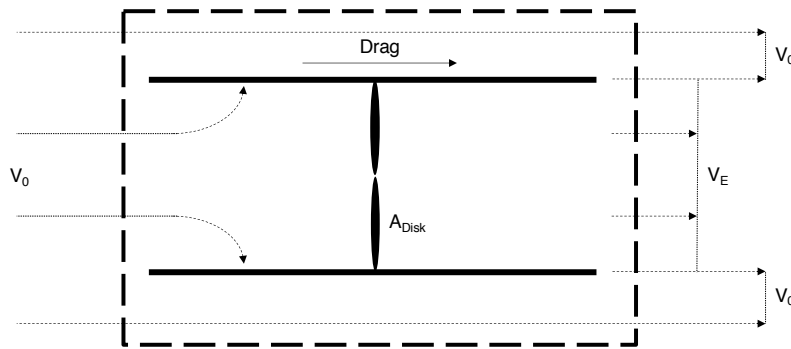


Figure 5-5: Actuator Disk Theory Diagram for a Simplified Ducted Fan

By assuming parallel streamlines and that the duct exit pressure is equal to the free stream pressure, and the exit velocity is uniform, the drag on a ducted fan submersed in a flow of velocity V_0 is:

$$Drag = \dot{m}(V_0 - V_E) \quad (5.18)$$

where \dot{m} is the mass flow rate inside the fan that is the product of the air density, the disk area, and the exit flow velocity:

$$\dot{m} = \rho A_{Disk} V_E \quad (5.19)$$

The drag coefficient of the ducted fan with respect to the disk area can be solved as:

$$C_{D_{Windmill, ActuatorDisk}} = \frac{Drag}{\frac{1}{2}\rho V_0^2 A_{Disk}} = \frac{\rho A_{Disk} V_E (V_0 - V_E)}{\frac{1}{2}\rho V_0^2 A_{Disk}} = 2\left(\frac{V_E}{V_0} - \left(\frac{V_E}{V_0}\right)^2\right) \quad (5.20)$$

Actuator disk theory thus shows that for a constant area duct, the maximum possible drag coefficient for this representation occurs when $V_E/V_0 = 0.5$ and is equal to 0.5.

This method is used for preliminary analysis of fan drag based on fan face area A_{Disk} , as applying requires simple inputs and does not require details about rotor blade geometry. However predictions of precise drag coefficients as functions of rotation rate of the rotor blades is not captured by this method.

For more precise drag modeling, given fan face area and blade and duct geometry is obtained, windmilling drag as a function of RPM is modeled using blade-element/vortex theory methods in XROTOR [121]. Blade-element/vortex theory involves computing thrust and torque of a rotor by dividing the blades into small radial segments, as shown in Figure 5-6 (a) and integrating the forces imparted on the blades by the air at each segment, shown in Figure 5-6 (b).

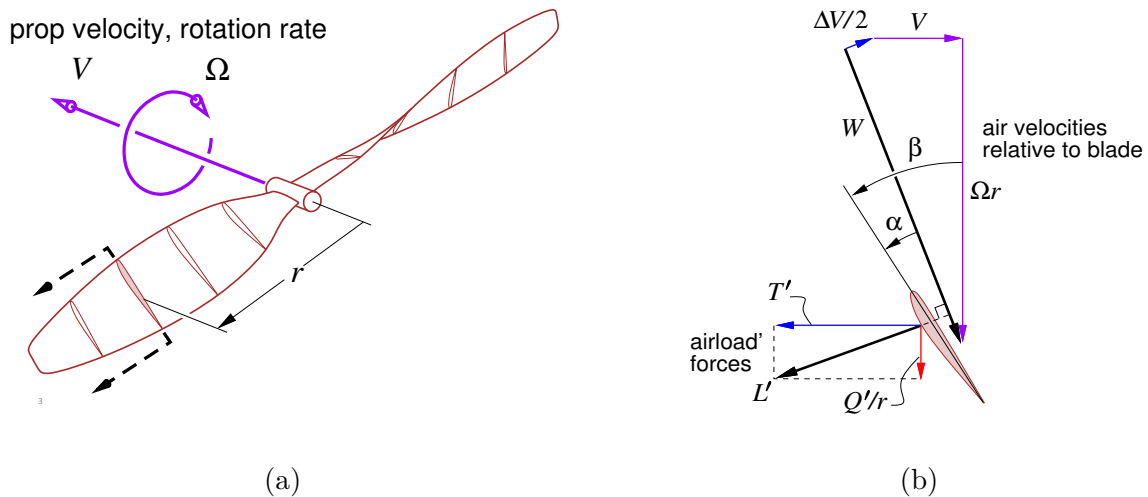


Figure 5-6: Blade Element Theory Diagram (a) and Force Vectors in a Blade Section Diagram (b), Figures from [122]

This theory is used to model the drag, power, and losses associated with ducted rotors as functions of RPM and flight velocity and requires detailed blade geometry and performance,

including blade count, angle distribution, and chord distribution and the lift and drag polars of the blade airfoils. If this information is not available, QPROP and XROTOR can be used to first design rotor geometries based on Minimum Induced Loss conditions and then be used to solve for the rotor off design performance. Results are sensitive the negative blade lift and drag coefficients that are expected during windmilling.

Within the framework shown in Figure 5-1, blade-element theory with XROTOR is utilized because it enables modeling windmilling drag as a function of fan RPM and thus a model of controlled drag. After obtaining blade geometry and airfoil polars, windmilling drag is obtained by modeling the fan performance at high enough advance ratios $\frac{V}{\Omega R}$, or low enough RPMs, that the resulting force on the blade sections have a negative direction.

5.2 Component-Based Aircraft Noise Module with Windmilling Fan Noise

The Component-Based Aircraft Noise Module is updated to include windmilling fan engine noise, shown in Figure 5-7. Gas generator source noise (core and jet) and fan source noise in normal operating conditions are modeled using ANOPP engine source noise models with the internal engine performance parameters from the retrofit hybrid aircraft. For engines operating in windmilling conditions, fan noise is modeled with the method described in section 5.2.1 while gas generator source noise (core and jet) is modeled ANOPP engine source noise models assuming the internal engine performance states are at idle thrust conditions.

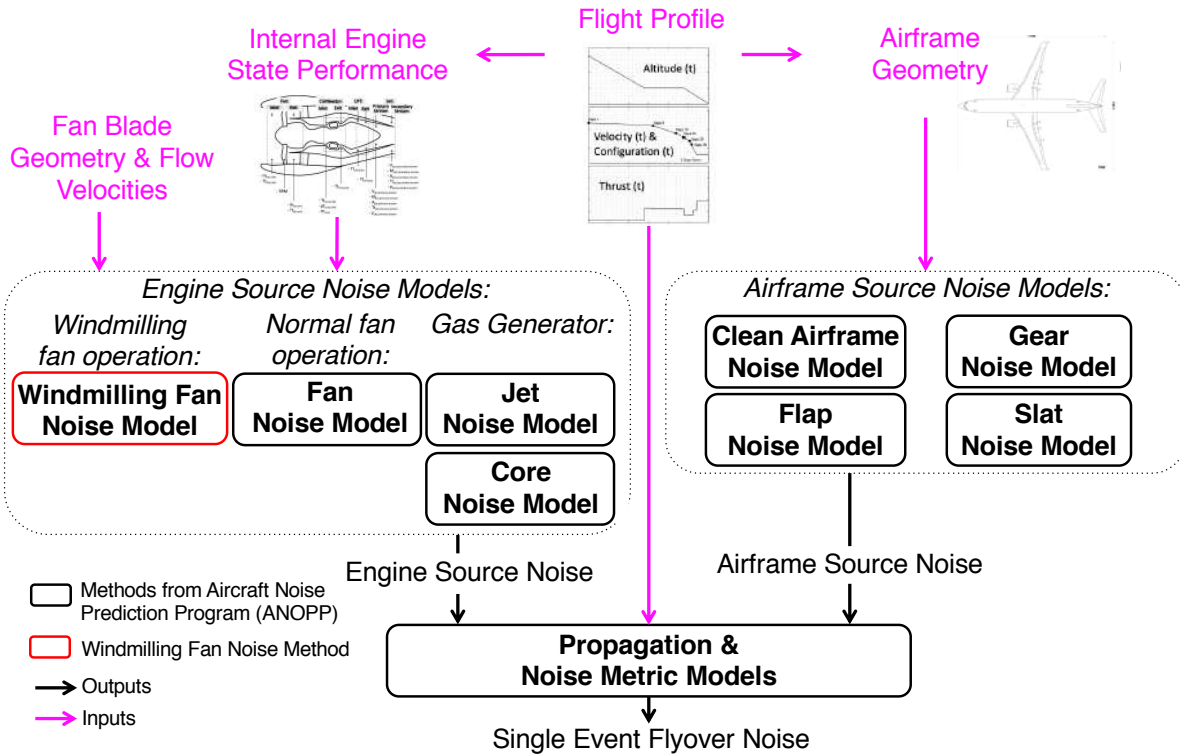


Figure 5-7: Component-Based Aircraft Noise Module, Including Windmilling Fan Noise

5.2.1 Windmilling Fan Noise Modeling

Noise sources that have not been previously included in the ANOPP model, such as fans in windmilling conditions, are added from an external method. The fan noise models within ANOPP are based on data correlations from engines operating near design conditions, suggesting that it is not an appropriate model for predicting noise of a windmilling fan. Instead, a model that enables fan noise modeling at the low RPMs typical of windmilling conditions is more appropriate, although may require a larger set of inputs.

Fan noise can be decomposed into broadband noise components, produced by turbulence interactions, and discrete tone noise components, attributed to lift and pressure fluctuations on either the rotor or stator blades that are periodic in time. Broadband noise components are summarized as follows:

- *Rotor-Wake Stator Interaction noise*, or noise generated by the interaction of stators with rotor wake turbulence created upstream [123], as represented in Figure 5-8.

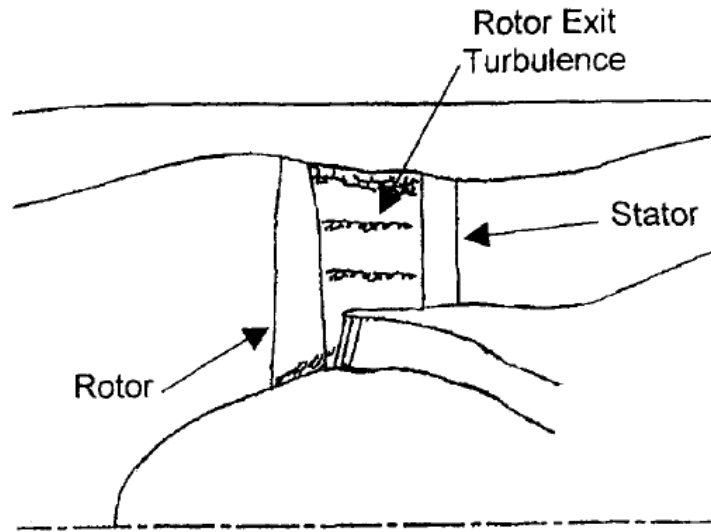


Figure 5-8: Representation of Noise Generation by Rotor Wake Turbulence Interacting with Stator, Figure from [124]

- *Self-noise*, or noise generated from the interaction of the turbulence in the blade boundary layer with the blade trailing edges [125], as represented in Figure 5-9.

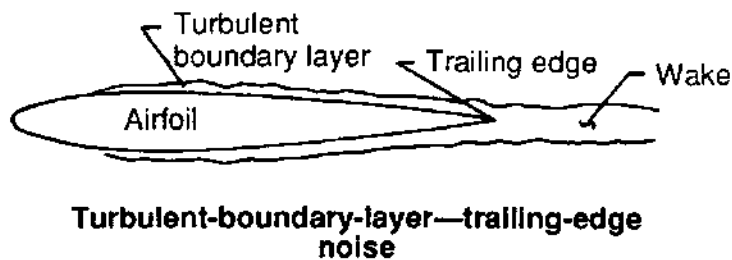


Figure 5-9: Blade Self Noise Representation, Figure from [126]

- *Tip/hub noise*, or noise generated by the additional interaction of the turbulent flow around the blades with the duct boundary layer and fan hub [125], as represented in Figure 5-10.

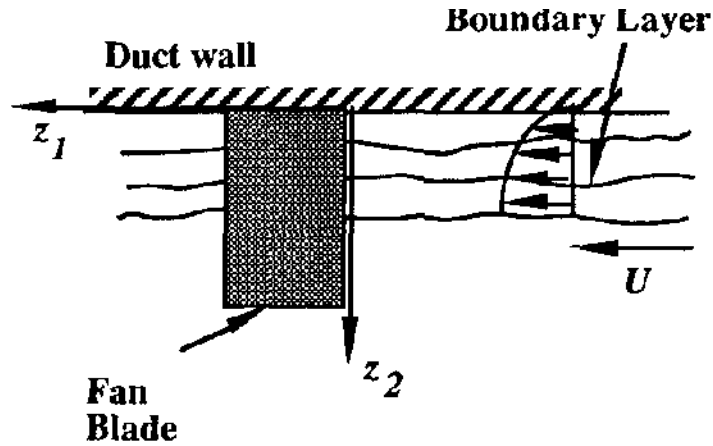


Figure 5-10: Representation of Duct Boundary Layer Interaction with Turbulence at Blade Tip, Figure from [125]

- *Stalling blade noise.* Because blades of rotors operating at the low RPMs typical of windmilling conditions may operate at very negative angles of attack, a noise mechanism that may be significant in windmilling fans is noise produced by the turbulence due to stalling blades [126], as represented in Figure 5-11.

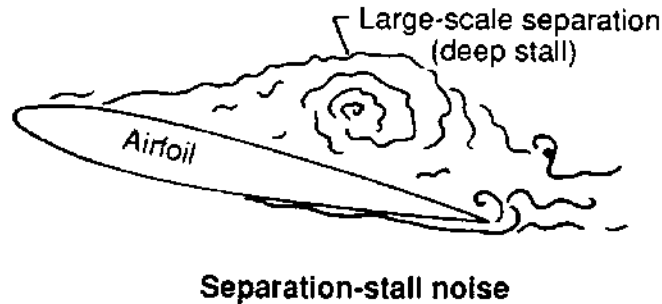


Figure 5-11: Representation of Stalling Blade Noise Mechanism, Figure from [126]

The methods for modeling each of these components in this framework are listed below.

For this method, **broadband fan noise** is modeled using the NASA Broadband Fan Noise Prediction System (BFaNS) [127], shown in Figure 5-12.

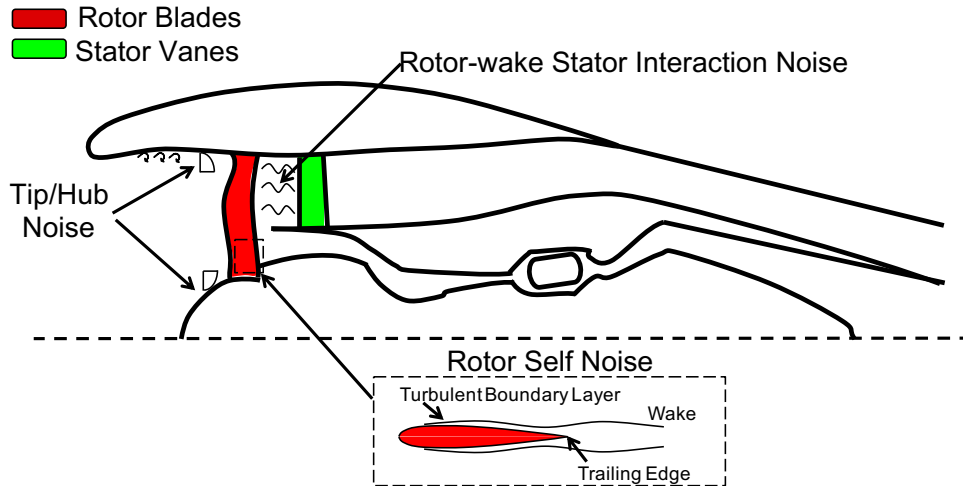


Figure 5-12: Broadband Fan Noise Components from BFANS used for Modeling Windmilling Fan Noise in Framework

BFaNS incorporates the expression by Hanson [124] for relating generated noise to inflow turbulence characteristics impinging on the rotor or stator and is dependent on the flow field and geometry characteristics. This theory is used to model tip/hub noise and rotor wake stator interaction noise. BFaNS also incorporates the method by Glegg [126] in order to model the broadband noise generated when boundary-layer turbulence convects past rotor and stator trailing edges. Thus BFANS is used in modeling broadband tip/hub noise, rotor self noise, and rotor wake stator interaction noise components in this framework. These models require detailed geometry of the blades, vanes, hub, and duct as well as the flow field characteristics and are divided as follows:

- **Rotor/stator turbulence interaction noise** and **tip/hub turbulent wake interaction noise**: the noise produced by the turbulent wakes produced by the rotor impacting the flow field of the stator is modeled assuming a random upwash from the rotor wakes impinges on the stator vanes. The noise produced by the contributing turbulence due to the duct and hub boundary layer on the rotor blades and stator vanes is modeled similarly. In BFANS, Glegg’s harmonic cascade theory for the noise response of incoming gusts on a cascade [128] is used with an update by Hanson [124] to account for the effects of lean and sweep in the blade geometry.

The blade and stator geometry is required for this method, including the blade twist

distribution, chord, span, number of blades, rotor-stator spacing, and duct geometry. The flow velocity triangles and pressure at the leading and trailing edges of the rotor blades and stator vanes is also required for this method.

The flow turbulence (defined by turbulent velocity and length scales) impacting the blades/vanes, divided into turbulent bands along the blade/vane radii, is also required for this method. The methodology for obtaining the turbulence characteristics in the rotor wake and duct boundary layer are as follows:

- Rotor Wake: In BFANS, the turbulence in the rotor wake impinging on the stator vanes is based on the correlations by Wygnanski et al [129], where the wake velocity defect ΔW , wake thickness δ_w , and wake turbulence $w'w'$ are given by equations 5.21, 5.22, 5.23:

$$\Delta W = \sqrt{\left(\frac{K_0|\vec{W}|^2\delta_2}{s - K_1\delta_2}\right)} \quad (5.21)$$

$$\delta_w = 2\sqrt{K_2^2\delta_2(s - K_1\delta_2)} \quad (5.22)$$

$$w'w' = K_3(\Delta W)^2 \quad (5.23)$$

In BFANS, the constants in these equations correspond to a symmetric airfoil. s is the streamwise distance downstream from the rotor trailing edges. $\frac{\delta_2}{b}$ is the momentum thickness, derived from cascade data from [130], and is a function of the dimensionless UR Lieblein diffusion factor D_f given by equation 5.24:

$$\frac{\delta_2}{b} = 0.006 + 0.0002e^{7.5D_f-1} \quad (5.24)$$

The turbulent length scale Λ of the wake is assumed proportional to the wake thickness δ_w as:

$$\Lambda = C\delta_w, C = 0.68 \quad (5.25)$$

which is based on the methodology by Glegg [123], who used a Von Karman type turbulence spectrum.

- Duct Boundary Layer: for modeling the tip/hub boundary layer interaction noise in BFANS, the duct and hub is assumed to have a turbulent flat plate boundary layer, and thus the boundary layer is assumed to be given by equation 5.26:

$$\delta = 0.37LR_L^{-\frac{1}{5}} \quad (5.26)$$

where the Reynolds number R_L is given by:

$$R_L = \frac{U_\infty L}{\nu} \quad (5.27)$$

where L is measured at the start of the duct and hub tip. The average turbulence intensity in the flat plate boundary layer is assumed to be 5% of the free-stream velocity based on turbulence profiles given in [131].

The turbulent length scale Λ of the boundary layer is assumed proportional to the boundary layer thickness δ as:

$$\Lambda = C\delta, C = 0.62 \quad (5.28)$$

which is based on the methodology by Glegg [123], who used a Von Karman type turbulence spectrum.

- **Self-noise:** rotor trailing edge boundary layer interaction noise is modeled based on an experimental database of isolated NACA 0012 airfoils [126]. This database is used to estimate the generated noise spectrum for a given airfoil based on Mach number, Reynolds Number, and angle of attack. The noise generated was shown to scale with the boundary layer thickness and velocity to the fifth power. For blades in a cascade, the self-noise component also includes the turbulent flow noise generated by more than one trailing edge. Thus a correction by Glegg [132] to account for the superposition of adjacent blades is also applied.

Regarding **stalling blade noise**; the models above do not provide methods for

modeling stalling blades. In lieu of this limitation, the literature gives an estimate of the approximate noise contribution magnitude from stalling blades. Several sources indicate from measurement that stalling blades may result in approximately an additional 10 dB to the total rotor noise [68] [126] [133].

Discrete tone noise of turbofans is attributed to lift fluctuations on either the rotor or stator blades that are periodic in time. The lift fluctuations generally originate from static pressure field modulations when a rotor chops an incoming wake or, as diagrammed in Figure 5-13, when the wakes and associating velocity and pressure fluctuations from the rotor impinge on the stator blades [36]. These pressure fluctuations form spinning pressure patterns, or duct modes, which either propagate to the far field or are coupled with destructive phase and amplitude matching from other modes and thus decay in the duct [134]. The aggregate of modes that propagate to the far field form the far-field tone noise. As argued in section 5.4.3, the impacts of tone noise for windmilling fans is expected to be negligible compared to the broadband noise components and thus only the broadband component of windmilling fan noise is considered in this thesis.

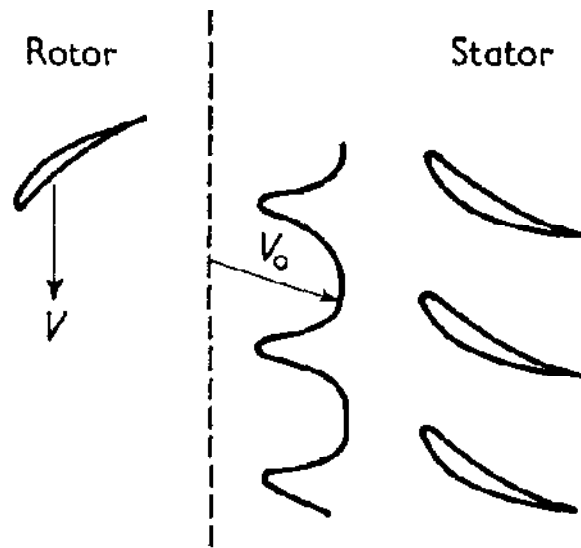


Figure 5-13: Effect of Rotor Flow on Stator, Figure adapted from [135]

Windmilling Fan Noise Modeling Inputs

Noise modeling of the windmilling fan components requires the blade, rotor, and duct geometry as well as the axial, radial, and tangential velocity components and pressures at

the leading and trailing edges of the rotors and stators. Given geometry of an existing ducted fan or one designed in XROTOR, as well as the operating RPM for the desired windmilling drag from XROTOR, the Ducted Fan Design Code (DFDC) [136] is used to obtain the flow field properties. These flow field properties, along with the duct and blade geometries of the fan, become the inputs into the broadband fan noise model, as diagrammed in Figure 5-14.

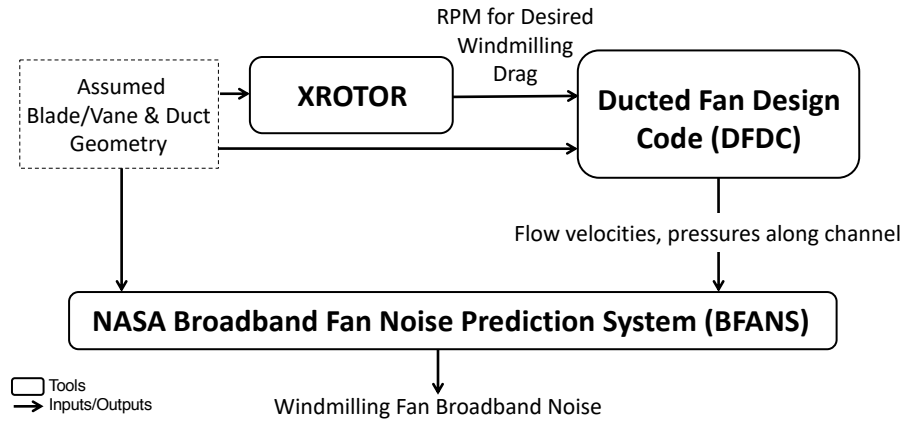


Figure 5-14: Flow Chart for Modeling Windmilling Fan Noise

In the DFDC method shown in Figure 5-15, induced velocities in the duct associated with the loading of the rotor blades are represented by vortex sheets of strength γ shed into the flow field. Loading and profile drag/viscous loss characteristics of the blade rows are determined with blade element theory. The viscous losses in the duct are represented by source sheets with the source strength σ obtained from the drag of the blades. These loading and loss effects are used in determining the flow fields in the duct.

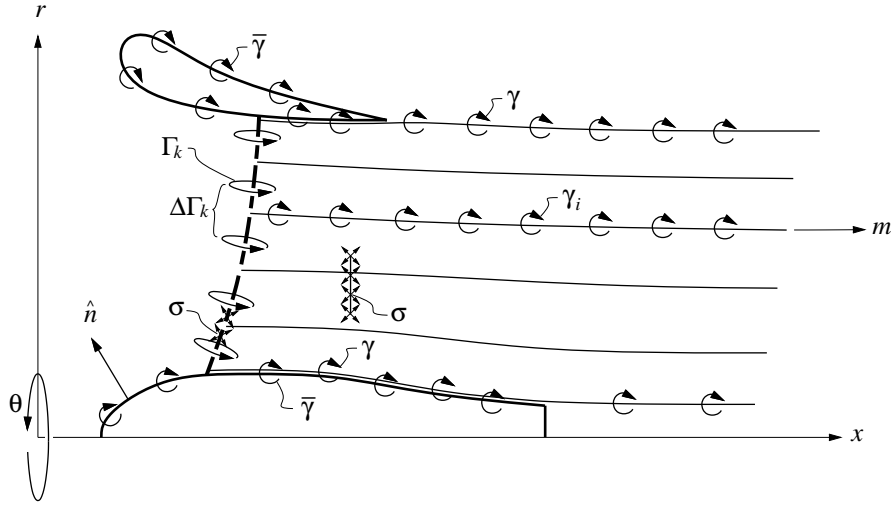


Figure 5-15: Ducted Fan Design Code method, Figure from [136]

Finally, total pressure p_o at any point in the duct is assumed equal to the freestream total pressure $p_{o\infty}$ plus any work and loss contributions \tilde{H} and \tilde{S} across the rotor or stator row and are obtained from equation 5.29:

$$p_o = p_{o\infty} + \rho(\tilde{H} - \tilde{S}) \quad (5.29)$$

where \tilde{H} is the cumulative enthalpy jump across disks given as a function of the rotation rate Ω and number of blades B by:

$$\Delta H_{disk} = \frac{\Omega B \Gamma}{2\pi}, \tilde{H} = \sum \Delta H_{disk} \quad (5.30)$$

and \tilde{S} is the cumulative entropy jump across disks given as a function of the mean velocity out the rotor V and friction drag C_f of the disk by:

$$\Delta S_{disk} = \frac{1}{2} V^2 C_f, \tilde{S} = \sum \Delta S_{disk} \quad (5.31)$$

5.3 Validation of Windmilling Engine Drag Coefficients

To determine the validity of Windmilling fan drag obtained when using the framework described in section 5.2.1, drag results were modeled for a representative CFM56-7B turbofan engine used on Boeing 737-800 aircraft and were compared with actuator disk theory and existing windmilling drag data.

To model the drag of the example fan with blade element theory in XROTOR, representative fan blade geometry was obtained by measuring the blades of an available CFM56-3 engine, pictured in 5-16. Engine thrust and drag values are expected to vary with the blade chord/blade radius and blade angle with radial location and therefore the modeled performance obtained from this geometry are compared to CFM56-7B engine performance and existing windmilling drag data for validation.



Figure 5-16: CFM56-3 Engine

The blade count was adjusted to the blade count of a CFM56-7B engine as was provided

in Janes [100]. Fan diameter was also scaled to represent the CFM56-7B engine diameter while maintaining constant blade chord/blade radius and blade angle with radial location. NACA 0012 airfoils were assumed, to be consistent the airfoils used for the development of the BFANS rotor self noise model. Finally, the blade angle distribution was adjusted in XROTOR such that, at an RPM of 3,000 and at a standard approach velocity of $V_{REF} + 10$ knots, a thrust of 5,000 lbs per engine was obtained. This operating condition corresponds to a standard final approach operating condition, with the RPM corresponding to this thrust and velocity obtained from the TASOPT engine state tables for this engine.

The final blade geometry is shown in Table 5.1.

Table 5.1: CFM56 Blade Geometry used in Blade Element Theory Model

Radial Location/Fan Radius	Blade Chord/Fan Radius	Blade Angle ($^{\circ}$)
0.41	0.15	60.0
0.48	0.15	56.6
0.56	0.17	52.4
0.65	0.17	48.4
0.74	0.18	44.4
0.83	0.19	41.1
0.90	0.19	38.4
0.95	0.20	36.1
0.99	0.21	34.8
1.00	0.21	34.1

For the representative windmilling operating condition, RPM was slowed until the rotor tip approached the maximum lift coefficient for this airfoil, or just before stall. This was chosen as the minimum RPM criteria because as mentioned in section 5.2.1, stalling blades have the potential to incur up to 10 dB of additional fan noise, which is undesirable. This criteria set the RPM for the maximum windmilling drag to be just before blade stall. XROTOR outputs for this representative windmilling case are shown in Figure 5-17.

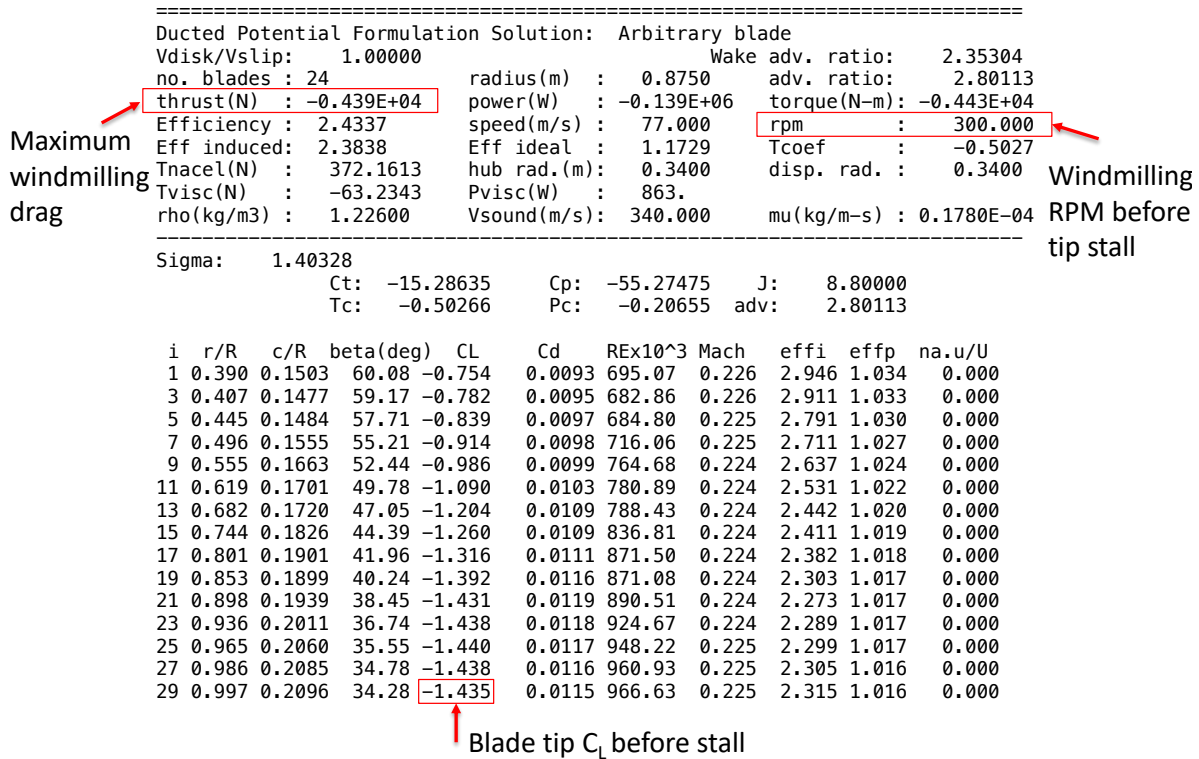


Figure 5-17: XROTOR Outputs for Modeled CFM56-7B-Size Engine at the Maximum Windmilling Drag Operating Condition

XROTOR results shown in Figure 5-17 indicate that the maximum windmilling drag for this engine is about 4390 Newtons/engine, or 986 lbs/engine and a drag coefficient of 0.5 with respect to area of the engine face. This is consistent with actuator disk theory, which predicts a maximum drag coefficient of 0.5 with respect to area of the engine face, as discussed in section 5.1.2.

Additionally, the XROTOR prediction of a drag coefficient of 0.5 with respect to area of the engine face was compared to existing data of windmilling engines shown in figures 5-18 (a) and (b), taken from *Gas Turbine Performance, 2nd Ed* [137]. Figure 5-18 (a) shows drag coefficients for windmilling engines versus takeoff specific thrust of turbofan and turbojet engines, while 5-18 (b) shows empirically derived additional drag coefficient due to flight mach number versus takeoff specific thrust. The total drag coefficient is the sum of these two components.

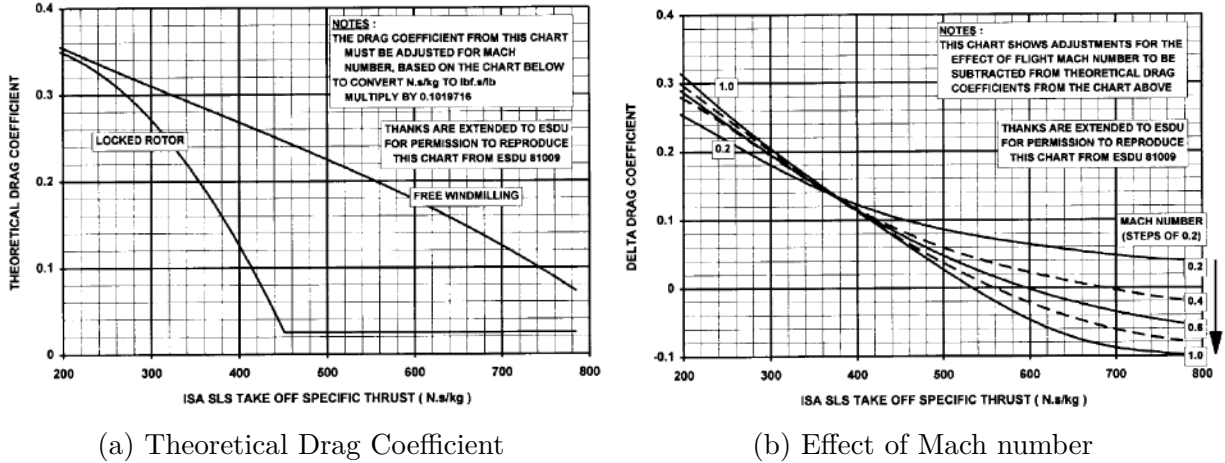


Figure 5-18: Turbojet and Turbofan Windmilling: Internal Drag Coefficient versus Specific Thrust and Mach Number; Figures from *Gas Turbine Performance, 2nd Ed* [137]

For a Boeing 737-800 with CFM56-7B engines, TASOPT engine state tables indicate a specific thrust of approximately 250 Ns/kg. At this specific thrust and at $V_{REF} + 10$ knots for an approach condition, Figures 5-18 (a) and (b) predict a theoretical and delta drag coefficient of approximately 0.33 and 0.21 respectively, or a total drag coefficient of 0.54. The XROTOR prediction is close to this data, albeit more conservative.

5.4 Validation of Fan Noise Model Adapted for Windmilling

To determine the validity of using the fan noise model described in section 5.2.1 for modeling windmilling fan noise, results were obtained from the model for the CFM56-7B-sized engine described in section 5.3 and were compared with available data at both standard approach and windmilling operating conditions.

5.4.1 Broadband Fan Noise Model Compared to ANOPP Fan Noise Module at Standard Approach Operating Conditions

Results obtained with the ANOPP fan noise module at various standard approach operating conditions were obtained and are compared to the framework fan model for windmilling

engines.

As input for the BFANS noise model, the flow velocities at the rotor and stator leading and trailing edges were obtained using DFDC as described in section 5.2.1. The representative duct and hub airfoil shape coordinates were based on available duct and hub airfoil coordinates from a NASA TN-3122 test report [138]. The duct and hub airfoil coordinates were scaled such that their thickness-to-fan diameter ratios, as well as the axial location of the rotor and stator vanes along the channel, were that of the nacelle geometry of the CFM56-7B as obtained in Janes [100]. The final geometry is shown in Figure 5-19.

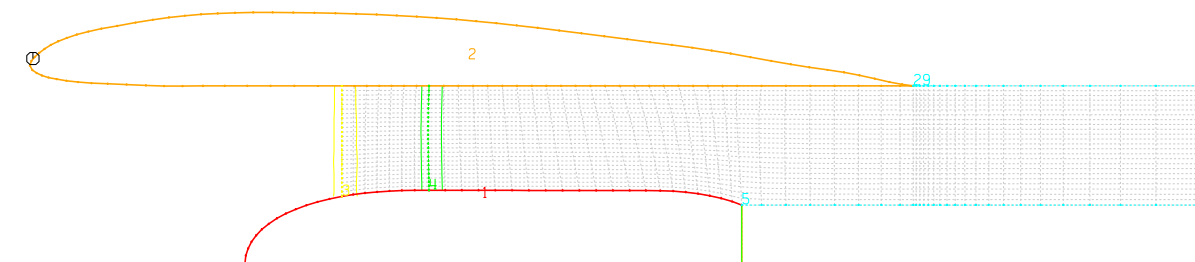


Figure 5-19: Assumed Duct and Hub Geometry used in DFDC to Obtain CFM56-7B Flow Velocities at the Rotor/Stator Leading and Trailing Edges

Broadband fan noise was obtained for four approach thrust conditions that correspond to the fan RPMs shown in Table 5.2 at a flight velocity of $V_{REF} + 10$ knots, based on the TASOPT engine state tables for the CFM56-7B engine. Overflight noise for a single engine was obtained with both ANOPP and the BFANS noise model at these RPMs and flight velocity at a simulated 120 m altitude observer. Table 5.2 also lists the $L_{A,MAX}$ noise outputs from both models.

Table 5.2: Overflight Noise Outputs of ANOPP and BFANS for a Representative CFM56-7B Engine at Altitude 120m

Fan Operating Condition		ANOPP Fan Noise Outputs	BFANS Fan Noise Outputs
Thrust/engine (lbs)	RPM	Broadband ($L_{A,MAX}$)	Broadband ($L_{A,MAX}$)
500	1600	67.70	68.05
1000	1900	71.04	71.52
3000	2500	77.90	78.03
5000	3000	81.66	81.31

Results from both models agree with each other at these operating conditions to within 0.5 dB or less, indicating consistency for modeling broadband fan approach noise between these two models.

5.4.2 Fan Noise Model Compared to Existing Data at Windmilling Conditions

Results obtained with the framework fan noise model was also compared with existing data to verify noise levels obtained on the component level and for noise levels obtained in windmilling conditions.

Existing fan noise data at the component level available in the literature is compared with component level noise obtained from the BFANS model for the representative CFM56-7B engine. The existing data is component level noise data obtained from a series of tests to examine the broadband fan noise of a Boeing 18 in fan rig, conducted in the Boeing Low-Speed Aeroacoustics Facility (LSAF) [71]. While the geometry of the Boeing 18 in fan is different from the representative CFM56-7B engine and thus the total noise levels are expected to be different, the data can be used to show the various noise component magnitudes relative to each other. Figure 5-20 shows an example comparison of component levels both from the Boeing test data in (a) and for the modeled representative CFM56-7B engine in (b). The conditions shown in the Boeing test data are for 55 percent RPM and the conditions modeled for the representative CFM56-7B engine were 60 percent RPM and a flight velocity of $V_{REF} + 10$ knots.

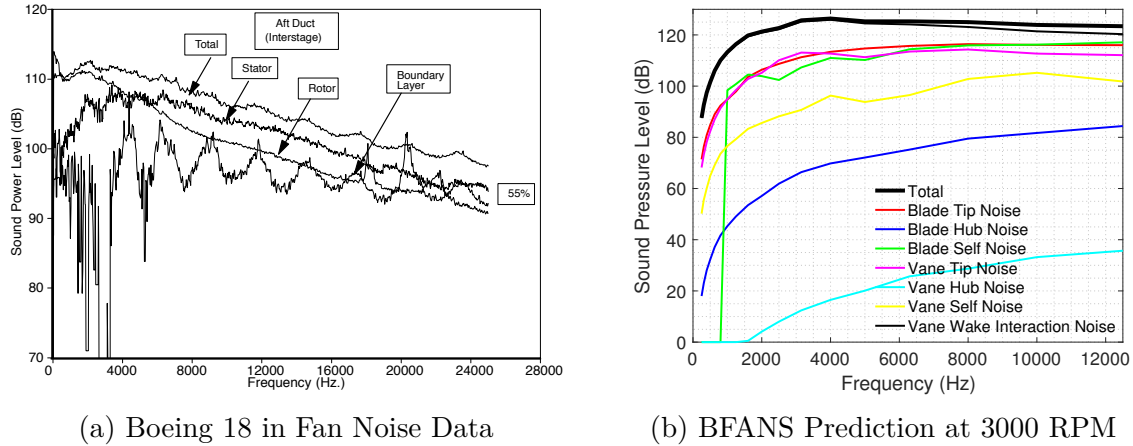


Figure 5-20: Fan Noise Component Breakdown Comparison between Boeing 18 in Fan Noise Data and Modeled CFM56-7B Engine; Figure (a) from [71]

The noise component data shown in the Boeing test data of Figure 5-20 (a) was broken into rotor self noise, rotor tip boundary layer noise, and net stator noise, which includes the stator interaction with the rotor wake. It was speculated in the Boeing 18 in fan test report [71] that the rise in the rotor and total noise at low frequencies was due to residual noise from the test rig. For frequencies above 5 kHz, where the low-frequency noise floor was not significant, some key takeaways from the data in Figure 5-20 (a) are that the noise is dominated by the stator interaction noise with the rotor wake followed by the rotor self noise and tip boundary layer noise, and that the boundary layer noise oscillates with frequency.

The modeled representative CFM56-7B shown Figure 5-20 (b) also shows the dominant noise component is the rotor stator interaction noise, which is consistent with the Boeing 18 in fan data and a main driver of the total noise results. The spectral oscillations in the tip boundary layer noise are not present in the modeled results. It is shown in [139] that these spectral oscillations in the tip boundary layer interaction noise occur as a result of the turbulence in the duct boundary layer being anisotropic. The framework model assumes isotropic turbulence, and thus this effect is not reflected in the fan broadband noise results.

The data from the Boeing 18 in fan test is also used to examine expected windmilling fan noise magnitude compared to standard approach operating conditions. Figure 5-21 (a) contains noise measurements of the engine at various operating conditions, including a windmilling operating condition compared to a 55 percent fan speed operating condition. As

a comparison, Figure 5-21 (b) shows the component noise breakdown of the representative CFM56-7B engine operating at the windmilling condition of 300 RPM derived in section 5.3, overlaid on the total noise obtained during the 3,000 RPM operating condition.

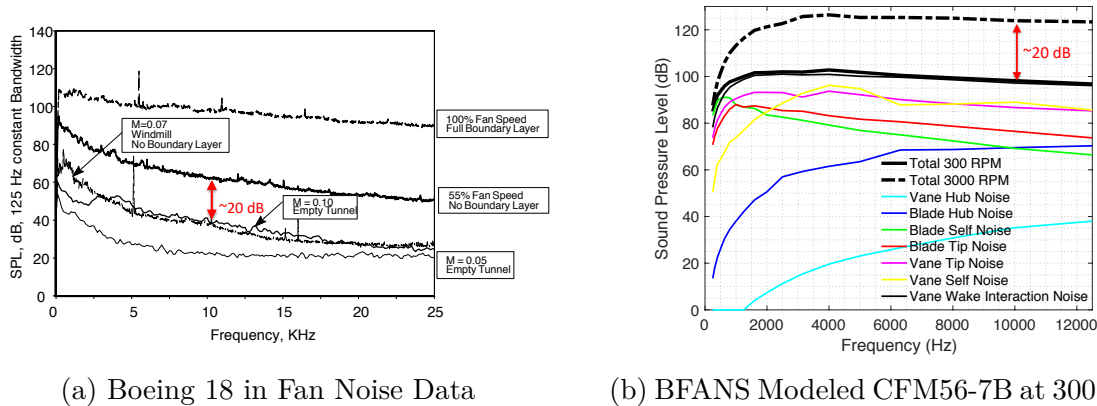


Figure 5-21: Comparison of Fan Noise During an Approach Condition versus Windmilling for Boeing 18 in Fan Noise Data and Modeled CFM56-7B engine; Figure (a) from [71]

While the fan geometry and operating conditions are not equivalent between these two cases, the data and modeled results shown in Figures 5-21 (a) and (b) indicate that windmilling fan broadband noise is approximately 20 dB below fan noise at standard approach conditions across the spectra. This is despite the differences in geometry in these cases. The difference in noise level between the modeled representative CFM56-7B at windmilling conditions and standard approach conditions is similar to the difference in noise level between the measured Boeing 18 in fan noise at windmilling and standard approach conditions.

5.4.3 Windmilling Fan Tone Noise

The impacts of tone noise for windmilling fans is expected to be negligible compared to the windmilling fan broadband components. To demonstrate this, the ANOPP fan noise module was used to model expected tone noise at the standard approach operating conditions from Table 5.2. The model included assumed fan tone noise liner treatment using fan inlet and fan exhaust suppression models based on four commercial engine databases [140]. The ANOPP broadband and tone noise results for these conditions are shown in Table 5.3.

Table 5.3: Broadband versus Tone Overflight Noise Outputs of ANOPP for a Representative CFM56-7B Engine at Altitude 120m

Fan Operating Condition		ANOPP Fan Noise Outputs	
Thrust/engine (lbs)	RPM	Broadband ($L_{A,Max}$)	Tonal ($L_{A,Max}$)
500	1600	67.70	57.41
1000	1900	71.04	60.71
3000	2500	77.90	67.82
5000	3000	81.66	71.66

The results in Table 5.3 show the fan tone noise is on average approximately 10 dB below the broadband noise on approach. Besides liner treatment, including lean and sweep in stator vane design has also been referenced as strategies to mitigate rotor stator interaction tones by increasing the variation in the phase of the rotor wakes interacting with the stators, thus causing more mode cancellation and fewer tones propagating to the far field [124][141]. These are thus potential design considerations that can be implemented to mitigate rotor-stator interaction tones. Thus, only broadband noise is modeled for windmilling fans in the remaining analyses.

Chapter 6

Case Studies of Advanced Operational Flight Procedures Performed by Hybrid Electric Aircraft with Windmilling Engine Drag

In this chapter, the framework presented in Chapter 5 is used to evaluate the approach noise impact of utilizing windmilling drag on approach by a representative hybrid electric aircraft. The representative hybrid electric aircraft is the Boeing 737-800 retrofitted for turboelectric engines.

The windmilling drag can be used to increase both the descent angle and deceleration rate during approach procedures. Both of these have been shown in Chapter 4 to reduce approach noise and the addition of windmilling drag enables flying these procedures in performance regimes beyond that of standard gas turbine aircraft. Thus to show the potential benefits of windmilling drag when applied to advanced approach procedures, the noise impacts are shown for the following three case studies:

- A steeper Approach with Windmilling Drag
- A Delayed Deceleration Approach with Windmilling Drag

- A Combined Delayed Deceleration Steeper Approach with Windmilling Drag

For each of these case studies, the hybrid electric aircraft utilizing windmilling drag is compared to a Boeing 737-800 performing a standard 3° continuous descent approach procedure with a standard deceleration rate.

6.1 Hybrid Electric Engine Retrofit Sizing Results

Given the framework for analyzing community noise impacts of advanced operational flight procedures described in Chapter 5, the use of windmilling drag on approach by hybrid electric aircraft for community noise reduction is analyzed. Hybrid electric aircraft example impacts is examined against performance of conventional turbofan aircraft.

For this thesis, the Boeing 737-800 aircraft with CFM56-7B engines is the aircraft for which its performance and noise impacts are the basis for comparison. The initial conditions, or characteristics of this aircraft that are relevant to the retrofit process, were assumed to be the conditions at takeoff obtained from TASOPT, which are:

$$\dot{m}_{core,conventional} = 51 \text{ kg/s (at takeoff)}$$

$$\dot{m}_{fan,conventional} = 223 \text{ kg/s (at takeoff)}$$

$$\text{Weight}_{fan,conventional} = 1,035 \text{ lbs/engine}$$

$$\text{Weight}_{core,conventional} = 4,500 \text{ lbs/engine}$$

$$\text{Weight}_{nacelle,conventional} = 1,360 \text{ lbs/engine}$$

$$\text{Weight}_{takeoff,conventional} = 171,660 \text{ lbs}$$

$$\text{Diameter}_{fan,conventional} = 63 \text{ in/engine}$$

$$C_{D,Takeoff,conventional} = 0.0731$$

$$\text{Velocity}_{Takeoff} = 176 \text{ knots}$$

$$\text{Power}_{core,Takeoff,conventional} = 10,250 \text{ kW/engine (at takeoff)}$$

Given these initial conditions, two retrofit hybrid electric aircraft were sized with the process given in Figure 5-4 using the self-cooled, 2035 timeframe technology level and superconducting, 2050 timeframe technology level introduced in Chapter 2 and summarized in Table 6.1. The maximum continuous motor output power available for the takeoff

condition and the power density and efficiencies for the generator, motor, rectifier, and inverters are indicated.

Table 6.1: Hybrid Retrofit Technology Level Assumptions

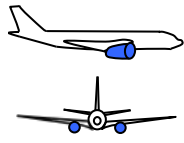
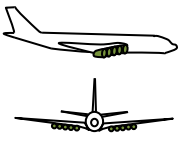
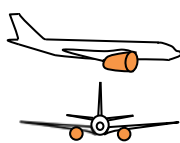
	Current State of the Art	Self-Cooled Prediction (2035 Timeframe)	Superconducting+Refrigeration Prediction (2050 Timeframe)
Max Continuous Power _{Gen/Motor} (MW)	0.2	2.5	35 (predicted)
Power Density _{Gen/Motor} (kW/kg)	2	13-16	~30
Power Density _{Inv/Rect} (kW/kg)	2.2	19	~30
$\eta_{Gen/Motor}$	0.95	0.99	0.99
$\eta_{Inv/Rect}$	0.95	0.99	0.99

For both cases, the engine configuration was assumed to be turboelectric with one gas generator core per wing supplying power to an electric generator which would supply electrical power to respective motors. The number of motors (and subsequently, the number of fans) for each case was determined to be the smallest number motors needed to produce the approximately 20 MW of total output power required on takeoff and constrained by the maximum continuous motor power available at the expected technology levels. For the self-cooled, 2035 timeframe, the retrofit aircraft was thus selected to have a minimum of 10 distributed total motors/fans, each producing 2MW of maximum power to meet the requirements with margin. For the superconducting, 2050 timeframe, the power requirements could be met with two motors, one for each wing.

It was assumed that the excess power generated during windmilling could be extracted into a resistor or dump battery. For sizing the retrofit hybrid electric aircraft, the maximum power generated during windmilling, which was outputted from XROTOR, was used to size a dump battery. The dump battery was assumed to have a battery specific power (BSP), or maximum power available per unit mass, of 2,700 W/kg, as was implemented by Hall et al [87]. This value was determined by fixing the ratio of battery specific energy (BSE) to BSP at the value for NASA's X-57 Maxwell batteries [142] and assuming the BSE of Li-S battery chemistry of 900 Wh/kg, as was implemented by Hall et al [87].

The details of the converged, retrofitted, hybrid electric aircraft, compared to the conventional aircraft are given in Table 6.2. Additional details about the weight assumptions of the resized components, as well as the assumption for the increase in drag, were given in section 5.1.1.

Table 6.2: Boeing 737-800 Retrofit Results Assuming Maintained Mission Range and Velocity, Airframe Geometry, at Different Technology Levels

	B738 Conventional Turboprop Aircraft	B738 “Turbo Electric” Retrofit 2MW Self-Cooled Motors	B738 “Turbo Electric” Retrofit 10MW Superconducting Motors
			
MTOW (lbs)	171,660	189,000	180,600
# Cores (total)	2	2	2
# Fans (total)	2	10	2
Fan Diameter (in)	63	30.2	65.4
$C_{D,Takeoff}$	0.0731	0.0843	0.0788
Weight _{fan} (lbs/wing)	1,035	880	1,100
Weight _{core} (lbs/wing)	4,500	5,500	5,110
Weight _{nacelles} (lbs/wing)	1,360	1,500	1,400
Weight _{motor} (lbs/wing)	–	2,000	800
Weight _{generator} (lbs/wing)	–	2,100	820
Weight _{rectifier} (lbs/wing)	–	1,420	650
Weight _{inverter} (lbs/wing)	–	1,400	630
Weight _{dumpbatt} (lbs/wing)	–	455	700
η_{elec}	–	0.96	0.96

The addition of the electric components and their efficiencies results in the retrofit aircraft for both technology levels being heavier and draggier. This result shows that a pure retrofit of an existing airframe for hybrid electric engines is not beneficial from an energy standpoint. However, the retrofit hybrid electric aircraft from these results can be used to demonstrate the potential benefits of using windmilling hybrid electric engines for noise abatement on approach.

6.2 Windmilling Engine Noise versus Drag of Retrofit Hybrid Electric Aircraft

The fans of both the distributed propulsion, 5 engine per wing retrofit hybrid electric aircraft and the 1 supercooled engine per wing retrofit hybrid electric aircraft were modeled in XROTOR to determine the maximum windmilling drag possible for each configuration. The fan rotor and stator chord/radius and blade angle/radius distribution from Table 5.1 and the duct and hub geometry from Figure 5-19 were used and re-scaled for the fan diameters of both retrofit hybrid electric aircraft architectures. Maximum total windmilling drag was assumed to occur at the minimum RPM that the fan could operate without the blade tips

stalling and is shown versus aircraft velocity in Table 6.3 for both architectures.

Table 6.3: RPM at Maximum Windmilling Drag (Assumed to Occur at Minimum RPM before Blade Tip Stall) versus Aircraft Velocity

Aircraft Velocity (knots)	Fan RPM at Maximum Windmilling Drag	
	1 Supercooled Engine per Wing	5 DP Engines per Wing
150	250	600
200	320	760
250	400	950

The resulting maximum total windmilling drag achieved with both engine configurations is shown in Figure 6-1. The drag from the landing gear of the Boeing 737-800 and the idle thrust of two CFM56-7B engines, both from BADA 4, are shown for comparison.

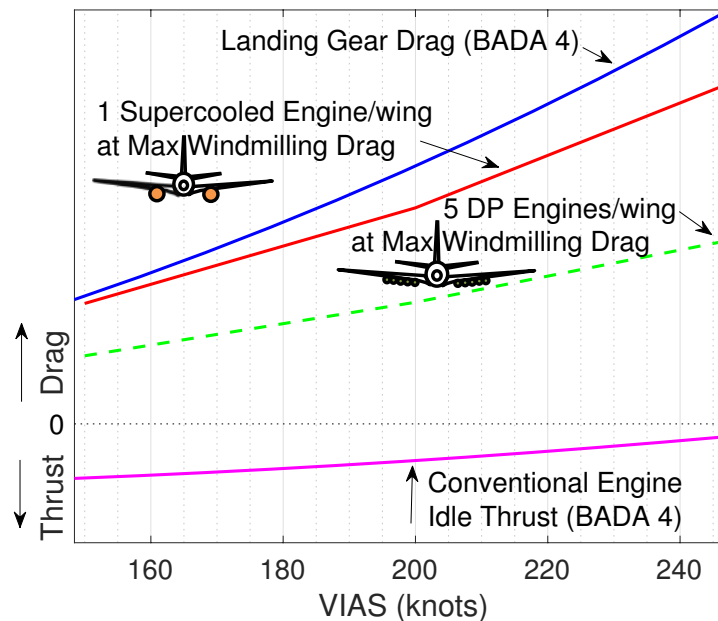


Figure 6-1: Maximum Windmilling Drag versus Velocity of Retrofit Distributed Engine and Supercooled Motors Compared to Conventional Aircraft Gear Drag and Idle Thrust

Figure 6-1 shows that the maximum windmilling drag of both retrofit aircraft increases with velocity. The maximum windmilling drag of the retrofit aircraft with one supercooled motor per wing is comparable to the total gear drag of the Boeing 737-800, particularly at

slow velocities. The maximum windmilling drag of the retrofit aircraft with one supercooled motor per wing is also about twice that of the distributed propulsion aircraft with 5 self-cooled fans per wing. This is due to the smaller diameter, distributed propulsion fans having less blade surface and therefore produce smaller lift and drag components than larger diameter fans despite the maximum windmilling RPM being higher for the smaller fans.

The resulting noise of fan of both the 5 distributed fans per wing retrofit hybrid electric aircraft and retrofit hybrid electric aircraft with supercooled motors was modeled in BFANS to determine the fan noise at maximum windmilling drag versus velocity. The resulting broadband noise at a 120m observer are shown in Figure 6-2. The idle thrust fan noise versus velocity predicted in ANOPP of the conventional CFM56-7B engine is also plotted for comparison.

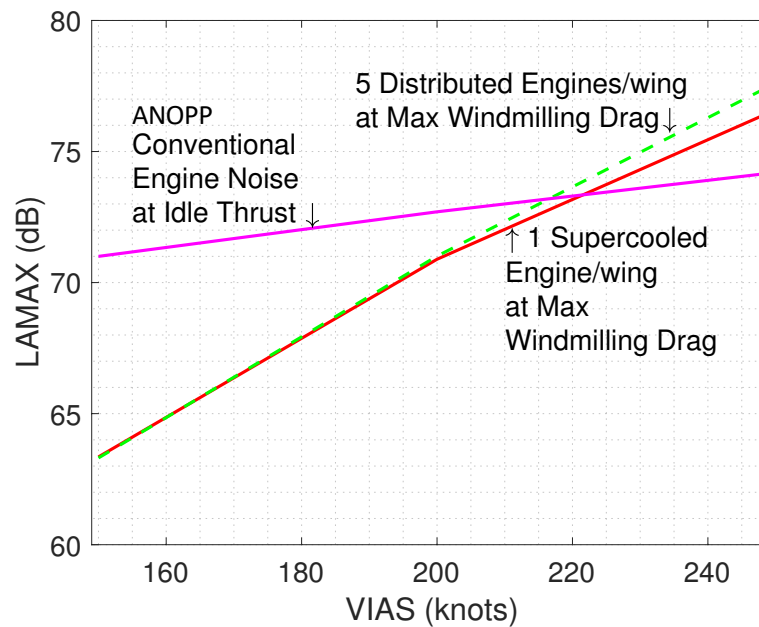


Figure 6-2: Broadband Overflight Noise Outputs for Fans of Retrofit Hybrid Electric Aircraft at Altitude 120m

The resulting noise prediction of the retrofit fans at low velocities is quieter than the ANOPP prediction for the idle thrust fan noise of the CFM56-7B and higher at velocities above a flight speed of approximately 220 knots. Thus the fan noise of the retrofit hybrid electric engine is expected to contribute no more to the overall noise of the aircraft than fans of the baseline turbofan aircraft at idle thrust conditions below a flight speed of 220

knots. If windmilling drag is used above 220 knots, the windmilling drag noise will have to be compared to the noise of other aircraft components to determine if it will contribute significantly to the overall aircraft noise.

The baseline aircraft used in the following case studies is the Boeing 737-800 with CFM56-7B engines, while the 2035 time frame retrofit hybrid electric aircraft with 5 distributed fans per wing employing windmilling drag is the alternative aircraft. The technology level of this aircraft was both more conservative compared to the estimated performance of the supercooled electronics of the 2050 timeframe aircraft as well as was shown to have more conservative maximum windmilling drag estimates as shown in Figure 6-1. Thus procedures utilizing the maximum windmilling drag of the distributed propulsion 2035 technology level aircraft is within the available performance space of both hybrid electric aircraft that are summarized in Table 6.2

It is assumed for the following case studies of retrofit-hybrid electric aircraft employing windmilling drag on approach that the final approach weight of both the baseline aircraft and the retrofit-hybrid electric aircraft employing windmilling drag on approach are equal. This is in order to provide a direct comparison of the windmilling effect versus no windmilling on noise without the additional impacts of weight on noise. An otherwise fully-loaded retrofit aircraft would be heavier than the baseline aircraft would have a higher stall velocity and thus higher final approach speeds which would result in higher airframe noise on the final descent.

6.3 Case Study 1: Performance and Noise Analysis of Steeper Approaches with Windmilling Drag

Use of the framework described in Chapter 5 is demonstrated on an example steeper descent approach procedure compared to a baseline continuous descent, 3° approach with a standard deceleration profile that follows the mean deceleration profile of Boeing 737-800s from BOS radar data in Figure 4-23. The motivation for analysis of this procedure is to examine the use of a hybrid electric aircraft employing windmilling drag in enabling steeper descents and

therefore reducing undertrack noise via increasing altitude versus distance to touchdown.

6.3.1 Steeper Approach Profile with Windmilling Drag

The steeper descent procedure with windmilling drag compared to the baseline profile are diagrammed in Figure 6-3. In the modified procedure, windmilling drag was used to enable a steeper descent and thus increase altitude versus distance to touchdown. During the steeper approach with windmilling drag, windmilling is assumed to occur from the Flaps 5 release to touchdown. The landing configuration flaps and gear were assumed deployed at the same altitude for each respective device as in the baseline case, where as high lift devices for earlier portions of the procedure were assumed to be deployed based on velocity. Gear release was assumed to occur at 2,000 ft and the stabilization point was assumed to be 1,700 ft for both cases.

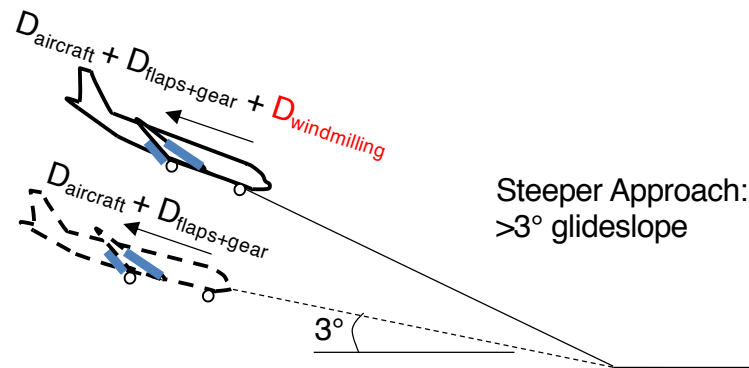


Figure 6-3: Baseline Profile with 3° Continuous Descent Compared to Steeper Descent Procedure with Windmilling Drag

The resulting modeled altitude, velocity, configuration, and thrust profiles are shown in Figure 6-4, with the baseline profiles in black and the hybrid electric aircraft profiles with windmilling drag shown in magenta.

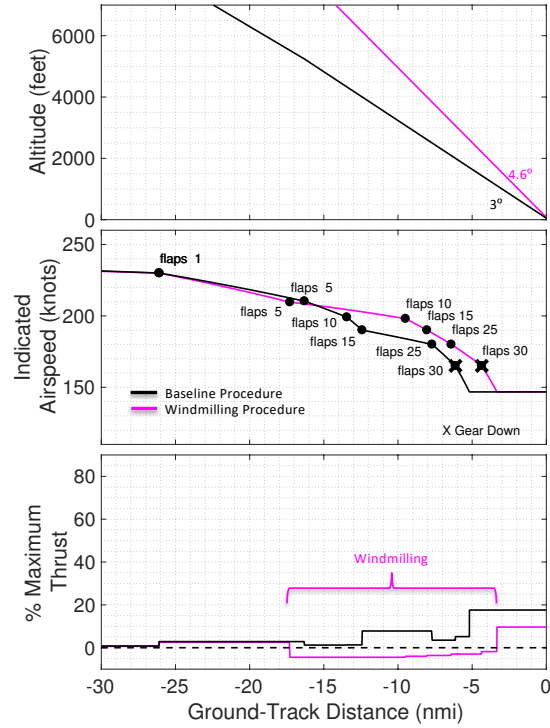


Figure 6-4: Modeled Altitude, Velocity, Configuration, and Thrust of the Baseline and Steeper Descent Profile with windmilling drag

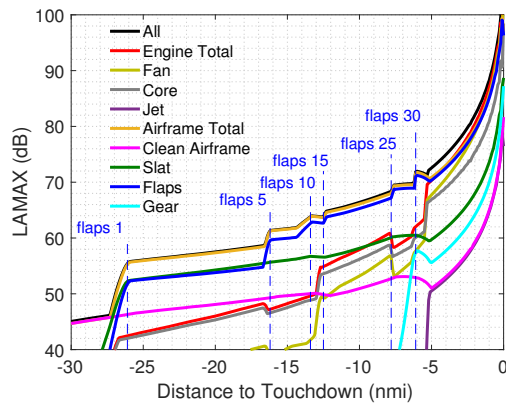
As can be seen the percent maximum thrust profile in Figure 6-4, engine thrust is negative where the windmilling drag is employed. A 4.6° steeper descent angle was obtained with the hybrid electric aircraft procedure when employing maximum windmilling drag (which increased with aircraft velocity) and adjustments to the velocity and configuration profiles between the Flaps 5 velocity and the stabilization point of 1,700 ft.

6.3.2 Single Event Flyover Noise Modeling of the Baseline and Steeper Approaches with Windmilling Drag

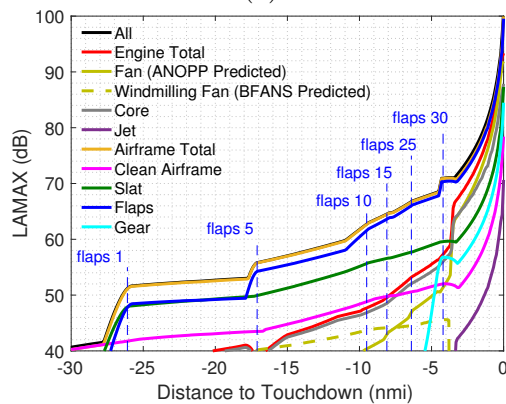
The baseline approach procedure was modeled along with the steeper descent approach procedure performed by the retrofit hybrid electric aircraft, both assuming a straight-in approach. Given these approach profiles and the performance and geometry data for the Boeing 737-800 from TASOPT, the single event flyover noise for both cases was obtained using the noise modeling method from Figure 5-7.

Figure 6-5 shows the breakdown of the magnitude of $L_{A,MAX}$ directly under the flight

track of each profile for each noise component. In Figure 6-5 (b), the predicted noise of the windmilling fans during the windmilling portion of the approach between 17 and 3 nmi to touchdown is shown in the dotted gold line, while for reference, the noise of two Boeing 737-800 conventional CFM56-7B engines at idle thrust is shown in the solid gold line. Both components are significantly less than the total noise and therefore as a source component do not significantly impact the total aircraft noise. The windmilling fan in this case therefore only impacts the total noise levels by enabling the aircraft to perform the steeper descent. The other noise components are reduced due to the increased altitude to touchdown. Additionally, because the gear is assumed to deploy at 2,000ft, the gear deployment location is closer to touchdown and thus the gear noise is only evident from about 4.5 nmi to touchdown for the windmilling steeper descent approach in Figure 6-5 (b).



(a)



(b)

Figure 6-5: $L_{A,MAX}$ Component Breakdown for (a) Baseline Approach and (b) Steeper Descent Windmilling Approach

To illustrate the noise reduction of the steeper 4.6° descent enabled with windmilling drag, the reduction in total $L_{A,MAX}$ under the flight track when flying the windmilling steeper descent procedure instead of the baseline 3° descent procedure is shown in Figure 6-6.

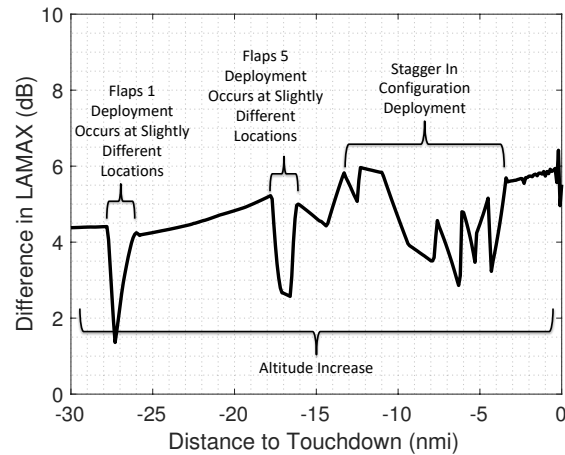
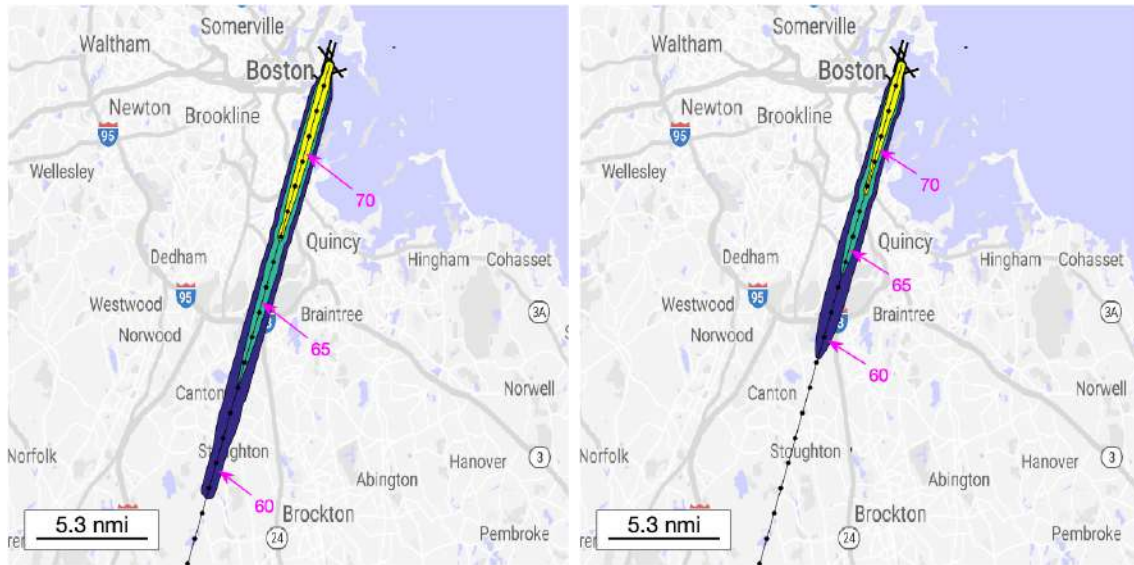


Figure 6-6: Reduction in $L_{A,MAX}$ (dB) Under the Flight Track for a Retrofit Hybrid Electric Aircraft Performing a 4.6° Descent with Windmilling Drag Compared to a Conventional Boeing 737-800 Performing a Baseline 3° Descent

There is an approximately 4-6 dB reduction in noise for the retrofit hybrid electric aircraft performing the steeper 4.6° descent by employing windmilling drag compared to the conventional Boeing 737-800 performing the baseline 3° approach. The spikes in the data reflect differences in locations where flaps and slats were deployed.

Finally, the $L_{A,MAX}$ noise contours of both the baseline 3° descent and steeper 4.6° descent are shown in Figure 6-7. In addition, the reduction in the $L_{A,MAX}$ noise contours when flying the steeper 4.6° descent compared to the baseline 3° descent and are shown on approach into Runway 4R at Boston Logan Airport (BOS) in Figure 6-8. Significant reductions in the noise along the entire approach procedure are apparent.



(a) Baseline 3° Descent

(b) 4.6° Descent with Windmilling Drag

Figure 6-7: $L_{A,MAX}$ (dB) Contours for the Retrofit Hybrid Electric Aircraft Performing a 4.6° Descent with Windmilling Drag Compared to a Conventional Boeing 737-800 Performing a Baseline 3° Descent

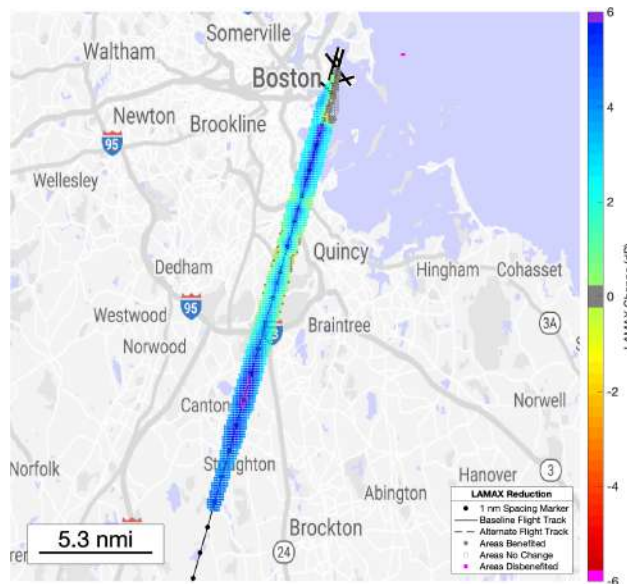


Figure 6-8: Reduction in $L_{A,MAX}$ 60 (dB) Contour for the Retrofit Hybrid Electric Aircraft Performing a 4.6° Descent with Windmilling Drag Compared to a Conventional Boeing 737-800 Performing a Baseline 3° Descent

The population exposure to the 60, 65, and 70 dB $L_{A,MAX}$ noise contours is also shown in Table 6.4, also indicating significant noise reductions for the steeper 4.6° descent compared

to the baseline 3° descent.

Table 6.4: Population Exposure of Baseline Approach Procedure versus Windmilling Steeper Descent Approach

$L_{A,MAX}$ Level (dB)		60	65	70
	Baseline	35,749	12,284	3,040
Population Exposure	Steeper Descent	21,160	7,863	798
	Decrease	14,589	4,421	2,242

The windmilling drag steeper descent procedure yields reductions in total population exposure at all levels.

Comparison of Retrofit Hybrid Electric Aircraft Steeper Descent with Windmilling to Conventional Boeing 737-800 Steeper Descent without Windmilling

When employing windmilling drag, the retrofit hybrid electric aircraft was found able to perform a 4.6° steeper descent while maintaining similar distances to decelerate at different configuration settings. For the conventional Boeing 737-800 operating at idle thrust until gear release at 2,000 ft, the steepest descent angle without windmilling while maintaining similar distances to decelerate at different configuration settings was found to be 3.4°. These flight profiles are shown in Figure 6-17, with the baseline 3° descent in black, the idle thrust 3.4° steeper descent in green, and the hybrid electric windmilling 4.6° descent in magenta.

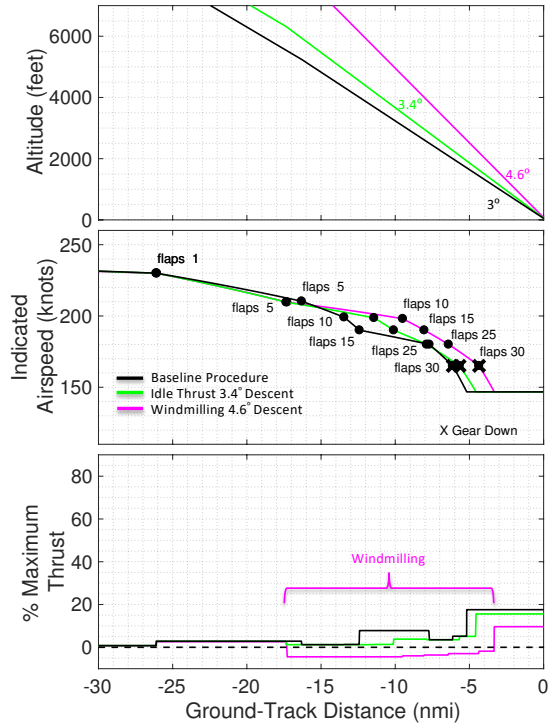


Figure 6-9: Modeled Altitude, Velocity, Configuration, and Thrust Baseline, Steeper Descent Profile without Windmilling Drag, and Steeper Descent Profile with Windmilling Drag

A comparison of the total $L_{A,MAX}$ undertrack of these procedures is shown in Figure 6-10. A conventional Boeing 737-800 performing an idle thrust 3.4° steeper descent yields an approximately 1 dB reduction in $L_{A,MAX}$ throughout the procedure compared to the baseline 3° descent. The retrofit hybrid electric aircraft performing the 4.6° steeper descent enabled by windmilling drag yields an approximately 4-6 dB reduction in $L_{A,MAX}$ throughout the procedure compared to the baseline 3° descent.

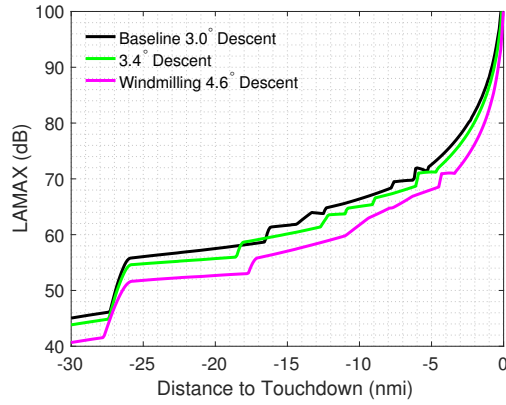


Figure 6-10: $L_{A,MAX}$ (dB) Under the Flight Track for a Retrofit Hybrid Electric Aircraft Performing a 4.6° Descent with Windmilling Drag and 3.4° Descent without Windmilling Drag, and a Conventional Boeing 737-800 Performing a 3° Descent

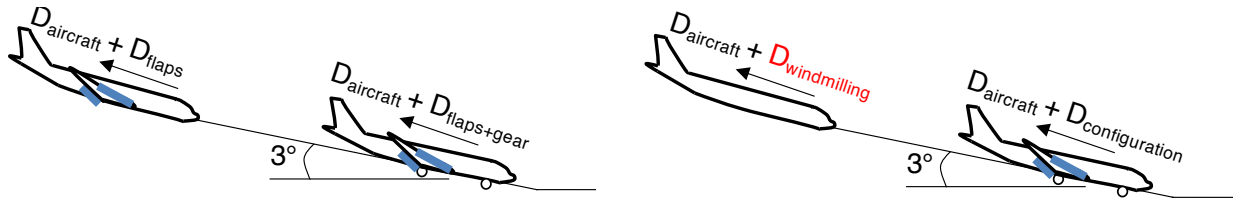
The results in Figure 6-10 show that the retrofit hybrid electric aircraft performing steeper descents by employing windmilling drag offers significant benefits compared to not only baseline continuous 3° descents, but also the steeper 3.4° descent, which is the limit of the conventional Boeing 737-800 drag performance capability without utilizing drag by configuring early.

6.4 Case Study 2: Performance and Noise Analysis of Delayed Deceleration Approaches with Windmilling Drag

Use of the framework described in Chapter 5 is demonstrated on an example delayed deceleration approach procedure compared to a baseline 3° continuous descent approach with a standard deceleration profile that follows the mean deceleration profile of Boeing 737-800s from BOS radar data in Figure 4-23. The motivation for the analysis of this procedure is to examine the use of a hybrid electric aircraft employing windmilling drag in increasing the maximum deceleration rate at various high lift device configurations. Doing so enables the aircraft to maintain higher airspeeds to a distance closer to touchdown. Doing so enables flap and slat deployment, and associated flap and slat noise, to be delayed to closer to touchdown.

6.4.1 Delayed Deceleration Approach Profile with Windmilling Drag

The delayed deceleration procedure with windmilling drag compared to the baseline profile is diagrammed in Figure 6-11. In the modified procedure, windmilling drag was used to enable a delayed deceleration and thus a delay flap and slat deployment to a distance that is to touchdown. Windmilling is assumed to occur from 250 knots to touchdown to the stabilization point at 1,700 ft. The landing configuration flaps and gear were assumed deployed at the same altitude for each respective device as in the baseline case, whereas the high lift devices for earlier portions of the procedure were assumed to be deployed based on velocity. The stabilization point was assumed to be 1,700 ft for both cases.



(a) Standard Deceleration Approach

(b) Delayed Deceleration Approach: Delay deceleration and configuring to closer to touchdown

Figure 6-11: Baseline Profile with Standard Deceleration Compared to Delayed Deceleration Procedure with Windmilling Drag

The resulting modeled altitude, velocity, configuration, and thrust profiles are shown in Figure 6-12, with the baseline profiles in black and the hybrid electric aircraft profiles with windmilling drag shown in magenta.

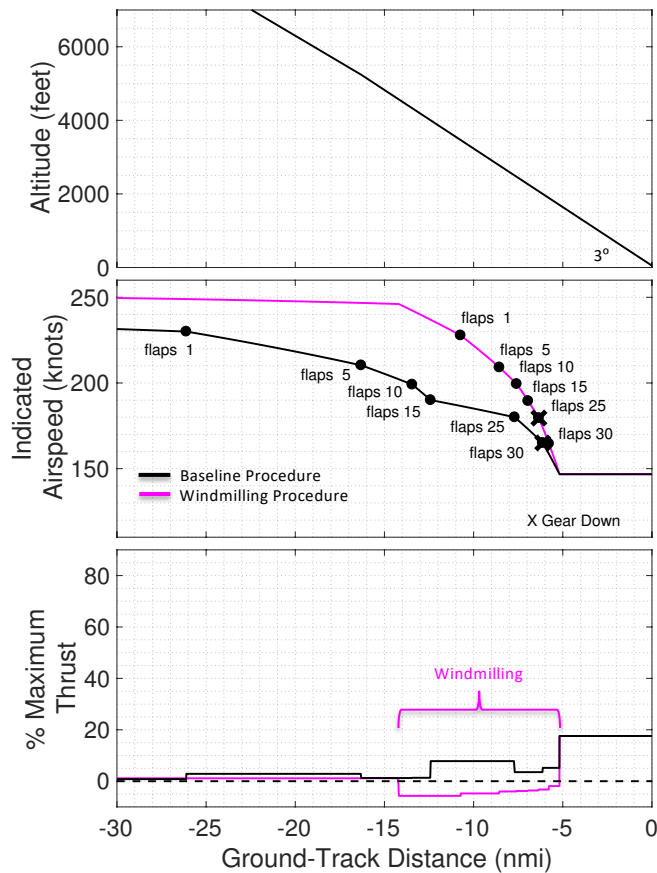


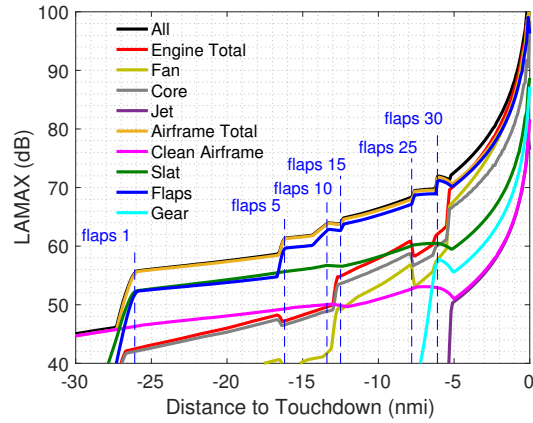
Figure 6-12: Modeled Altitude, Velocity, Configuration, and Thrust Baseline and Delayed Deceleration Profile with Windmilling Drag

As can be seen the percent maximum thrust profile in Figure 6-4, engine thrust is negative where the windmilling drag is employed. In addition, the higher deceleration rate obtained in the hybrid electric aircraft procedure with windmilling drag enables the high lift device deployment to occur closer to touchdown. This is not typically achievable during a standard 3° continuous descent procedure because high lift devices are needed for the aircraft to have enough drag to slow down to the final approach velocity before the stabilization point.

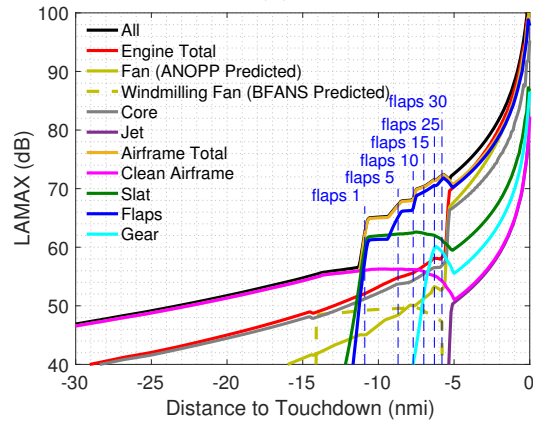
6.4.2 Single Event Flyover Noise Modeling of Baseline and Delayed Deceleration Approaches with Windmilling Drag

The baseline approach procedure with the standard deceleration was modeled along with the delayed deceleration procedure with the retrofit hybrid electric aircraft, with both aircraft flying a straight-in approach. Given these approach profiles and the performance and geometry data for the Boeing 737-800 from TASOPT, the single event flyover noise for both cases obtained using the noise modeling method from Figure 5-7.

Figure 6-13 shows the breakdown of the magnitude of $L_{A,MAX}$ directly under the flight track of each profile for each noise component. In Figure 6-13 (b) the predicted noise of the windmilling fans during the windmilling portion of the approach between 15 and 5 nmi to touchdown is shown in the dotted gold line, while for reference, the noise of two Boeing 737-800 conventional CFM56-7B engines at idle thrust is shown in the solid gold line. Both components are significantly less than the total noise and therefore as a source component do not significantly impact the total aircraft noise. The windmilling fan therefore only impacts the total noise levels by enabling the aircraft to perform the delayed deceleration on a continuous descent approach. The configuration noise components were thus reduced due to the delayed deceleration and delay in configuration deployment to closer to touchdown.



(a)



(b)

Figure 6-13: $L_{A,MAX}$ Component Breakdown for (a) Baseline, Standard Deceleration Approach and (b) Delayed Deceleration Windmilling Approach

To illustrate the contribution to noise reduction under the flight track of the delayed deceleration descent enabled with windmilling drag, the reduction in total $L_{A,MAX}$ under the flight track for the aircraft flying the windmilling delayed deceleration procedure instead of the baseline standard deceleration procedure is shown in Figure 6-14.

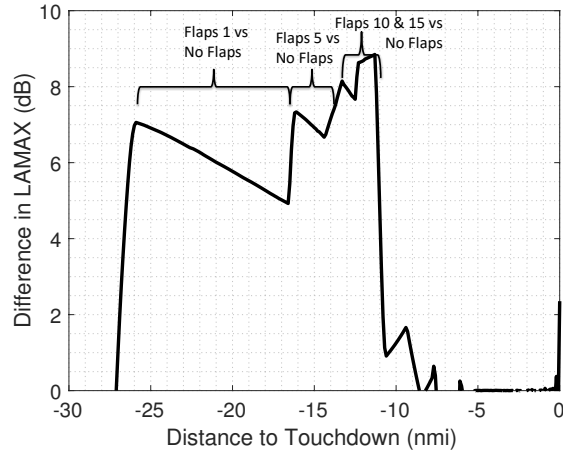
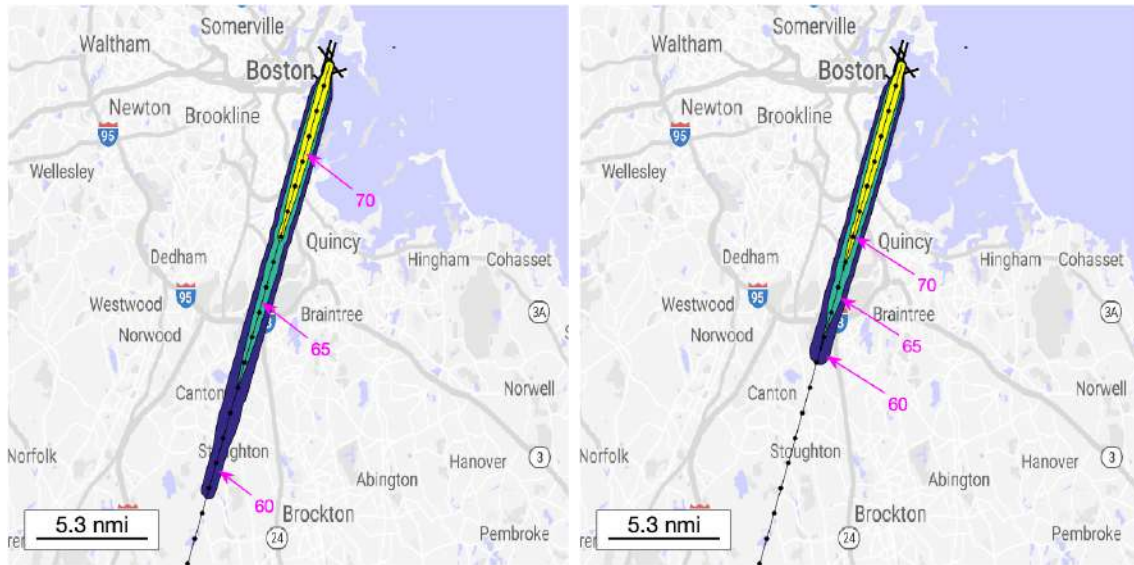


Figure 6-14: Reduction in $L_{A,MAX}$ (dB) Under the Flight Track for a Retrofit Hybrid Electric Aircraft Performing a delayed deceleration approach with Windmilling Drag Compared to a Conventional Boeing 737-800 Performing a Baseline Standard Deceleration Approach

There is a reduction in noise of approximately 5-6 dB between 26 and 17 nmi to touchdown for the retrofit hybrid electric aircraft performing the delayed deceleration approach with windmilling drag compared to the conventional Boeing 737-800 performing the baseline standard deceleration approach due to the delay in deployment of flaps 1. Additional reductions of approximately 7-9 dB also occur between about 17 to 10 nmi to touchdown due to the delay in deployment of flaps 5 through 15. The two procedures have the same noise impacts from about 10 nmi to touchdown.

Finally, the $L_{A,MAX}$ noise contours of both the baseline standard deceleration profile and delayed deceleration profile with windmilling drag is shown in Figure 6-15. In addition, the reduction in the $L_{A,MAX}$ noise contours when flying the delayed deceleration approach with windmilling drag compared to the baseline standard deceleration approach and are shown on approach into Runway 4R at Boston Logan Airport (BOS) in Figure 6-16. Significant reductions in the noise along the entire approach procedure are apparent beyond about 10 nmi from touchdown.



(a) Baseline Standard Deceleration Approach (b) Delayed Deceleration Approach with Windmilling Drag

Figure 6-15: $L_{A,MAX}$ (dB) Contours for the Retrofit Hybrid Electric Aircraft Performing a Delayed Deceleration Approach with Windmilling Drag Compared to a Conventional Boeing 737-800 Performing a Baseline Standard Deceleration Approach

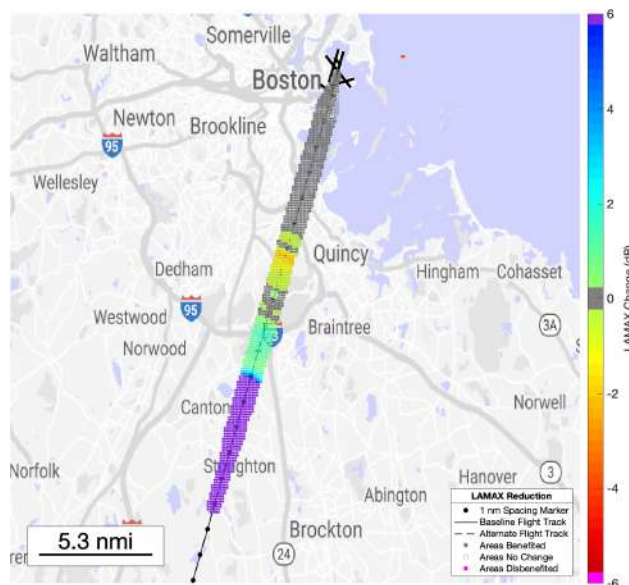


Figure 6-16: Reduction in $L_{A,MAX}$ 60 (dB) Contour for the Retrofit Hybrid Electric Aircraft Performing a Delayed Deceleration Approach with Windmilling Drag Compared to a Conventional Boeing 737-800 Performing a Baseline Standard Deceleration Approach

Population exposure at each of the 60 dB, 65 dB, and 70 dB $L_{A,MAX}$ noise levels for the delayed deceleration approach profile compared to the baseline approach are shown in Table

6.5.

Table 6.5: Contour Area of Baseline Approach Procedure versus Windmilling Delayed Deceleration Approach

$L_{A,MAX}$ Level (dB)		60	65	70
Baseline		35,749	12,284	3,040
Population Exposure	Delayed Deceleration	27,919	12,107	3,040
Decrease		7,830	117	0

Reduction in population exposure is most significant at the 60 and 65 dB noise levels.

Comparison of Retrofit Hybrid Electric Aircraft Delayed Deceleration Approach to Conventional Boeing 737-800 Delayed Deceleration Approach without Windmilling

When using windmilling drag on a 3° continuous descent, the retrofit hybrid electric aircraft was found able to delay decelerating from 250 knots until about 14 nmi to touchdown and delay deploying flaps until about 11 nmi to touchdown while still being able to slow to the final approach velocity at 1,700 ft. For the conventional Boeing 737-800 operating at idle thrust until gear release at 2,000 ft, the aircraft can only delay deploying flaps until about 19 nmi to touchdown in order to still be able to slow to the final approach velocity at 1,700 ft. These flight profiles are shown in Figure 6-17, with the baseline, standard deceleration profile in black, the idle thrust delayed deceleration in green, and the hybrid electric windmilling delayed deceleration in magenta.

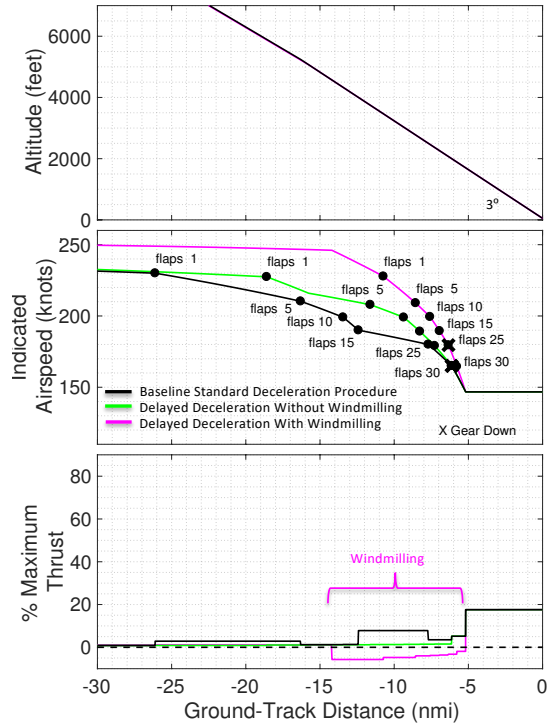


Figure 6-17: Modeled Altitude, Velocity, Configuration, and Thrust Baseline Standard Deceleration Profile, Delayed Deceleration Approach Profile without Windmilling Drag, and Delayed Deceleration Approach Profile with Windmilling Drag

A comparison of the total undertrack $L_{A,MAX}$ noise of these procedures is shown in Figure 6-18. A conventional Boeing 737-800 performing an idle thrust delayed deceleration approach has approximately 6-8 dB reduction in $L_{A,MAX}$ compared to the baseline approach between 27 and 19 nmi. However, the retrofit hybrid electric aircraft performing the delayed deceleration approach with windmilling drag yields an approximately 6-8 dB reduction in $L_{A,MAX}$ until even closer to touchdown (between 27 and 11 nmi).

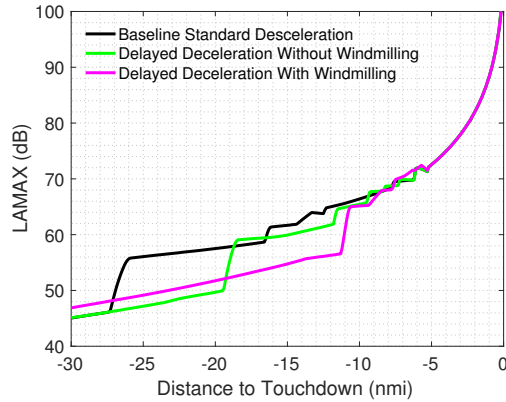


Figure 6-18: $L_{A,MAX}$ (dB) Under the Flight Track for a Retrofit Hybrid Electric Aircraft Performing a Delayed Deceleration Approach with Windmilling Drag and Delayed Deceleration Approach without Windmilling Drag, and a Conventional Boeing 737-800 Performing a Baseline Standard Deceleration Approach

The results in Figure 6-18 show that the retrofit hybrid electric aircraft performing delayed deceleration approaches with windmilling drag offers significant benefits compared to not only baseline continuous 3° descents with standard deceleration profiles, but also idle thrust, delayed deceleration, 3° continuous descents. Windmilling improves the drag performance of the retrofit hybrid electric aircraft and thus enables it to delay deploying flaps until 11 nmi, compared to 19 nmi which is the limit of the conventional Boeing 737-800 drag performance capability at idle thrust.

6.5 Case Study 3: Performance and Noise Analysis of Combined Delayed Deceleration Steeper Approaches with Windmilling Drag

Use of the framework described in chapter 3 is demonstrated on an example combined delayed deceleration steeper approach procedure compared to a baseline, 3° continuous descent approach with a standard deceleration profile that follows the mean deceleration profile of Boeing 737-800s from BOS radar data in Figure 4-23. The motivation for the analysis of this procedure is to examine the use of a hybrid electric aircraft employing windmilling drag in both increasing the maximum deceleration of the aircraft at the early Flaps 1 and Flaps 5 configurations, where most of the noise benefit of the delayed deceleration approach is obtained, and then in increasing the glideslope at later configurations, where most of the noise benefit of the steeper approach is obtained. Doing so enables the aircraft in the early portion of the descent to maintain higher airspeeds to a closer distance to touchdown and thus Flaps 1 and 5 deployment, and associated flap and slat noise, can be delayed to closer to touchdown. It also enables a higher altitude of the aircraft during the rest of the descent.

6.5.1 Combined Delayed Deceleration Steeper Approach Profile with Windmilling Drag

The combined delayed deceleration, steeper approach procedure with windmilling drag compared to the baseline profile are diagrammed in Figure 6-19. In the modified procedure, windmilling drag was used to enable a delayed deceleration and thus delay flap and slat deployment of the Flaps 1 and 5 configurations to a closer distance to touchdown. It also enables the aircraft to perform a steeper descent at a standard deceleration rate for the rest of the approach. Windmilling is assumed to occur from 250 knots to touchdown to the stabilization point of 1,700 ft. The landing configuration flaps and gear were assumed deployed at the same altitude for each respective device as in the baseline case, where as high lift devices for earlier portions of the procedure were assumed to be deployed based on

velocity. The stabilization point was assumed to be 1,700 ft for both cases.

Delayed Deceleration Approach at 3° glideslope:
Delay deceleration and configuring to closer to
touchdown

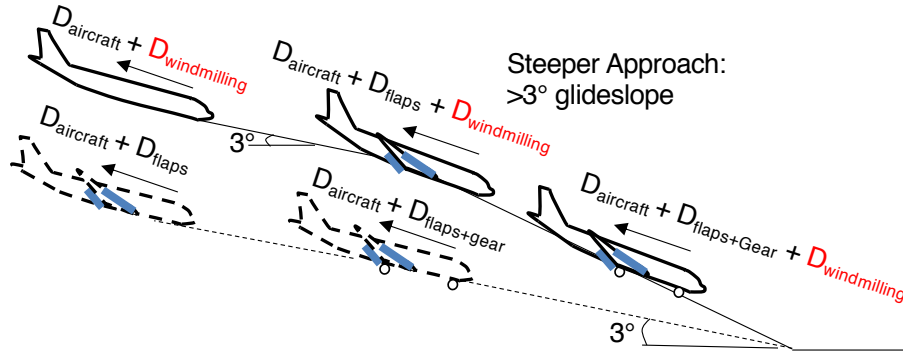


Figure 6-19: Baseline Profile with Standard Deceleration Compared to Combined Delayed Deceleration Steeper Procedure with Windmilling Drag

The resulting modeled altitude, velocity, configuration, and thrust profiles are shown in Figure 6-20, with the baseline profiles in black and the hybrid electric aircraft profiles with windmilling drag shown in magenta.

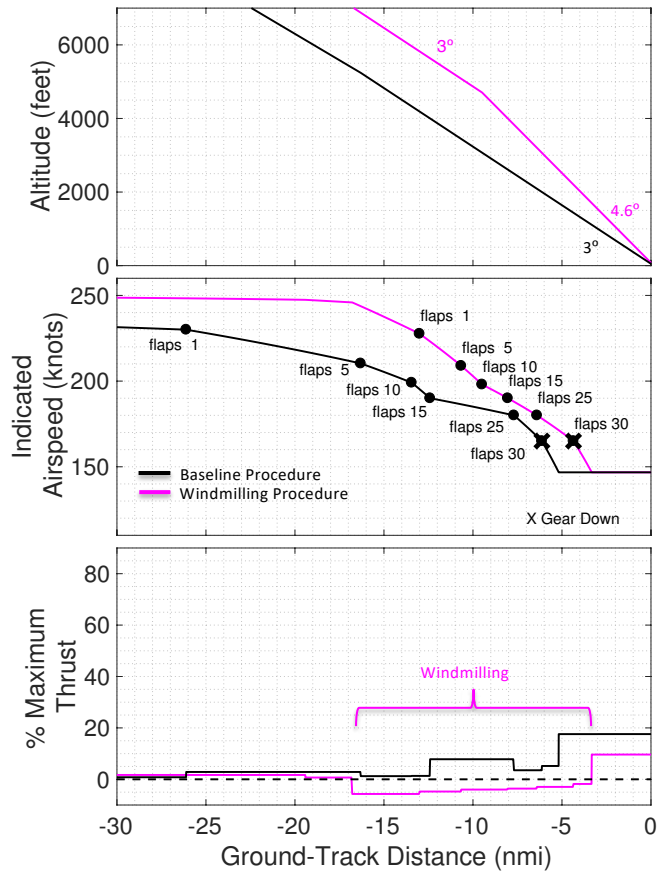


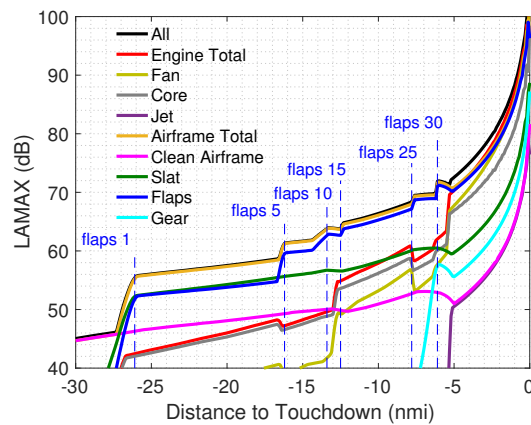
Figure 6-20: Modeled Altitude, Velocity, Configuration, and Thrust Baseline and Combined Delayed Deceleration, Steeper Profile with Windmilling Drag

As can be seen the percent maximum thrust profile in Figure 6-20, engine thrust is negative where the windmilling drag is employed.

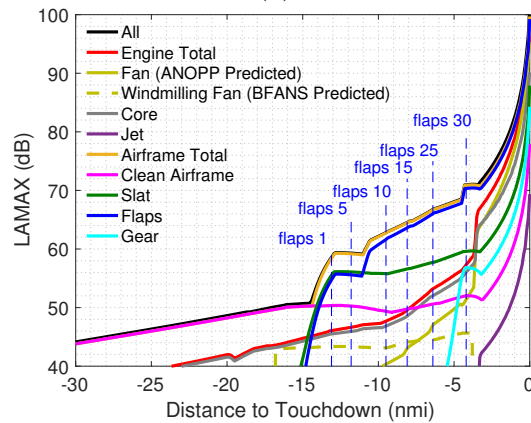
6.5.2 Single Event Flyover Noise Modeling of Baseline and Combined Delayed Deceleration Steeper Approaches with Windmilling Drag

The baseline approach procedure with the standard deceleration was modeled along with the combined delayed deceleration steeper procedure with the retrofit hybrid electric aircraft on a straight approach. Given these approach profiles and the performance and geometry data for the Boeing 737-800 from TASOPT, the single event flyover noise for both cases obtained using the noise modeling method from Figure 5-7.

Figure 6-21 shows the breakdown of component $L_{A,MAX}$ noise directly under the flight track for each noise component. In Figure 6-21 (b) the predicted noise of the windmilling fans during the windmilling portion of the approach between 17 and 3.8 nmi to touchdown is shown in the dotted gold line, while for reference, the noise of two Boeing 737-800 conventional CFM56-7B engines at idle thrust is shown in the solid gold line. Both components are significantly less than the total noise and therefore as a source component do not significantly impact the total aircraft noise. The windmilling fan therefore only impacts the total noise levels by enabling the aircraft to perform the combined delayed deceleration steeper approach. The other noise components thus reduced due to the delayed deceleration and increased altitude to touchdown.



(a)



(b)

Figure 6-21: $L_{A,MAX}$ Component Breakdown for (a) Baseline, Standard Deceleration Approach and (b) Combined Delayed Deceleration and Steeper Windmilling Approach

To illustrate the contribution to noise reduction under the flight track for the combined

delayed deceleration steeper descent enabled with windmilling drag, the reduction in total $L_{A,MAX}$ under the flight track when flying the combined windmilling steeper delayed deceleration procedure instead of the baseline procedure is shown in Figure 6-22.

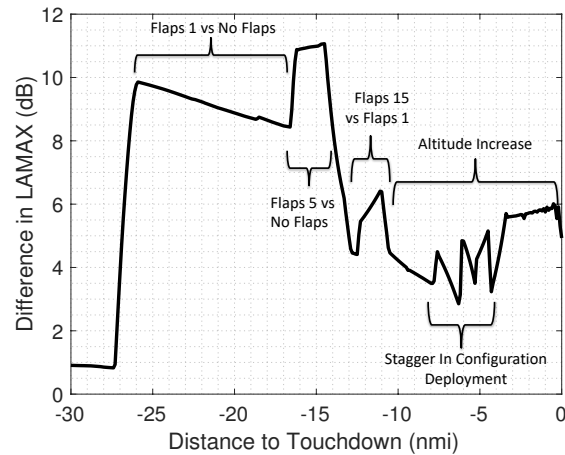


Figure 6-22: Reduction in $L_{A,MAX}$ (dB) Under the Flight Track for a Retrofit Hybrid Electric Aircraft Performing a Combined Delayed deceleration Steeper approach with Windmilling Drag Compared to a Conventional Boeing 737-800 Performing a Baseline Standard Deceleration Approach

There is an approximately 8-10 dB reduction in noise between 26 and 17 nmi to touchdown for the retrofit hybrid electric aircraft performing the combined delayed deceleration steeper approach with windmilling drag compared to the conventional Boeing 737-800 performing the baseline standard deceleration approach due to both the delay in deployment of flaps 1 and the additional altitude gain from the steeper descent. Additional reductions of approximately 11 dB also occur between about 17 to 12 nmi to touchdown due to the delay in deployment of flaps 5 and altitude increase. Finally, average reductions in noise of about 4-5 dB occur due to the altitude increase from about 10 nmi to touchdown.

Finally, the $L_{A,MAX}$ noise contours of both the baseline standard deceleration profile and combined delayed deceleration steeper approach profile with windmilling drag is shown in Figure 6-23. In addition, the reduction in the $L_{A,MAX}$ noise contours when flying the combined delayed deceleration steeper approach with windmilling drag compared to the baseline standard deceleration approach and are shown for this procedure on approach into Runway 4R at Boston Logan Airport (BOS) in Figure 6-24. Significant reductions in the

noise along the entire approach procedure are apparent.

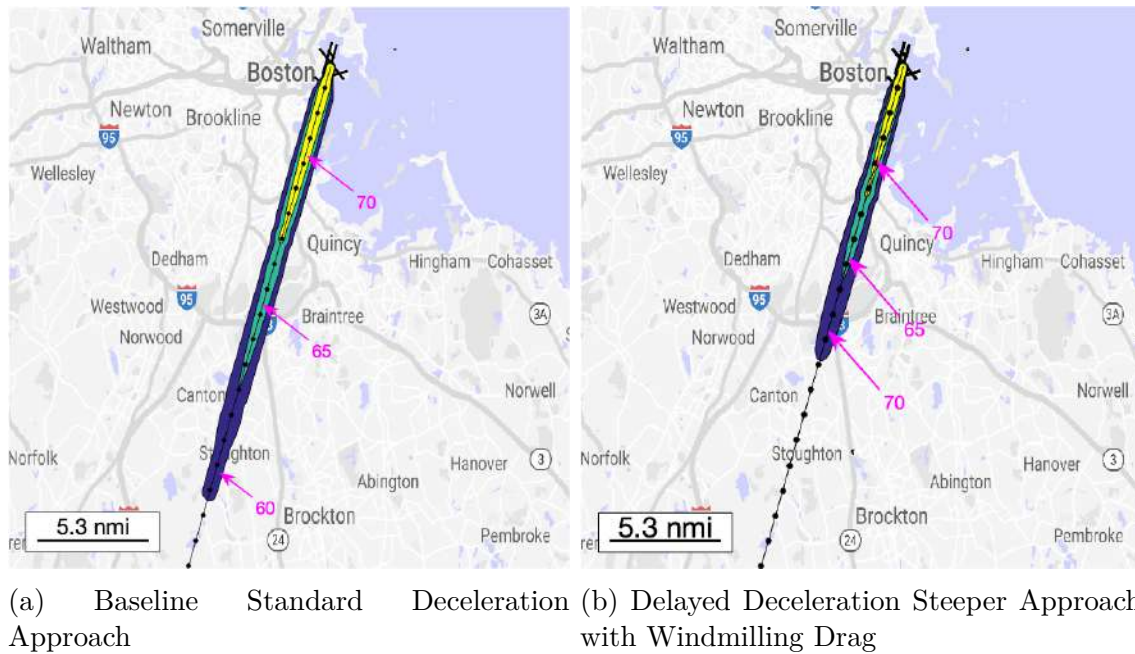


Figure 6-23: $L_{A,MAX}$ (dB) Contours for the Retrofit Hybrid Electric Aircraft Performing a Delayed Deceleration Approach with Windmilling Drag Compared to a Conventional Boeing 737-800 Performing a Baseline Standard Deceleration Approach

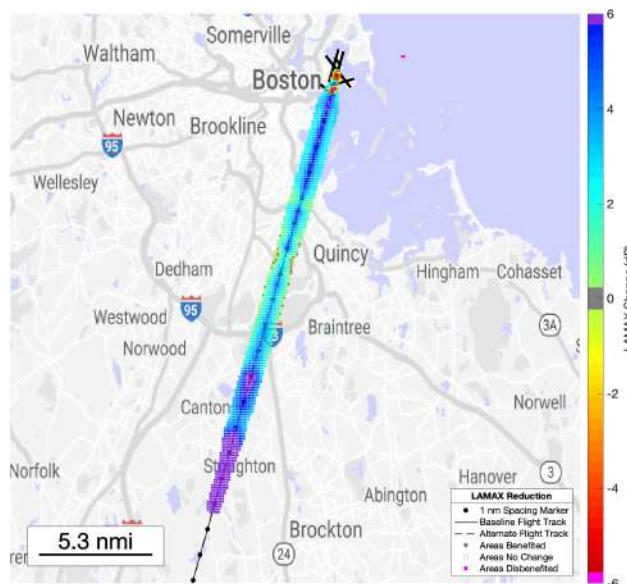


Figure 6-24: Reduction in $L_{A,MAX}$ 60 (dB) Contour for the Retrofit Hybrid Electric Aircraft Performing a Combined Delayed Deceleration Steeper Approach with Windmilling Drag Compared to a Conventional Boeing 737-800 Performing a Baseline Standard Deceleration Approach

The population exposure to the 60, 65, and 70 dB $L_{A,MAX}$ noise contours is shown in Table 6.6, also indicating significant noise reductions for the combined delayed deceleration steeper approach with windmilling drag descent compared to the baseline 3° descent.

Table 6.6: Population Exposure of Baseline Approach Procedure versus Combined Delayed Deceleration Steeper Approach with Windmilling Drag

$L_{A,MAX}$ Level (dB)		60	65	70
	Baseline	35,749	12,284	3,040
Population Exposure	DDA Steeper Descent	21,426	7,883	800
	Decrease	14,323	4,401	2,240

The combined delayed deceleration steeper approach with windmilling drag yields reductions in total population exposure at all levels. The population exposure reduction is similar to the windmilling steeper, 4.6° descent procedure with a standard deceleration.

6.6 Chapter 6 Conclusion

The case studies of this chapter also show that a retrofit hybrid electric aircraft employing windmilling drag can perform approach procedures that yield significant noise benefits compared to the flight performance capabilities of conventional aircraft. The predicted noise of windmilling fans was shown to be significantly lower than the other noise components of a typical airframe (such as high lift devices) and therefore the noise impact of windmilling drag was shown to be only due to how it impacted the aircraft flight performance.

Windmilling fans were shown to offer significant noise reductions both in steeper descent approaches and delayed deceleration approaches in the conceptual studies of this chapter. While the examples presented showed the performance capability one aircraft, the windmilling fan may offer the performance of larger deceleration rates and steeper descent angles depending on the aircraft design and trades between other components of the flight profile, such as configuration setting. For example, an early deceleration and fully configured aircraft with maximum windmilling drag would be able to descend at a steeper angle than the aircraft with a standard deceleration rate that was presented in Figure 6-4. Additional

details of how windmilling engines will be integrated into airframes and potential options for optimization of fan design for better drag and noise performance require further study.

One consideration for the design of these procedures is that the maximum descent angle that can be achieved will also be limited by the aircraft's ability to conduct a safe go-around procedure from a given decision height. Hileman et al [6] presents a relationship between the maximum flight path angle for a safe go-around and decision height, final approach velocity, time delay due to the pilot and engine spool-up response, and load limit due to the aggressiveness of the pull-up. Hileman et al shows that for a final approach speed of 148 knots (which was used in the examples shown in Chapter 6), a decision height of 100 ft, and load factor of 1.3g, the maximum flight path angle for a safe go-around is about 4°-5.5° with a 5 to 3 second time delay typical of aircraft with standard gas turbine engines. The maximum descent angle of the steeper approach case presented in Figure 6-4 of 4.6° is within this range, though steeper angles require slower approach velocities depending on the delay in pilot response and engine spool-up time. Studies have indicated [85] that the spool-up time of hybrid electric fans is expected to be more rapid than the maximum 5 seconds required to transition from flight idle to 95% thrust required by FAR 33.73 [143], however these trade-offs also require future study.

In addition, it was assumed the final approach weight of both the baseline aircraft and the retrofit-hybrid electric aircraft employing windmilling drag on approach were equal. This was in order to provide a direct comparison of the windmilling effect versus no windmilling on noise without the additional impacts of weight on noise. This assumption implies that the extra weight due to the hybrid electric aircraft retrofit is accounted for with a reduction in fuel or payload capacity. An otherwise fully-loaded retrofit aircraft would be heavier than the baseline aircraft would have a higher stall velocity and thus higher final approach speeds, which would result in higher airframe noise on the final descent. Resizing the aircraft may mitigate this issue (for example, by resizing the aircraft for a higher wing surface area to reduce final approach velocity). Incorporating a full optimization formulation for hybrid electric aircraft in a TASOPT-like framework would indicate how the aircraft as a whole would have to be modified for this concept. These design trades for actual implementation of this concept require further study.

Chapter 7

Conclusion

7.1 Thesis Framework and Analysis Results Summary

A framework for analyzing aircraft community noise impacts of advanced operational approach and departure procedures of conventional aircraft was developed, which includes detailed engine and airframe source noise ANOPP models. This enables the framework to model the noise impacts of not only thrust modifications as in Noise-Power-Distance based models, but also the impacts of aircraft speed and configuration changes. Because these models require detailed thrust and velocity profiles as well internal engine states, a flight profile generation module was developed to generate the detailed input data using a combination of BADA4 data and TASOPT aircraft and engine models. While not a primary focus of this thesis, fuel burn can also be modeled and thus considered with the design of noise abatement flight procedures with this framework.

The performance and noise of conventional aircraft performing several noise abatement approach and departure procedure concepts were assessed with this framework. The example applications showed how flight path angle, speed, and configuration changes impact performance and noise and how these factors may be designed in advanced operational procedures for noise reduction. The case studies of conventional aircraft show that for modern aircraft, changes in aircraft speed have minimal impact on the overall departure noise. This is because reasonable changes in speed on departure from standard departures

do not significantly impact engine noise, which is the dominate source in departure, nor significantly impact climb performance. Changes in climb altitude via a thrust increase have a more significant impact on departure noise. An increase in the climb angle in departure via a thrust increase results in higher altitudes but also higher engine noise, and therefore a redistribution of the noise where some regions are benefited and some regions are dis-benefited. Thus the population distribution for where the departure is implemented would have to be considered in order to determine the best location of thrust modifications.

During approach, flying continuous descents as opposed to level segments was shown to result in decreases in both thrust, and subsequent engine noise, as well as yield higher altitudes for more distance to touchdown in the descent, which also decreases overall aircraft noise. In addition, unlike in departure, the case studies of conventional aircraft showed that for modern aircraft on arrival, changes in approach airspeed can have a significant impact on the overall aircraft noise. Engine thrust on approach is often low and thus airframe noise components, such as flap and slat noise, have a more significant impact during approach than during departure. If aircraft decelerate early in an approach, then flaps and slats must be released. These devices are shown to have a significant impact on approach noise. Thus delaying deceleration and subsequent configuration deployment can yield significant noise reductions, as was shown on example narrow and wide body aircraft. The delayed deceleration approach was test flown on the Boeing ecoDemonstrator for flyability and significant noise reductions were observed in the modeled noise impacts of the flight test results using the framework.

A summary of the noise impacts of each of the conventional aircraft procedures assessed is shown in Table 7.1.

Table 7.1: Summary of Advanced Procedure Noise Impact for Conventional Aircraft

Procedure	Noise Impact
Delayed Deceleration Approach	Delayed deceleration approach procedures are flyable (as shown in the B777 Flight Demonstration) and yield 6-10 dB undertrack noise reduction compared to baseline procedures
Continuous Descent Approach	Continuous descent approaches yield 2 dB noise reductions in noise under the flight track compared to approaches with level segments before the region of glideslope intercept
Steeper Approach	3.77° steeper approaches yield 4-5 dB reductions in noise under the flight track compared to 3° ILS approaches
High Thrust Climb	High initial thrust on departure results in noise increase close to takeoff due to increased engine noise and a noise reduction further out
Reduced Speed Departure	While reducing climb speed reduces clean airframe noise, engine noise is dominate on departure and thus reducing departure climb speed does not significantly impact overall aircraft departure noise
Noise Abatement Departure Procedure 1 and 2 (NADP 1 and 2)	Changes in the acceleration location on departure results in small differences in community noise compared to current procedures. Standard departures in US are consistent with NADP 2 and is close to the minimal noise impact

The framework was extended to also include the functionality to analyze the flight performance of retrofit hybrid electric aircraft and the drag and noise impacts of windmilling engines. This included using XROTOR to assess the drag performance of windmilling fans at different RPMs and BFANS as the broadband noise model for windmilling fans. Boeing 737-800s retrofitted for hybrid electric engines were conceptually sized with 2035 timeframe and 2050 timeframe electrified engine technologies to obtain fan sizes for each assumption. The blade geometry of an available CFM56-3 engine was scaled to the fan diameter for each technology assumption and the maximum windmilling drag versus aircraft velocity and windmilling fan noise was assessed with the framework. The predicted noise of windmilling fans was shown to be significantly lower than the other noise components of a typical airframe and therefore the noise impact of windmilling drag was shown to be only how it impacts the

aircraft flight performance.

The noise of hybrid electric aircraft performing noise abatement approach procedure concepts that take advantage of windmilling drag were compared to the noise of conventional gas-turbine engine aircraft. The retrofit aircraft sized with the 2035 timeframe technology level assumption, which required distributed propulsion and 5 fans per wing, was found to produce less windmilling drag than the 2050 timeframe technology level assumption with 1 large fan per wing and therefore the hybrid electric aircraft approach procedures were designed assuming the lower drag of the 2035 timeframe technology level assumption as the limit case. Windmilling fans employed by the retrofit hybrid electric aircraft were shown to offer significant noise reductions both in steeper descent approaches and delayed deceleration approaches compared to approaches that can be performed by conventional Boeing 737-800 aircraft which were limited by drag performance.

A summary of the noise impacts of each of the hybrid electric aircraft procedures assessed is shown in Table 7.2.

Table 7.2: Summary of Advanced Procedure Noise Impact for Hybrid Electric Aircraft Using Windmilling Drag

Procedure	Noise Impact
Steeper Approach with Windmilling Drag	Steeper approach with windmilling drag yields 4-6 dB noise reductions under the flight track throughout the entire procedure compared to 3° continuous descent approaches performed by conventional aircraft
Delayed Deceleration Approach with Windmilling Drag	Delayed deceleration approaches with windmilling drag yields 4-8 dB noise reductions under the flight track compared to 3° continuous descent approaches 10 nmi from touchdown and beyond
Combined Delayed Deceleration Steeper Approach with Windmilling Drag	Combined Delayed Deceleration Approach and Steeper Final Descent with windmilling drag yields 9-11 dB noise reductions under the flight track prior to 10 nmi to touchdown and 4-6 dB noise reductions under the flight track between 10 nmi to touchdown compared to 3° continuous descent approaches performed by conventional aircraft

7.2 Primary Contributions

In this thesis, a framework was developed that considers the aircraft, flight procedure, and noise components for analysis of community noise impacts of advanced operational flight procedures for conventional and hybrid electric aircraft utilizing windmilling engines.

The framework was used to evaluate noise impact of several advanced flight procedures:

- Delayed Deceleration Approach
- Continuous Descent Approach
- Steeper Approach
- High Thrust Climb
- Reduced Speed Departure
- Noise Abatement Departure Procedure 1 and 2

The windmilling drag concept to obtain quiet drag on approach was identified as a benefit attribute for hybrid electric aircraft. In addition, a model was developed for windmilling engine drag and noise.

Finally, the framework was used to evaluate several advanced flight procedures for retrofit hybrid electric aircraft using windmilling drag:

- Steeper Approach with Windmilling Drag
- Delayed Deceleration Approach with Windmilling Drag
- Combined Delayed Deceleration Approach and Steeper Final Descent with Windmilling Drag

7.3 Discussion and Future Work

The framework to analyze the community noise impacts of advanced operational flight procedures of conventional and hybrid electric aircraft shown in this thesis can be used for the aircraft that are contained in the BADA 4 drag database and retrofit hybrid electric aircraft. A continuing step in future developments of this framework would be to include

capability for the systems level sizing and analysis of additional hybrid electric or fully electric aircraft.

Additionally, there is also a key need for validation of the noise benefits of the flight procedures demonstrated. The models show significant noise reductions for many flight procedures but results need to be compared to noise measurements for validation. In addition to noise validation, operational implications of the procedures identified as having benefit need to be evaluated. For example, delayed deceleration approach procedures, which were showed to have noise benefits for both conventional and hybrid electric aircraft, have implementation challenges. These challenges include the ability of pilots to know where to begin the deceleration for different aircraft weights and wind conditions and how air traffic controllers will sequence aircraft with different deceleration rates. These challenges require further study.

Finally, the hybrid electric aircraft examples shown in this thesis were of retrofit hybrid electric aircraft on approach compared to a conventional aircraft landing at the same approach weight in order to show the noise benefits of the windmilling fan concept on its own. Incorporating a full optimization formulation for hybrid electric aircraft in a TASOPT-like framework would indicate how the aircraft as a whole would have to be modified for this concept and thus building such a model is a subject for future study. The details of how windmilling engines will be integrated into aircraft airframes and potential options for optimization of fan design for better drag and noise performance were not discussed in this thesis. Thus doing these design trades for actual implementation of this concept is also a subject for future study.

Bibliography

- [1] Jensen, L., Thomas, J., Brooks, C., et al., “Analytical Approach for Quantifying Noise from Advanced Operational Procedures,” *Europe Air Traffic Management Research and Development Seminar*, 2017. URL http://www.atmseminarus.org/seminarContent/seminar12/papers/12th_ATM_RD_Seminar_paper_135.pdf.
- [2] Federal Aviation Administration, “FAA History of Noise,” , 2018. URL https://www.faa.gov/regulations_policies/policy_guidance/noise/history/.
- [3] Thomas, J., Yu, A., Li, C., et al., “Advanced Operational Procedure Design Concepts for Noise Abatement,” *Thirteenth USA/Europe Air Traffic Management Research and Development Seminar*, Vienna, 2019.
- [4] Drela, M., “Design Drivers of Energy-Efficient Transport Aircraft,” *SAE International Journal of Aerospace*, Vol. 4, No. 2, 2011, pp. 602–618. <https://doi.org/10.4271/2011-01-2495>.
- [5] Thomas, J., and Hansman, R. J., “Framework for Analyzing Aircraft Community Noise Impacts of Advanced Operational Flight Procedures,” *Journal of Aircraft*, Vol. 54, No. 4, 2019. <https://doi.org/10.2514/1.C035100>.
- [6] Hileman, J., Reynolds, T., de la Rosa Blanco, E., et al., “Development of Approach Procedures for Silent Aircraft,” *45th AIAA Aerospace Sciences Meeting and Exhibit Special Session – Towards A Silent Aircraft*, Reno, Nevada, 2007. <https://doi.org/10.2514/6.2007-451>.
- [7] Crichton, D., De La Rosa Blanco, E., Law, T. R., et al., “Design and Operation for Ultra Low Noise Take-Off,” *45th AIAA Aerospace Sciences Meeting*, Reno, Nevada, 2007. <https://doi.org/10.2514/6.2007-456>.
- [8] Bradley, M. K., and Droney, C. K., “Subsonic Ultra Green Aircraft Research: Phase II – Volume II – Hybrid Electric Design Exploration,” Tech. Rep. NASA/CR-2015-218704, Hampton, Virginia, 2015.
- [9] Burley, C., Brooks, T. F., Hutcheson, F. V., et al., “Noise Scaling and Community Noise Metrics for the Hybrid Wing Body Aircraft,” *20th AIAA/CEAS Aeroacoustics Conference*, Atlanta, 2014. <https://doi.org/10.2514/6.2014-2626>.
- [10] Lockard, D., and Lilley, G., “The Airframe Noise Reduction Challenge,” Tech. Rep. NASA/TM-2004-213013, Hampton, Virginia, 2004.

- [11] Zaporozhets, O., Tokarev, V. I., and Attenborough, K., *Aircraft Noise: Assessment, Prediction and Control*, Spon Press, New York, NY, 2011.
- [12] Fleming, G. G., “Aviation Environmental Design Tool (AEDT),” Tech. Rep. DOT-VNTSC-FAA-16-11, Federal Aviation Administration, Washington, DC, 2016.
- [13] Harris, C. M., “Absorption of Sound in Air versus Humidity and Temperature,” *Journal of the Acoustical Society of America*, Vol. 40, No. 1, 1966, pp. 148–159. <https://doi.org/10.1121/1.1910031>.
- [14] Chien, C., and Soroka, W., “Sound Propagation Along an Impedance Plane,” *Journal of Sound and Vibration*, Vol. 43, No. 1, 1975, pp. 9–20. [https://doi.org/10.1016/0022-460X\(75\)90200-X](https://doi.org/10.1016/0022-460X(75)90200-X).
- [15] Smith, M. J. T., *Aircraft Noise*, Cambridge University Press, Cambridge, 1989. <https://doi.org/10.1017/CBO9780511584527>, URL <http://ebooks.cambridge.org/ref/id/CBO9780511584527>.
- [16] U.S. Government Publishing Office, “Part 36-Noise Standards: Aircraft Type and Airworthiness Certification,” , 2016.
- [17] Trani, A. A., and Roa, J., “CEE 4674 Airport Planning and Design,” Tech. rep., 0. URL http://128.173.204.63/courses/cee4674/cee4674_pub/BasicNoiseCalculations.pdf.
- [18] Airbus, “Getting to Grips with Aircraft Noise,” Tech. rep., 2003. URL http://dream-air.ru/new/pilotam/AircraftNoise-copy_2-.pdf.
- [19] Kerrebrock, J. L., *Aircraft Engines and Gas Turbines*, 2nd ed., MIT Press, Cambridge, Massachusetts, 1992. URL <https://mitpress.mit.edu/books/aircraft-engines-and-gas-turbines>.
- [20] Hileman, J., “FAA Perspectives on Challenges Posed by Aircraft Noise,” , 2017. URL <https://www.panynj.gov/content/dam/port-authority/aircraft-noise/nycar-presentation-oct-2017.pdf>.
- [21] Federal Aviation Administration, “Performance Based Navigation,” , 2017. URL https://www.faa.gov/nextgen/how_nextgen_works/new_technology/pbn/in_depth/.
- [22] EUROCONTROL, “Introducing Performance Based Navigation (PBN) and Advanced RNP (A-RNP) 21,” Tech. rep., 2013.
- [23] Federal Aviation Administration, “NextGen – Greener Skies Over Seattle = Greener Skies Over the USA,” , 2012. URL <https://www.faa.gov/nextgen/snapshots/stories/?slide=6>.
- [24] Harrison, S., “FAA Dispersing Charlotte Douglas Departures to Scatter Jet Noise,” , 2016. URL <http://www.charlotteobserver.com/news/politicsgovernment/%0Darticle89601182.html>.

- [25] Torres, E., “Sick of Logan Plane Noise, Residents Let FAA Hear It,” , 2015. URL <https://www.bostonglobe.com/metro/regionals/south/2015/12/04/sicklogan-%0Dplane-noise-residents-let-faa-hear/DaOLEonLslgIlVUqHQR76H/story.html>.
- [26] Scovel, C. L., “FAA’s Progress and Challenges in Advancing the Next Generation Air Transportation System,” Tech. rep., U.S. Department of Transportation, 2013.
- [27] MASSPORT, “Massport and FAA RNAV Pilot Study Overview Public Briefing,” Tech. rep., 2017.
- [28] Timar, S., Hunter, G., and Post, J., “Assessing the Benefits of NextGen Performance-Based Navigation,” *Air Traffic Control Quarterly*, Vol. 21, No. 3, 2016. <https://doi.org/10.2514/atcq.21.3.211>.
- [29] Brink, M., Wirth, K., Schierz, C., et al., “Annoyance Responses to Stable and Changing Aircraft Noise Exposure,” *The Journal of the Acoustical Society of America*, Vol. 125, No. 5, 2008, pp. 2930–41. <https://doi.org/10.1121/1.2977680>.
- [30] Ollerhead, J. B., “The CAA Aircraft Noise Contour Model : ANCON Version 1,” Tech. rep., Civil Aviation Authority/Department of Transport, Cheltenham, England, 1992.
- [31] Mavris, D., and Perullo, C., “Project 43 Noise Power Distance Re-Evaluation,” Tech. rep., 2017.
- [32] Bertsch, L., Guérin, S., Looye, G., et al., “The Parametric Aircraft Noise Analysis Module - Status Overview and Recent Applications,” *17th AIAA/CEAS Aeroacoustics Conference 2011 (32nd AIAA Aeroacoustics Conference)*, 2011. <https://doi.org/10.2514/6.2011-2855>.
- [33] Pietrzko, S., and Butikofer, R., “FLULA-Swiss Aircraft Noise Prediction Program,” *Annual Conference of the Australian Acoustical Society*, Adelaide, Australia, 2002.
- [34] Zorumski, W. E., “Aircraft Noise Prediction Program (ANOPP) Theoretical Manual,” Tech. Rep. NASA-TM-83199, National Aeronautics and Space Administration, Hampton, Virginia, 1982.
- [35] Stone, J., Groesbeck, D., and Zola, C., “An Improved Prediction Method for Noise Generated by Conventional Profile Coaxial Jets,” Tech. Rep. NASA-TM-82712, Lewis Research Center, Cleveland, OH, 1981.
- [36] Heidmann, M., “Interim Prediction Method for Fan and Compressor Source Noise,” Tech. Rep. NASA-TM-71763, Lewis Research Center, Cleveland, OH, 1979.
- [37] Dobrzynski, W., and Pott-Pollenske, M., “Slat Noise Source Studies for Farfield Noise Prediction,” *7th AIAA/CEAS Aeroacoustics Conference and Exhibit*, Maastricht, Netherlands, 2001. <https://doi.org/10.2514/6.2001-2158>.

- [38] Pott-Pollenske, M., Dobrzynski, W., Buchholz, H., et al., “Airframe Noise Characteristics from Flyover Measurements and Predictions,” *12th AIAA/CEAS Aeroacoustics Conference*, Cambridge, Massachusetts, 2006, pp. 2069–2082. <https://doi.org/10.2514/6.2006-2567>.
- [39] Rossignol, K. S., “Development of an Empirical Prediction Model for Flap Side-Edge Noise,” *16th AIAA/CEAS Aeroacoustics Conference (31st AIAA Aeroacoustics Conference)*, Stockholm, Sweden, 2010. <https://doi.org/10.2514/6.2010-3836>.
- [40] Fink, M., “Airframe Noise Prediction Method,” Tech. Rep. FAA-FRD-77-29, 1977.
- [41] Guo, Y., “Aircraft Slat Noise Modeling and Prediction,” *16th AIAA/CEAS Aeroacoustics Conference*, Stockholm, Sweden, 2010. <https://doi.org/10.2514/6.2010-3837>.
- [42] Guo, Y., “An Improved Landing Gear Noise Prediction Scheme,” Tech. Rep. NASA/CR-NAS1-NNL04AA11B, The Boeing Company, Huntington Beach, California, 2006.
- [43] Guo, Y., “Aircraft Flap Side Edge Noise Modeling and Prediction,” *17th AIAA/CEAS Aeroacoustics Conference (32nd AIAA Aeroacoustics Conference)*, The Boeing Company, Portland, Oregon, 2011. <https://doi.org/10.2514/6.2011-2731>.
- [44] Guo, Y., “Empirical Prediction of Aircraft Landing Gear Noise,” Tech. Rep. NASA/CR-2005-213780, Boeing Phantom Works, Long Beach, California, 2005.
- [45] Antoine, N. E., and Kroo, I. M., “Framework for Aircraft Conceptual Design and Environmental Performance Studies,” *AIAA Journal*, Vol. 43, No. 10, 2005, pp. 2100–2109. <https://doi.org/10.2514/1.13017>.
- [46] Werner-Westphal, C., Heinze, W., and Horst, P., “Multidisciplinary Integrated Preliminary Design Applied to Unconventional Aircraft Configurations,” *Journal of Aircraft*, Vol. 45, No. 2, 2008, pp. 581–590. <https://doi.org/10.2514/1.32138>.
- [47] Jensen, L., and Hansman, R. J., “Data-Driven Flight Procedure Simulation and Noise Analysis in a Large-Scale Air Transportation System,” Ph.D. thesis, Massachusetts Institute of Technology, 2018.
- [48] Morscheck, F., “Noise Mitigation Optimization of A-RNP/RNP AR Approaches,” *2018 Aviation Technology, Integration, and Operations Conference*, Atlanta, Georgia, 2018. <https://doi.org/10.2514/6.2018-3996>.
- [49] Federal Aviation Administration, “FAA Order 8260.3D: United States Standard for Terminal Instrument Procedures (TERPS),” Tech. rep., 2018.
- [50] “Performance Based Navigation (PBN) Implementation and Usage,” , 2019. URL <https://www.faa.gov/nextgen/pbn/dashboard/#>.

- [51] Yu, A., and Hansman, R. J., “Aircraft Noise Modeling of Dispersed Flight Tracks and Metrics for Assessing Impacts,” Ph.D. thesis, Massachusetts Institute of Technology, 2019.
- [52] International Civil Aviation Organization, “Document 8168 - Aircraft Operations,” Tech. rep., 2006.
- [53] Irving, D., “Steep Takeoffs Land JWA on ‘Scariest Airports’ List – Orange County Register,” , 2012. URL <http://www.ocregister.com/2012/07/20/steep-takeoffs-land-jwa-on-scariest-airports-list/>.
- [54] Behere, A., Lim, D., Kirby, M., et al., “Alternate Departure Procedures for Takeoff Noise Mitigation at Atlanta Hartsfield-Jackson International Airport,” *AIAA Scitech 2019 Forum*, San Diego, California, 2019. <https://doi.org/10.2514/6.2019-2090>.
- [55] Hebly, S. J., and Visser, H. G., “Advanced Noise Abatement Departure Procedures: Custom Optimized Departure Profiles,” *AIAA Guidance, Navigation and Control Conference and Exhibit*, Honolulu, Hawaii, 2008. <https://doi.org/10.2514/6.2008-7405>.
- [56] Reynolds, T., Sandberg, M., Thomas, J., et al., “Delayed Deceleration Approach Noise Assessment,” *16th AIAA Aviation Technology, Integration, and Operations Conference*, Reston, Virginia, 2016. <https://doi.org/10.2514/6.2016-3907>.
- [57] Reynolds, T. G., Ren, L., Clarke, J. P. B., et al., “History, Development and Analysis of Noise Abatement Arrival Procedures for UK Airports,” *AIAA 5th Aviation Technology, Integration and Operations Forum*, Arlington, VA, 2005. <https://doi.org/10.2514/6.2005-7395>.
- [58] Clarke, J. P. B., Ho, N. T., Ren, E., et al., “Continuous Descent Approach: Design and Flight Test for Louisville International Airport,” *Journal of Aircraft*, Vol. 41, No. 5, 2004, pp. 1054–1066. <https://doi.org/10.2514/1.5572>.
- [59] Bertsch, L., Looye, G., Anton, E., et al., “Flyover Noise Measurements of a Spiraling Noise Abatement Approach Procedure,” *Journal of Aircraft*, Vol. 48, No. 2, 2011, pp. 436–448. <https://doi.org/10.2514/1.C001005>.
- [60] Heathrow, “How to Land 650 Aircrafts in 1 Day,” , 2016. URL <https://www.heathrow.com/latest-news/heathrow-arrivals-whats-involved-with-landing-an-aircraft-at-the-uks-busiest-airport>.
- [61] Gregson, S., “London Heathrow Airport 3.2 Degrees Slightly Steeper Approach Trial Report,” Tech. rep., 2016.
- [62] Visser, H. G., and Wijnen, R. A., “Optimization of Noise Abatement Arrival Trajectories,” *Journal of Aircraft*, Vol. 38, No. 4, 2001, pp. 607–615. <https://doi.org/10.2514/2.2838>.
- [63] Scholz, M., and Abdelmoula, F., “Active Noise Abatement Using the Newly Developed Pilot Assistance System LNAS,” *InterNoise 2017*, Hong Kong, 2017.

- [64] Pott-Pollenske, M., Almonet, D., Jochen, W., et al., “On the Semi-Empirical Prediction of Spoiler Noise,” *2018 AIAA/CEAS Aeroacoustics Conference*, Atlanta, Georgia, 2018. <https://doi.org/10.2514/6.2018-3800>.
- [65] Boeing Commercial Airplanes, “737 Airplane Characteristics for Airport Planning,” Tech. rep., 2013. URL <http://www.boeing.com/assets/pdf/commercial/airports/acaps/737.pdf>.
- [66] Storms, B., Jaeger, S., Hayes, J., et al., “Aeroacoustic Study of Flap-Tip Noise Reduction Using Continuous Moldline Technology,” *6th Aeroacoustics Conference and Exhibit*, Lahaina, HI, 2012. <https://doi.org/10.2514/6.2000-1976>.
- [67] Quayle, A., Dowling, A., Babinsky, H., et al., “Landing Gear for a Silent Aircraft,” *45th AIAA Aerospace Sciences Meeting and Exhibit*, Reno, 2007. <https://doi.org/10.2514/6.2007-231>.
- [68] Shah, P., Mobed, D., and Spakovszky, Z., “Engine Air-Brakes for Quiet Air Transport,” *45th AIAA Aerosciences Meeting and Exhibit*, Reno, Nevada, 2007. <https://doi.org/10.2514/6.2007-1033>.
- [69] Borst, H., “Summary of Propeller Design Procedure and Data,” Tech. rep., Henry V. Borst and Associates, Rosemont, 1973.
- [70] Dittmar, J. H., and Jeracki, R. J., “Additional Noise Data on the SR-3 Propeller,” Tech. Rep. NASA-TM-81735, Lewis Research Center, Cleveland, 1981.
- [71] Ganz, U. W., Joppa, P. D., Patten, T. J., et al., “Boeing 18-inch Fan Rig Broadband Noise Test,” Tech. Rep. NASA CR-1998-208704, NASA Langley Research Center, Hampton, 1998.
- [72] Airbus, “Airbus, Rolls-Royce, and Siemens Team Up for Electric Future Partnership Launches E-Fan X Hybrid-Electric Flight Demonstrator,” , 2017. URL <http://www.airbus.com/newsroom/press-releases/en/2017/11/airbus--rolls-royce--and-siemens-team-up-for-electric-future-par.html>.
- [73] Felder, J., Kim, H., and Brown, G., “Turboelectric Distributed Propulsion Engine Cycle Analysis for Hybrid-Wing-Body Aircraft,” *47th AIAA Aerospace Sciences Meeting including The New Horizons Forum and Aerospace Exposition*, Orlando Florida, 2009, pp. 1–25. <https://doi.org/10.2514/6.2009-1132>.
- [74] Welstead, J., and Felder, J. L., “Conceptual Design of a Single-Aisle Turboelectric Commercial Transport with Fuselage Boundary Layer Ingestion,” *AIAA SciTech Forum 54th AIAA Aerospace Sciences Meeting*, San Diego, California, 2016. <https://doi.org/10.2514/6.2016-1027>.
- [75] Patterson, M. D., and Borer, N. K., “Approach Considerations in Aircraft with High-Lift Propeller Systems,” *17th AIAA Aviation Technology, Integration, and Operations Conference (AVIATION 2017)*, Denver, Colorado, 2017. <https://doi.org/10.2514/6.2017-3782>.

- [76] Brelje, B. J., and Martins, J. R., “Electric, Hybrid, and Turboelectric Fixed-Wing Aircraft: A Review of Concepts, Models, and Design Approaches,” *Progress in Aerospace Sciences*, Vol. 104, 2019. <https://doi.org/10.1016/j.paerosci.2018.06.004>.
- [77] European Commission, “Flightpath 2050 Europe’s Vision for Aviation,” , 2001.
- [78] Ashcraft, S. W., Padron, A. S., Pascioni, K. A., et al., “Review of Propulsion Technologies for N+3 Subsonic Vehicle Concepts,” Tech. Rep. NASA/TM-2011-217239, Cleveland, OH, 2011.
- [79] Follen, G., DelRosario, R., Wahls, R., et al., “NASA’s Fundamental Aeronautics Subsonic Fixed Wing Project: Generation N+3 Technology Portfolio,” *SAE 2011 AeroTech Congress and Exhibition*, 2011. <https://doi.org/10.4271/2011-01-2521>.
- [80] Jankovsky, A., “Airplane Concepts,” , 2017. URL <https://www1.grc.nasa.gov/aeronautics/hep/airplane-concepts/>.
- [81] Airbus, “E-Fan X,” , 2019. URL <https://www.airbus.com/innovation/future-technology/electric-flight/e-fan-x.html>.
- [82] Rosero, J. A., Ortega, J. A., Aldabas, E., et al., “Moving Towards a More Electric Aircraft,” *IEEE Aerospace and Electronic Systems Magazine*, Vol. 22, No. 3, 2007, pp. 3–9. <https://doi.org/10.1109/MAES.2007.340500>.
- [83] Hoelzen, J., Liu, Y., Bensmann, B., et al., “Conceptual Design of Operation Strategies for Hybrid Electric Aircraft,” *Energies*, Vol. 11, No. 1, 2018, pp. 1–26. <https://doi.org/10.3390/en11010217>.
- [84] Thauvin, J., Barraud, G., Budinger, M., et al., “Hybrid Regional Aircraft: A Comparative Review of New Potentials Enabled by Electric Power,” *AIAA Propulsion and Energy Forum 52nd AIAA/SAE/ASEE Joint Propulsion Conference*, Salt Lake City, Utah, 2016. <https://doi.org/10.2514/6.2016-4612>.
- [85] Armstrong, M., Ross, C., Phillips, D., et al., “Stability, Transient Response, Control, and Safety of a High-Power Electric Grid for Turboelectric Propulsion of Aircraft,” Tech. Rep. NASA/CR-2013-217865, 2013.
- [86] Stoll, A. M., Bevirt, J., Moore, M. D., et al., “Drag Reduction Through Distributed Electric Propulsion,” *14th AIAA Aviation Technology, Integration, and Operations Conference*, Atlanta, Georgia, 2014, pp. 16–20. <https://doi.org/10.2514/6.2014-2851>.
- [87] Hall, D., Greitzer, E., Dowdle, A., et al., “Feasibility of Electrified Propulsion for Ultra-Efficient Commercial Aircraft, Final Report,” Tech. Rep. NASA/CR-2019-220382, Cleveland, OH, 2019.
- [88] Kim, H. D., “Distributed Propulsion Vehicles,” Tech. Rep. E-17361, Cleveland, OH, 2010.

- [89] Berton, J. J., and Nark, D. M., “Low-Noise Operating Mode for Propeller-Driven Electric Airplanes,” *24th AIAA/CEAS Aeroacoustics Conference*, Atlanta, Georgia, 2018. <https://doi.org/10.2514/6.2018-3599>.
- [90] Synodinos, A., Self, R., and Torija, A., “Preliminary Noise Assessment of Aircraft with Distributed Electric Propulsion,” *2018 AIAA/CEAS Aeroacoustics Conference*, Atlanta, Georgia, 2018. <https://doi.org/10.2514/6.2018-2817>.
- [91] Hepperle, M., “Electric Flight – Potential and Limitations Abbreviations and Symbols,” *Energy Efficient Technologies and Concepts of Operation*, Braunschweig, Germany, 2012. URL <https://elib.dlr.de/78726/%0A>.
- [92] Rheume, J., and Lents, C., “Energy Storage for Commercial Hybrid Electric Aircraft,” *SAE Technical Paper Series*, 2016. <https://doi.org/10.4271/2016-01-2014>.
- [93] Barnes, J. P., “Regenerative Electric Flight Synergy and Integration of Dual role Machines,” *AIAA SciTech Forum 53rd AIAA Aerospace Sciences Meeting*, Kissimmee, Florida, 2015, pp. 1–15. <https://doi.org/10.2514/6.2015-1302>.
- [94] National Academies of Sciences Engineering and Medicine, “Commercial Aircraft Propulsion and Energy Systems Research: Reducing Global Carbon Emissions,” Tech. rep., National Academy Press, 2016.
- [95] Jansen, R., Bowman, C., Jankovsky, A., et al., “Overview of NASA Electrified Aircraft Propulsion (EAP) Research for Large Subsonic Transports,” Tech. Rep. GRC-E-DAA-TN42710, Atlanta, Georgia, 2017.
- [96] Anton, J., and Ruff-Stahl, H.-J., “Competitiveness of Hybrid Electric Aircraft on Short Range Scheduled Flights,” *International Journal of Aviation, Aeronautics, and Aerospace*, Vol. 5, No. 3, 2018. <https://doi.org/10.15394/ijaaa.2018.1240>.
- [97] Nuic, A., “User Manual for the Base of Aircraft Data (BADA) Revision 3.12,” Tech. rep., Eurocontrol, 2013.
- [98] Drela, M., “Transport Aircraft System OPTimization, Technical Description,” Tech. rep., Massachusetts Institute of Technology, Cambridge, 2016.
- [99] Jane, F., *All the World’s Aircraft*, London, 1912.
- [100] *IHS Jane’s aero-engines*, IHS, Jane’s Information Group, Coulsdon, 2013. URL <https://lib.ku.edu/databases/ihs-janes-aero-engines>.
- [101] Federal Aviation Administration, “Aircraft Weight and Balance Control,” Tech. rep., Washington, D.C., 2005. URL https://www.faa.gov/documentLibrary/media/Advisory_Circular/AC120-27E.pdf.
- [102] U.S. Government Publishing Office, “14 CFR Part 25 - Airworthiness Standards: Transport Category Airplanes | US Law | LII / Legal Information Institute,” , 2017. URL <https://www.law.cornell.edu/cfr/text/14/part-25>.

- [103] Liebeck, R., *Airplane Design*, Department of Mechanical and Aerospace Engineering, University of California, Irvine, Irvine, 2014.
- [104] Emmerling, J. J., Kazin, S. B., and Matta, R. K., “Core Engine Noise Control Program, Volume III, Supplement 1 - Prediction Methods,” Tech. Rep. FAA-RD-74-125, III-I, 1976.
- [105] Society of Automotive Engineers, “Gas Turbine Jet Exhaust Noise Prediction,” Tech. Rep. ARP876, SAE Aerospace Recommended Practice, 1994.
- [106] Stone, J. R., and Montegani, F. J., “An Improved Prediction Method for the Noise Generated in Flight by Circular Jets,” Tech. Rep. NASA-TM-81470, Atlanta, Georgia, 1980.
- [107] Rawls, J., “Boeing Airframe Noise Model (BAF),” Tech. rep., National Aeronautics and Space Administration, 2012.
- [108] Putnam, T., Lasagna, P., and White, K., “Measurements and Analysis of Aircraft Airframe Noise,” *Aeroacoustics: STOL Noise; Airframe and Airfoil Noise*, Vol. 45, 1976, pp. 363–378. <https://doi.org/10.2514/6.1975-510>.
- [109] Fethney, P., “An Experimental Study in Airframe Self-Noise,” *Aeroacoustics: STOL Noise; Airframe and Airfoil Noise*, Vol. 45, 1976, pp. 379–403. <https://doi.org/10.2514/6.1975-511>.
- [110] Guo, Y., and Thomas, R., “On Aircraft Trailing Edge Noise,” *25th AIAA/CEAS Aeroacoustics Conference*, Delft, The Netherlands, 2019. <https://doi.org/10.2514/6.2019-2610>.
- [111] “Standard Values of Atmospheric Absorption as a Function of Temperature and Humidity,” Tech. rep., Society of Automotive Engineers, 1975.
- [112] Federal Aviation Administration, “Aircraft Noise Levels,” , 2012. URL https://www.faa.gov/about/office_org/headquarters_offices/apl/noise_emissions/aircraft_noise_levels/.
- [113] European Aviation Safety Agency, “EASA certification noise levels,” , 2018.
- [114] Flight Safety Foundation, “Stabilized Approach FSF ALAR Briefing Note 7.1,” Tech. rep., Alexandria VA, 2009.
- [115] “ILS OR LOC RWY 04R,” , 2018. URL <https://skyvector.com/files/tpp/2005/pdf/00058IL4R.PDF>.
- [116] Airbus, “Control your Speed, During Descent, Approach and Landing,” *Safety First*, , No. 24, 2017. URL https://safetyfirst.airbus.com/app/themes/mh_newsdesk/pdf.php?p=21925.
- [117] Federal Aviation Administration, “FAA Order JO 7110.65Y: Air Traffic Control,” Tech. rep., 2019.

- [118] Norris, G., “A Look At Boeing’s 777 EcoDemonstrator,” *Aviation Week*, 2020. URL <https://aviationweek.com/special-topics/sustainability/look-boeings-777-ecodemonstrator>.
- [119] “RNAV (RNP) Z RWY 31,” , 2013. URL <https://skyvector.com/files/tpp/2005/pdf/00669RRZ31.PDF>.
- [120] Manwell, J. F., McGowan, J. G., and Rogers, A. L., *Wind Energy Explained-Theory, Design, and Application*, 2nd ed., John Wiley & Sons Ltd., West Sussex, 2009.
- [121] Drela, M., and Youngren, H., “XROTOR User Guide,” Tech. rep., Massachusetts Institute of Technology, Cambridge, 2003.
- [122] Drela, M., “Propeller Performance Relations,” Tech. rep., 2016.
- [123] Glegg, S., “Broadband Noise from Ducted Prop Fans,” *15th AIAA Aeroacoustics Conference*, Long Beach, California, 1993. <https://doi.org/10.2514/6.1993-4402>.
- [124] Hanson, D. B., “Theory for broadband Noise of Rotor and Stator Cascades with Inhomogeneous Inflow Turbulence Including Effects of Lean and Sweep,” Tech. Rep. NASA / CR-2001-210762, NASA Glenn Research Center, 2001.
- [125] Glegg, S. A. L., and Jochault, C., “Broadband Self-Noise from a Ducted Fan,” *AIAA Journal*, Vol. 36, No. 8, 2012, pp. 1387–1395. <https://doi.org/10.2514/3.13980>.
- [126] Brooks, T. F., Pope, D. S., and Marcolini, M. A., “Airfoil Self-Noise and Prediction,” Tech. Rep. NASA-RP-1218, Hampton, Virginia, 1989.
- [127] Morin, B. L., “Broadband Fan Noise Prediction System for Turbofan Engines Volume 2 : BFaNS User ’s Manual and Developer ’s Guide,” Tech. Rep. NASA/CR-2010-216898/VOL2, NASA, 2010.
- [128] Glegg, S. A., “The Response of a Swept Blade Row to a Three-Dimensional Gust,” *Journal of Sound and Vibration*, Vol. 227, No. 1, 1999, pp. 29–64. <https://doi.org/10.1006/jsvi.1999.2327>.
- [129] Wygnanski, I., Champagne, F., and Marasli, B., “On the Large-Scale Structures in Two-Dimensional, Small-Deficit, Turbulent Wakes,” *J. Fluid Mechanics*, Vol. 168, 1986, pp. 31–71. <https://doi.org/10.1017/S0022112086000289>.
- [130] Leiblein, S., “Experimental Flow in Two-Dimensional Cascades,” *Aerodynamic Design of Axial-Flow Compressors*, NASA SP-36, 1965.
- [131] Hinze, J., *Turbulence*, 2nd ed., McGraw-Hill Inc., NY, 1987.
- [132] L. Glegg, S. A., “Airfoil Self-Noise Generated in a Cascade,” *AIAA Journal*, Vol. 36, No. 9, 2008, pp. 1575–1582. <https://doi.org/10.2514/2.583>.

- [133] Buck, S., “Measurement of Flow Separation Noise on a Full-Scale Wind Turbine,” *2018 AIAA/CEAS Aeroacoustics Conference*, Atlanta, Georgia, 2018. <https://doi.org/10.2514/6.2018-3462>.
- [134] Envia, E., “Fan Noise Source Diagnostics Test - Vane Unsteady Pressure Results,” *8th AIAA/CEAS Aeroacoustics Conference & Exhibit*, Breckenridge, 2002. <https://doi.org/10.2514/6.2002-2430>.
- [135] Sharland, I. J., “Sources of Noise in Axial Flow Fans,” *Journal of Sound and Vibration*, Vol. 1, No. 3, 1964, pp. 302–322. [https://doi.org/10.1016/0022-460X\(64\)90068-9](https://doi.org/10.1016/0022-460X(64)90068-9).
- [136] Drela, M., and Youngren, H., “Axisymmetric Analysis and Design of Ducted Rotors,” 2005, pp. 1–20. URL <http://web.mit.edu/drela/Public/web/dfdc/DFDCtheory12-31.pdf>.
- [137] Walsh, P., and Fletcher, P., *Gas Turbine Performance*, 2nd ed., Blackwell Publishing Inc., 1998.
- [138] Mort, K. W., “Performance Characteristics of a 4-Foot-Diameter Ducted Fan At Zero Angle of Attack for Several Fan Blade Angles,” Tech. Rep. NASA-TN3122, Ames Research Center, Moffett Field, CA, 1965.
- [139] Glegg, S., and Walker, N., “Fan Noise from Blades Moving Through Boundary Layer Turbulence,” *5th AIAA/CEAS Aeroacoustics Conference and Exhibit*, Bellevue, 1999. <https://doi.org/10.2514/6.1999-1888>.
- [140] Kontos, K. B., Kraft, R. E., and Gliebe, P. R., “Improved NASA-ANOPP Noise Prediction Computer Code for Advanced Subsonic Propulsion Systems, Volume 2: Fan Suppression Model Development,” Tech. Rep. NASA-CR-202309, Cincinnati, OH, 1996.
- [141] Ommi, F., and Azimi, M., “Main Fan Noise Mitigation Technologies in Turbofan Engines,” *Aviation*, Vol. 18, No. 3, 2014, pp. 141–146. <https://doi.org/10.3846/16487788.2014.969881>.
- [142] Gibbs, Y., “NASA Armstrong Fact Sheet: NASA X-57 Maxwell,” , 2017. URL <https://www.nasa.gov/centers/armstrong/news/FactSheets/FS-109.html>.
- [143] “Power or Thrust Response - 14 CFR § 33.73,” , 1971.